



HAL
open science

Fabrication of large-area hybrid perovskite solar cells

Sophie Bernard

► **To cite this version:**

Sophie Bernard. Fabrication of large-area hybrid perovskite solar cells. Material chemistry. Université de Picardie Jules Verne, 2022. English. NNT : 2022AMIE0036 . tel-04066620

HAL Id: tel-04066620

<https://theses.hal.science/tel-04066620v1>

Submitted on 12 Apr 2023

HAL is a multi-disciplinary open access archive for the deposit and dissemination of scientific research documents, whether they are published or not. The documents may come from teaching and research institutions in France or abroad, or from public or private research centers.

L'archive ouverte pluridisciplinaire **HAL**, est destinée au dépôt et à la diffusion de documents scientifiques de niveau recherche, publiés ou non, émanant des établissements d'enseignement et de recherche français ou étrangers, des laboratoires publics ou privés.



Thèse de doctorat

*Mention : Matériaux, transport et stockage de l'énergie
Spécialité : Chimie des Solides et Sciences des Matériaux*

présentée à

l'Ecole Doctorale en Sciences, Technologie, Santé (ED 585)

De l'Université de Picardie Jules Verne

par

Sophie Bernard

Pour obtenir le grade de Docteur de l'Université de Picardie Jules Verne

Fabrication de dispositifs photovoltaïques sur grande surface à base de perovskite hybride

Soutenue le 17 Janvier 2022, après avis des rapporteurs, devant le jury d'examen composé de :

M^{me} S. CASSAIGNON, Professor, Sorbonne Université,
M. J. BOUCLE, Associate Professor HDR, Université de Limoges,
M^{me} Z. CHEN, Research Scientist HDR, ESPCI ParisTech,
M. T. AERNOUITS, R&D Group Leader, IMEC,
M^{me} S. BERSON, R&D Group Leader, CEA,
M. P. SCHULTZ, Research Director HDR, CNRS,
M. A. NGUYEN VAN NHIEN, Associate Professor, CNRS,
M. F. SAUVAGE, Research Director HDR, UPJV,
M. J. ROUSSET, R&D Group Leader, EDF R&D,
M. S. JUTTEAU, R&D Engineer, EDF R&D,

Présidente
Rapporteur
Rapportrice
Examineur
Examinatrice
Examineur
Examineur
Directeur
Invité
Invité



Newton said, *“It is much better to do a little with certainty and leave the rest for others that come after you, than to explain all things by conjecture without making sure of anything”*.

I guess I did little without making sure of anything.
Good luck to the others following and enjoy the journey.

Acknowledgements

Il y a quelque chose de réellement final dans le fait de rédiger les remerciements de sa thèse. Les expériences, la rédaction et la soutenance sont terminées. Il me reste toutes les personnes qui m'ont marquée, soutenue et entourée pendant ces années particulières.

En premier lieu, je souhaite remercier les membres de mon jury qui ont accepté d'évaluer mes travaux. Un grand merci donc à Johann Bouclé et Zhuoying Chen qui ont accepté d'être les rapporteurs de cette thèse, à Sophie Cassaigon, présidente du jury, et à Tom Aernoult et Solenn Berson d'avoir accepté le rôle d'examineur. Merci également à Philip Schultz et Albert Nguyen van Nhien qui malgré une demande tardive, ont accepté de rejoindre mon jury. Merci à tous pour les questions et les échanges enrichissants pendant la soutenance.

Ces trois dernières années ont été une expérience unique, et mouvementée, ce n'est rien de le dire. Rien n'aurait été possible sans la confiance que m'ont accordée mon directeur de thèse, Frédéric Sauvage, et mes encadrants, Jean Rousset et Sébastien Jutteau. Merci Frédéric pour les échanges que nous avons eu, ainsi que les idées et remarques que tu as pu avoir sur mes travaux et mon manuscrit pour me permettre de progresser. Merci à Sébastien, la patience faite homme. Et merci Jean, à la bonne humeur communicative, toujours disponible pour s'arracher les cheveux devant mes courbes IV. Votre écoute et votre disponibilité ont été mon roc dans mes périodes d'angoisse.

Je tiens aussi à remercier toutes les personnes avec qui j'ai travaillé ou que j'ai croisé, à l'IPVF ou ailleurs. Merci donc à Matthieu Versavel, et Cédric Guérard de m'avoir accueilli au sein de EDF, d'abord en stage, puis en thèse. Merci à tout le groupe R17, Jorge, Romain, Valérie, Mireille, Régis, Sophie, toujours présents et aidants. A Armelle, ta bienveillance n'aura jamais cessé d'égailler mes journées au laboratoire. Cœur sur toi, edelweiss de mes sommets enneigés. A Nicolas, je te confie Sabrina et Jekyll, bon courage ! A Stefania, my darling, la meilleure voisine de bureau que l'on puisse avoir. A Sam, soutien indéfectible, au baby-foot et ailleurs. A Solène, mon incroyable voisine du 14^e. Mention spéciale aux doctorants EDF, aux anciens et aux nouveaux. A Adrien, Fabien et Arpit, qui m'ont initié au football. A Margot, Emilie, Olivier et Anatole, pour nos soirées ciné. A la relève, Marie, Salim, Thomas et Eliza, encore dans la tourmente ! Pensée spéciale pour Célia, qui reprend ce sujet de thèse : Force et bravoure, je te fais confiance pour le sublimer. Merci à tous ceux aussi, qui ont peuplé mes journées au laboratoire, aux conférences, aux bars. Merci à Karolien, à Rafaël, à Capucine, à Guillaume, à tous les Thomas, à Vincent, à Amadéo, à Davide, à Marion, à Stéphanie, à Iwan, à Van-Son, à Julie ... J'en oublie sûrement, j'espère qu'ils me pardonneront.

Pour finir, je voudrais remercier mes proches. Mes amis et ma famille. Ceux qui, sans rien y connaître m'ont écouté me plaindre et m'enthousiasmer pendant presque 4 ans. A tous les hochements de tête patients, les coups de fils de soutien, les câlins, les petits mots quand il le fallait. A ceux qui sont venus ou ont écoutés ce 17 janvier, juste pour être là. Merci d'avoir partagé ça avec moi. Merci d'être et d'avoir été là.

Votre soutien m'a été infiniment précieux. Cette thèse est avant tout la vôtre. Du fond du cœur, merci.

Table of contents

ACKNOWLEDGMENTS	4
TABLE OF CONTENTS	6
ABBREVIATIONS AND SYMBOLS	9
GENERAL INTRODUCTION	11
<u>Chapter 1: State of The Art</u>	
1. Introduction	15
1.1 Global energy landscape	15
1.2 Solar Energy	16
1.3 Tandem solar cells	18
1.4 Perovskite solar cells	21
2. Crystallization model	24
2.1 Lamer Theory	24
2.2 Discussion	29
3. Scalable deposition of perovskite absorber	31
3.1 Spin-coating method: Locks and constraints	31
3.2 Scalable deposition methods overview	32
3.3 Slot-die coating deposition process	35
4. Solvent extraction strategies	36
4.1 Anti-solvent method	36
4.2 Solvent evaporation mechanism	37
4.3 Alternative solvent extraction systems	38
5. Conclusion	42
6. References	43
<u>Chapter 2: Methodology of fabrication of the perovskite device and effect of surfactant addition</u>	
1. Introduction	57

2.	Device architecture and fabrication protocol	59
2.1	Preparation and etching of the substrate	60
2.2	TiO ₂ bi-layer deposition	60
2.3	HTL deposition and evaporation of the gold electrodes	62
3.	Perovskite Absorber Layer By Slot-Die coating	63
3.1	Presentation of the slot-die configuration	63
3.2	Optimization of the coating parameters	65
3.3	The drying step	70
4.	Surfactant addition in the perovskite solution	73
4.1	Nucleation theory and surface energy tailoring	73
4.2	Composition and structure of surfactants	74
4.3	Deposition of Cs _{0,2} FA _{0,8} Pb(I _{0,95} Br _{0,05}) ₃ perovskite	75
4.4	Deposition of Cs _{0,17} FA _{0,73} Pb(I _{0,6} Br _{0,4}) ₃ perovskite	85
5.	Conclusion	95
6.	References	96

Chapter 3: Addition of methylammonium chloride

1.	Preliminary spin-tests	102
1.1	Differences between anti-solvent and vacuum aspiration solvent extraction methods	102
1.2	Influence of the MACl addition	104
2.	Optimisation of the slot-die deposition conditions	108
2.1	Effect of the MACl addition on the crystal structure	108
2.2	Effect of the MACl addition on the perovskite morphology	110
2.3	Influence of the annealing conditions on the perovskite film properties	112
3.	Full devices performances	117
3.1	Small-cells performances	117
3.2	Modules	120
4.	Stability tests	122
4.1	Encapsulation of perovskite devices	122
4.2	Encapsulation impact on the devices performances	123
4.3	Impact of annealing conditions on full devices stability	124
4.4	Post-mortem characterization of aged devices	125

5. Conclusion	131
6. References	132

Chapter 4: Synergic action of surfactant and MACL addition

1. Morphological and structural analysis	141
1.1 Grain size analysis	141
1.2 Surface roughness analysis	142
1.3 Crystal structure analysis	146
1.4 Optical properties	147
1.5 Crystallization mechanism	148
2. Full devices performances	149
2.1 Spiro-OMeTAD as Hole Transport layer	150
2.2 PTAA as Hole Transport Layer	152
2.3 Aging in dark conditions	155
3. Integration in semi-transparent perovskite cells architecture	157
3.1 ITO deposition and fabrication of the solar cells	157
3.2 Morphological characterization	158
3.3 Optical properties	159
3.4 Semi-transparent solar cells performances	160
3.5 Aging in dark conditions	163
4. Tandem performances projection	165
5. Conclusion	168
6. References	170
GENERAL CONCLUSION	175
APPENDIX	178
RESUME EN FRANÇAIS	198

Abbreviations & Symbols

3DPS	3-(Decylmethylammonio)propanesulfonate inner salt	
AZO	Aluminum-doped zinc oxide	
Br	Bromide	
Cl	Chloride	
CL	Cathodoluminescence	
Cs	Cesium	
DMF	N,N-Dimethylformamide	
DMSO	Dimethyl sulfoxide	
DPSO	Diphenyl sulfoxide	
E_g	Bandgap Energy	eV
FA	Formamidinium	
FAI	Formamidinium Iodide	
FF	Fill Factor	%
FK209 Co(III)	Tris[2-(1H-pyrazol-1-yl)-4-tert-butylpyridine bis(trifluoromethylsulfonyl)imide)]	cobalt(III)tris
FTO	Fluorine-doped Tin Oxide	
I	Iodide	
ITO	Indium Tin Oxide	
J_{sc}	Short-circuit Current Density	mA/cm ²
J-V	Current density-voltage	
LiTFSI	lithium bistrifluoromethanesulfonimide	
MA	Methylammonium	
MACl	Methylammonium Chloride	
MPP	Maximum Power Point	
NMP	1-méthyl-2-pyrrolidone	
P	Pressure	mbar
PbI₂	Lead Iodide	
PCE	Power Conversion Efficiency	%

PEEK	poly-etherethercetone	
PSCs	Perovskite Solar Cells	
PTAA	Poly(triarylamine)	
Pvk	Perovskite	
R_i	Ionic radius	nm
Rpm	Rotation per minute	
S_a	Arithmetical Mean Height	μm
SEM	Scanning Electron Microscope	
T	Temperature	°C/K
TAA	titanium diisopropoxide dis(acetylacetonate)	
tBP	4-tertbutylpyridine	
TiO₂	Titanium dioxide	
V_{oc}	Open-circuit Voltage	V
XRD	X-ray Diffraction	

General Introduction

Although photovoltaic electric production still provides only a small fraction of the global energy supply in 2021, according to the latest GIEC report: “*it has one of the largest technical potential of all energy sources and, in concert with technical improvements and resulting cost reductions, could see dramatically expanded use in the decades to come.*”. However, reducing cost depends on the level of solar energy deployment combined with continuous R&D efforts to improve the performance and reliability of the PV technologies.

To this end, emerging PV technologies, such as hybrid perovskite material, represent an exciting pathway to spur up solar energy at the forefront of energy supply. Several intrinsic hybrid perovskite properties, such as high absorption coefficients, long carrier diffusion lengths, and possible bandgap tuning, are well suited for photovoltaic conversion. The swift improvement of the perovskite-based devices performances has already made it the rising star of the photovoltaic world. Today, the best device demonstrates an efficiency of 25.5% (**Fig. A**). For practical industrial applications, though, perovskite technologies must be more stable and demonstrate their scalability compatibility.

This thesis focused on the various issues related to the transfer of perovskite material toward scalable deposition methods. During the past few years, remarkable progress in large-scale PSC manufacturing has been made (**Fig. A**). The surge in performance of small-area devices is ascribed mainly to the improved composition and morphology of perovskite thin films owing to innovations in solution chemistry, device architecture, interfaces passivation, and deposition processes. These developments have been readily transferred to tandem structures, resulting in increased efficiency closely following the trend of single-junction silicon devices. By contrast, the efficiencies of large-area perovskite modules notably lag behind those of single-cell devices, pointing out the need for further investigations. Ink composition engineering plays a vital role in forming high-quality perovskite to achieve precise control of the crystallization process during device fabrication. Keeping this in mind, we focused on the composition of the perovskite solution to fit the new constraints related to upscale fabrication.

This thesis is divided into four chapters. The first one is dedicated to the state-of-the-art survey on photovoltaic energy and, more specifically, perovskite-based solar cells. The properties of the perovskite material, the existing crystallization models, the different deposition methods, and the associated solvent extraction systems are detailed herein.

The second chapter describes all the steps leading to the fabrication of a complete device that has been carried out during this work. A n-i-p reference structure composed of a bilayer of TiO₂ to transport the photogenerated electrons, Spiro-OMeTAD for the holes

transport, and a gold top electrode were fabricated. A method combining the slot-die deposition of the perovskite solution and solvent extraction by aspiration has been developed for the absorber layer deposition. The deposition process of the perovskite absorber is decomposed into two parts: The optimization of the slot-die deposition parameters and then a study focusing on the addition of a zwitterionic surfactant into the perovskite solution.

The third chapter is dedicated to the fabrication of a $\text{Cs}_{0.17}\text{FA}_{0.83}\text{Pb}(\text{I}_{0.83}\text{Br}_{0.17})_3$ perovskite layer with the addition of MACl as a complexing agent. The characteristics of the perovskite material depending on the additive concentration and annealing conditions are presented. We also studied the stability of encapsulated complete perovskite-based devices, exposed under one sun illumination for 300 hours. Finally, 12 cm^2 modules have been fabricated with an optimized MACl ratio.

In the last chapter, the zwitterionic surfactant and the MACl properties have been combined to obtain a high-quality perovskite layer. Notably, a particular focus has been dedicated to surface roughness properties. In this part, the performances of solar devices with two different hole transport layers (Spiro-OMeTAD and PTAA) have been compared. With the ultimate aim of validating the compatibility of our structure for tandem applications, we fabricated semi-transparent devices and characterized their performances. Finally, the pseudo-tandem potential efficiencies have been calculated.

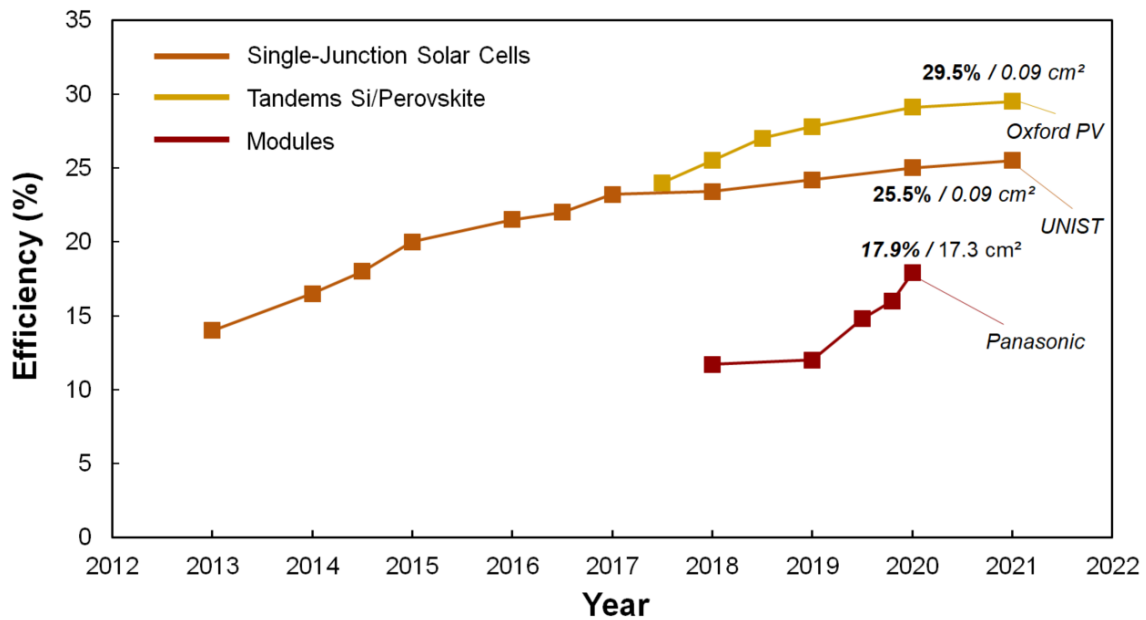


Figure A: Efficiency evolution of perovskite-based devices [NREL].

CHAPTER 1:

State Of The Art

The first chapter of this Ph.D. dissertation aims to describe the general context of this study and our motivations.

The first part outlines the world energy context and the special place of solar energy in the global production landscape. We especially develop the field of single-junction perovskite devices and tandem technologies, including their properties and potential applications.

Then, we present the different existing theoretical models describing the crystallization mechanisms. The specific case of thin-films perovskite crystallization will be emphasized.

The third part lists the different upscale deposition techniques employed for the perovskite films. In particular, the slot-die deposition technique will be emphasized together with its commercial applications, which is at the core of this thesis.

Lastly, we highlight the drying step's role as part of the fabrication of the perovskite layer. Several solvent extraction systems will be presented to assist the film's crystallization.

SUMMARY

1. Introduction	15
2. Crystallization model	24
3. Scalable deposition of perovskite absorber	31
4. Solvent extraction strategies.....	36
5. Conclusions.....	42
6. References.....	43

1. Introduction

1.1. Global energy landscape

The energy sector underpins all aspects of our modern societies. With a growing world population, estimated to reach 9.7 billion in 2050¹, and emerging countries in full development, energy demand will continue to increase in the future years. Despite the global coronavirus pandemic, which strongly subdues global energy consumption in 2020, demand for all fossil fuels has continued to grow significantly in 2021.²

Nowadays, more than 80% of the world's primary energy consumption originates from fossil resources (gas, coal, oil) (**Figure I-1.a.**), representing over 500 exajoules.³ In 2021, coal-based energy consumption alone was projected to increase by 60% by the end of the year compared to 2020 levels. The combustion of fossil fuels is responsible for most global greenhouse gas emissions and air pollution. Even if the restrictions due to the Covid-19 pandemic generated a temporary drop of 8% in the CO₂ global emissions of 2020 compared to 2019, the general tendency demonstrates a gain of almost 5% by year in the last decades (**Figure I-1.b.**). Moreover, the fossil fuel reserves depletion generates more difficulties of extraction and thus raises the operational cost and investments that can hamper long-term supply in the future. These resources are also largely unequally distributed, which is a source of geopolitical pressures in critical areas.²

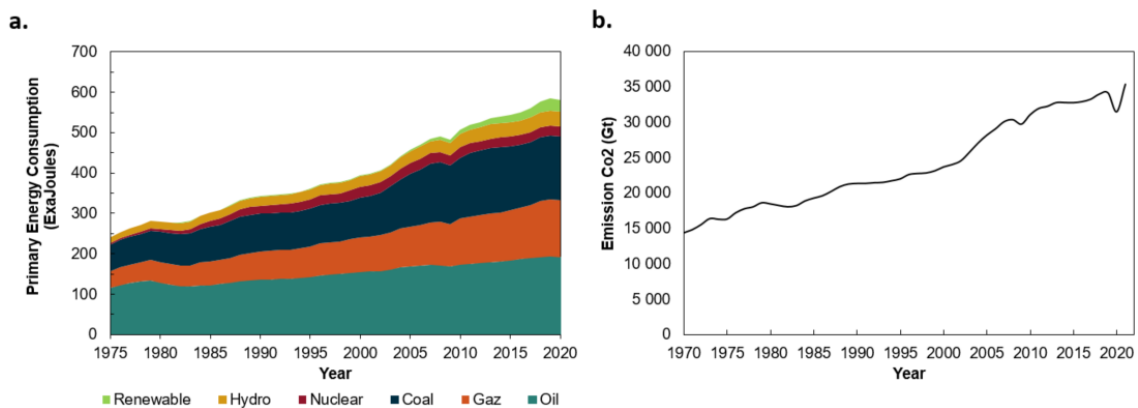


Figure I-1: a. World Primary energy consumption by fuel resources. Data extracted from ref. [4]. b. Global energy-related CO₂ emission. Datas are reproduced from ref. [3].

Global warming awareness is becoming a societal issue that cannot be avoided. The scientific community has expressed its concern since the 1950s, but few tangible measures have been deployed since that time. During recent international climate negotiations, most actors are committed to diminishing their carbon footprint for limiting Earth's global warming to 1.5°C.⁵ However, to hold this commitment, a rebalancing of

primary energy resources by renewable resources is essential. Demand for renewable energies grew by 3% in 2020 and is set to increase across all key sectors (power, heating, industry, and transport).⁶

1.2. Solar Energy

The early development of solar technologies started about 150 years ago. In 1839, Edmond Becquerel, a young French physicist, discovered the photo-galvanic effect based on the visualization of a built-in cell voltage and electrical current when exposing metal electrode modified halide to light. The photovoltaic effect theory is briefly displayed in **Annex 1**. Forty-five years later, Charles Fritts first exploited this effect by installing the world's first rooftop photovoltaic solar array, using 1%-efficient selenium cells, on a New York City.⁷ The development of solar technologies stagnated until mid of the 20th century because of the large availability of coal and petroleum and the lack of materials, particularly semiconductors.

However, during the Cold War, the following space programs triggered the revolution of photovoltaics (PV) and solar-powered systems, thanks to the fast democratization of p-n transistors. In 1958, the first space solar panel equipped the American satellite Vanguard 1 and, in 1967, Soyuz 1 became the first crewed spacecraft powered by solar panels. In addition, the oil embargo of 1973 and the following economic and energy crisis prompted a reorganization of energy policies worldwide and brought attention to solar technologies to the general population.

In addition, in light of rising global warming concerns, PV technologies represent a new way to consider the future energy landscape. In the mid-1990s, residential and commercial rooftop solar and utility-scale photovoltaic power stations accelerated again due to oil and natural gas supply issues. In the 2000s, the favorable energetic policy of the European Union contributed to a high level of investments and a high number of PV deployments in Europe (**Figure I-2.a**).

The improved PV power efficiency and the increasing market maturity led to the downward trend in solar PV module costs. Between December 2009 and December 2019, crystalline silicon module prices declined between 87% and 92%, depending on the technology, reaching an average price of 0.3 \$/Watt (**Figure I-2.b**). More than half of the renewable capacity added in 2019 achieved lower electricity costs than new coal. Electricity cost from utility-scale solar PV fell by 13% by year, reaching nearly seven US cents the kilowatt-hour (kWh) in 2019. Such recent module cost reduction is mainly due to larger productions lines, module manufacturing, process optimization, and efficiency gains associated with increased adoption of newer cell architecture types.

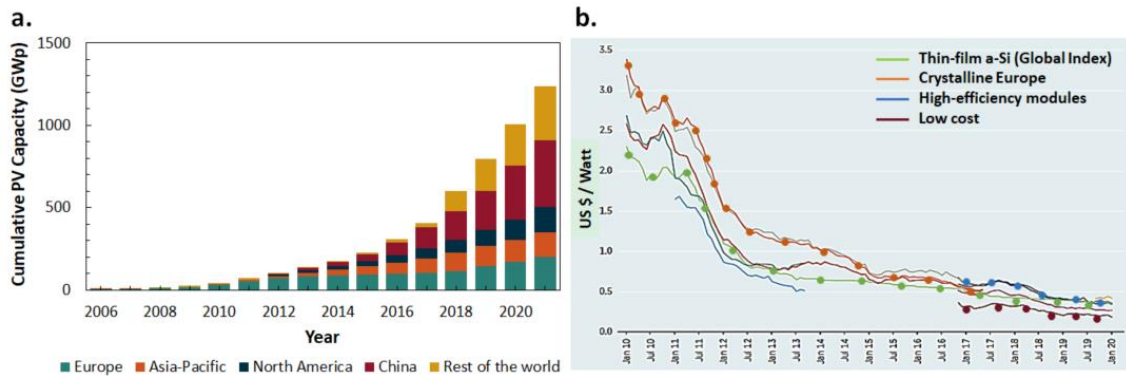


Figure I-2: a. Global growth of cumulative PV capacity in gigawatts (GWp) with regional shares. Data extracted from ref. [6]. **b.** Average monthly solar PV module prices by technology and manufacturing country sold in Europe, 2010 to 2020. Reproduced from ref. [8].

For several years, the worldwide growth of solar PV was driven by European deployment. However, larger-scale industrialization to sustain the PV democratization has shifted to Asia, especially China, the largest PV market since 2018. Worldwide, the share of renewables in electricity generation increased by 25% in 2021 compared to 2020, mainly due to new solar PV and wind installations. Global PV capacity has grown on average by 20% per year since 2000. This new capacity addition is the highest among all renewable energy technologies for the last decade. As a result, the total installed capacity reached a power of 1050 GW at the end of 2020, led by China, which almost represents half of this capacity (i.e., 408 GW). In 2021, solar PV electricity generation alone is expected to approach 1000 TWh⁶, representing 3% of the world electricity production mix.

Recently, the research applied in photovoltaics has prompted the emergence of a large number of technologies. **Figure I-3** pools together the evolution of photovoltaic efficiencies for the different technologies since 2000. A short description of silicon and thin-film PV technologies is displayed in **Annex 2**.

Today, the solar technologies market is dominated by silicon-based technology, mainly represented by single-crystalline technology.⁹ However, thin films technologies based on alternative materials like Cadmium Telluride (CdTe), copper indium gallium diselenide (CIGS), and other materials (dye-sensitized, Concentrated PV, organic PV) have gradually emerged. Among recent technologies, hybrid perovskite solar cells became one of the most promising paths to compete or combine with silicon technology.

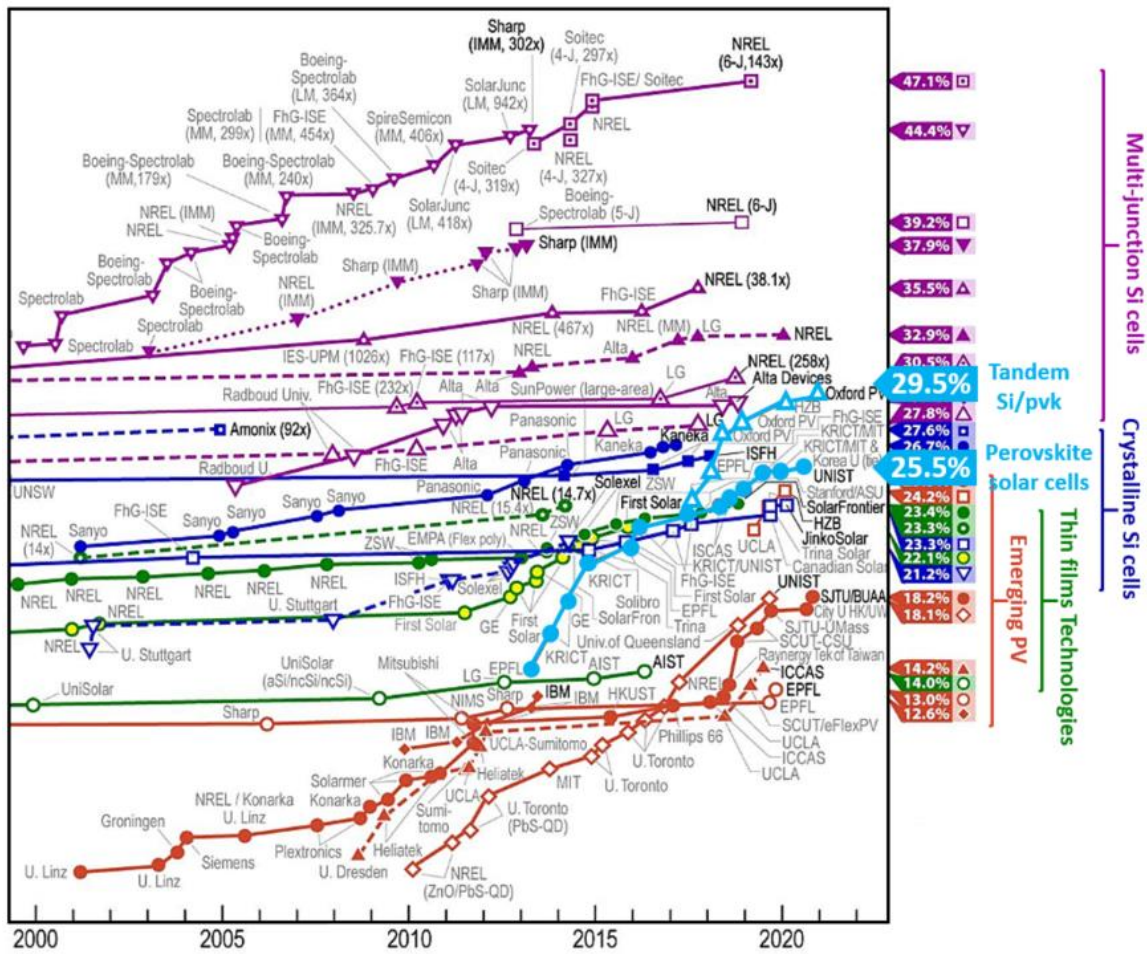


Figure I-3: Evolution of photovoltaic efficiencies by sector from 1975 to 2021. Extracted from Best Research-cell Efficiencies Chart of NREL [10]. This graph is regularly updated by the National laboratory Renewable Energy Laboratory (NREL). An original version is displayed in Annex 3.

1.3. Tandem solar cells

The power conversion efficiency of solar cells is a crucial driver for reducing the cost per area of PV electricity. Despite a rapid improvement in the solar cells efficiency for the last twenty years, the best technologies are now approaching further to the Shockley-Queiser (SQ) thermodynamic limit (**Figure I-4.a.**). Therefore, tandem solar cells, combining a low bandgap bottom cell and a higher bandgap top cell, represent a promising way to cross the threshold of 30% PCE. Under illumination, each cell produces an electric current in response to different wavelengths domains, improving the cell's electrical conversion potential (**Figure I-4.b.**).

Perovskites have been proven to be an excellent top cell candidate for multi-junction solar cells due to their tunable bandgap, easy fabrication, and potential low-cost fabrication.¹¹⁻

¹⁴ Since silicon (Si) solar cells dominate the current market, incorporating perovskite cells onto commercial Si solar cells represents a substantial stake in the industrialization of perovskite solar cells.¹³

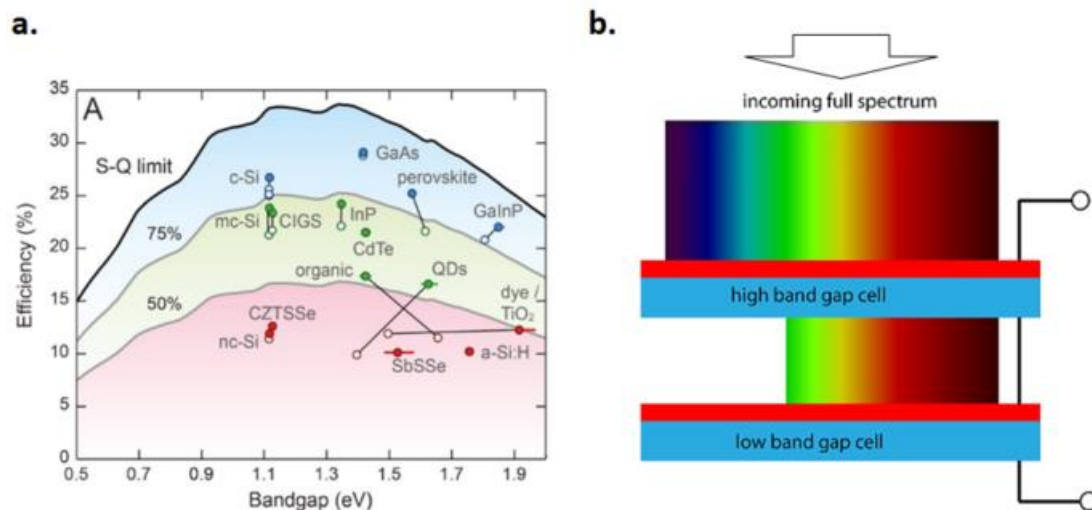


Figure I-4: **a.** Record efficiency of solar cells of different materials against their bandgap compared to the associated SQ limit (top solid line). Reproduced from ref. [15]. **b.** Series connected tandem solar cell. Adding more devices allows for each device to be optimized to a narrower spectrum giving a higher overall efficiency. Reproduced from ref. [12].

Two types of tandem architectures exist: two-terminal devices (2T), also called monolithic tandem cells, and four-terminal cells (4T) composed of a stack of two distinct solar cells (**Figure I-5.a.**). Even if the goal remains the same, each configuration has pros and cons.

A 2T junction is a monolithic configuration where the perovskite layer is deposited upon the bottom layer, generally a Si p-n junction. The integration process can be complicated. The Si surface properties directly affect the deposition of the top cell. Textured pyramidal silicon surfaces especially represent a major challenge to the uniform deposition of the perovskite layer.¹⁶ Thus, the top-cell has to be fabricated without damaging the bottom cell. In addition, the 2T tandem needs a fine-tuning of the bandgap and thickness to match the current produced by both cells (**Figure I-5.b.**). Moreover, the stability of the whole device is currently limited by the perovskite top cell.

In 2020, a 2T Pvk/Si tandem solar cells reached a certified value of 29.5% PCE on a ~ 1 cm² device area.¹⁷ This put additional credit to the tandem approach to pave the way of achieving 30% efficiency as a milestone (**Figure I-5.c.**).

In a 4T configuration, the cell components are electrically independent as a result of the physical separation of the two sub-cells. It allows the optimization of the two devices

independently. However, the inclusion of 3 transparent interlayers can generate significant optical losses, and the use of 4 terminals could increase the final cost due to integration and additional materials (TCO, metals).¹⁸ Recently, fine-tuning of the optical path by optimizing the Si surface patterning and optimizing the perovskite layer thickness allowed B. Chen *et al.* to reach a 28.2% PCE with a 4T Si/perovskite tandem device (Figure I-5.c).¹⁹

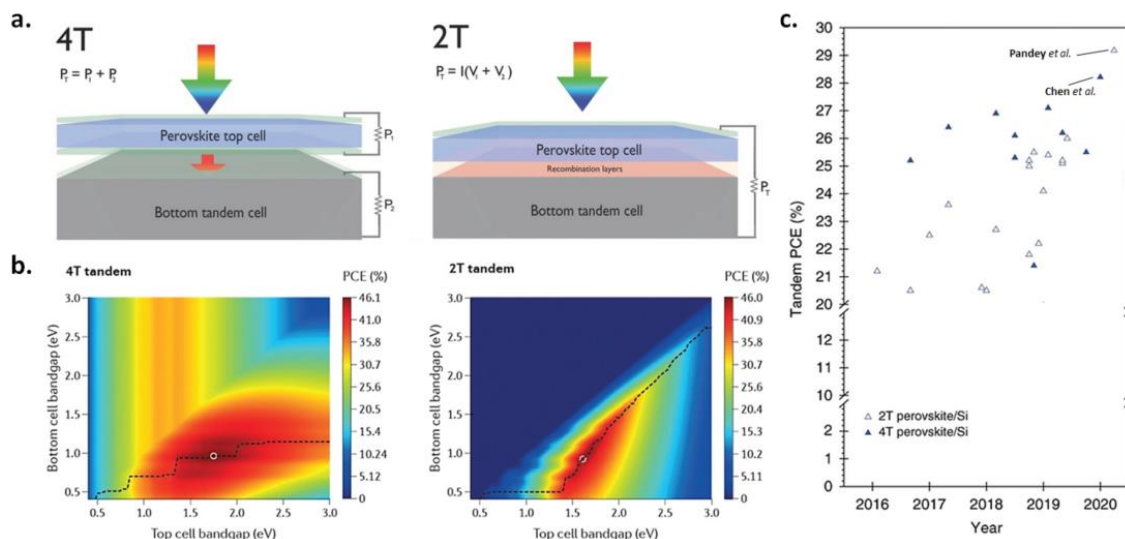


Figure I-5: a. 4T and 2T series-connected tandem configurations. Reproduced from ref. [11]. b. Theoretical maximum PCE for 2T and 4T tandem solar cells. Reproduced from ref. [13]. c. PCE progress of perovskite-based tandem solar cells. Reproduced from ref. [19].

Currently, Pvk/Si tandem solar cells are already being developed for future commercial applications. Notably, Oxford PV¹⁷ and Swift Solar²⁰ have developed industrial-scale pilot lines. However, the efficiency gain increases the complexity and manufacturing prices. To date, their application has been limited to particular cases, notably in aerospace, where their high power-to-weight ratio is desirable. To enable the broader application of perovskite-based multi-junction solar cells, the stability of perovskite cells needs to be comparable to those of other relevant technologies, such as c-Si or CIGS. Moreover, the reported single-junction perovskite and multi-junction cells have been fabricated in small areas. More extensive researches have to be conducted to generate efficient large-scale tandem devices.

1.4. Perovskite Solar Cells

Perovskite solar cells achieved a swift increase in performance during the last ten years, attaining a single-junction record of 25.5% in 2021.²¹ Moreover, perovskite solar cells are expected to be highly cost-effective in production, making this technology an attractive option for industrial production and commercialization.²² However, the transfer from lab cells to scaling-up fabrication processes and the perovskite stability remain highly challenging.

1.4.1. History

Organic-inorganic hybrid perovskite solar cells have benefited from dye-sensitized solar cells (DSSC) technology. In 2009, Kojima *et al.* reported an efficiency of 3.8% for a perovskite-based device using methylammonium lead iodide as the absorber in nanoporous TiO₂ for DSSC.²³ However, research for these materials did not spark immediate attention in the scientific community because of their low efficiency and low stability in conjunction with a liquid electrolyte based on I₃⁻/I. In 2011, Park *et al.* successfully improved the material stability and reached a 6.5% PCE²⁴ using the same dye-sensitized concept. Then, Park *et al.* contacted the perovskite layer with a solid-state spiro-OMeTAD hole transport layer²⁵, and soon after, Snaith *et al.*, achieving efficiencies above 10%.²⁶ This efficiency was raised to 15% by developing a two-step deposition process.²⁷ As a result, a range of new solution-based deposition strategies and higher efficiencies were reported.²⁸⁻³⁰ In 2015, for the first time, a perovskite device tailored by researchers at KRICT (South Korea) achieved a record efficiency over 20% (non-stabilized).³¹ Then, optimization of the transport layers, the perovskite material, and the electrode³²⁻³⁴ combined with the interfaces passivation^{35,36} allowed to set quickly new perovskite records. Today, the best cell efficiency is 25.5%, claimed by Jeong *et al.*²¹

1.4.2. Crystal Structure

Organic-inorganic hybrid lead halide perovskite is generally labeled as an ABX₃ compound, where A is an organic cation, most often methylammonium MA⁺ (CH₃NH₃⁺) or formamidinium FA⁺ (HC(NH₂)₂²⁺), B is a metal, usually lead (Pb²⁺) or tin (Sn²⁺), and X is iodide (I⁻), bromide (Br⁻) and/or chloride (Cl⁻). A schematic representation of the perovskite crystal structure is displayed in **Figure I-6**.

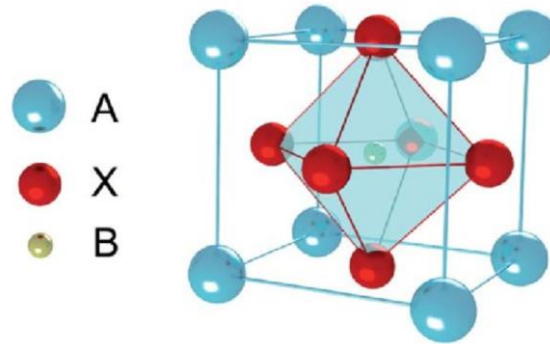


Figure I-6: ABX_3 perovskite structure

First described by Goldsmith in the 1920s, it was named after the CaTiO_3 structure. The ideal perovskite crystal structure has cubic symmetry, with a corner-sharing BX_6 octahedral structure and cub-octahedral voids occupied by the A cations. However, depending on the composition of the perovskite, possible distortion of the former cubic structure can occur, leading to symmetry breaking. This can be anticipated using the so-called Goldsmith tolerance factor t , which can be determined using the following equation (Eq.1).

$$t = \frac{r_A + r_X}{\sqrt{2}(r_B + r_X)} \quad (\text{Eq.1})$$

With r_A and r_B , the radius of cations A and B and, r_X the radius of the anion. The empirical tolerance factor t allows predicting which structure is preferentially formed. The crystal structure can change depending on the size and interaction of the A cation and the corner-sharing BX_6 octahedral.³⁷ When t is between 0.9-1.0, the crystal structure is cubic. Between 0.71 and 0.9, the perovskite is distorted into orthorhombic, tetragonal, or rhombohedral structures if the A-cation is too small or the B-cation becomes too large. For t higher or lower than 0.71-1, a non-perovskite structure is formed.

1.4.3. Composition Engineering

1.4.3.1. Multi-cations compositions

The perovskite absorber archetypal composition is the methylammonium lead iodide ($\text{CH}_3\text{NH}_3\text{PbI}_3$). It will be noted MAPI in the following of the thesis. In its most common form, the methylammonium lead tri-iodide adopts a tetragonal structure. However, the high volatility of the methylammonium (MA) cation penalizes the long-term stability of the devices.^{38,39} Due to its soft matter nature, the MA-based perovskite structure demonstrates significant structural changes occurring for temperatures above 85°C . The decomposition of the perovskite material into methylamine (CH_3NH_2) and

hydrogen iodide (HI) gases results in a film degradation into PbI_2 .⁴⁰ It represents a considerable problem in regions with high insolation and high operating temperatures.

Recently, research efforts have been shifted to methylammonium-free compositions to improve the stability of the perovskite material.⁴¹ Due to its more favorable optical bandgap of around 1.45 eV and higher thermal stability, the Formamidinium (FA) cation is currently the best candidate for high-efficiency PSCs. However, the larger size of the FA cation ($R_{\text{FA}^+} = 0.19\text{-}0.22$ nm compared to $R_{\text{MA}^+} = 0.18$ nm) can create a lattice distortion. In fact, the cation size induces low-temperature lattice strains, which relax through a tilt of the octahedral site.⁴² Z. Li *et al.* demonstrated that, at ambient temperature, the FAPI composition stabilizes in a δ phase. The photo-active α phase is thermodynamically stable only above 160 °C.³⁷ **Figure I-7** illustrates that the formation of yellow δ -phase FAPbI_3 can be suppressed by optimizing the tolerance factor by incorporating smaller cations such as Cs^+ . It is also possible to stabilize the α -phase FAPbI_3 by mixed compositions with the inclusion of halides like Br^- or cations like MA^+ .⁴³

Consequently, the mixed cation CsFA perovskite composition affords to stabilize the α -phase at lower temperatures, leading to enhanced thermal and moisture stability of the perovskite material.⁴⁴ The improved stability and better crystallinity lead to enhanced opto-electronic properties of the solar cells, including better carrier mobility and diffusion lengths.⁴³ Therefore, mixed cations into the lead halide perovskite represent a promising path toward more stable devices, therefore more promising for the upscale and industrialization steps.⁴⁵

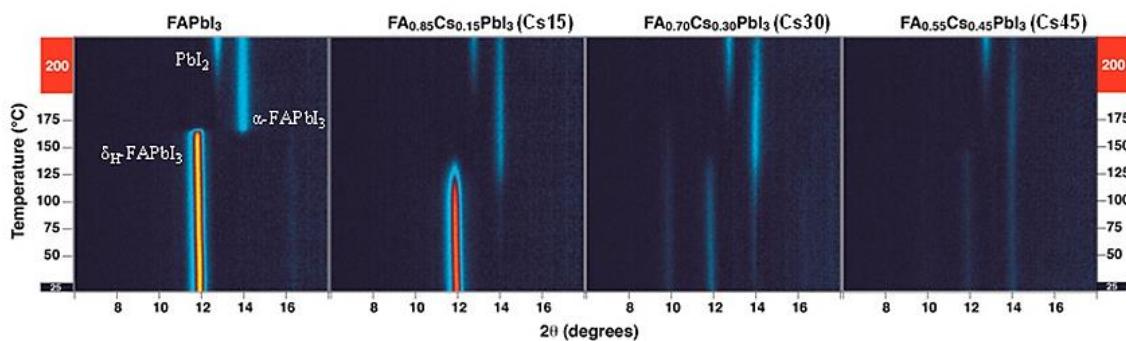


Figure I-7: Temperature-dependent XRD of FA-based perovskite with gradual augmentation of the cesium content. Reproduced from ref. [42].

1.4.3.2. Bandgap Tailoring

One of the intensively studied development paths for perovskite solar cells is their final integration into tandem architecture. Perovskite solar cells yield numerous advantages as a top-cell candidate. One of them is the possibility to tune its bandgap towards the

optimum value of around 1.7 eV, notably by halide substitution of iodide by bromide (**Figure I-8.a.**)^{46,47}

However, in $\text{Cs}_x\text{FA}_{1-x}\text{Pb}(\text{Br}_y\text{I}_{1-y})_3$ perovskite composition, a bromide ratio y superior to 0.2 can induce a phase segregation (Br-rich and I-rich domains), which is a significant drawback also for the long-term stability. However, this reaction can be hampered by increasing the Cs content, as demonstrated by Bush *et al.*, who highlighted two stable compositions with a bandgap of over 1.65 eV: $\text{Cs}_{0.25}\text{FA}_{0.75}\text{Pb}(\text{Br}_{0.2}\text{I}_{0.8})_3$ ($E_g = 1.68\text{eV}$) and $\text{Cs}_{0.4}\text{FA}_{0.6}\text{Pb}(\text{Br}_{0.3}\text{I}_{0.7})_3$ ($E_g = 1.75\text{eV}$) (**Figure I-8.b.**)

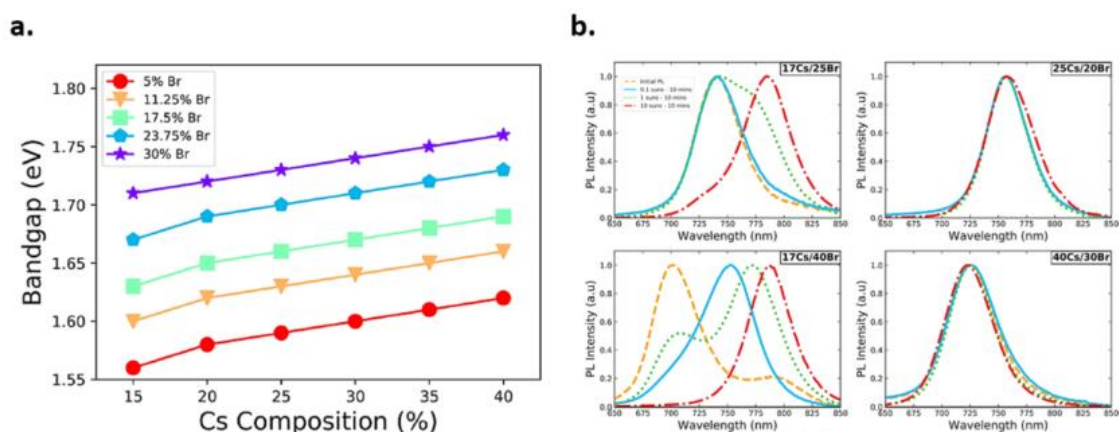


Figure I-8: **a.** Bandgap vs. perovskite composition for $\text{Cs}_x\text{FA}_{1-x}\text{Pb}(\text{Br}_y\text{I}_{1-y})_3$ compositional space, showing a change in Cs+ ratio along the x-axis and a change in Br- ratio 5 to 30% as separate lines. **b.** Device PL data, which compared perovskites composition with different Cs/Br ratios. Reproduced from ref. [48].

An additional strategy to increase the bandgap consists of incorporating chloride anions in the perovskite structure to form a triple halides composition. For example, J. Xu *et al.* studied the influence of Cl^- inclusion on the phase stability for different CsFA compositions. The optimized halides ratio ($\text{Br}_{0.15}\text{I}_{0.8}\text{Cl}_{0.05}$) led to a bandgap value of 1.67 eV and achieved as high as 27% stabilized power conversion efficiency (PCE) on a 1 cm^2 tandem Si/Perovskite device area.⁴⁹

2. Crystallization model

2.1. La Mer Theory

Viktor La Mer proposed a model describing nucleation and crystal growth mechanisms in a liquid.⁵⁰ His model is said to be “atom-mediated” and initially considers monomers' movement and interactions.

As illustrated in **Figure I-9.a**, in the perovskite precursors solution, the La Mer curve depicts the change of precursors concentration in solution over time. The main parameters to describe the overall nucleation and crystal growth phenomena, which impact the final crystal size and morphology, are:

- C_s , the limit of solubility. The precursors start to precipitate but dissolve back in the solution.
- C^*_{min} , the minimum concentration before entering into the supersaturation state.
- C^*_{max} , the maximum concentration of the supersaturation state.

According to the La Mer model, the crystallization process can be decomposed into three main stages (**Figure I-9. a.**), detailed in the following parts.

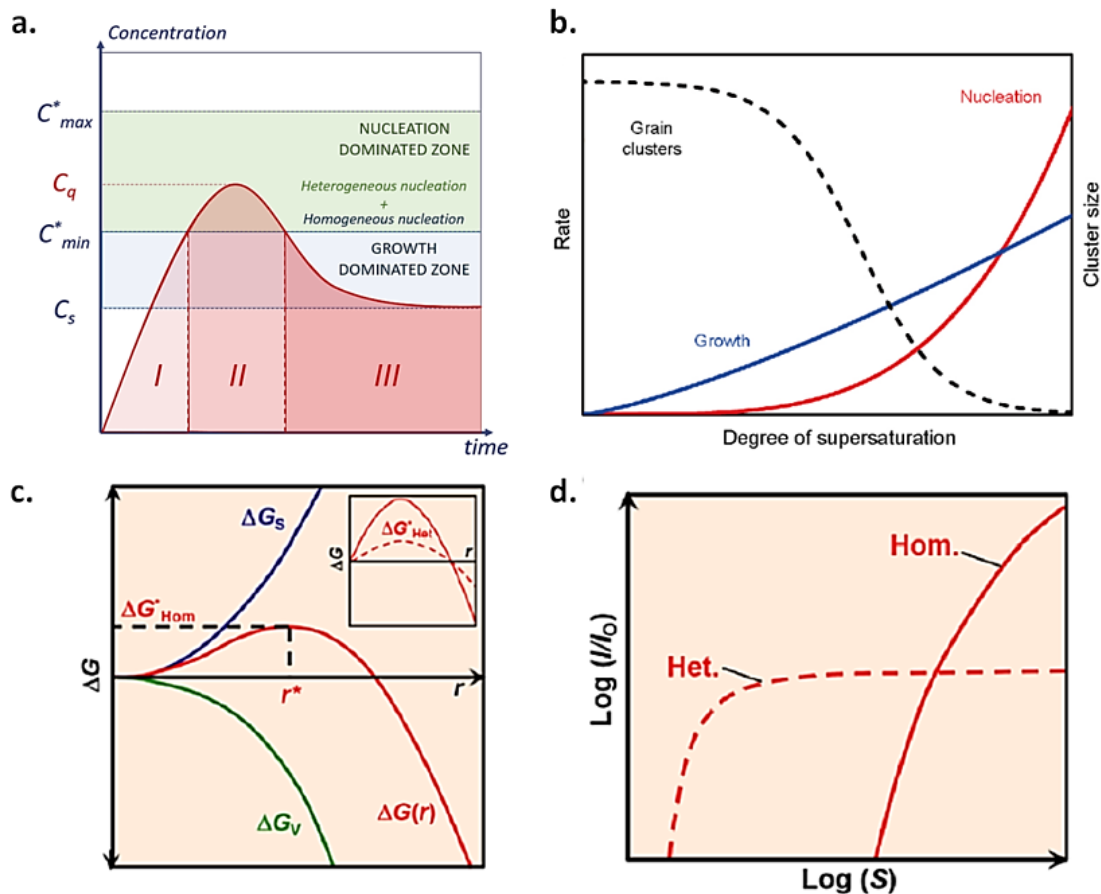


Figure I-9: **a.** La Mer curve adapted from ref. [50,51]. **b.** Nucleation (red trace) and growth (blue trace) rates as a function of the supersaturation degree and influence on the grain cluster size (dashed black trace). Reproduced from ref. [52]. **c.** Free energy change (ΔG), surface free energy (ΔG_s) and volume free energy (ΔG_v) changes, with a function of nucleus radius (r) for homogeneous nucleation and heterogeneous nucleation. Reproduced from ref. [53,54]. **d.** Normalized nucleation rate as a function of supersaturation ratio for homogeneous and heterogeneous nucleation. Reproduced from ref. [53,54].

2.1.1. Pre-nucleation process

When the solvent starts to evaporate ($t = 0$), the concentration of precursors increases along a straight line. The slope of the curve between C_0 and C_{min} depends on the solvent extraction methods. In the case of a perovskite film, the extraction can occur either by forced evaporation of the solvent (air blow, aspiration, or annealing) or dripping of an anti-solvent on the substrate. The different extractions methods will be further described in **part 4**.

When C exceeds C_s , the precursors begin to precipitate. In the classical theory of nucleation, nucleation and growth are governed by the variation of particles' Gibbs free energy ΔG (**Eq.2**). A nucleus is regarded as a sphere of a condensed phase, and its total free energy is defined as the sum of the surface free energy ΔG_s and the bulk free energy ΔG_v .

$$\Delta G = \Delta G_s + \Delta G_v \quad (\text{Eq.2})$$

ΔG represents the positive free energy between the particle surface and the bulk and is defined as:

$$\Delta G = 4\pi r^2 \gamma + \frac{4}{3}\pi r^3 \Delta G_v \quad (\text{Eq.3})$$

Here, ΔG quantity is proportional to the radius r of sphere nuclei and γ the interfacial energy by surface unit. ΔG_v depends on the Boltzmann's constant k_B , the temperature T , the molar volume V and the degree of supersaturation of the solution $\frac{C}{C_{min}}$:

$$\Delta G_v = \frac{-k_B \cdot T \cdot \ln \left(\frac{C}{C_{min}} \right)}{V} \quad (\text{Eq.4})$$

When the solution is in a supersaturation state, ΔG_v is a negative quantity. The critical nuclei radius r^* depends whether ΔG_v overcomes ΔG_s and is defined by $d(\Delta G)/dr = 0$. The pre-nucleation phase starts between C_s and C^*_{min} , where the increase of the solution concentration tends to form larger nuclei. As long as r is smaller than r^* , the formed nuclei dissolve back in solution (**Figure I-9.c**). When the concentration C of the solution increases above the supersaturation concentration C^*_{min} , the nuclei radius reaches r^* , and the nucleation stage starts. Therefore, depending on the intensity of the solvent extraction method, it shortens the time for the solution to reach supersaturation ($C > C_{min}$), which will impact the number of nuclei formed (**Figure I-9.b**).^{51,55-57}. This aspect will be further investigated in **Chapter 2. part. 3.3**.

Moreover, it must be noted that, depending on temperature and pressure, the supersaturation and solubility concentration can have different values, which strongly impact the thermodynamic and kinetic factors of the reaction.

2.1.2. Self-seeding or Self-nucleation stage

Once the nucleation radius increases above r^* , it adopts a more stable spherical or ellipsoidal shape to minimize the total free Gibbs surface energy. As the concentration increases to C^*_{min} , subsequent growth occurs simultaneously by atomic aggregation around the nuclei. La Mer model considers nucleation as a single process, but according to classical theory, nucleation can occur either in a heterogeneous or in a homogeneous manner.⁵³

On the first hand, during homogeneous nucleation, nuclei are forming spontaneously in the solution volume. On the other hand, in the case of heterogeneous nucleation, perovskite nucleates on liquid/solid interfaces (such as a substrate or pre-seeded nucleation centers). It imposes to take into account interfacial energy related to the wetting of the solution on foreign surfaces. If the solution has a high wettability on the surface, the component γ of the surface free energy ΔG_s (Eq.3) is reduced. Consequently, heterogeneous nucleation becomes energetically favored rather than homogeneous nucleation and is given by the following equation.

$$\Delta G_{\text{Heterogeneous}} = \varphi \Delta G_{\text{Homogeneous}} \quad (\text{Eq.5})$$

The coefficient φ depends on the contact angle, which is related to the wettability of the solution on the foreign surface. As shown in **Figure I-9.d**, heterogeneous nucleation readily occurs at a lower saturation. However, the heterogeneous nucleation rate is limited by the total area of foreign surfaces. Thus, a high extraction rate of the solvent resulting in a high supersaturation degree of the solution naturally favors the homogeneous nucleation. This promotes a higher density of nuclei centers. Though, a high density of nucleation centers formed in the solution volume can result in multilayer perovskite morphology, where multiple horizontal grains joints are visible in the thickness of the perovskite film.⁵⁸

Therefore, several studies point out the advantage of heterogeneous nucleation during perovskite drying in growing uniform monolayers films.⁵⁹⁻⁶¹ This can be achieved by increasing the roughness of the substrate, the temperature or inducing pre-seeding by introducing foreign molecules in the solution.⁶²

2.1.3. Growth stage

The competition between nucleation and growth is balanced by the monomer concentration. When the solution concentration C reaches C_q , the maximum concentration of the solution, it becomes more likely for a single atom to join an existing cluster rather than forming a new nucleation center. As soon as new nuclei formation stops, growth becomes the dominant mechanism of precursors consumption by aggregation around existing clusters. Consequently, the solution concentration decreases. The Fick diffusion law can describe the diffusion of the precursors from the solution to the particle surface according to Eq.6:

$$J = 4\pi r^2 D \frac{dC}{dx} \quad (\text{Eq.6})$$

Where J , r , D , C and x are representing the total flux of precursors, the particle radius, the diffusion coefficient, and the monomer concentration at a distance (x) from the surface, respectively. Particles suspended in a liquid randomly move around due to Brownian motion. As illustrated in **Figure I-10.a**, a diffusion layer is formed around individual particles at the solid-liquid interface.

The flux of precursors can be considered constant regardless of the distance (x) from the surface due to the steady-state of solute diffusion.⁶¹ In addition, the particle growth is due to precursors' agglomeration and reaction on the particle surface.⁵³ Thus, the precursor's flux becomes dependent on the surface reaction rate k and can be expressed as:

$$J = 4\pi r^2 k (C - C_s) \quad (\text{Eq.7})$$

Where C is the concentration of the solute at the particle/solution interface.

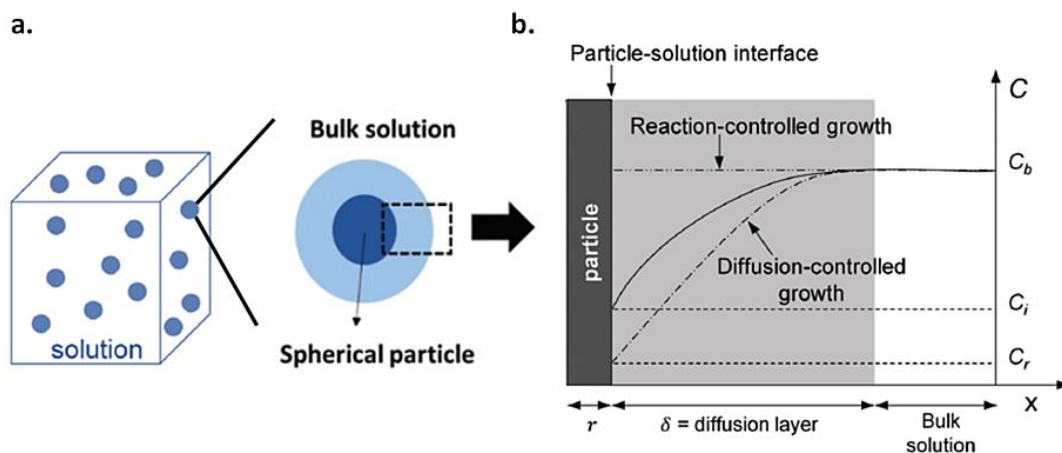


Figure I-10: Schematic illustration of the diffusion model and particle growth modes in supersaturation condition. **a.** Particles suspended in a liquid phase and, **b.** Particle concentration

profiles of diffusion and reaction-controlled growth modes. c and x indicate monomer concentration in solution and distance from the surface, respectively. Reproduced from ref. [52,59].

The balance between the nucleation rate and the growth rate determines the final perovskite film morphology. The generation of a limited number of nuclei leads to large dendritic perovskite morphologies. On the contrary, a large density of nucleation centers will result in small grains with numerous grain boundaries.

To form large and well-packed perovskite crystals with excellent coverage over the surface, reaching a high nucleation rate before the onset of crystal growth is of critical importance. The most effective approach to optimize the nucleation-growth process is to simultaneously limit the crystal growth and enhance the nucleation rate to ensure good nucleation seeding before triggering crystal growth. Several ink tailoring strategies have been reported in the literature to control this nucleation-growth equilibrium, including solvent ratio optimization, additives, and integration of interlayers in the perovskite stack.

2.2. Discussion

The La Mer model, completed by classical nucleation theory, is helpful to understand better the crystallization of the perovskite thin films, especially when dealing with larger deposition areas. With this aim, the literature reports worth phenomena which can complement La Mer's theory.

2.2.1. Ostwald ripening

In solution, when two nanoparticles of different sizes collide by Brownian movement, atoms transfer can occur from the smaller cluster surface to the larger one.^{63,64} The movement of surface atoms is driven by the minimization of the surface-free Gibbs energy of the overall particles. In other words, atoms populating higher energy surfaces migrate to lower surface energies. As a result, the growth of larger particles with lower surface energy is faster compared to smaller particles which tend upon time to disappear, either dissolving back in solution or being assimilated by the larger one. This phenomenon is the Ostwald ripening, as illustrated in **Figure I-11.a**.

In 2017, Hu *et al.*⁶⁵ pointed out a non-linear variation of the monomer concentration during the nucleation process (**Figure I-11.b**). This variation was attributed to the dissolution of small nucleation centers back in solution. The local dissolution of primary nuclei in solution can create local concentration gradients, which can impact crystal growth. Thus, contrary to the linear evolution assumed by the La Mer model, Ostwald ripening induces a second nucleation process controlled by the aggregation of small primary nucleation centers. You *et al.* qualified this model of "particle-oriented"⁵¹, in

contrast to the “atom-mediated” La Mer model. This phenomenon greatly influences the morphology of the final layer by acting on the final concentration of nucleation centers and, by extension, on the number and size of the grains.⁶⁶

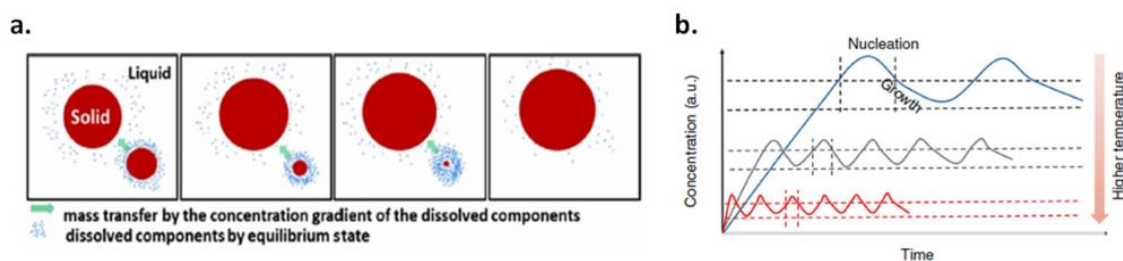


Figure I-11: **a.** Schematic representation of Ostwald ripening. Reproduced from [67]. **b.** The schematic diagram of nucleation and growth with time, based on various heating temperatures. Reproduced from [65].

2.2.2. Oriented-attachment

According to the Oriented-Attachment mechanism (OA)^{50,68}, nanoparticles tend to bind along common crystallographic planes to decrease the average surface energy of the total system.

Before the collision, the energetically favorable crystalline orientation influences the movement of nanoparticles. Nanoparticles can rotate to adjust crystal organization and vacancy alignment before the collision and coarsening. If the collision and attachment occur before the correct alignment of the crystallographic planes, Van der Waals forces lead to the rearrangement of the particles and impose torsional movements on the structure. Close orientation favors the coarsening of neighbor particles (**Figure I-12**), creating larger crystallites. Notably, highly-oriented perovskite films demonstrate better electronic properties, i.e., enhanced charge mobility ($>10 \text{ cm}^2 \text{ V}^{-1} \text{ s}^{-1}$) along (110) preferential orientation and lower traps density which are two inter-related parameter.⁶⁹

The Oriented-Attachment mechanism is highly dependent on the particle growth rate and, by extension, the solvent extraction speed. The greater the particle concentration of the solution is, the greater the monomer's collision factor will be. A high collision factor implies a rapid aggregation of the nanoparticles, which have less time to reorient themselves according to the common crystallographic plane. Thus, as previously mentioned, mitigating the growth rate is of critical importance, not only to ensure a proper nucleation density but also to allow particles to align appropriately.⁶⁸

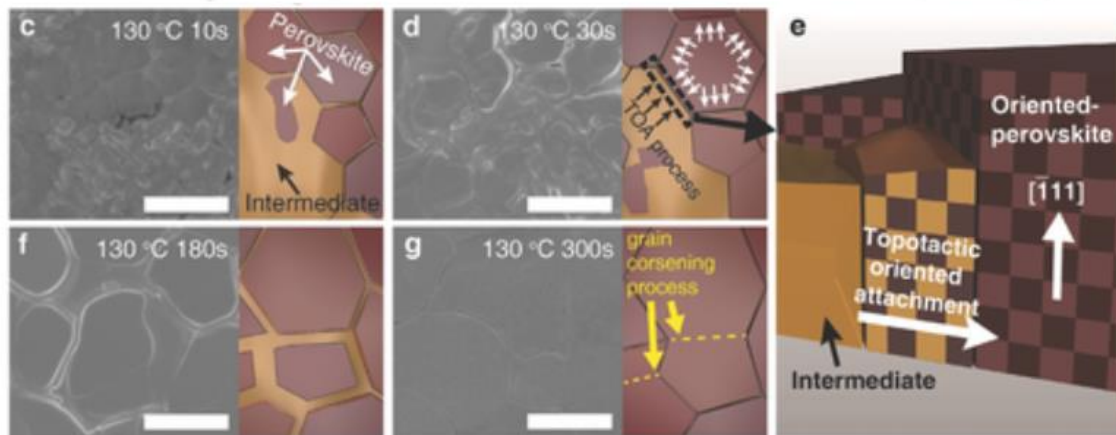


Figure I-12: Crystallographic orientation and growth mechanism. Schematic of the oriented-attachment process during crystallization. The scale bar is 2 μm . Reproduced from ref. [69].

Finally, if the La Mer theory is an interesting basis to describe the mechanism of the perovskite film crystallization, this model shows some limitations which can be completed, especially regarding the “burst-nucleation hypothesis,” which suggests instantaneous and isotropic nucleation in solution. Thus, in addition to the classical nucleation theory, numerous experimental works refined the understanding of nuclei formation. Among them, Ostwald ripening and oriented attachments are important examples that require to be considered during the fabrication of perovskite thin films.

3. Scalable deposition of perovskite absorber

In this part, the most representative and potential scalable deposition methods for perovskite films are discussed. We will focus on perovskite films deposited through solution-based processes, even though other physical deposition techniques have been largely explored, such as vapor-phase deposition methods (CVD, PVD, ALD), which recently demonstrated encouraging results.⁷⁰

3.1. Spin-coating method: Locks and constraints

In 2021, Jeong *et al.* achieved a record cell of 25.5% efficiency (25.2% certified)²¹, demonstrating the potential of perovskite solar cells for industrial applications. However, this encouraging result has been achieved on small areas (active area $< 0.1 \text{ cm}^2$), using the spin-coating deposition method to fabricate the perovskite layer. As illustrated in **Figure I-13.a**, a proper amount of precursor solution is first dispensed upon the substrate. Then, the latter is rotated at high speed to remove the excess of solution and solvent. Combined with an anti-solvent dripping method, this deposition method affords to reach so far the best device efficiencies.

However, spin-coating is not a viable technique for up-scaling the perovskite technology on larger areas. In addition, this process induces a significant fraction (>90%) of material waste during the rotation, which poses a significant obstacle to the transfer of the process into manufacturing. Moreover, in the case of perovskite deposition, this procedure has often been shown to be highly human-dependent, partly explaining the often significant differences found in the literature between different works using the same preparation method. Moreover, in the case of large substrates (> 100cm²), spin-coating can show uneven spreading of the layer, which inevitably leads to significant inhomogeneity, thus detrimental to the device's performance.⁷¹ To date, the largest module fabricated by the spin-coating method demonstrated a 12.6% efficiency on a 20.3 x 20.3 cm² area (**Figure I-13.b.**).

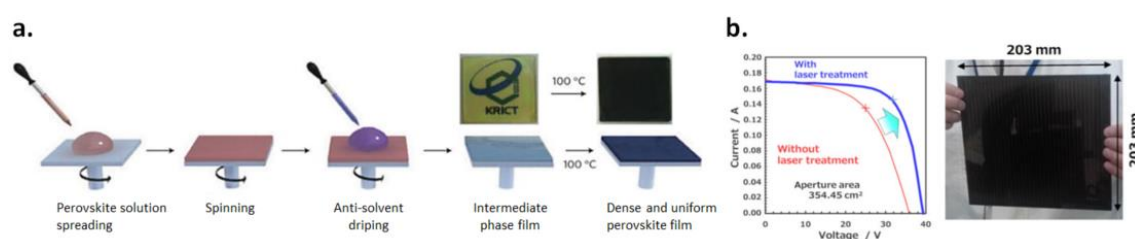


Figure I-13: **a.** One-step spin-coating technique. Reproduced from ref. [72]. **b.** 20x20 cm² module, with a perovskite layer fabricated by spin-coating method. Reproduced from ref. [73].

3.2. Scalable deposition methods overview

As an alternative to spin-coating, several large-scale compatible manufacturing techniques have been investigated. For solution-based deposition techniques, perovskite precursors are first dissolved in organic solvents and deposited on large substrates. Among them, blade-coating⁷⁴, spray-coating⁷⁵, screen-printing⁷⁶, or slot-die coating⁷⁷ are interesting candidates for manufacturing large-area perovskite solar cells. Schematic representations of these deposition techniques are displayed in **Figure I-14.a.**

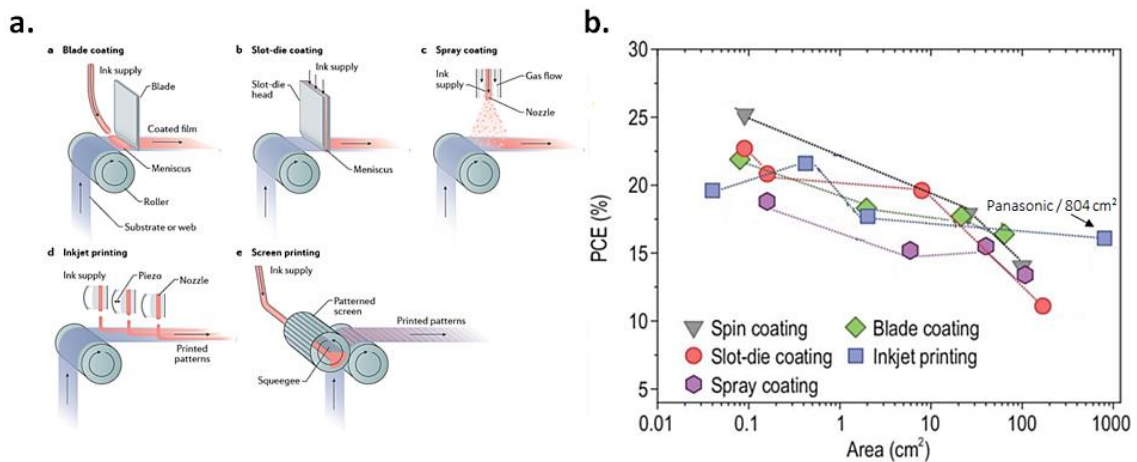


Figure I-14: **a.** Solution-based scalable solution deposition methods for large-scale fabrication of perovskite solar cells, including blade coating (panel a), slot-die coating (panel b), spray coating (panel c), inkjet printing (panel d), and screen printing (panel e). Reproduced from ref. [78]. **b.** Certified power conversion efficiency records for champion perovskite solar cells and modules. Reproduced from ref. [79].

Recently, the perovskite solar cells fabricated using industrially compatible techniques started to compete with spin-coated devices. The champion modules chart established by the NREL is displayed in **Annex 4**. For instance, in 2021, Xu *et al.* achieved a 21.35% efficiency for a lab-scale perovskite solar cell fabricated by the slot-die technique.⁸⁰ This result matches the previous record set by blade coating technique, yielding 21.9% efficiency employing cadmium iodide surface treatment⁸¹. In parallel, modules areas and efficiencies are continuing to increase. Notably, combining slot-die coating and a high-pressure nitrogen blow, M. Du *et al.* reached over 22% efficiency for a 16 cm² module⁸². The best perovskite cell and module results are gathered in **Table I-1**.

These very encouraging results triggered the industry interest for larger perovskite modules. In 2019, the Chinese company MicroQuanta claimed the first perovskite-based large module of 200x800 cm², yielding a 14.24% efficiency.⁸³ Since then, several new initiatives have emerged from industrial partners. Another Chinese company, Utmolight Corp., achieved a PCE of 20.5% for a mini-module with an active area of 63.98 cm².⁸⁴ In 2020, the Japanese company Panasonic Corp. announced the world's highest PCE of 17.9% for a larger perovskite module (> 800 cm²).^{85,86} China invested heavily in the industrialization of perovskite technology with a plan to develop a 1GW perovskite cell production line by 2022.⁸⁷

Although significant progress has been made, the PCE of perovskite modules still lags behind the state-of-the-art small area (~ 0.1 cm²) cells fabricated by spin coating (**Figure I-14.b**). Indeed, when the device area of the solar cells increases, the PCE tends to decrease. In the case of the perovskite solar cells and modules, the efficiency loss is

mainly due to non-uniform deposition/crystallization of all functional layers, i.e., the perovskite layer, both electron-transport and hole transport layers, and the back electrode.

Table I-1: Notable perovskite solar cells and module records obtained by different fabrication processes.

Architecture	Absorber deposition method	Active Area	PCE	Ref.
		cm^2	%	
FTO/FAPI/OAI/Spiro-OMeTAD/Au	Spin-coating	0.08	25.6	[21]
FTO/c-TiO ₂ /m-TiO ₂ /FAMA/P3HT/Au		24.97	17.1	[88]
FTO/SnO ₂ /KCsFAMA/Spiro-OMeTAD/Au		53.64	17.8	[89]
FTO/c-TiO ₂ /m-TiO ₂ /MAPI/fMoS ₂ /Spiro-OMeTAD/Au		108	13.4	[90]
FTO/c-TiO ₂ /m-TiO ₂ /MAPI/Spiro-OMeTAD/Au		354	12.6	[73]
FTO/c-TiO ₂ /m-TiO ₂ /FAMA/P3HT/Au	Bar-coating	24.97	17.2	[88]
FTO/SnO ₂ /MAPI/Spiro-OMeTAD/Au	Spray-coating	0.1	16.3	[91]
ITO/NiO _x /MAPI/C60/BCP/Ag		10.4	6.18	[92]
FTO/TiO ₂ /MAPI-Cl/PTAA/Au		40	15.5	[93]
FTO/m-TiO ₂ /C60/MAPI/Spiro-OMeTAD/Au	Inkjet	1	17.9	[94]
FTO/c-TiO ₂ /m-TiO ₂ /MAPI/m-ZrO ₂ /Carbon		1.5	9.1	[95]
FTO/c-TiO ₂ /PCBM/MAPI/Spiro-OMeTAD/Au	Blade-coating	0.09	21.9	[81]
ITO/PTAA/MAPI/C60/BCP/Cu		42.9	15.86	[96]
FTO/c-TiO ₂ /m-TiO ₂ /MAPI/P3HT/Au		100	4.3	[97]
ITO/PTAA/MAPI/C60/BCP/Ag	Slot-die coating	0.09	21.35	[80]
FTO/c-TiO ₂ /FACs/[M ₄ N]BF ₄ /Spiro-OMeTAD/Au		16	19.4	[82]
FTO/NiMgLiO/Ag/FACs/C60/BCP/Ag		20.77	16.63	[45]
ITO/SnO ₂ /CsFA/Spiro-OMeTAD/Au		52	11.6	[98]
FTO/c-TiO ₂ /m-TiO ₂ /m-ZrO ₂ /Cu:NiO _x /Carbon		70	12.1	[99]
ITO/TiO ₂ /MAPI/Spiro-OMeTAD/Au		200	11.8	[100]

3.3. Slot-die coating deposition process

Similarly to spin-coating, both one-step and two-step slot-die deposition have been studied. Generally, the two-step technique allows better control of the final layer morphology by finely monitoring the PbI_2 layer crystallization.^{101–103} In addition, within the development of perovskite/silicon tandems, the deposition on a surface with a pyramidal texture requires a high coverage rate favored by the sequential deposition method.

However, the one-step procedure is less complex in processing and affords to reduce the coating time. This makes this procedure more compatible with large-scale production. During the one-step protocol, the slot-die deposition is usually followed by a drying step to evacuate the solvent properly. Depending on the drying techniques selected, the solution chemistry and processing conditions developed for spin coating cannot be directly applied in other scalable deposition methods. Thus, the incorporation of additives into the perovskite precursor's solution has been widely studied in the literature to promote nucleation and slow down the growth rate. Notably, perovskite thin films derivated from chloride-containing precursors or additives present larger grains due to their preferential coordination with PbI_2 , which delays subsequent growth.^{104–107} In a similar way, the record cell efficiency obtained by slot-die used the potassium thiocyanate as an additive to enhance the electronic properties of the perovskite layer.⁸⁰ (**Figure I-15.a.**) It is also possible to vary the nature of the lead precursor (PbCl_2 ¹⁰⁴, $\text{Pb}(\text{NO}_3)_2$ ¹⁰⁸, and PbAc_2 ¹⁰⁹) to influence the kinetics of crystal growth (**Figure I-15.b.**). Finally, optimization of the solvent mix enables to accelerate the drying of the perovskite layer, especially in the case of air blowing or vacuum aspiration systems. For example, it is possible to combine volatile (Acetonitrile, 2-methoxyethanol) and low-volatile (DMF, DMSO, NMP) coordinating solvents to achieve both fast drying and large perovskite grains at room-temperature.^{72,110,111} Combining a double-additive strategy, i.e., methylammonium chloride (MACl) and hexamethylphosphoramide (HP), Z. Yang *et al.*⁴⁵ recently achieved a new world record for perovskite modules fabricated by slot die, yielding an efficiency of 16.63 % on 20.77 cm² (**Figure I-15.c.**). Such promising results encouraged industrial companies to bet on slot-die technology to develop further large surface Si/perovskite tandems (**Figure I-15.d.**).

To date, the best single-junction solar cell with an efficiency of 21.35%⁸⁰ has been fabricated by the one-step slot-die deposition method. Recently A.S. Subbiah *et al.* reported a slot-die-coated perovskite/silicon monolithic 2-terminal tandem achieving a PCE of 23.8% using a textured silicon bottom cell.¹¹²

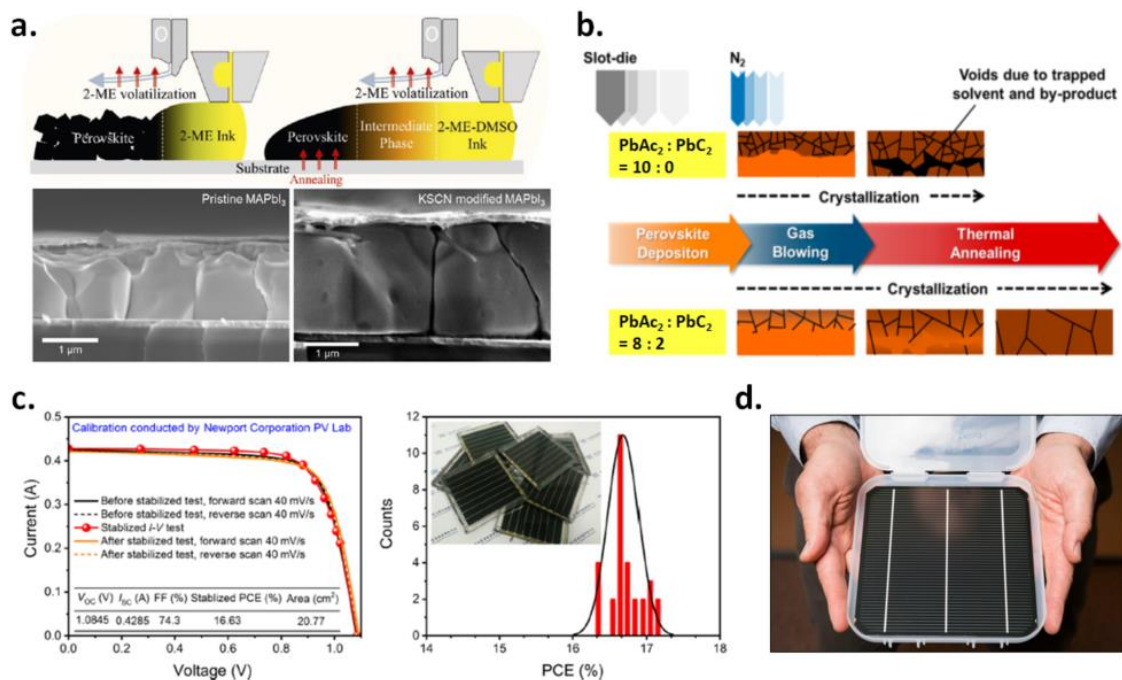


Figure I-15: Slot-die deposition techniques. **a.** SEM images of perovskite films deposited by spin-coating and slot-die coating assisted by hot-casting treatment. Reproduced from ref. [113]. **b.** Schematic diagram of the perovskite film formation mechanism via mix-precursors strategy. Reproduced from ref. [109]. **c.** I-V curves of perovskite-based modules and reproducibility statistics [45]. **d.** Wafer size perovskite module. Oxford PV.

Although many different deposition techniques were explored for the manufacturing of PSCs, the slot-die coating remains one of the most investigated techniques and probably the most preferred deposition route. However, even if the additives strategy displays encouraging results to slow down the crystal growth, the final film morphology depends highly on the solvent extraction method. Indeed, a rapid solvent extraction from the perovskite precursor solution is crucial to reach the supersaturation state more rapidly, thus promoting higher nuclei numbers.

4. Solvent extraction strategies

4.1. Anti-solvent method

The anti-solvent method is widely used to fabricate perovskite solar cells. Its utilization allows reaching the highest lab performances.^{21,49,114} To quickly enter into the supersaturation regime, a non-polar “anti-solvent” is dripped on the perovskite layer. The latter requires to be not miscible with the perovskite precursors. For a larger sample, the perovskite layer can also be immersed in an anti-solvent bath. The concentration of the perovskite precursors in the remaining solvent mixture then sharply increases and triggers

the crystallization mechanism. Generally, the polar precursor solvents can be DMF (N, N-dimethylformamide)^{111,115–117} or GBL (γ -butyrolactone).^{93,118} These solvents are commonly composed of a fraction of DMSO (Dimethylsulfoxide)^{68,111,115,117,119,120} or more rarely of NMP (N-méthyl-2-pyrrolidone)^{68,111,121}, which makes it possible to generate solvent-precursor adducts. The anti-solvent can be toluene¹²⁰, isopropanol (IPA)¹¹⁵, diethylther (DEE)²⁸, chlorobenzene (CB)^{119,122} or benzene¹²³. However, the anti-solvent method presents homogeneity issues when increasing the film size.¹²³ In addition, while several slot-die efficiency records are still based on anti-solvent derived methods (bath or dripping)^{45,77,78}, it requires a large amount of potentially toxic solvents, which can be detrimental for future industrial applications.¹²⁴

4.2. Solvent evaporation mechanism

As illustrated in **Figure I-16**, the solvent in the gaseous form will fill a volume of surface S and height H during evaporation. This volume of air is defined according to a total pressure P_t . If we consider the air above as a mixture of ideal gases, the contribution of the solvent evaporation to the total pressure P_t is defined as the partial pressure P_{*i} . The total pressure P_t can be expressed as the sum of the partial pressures of gases.¹²⁵

To allow the total evaporation of the solvent and the production of a high-quality film, it is necessary to maintain partial pressure of the solvent P_{*i} lower than the saturated vapor pressure, P_g . The value of the evaporation flow is determined by the pressure difference ΔP between the values of partial pressure P_{*i} and saturated vapor pressure P_g . If the partial pressure reaches P_g , the volume is saturated, and the evaporation flux stops. However, evaporated solvent remains in a saturated boundary layer near the substrate surface, even in a large available volume, which slows down the evaporation flux. Therefore, it is necessary to evacuate the evaporated solvent molecules quickly to promote high nucleation.

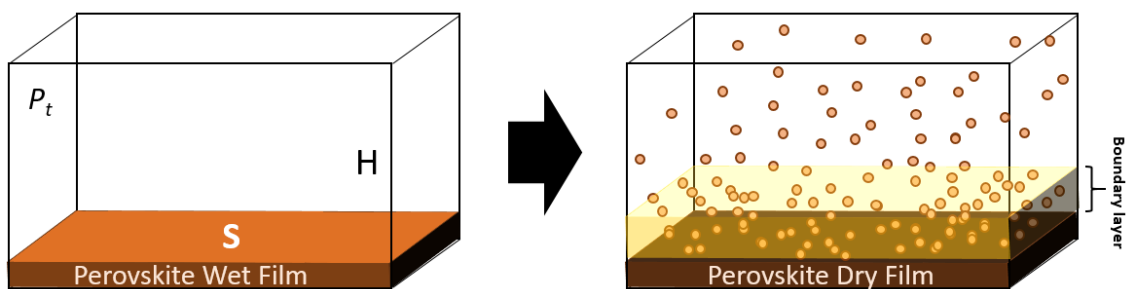


Figure I-16: Evaporation of a perovskite wet film in a not polluted defined volume V . The solvent of the perovskite film can evaporate as long as the gas vapor pressure P^* value is under the vapor pressure P_g .

4.3. Alternative solvent extraction systems

4.3.1. Forced gas-flow

4.3.1.1. Air blowing

The most widespread drying systems apply an air blow (dry air or N_2) on the sample's surface (**Figure I-17.a**). A gas nozzle is generally associated with the slot-die's deposition head and dries the perovskite immediately after deposition. Du *et al.* achieved over 19% power conversion efficiency on 16 cm² perovskite modules, thus validating the compatibility of this method for larger substrates. However, to efficiently evacuate the solvent, a high-pressure gas flow is needed. Insufficient blowing pressure can result in inhomogeneous film coverage and dendritic morphology due to poor nucleation.¹²⁶

To overcome this constraint, L. Gao *et al.* proposed a more efficient method called the "Air Knife Method" (MAK). Contrary to vertical airflow, MAK induces a parallel airflow very close to the substrate surface (**Figure I-17.b**), thus decreasing the boundary layer h above the forming layer. With this procedure, it is possible to accelerate the evaporation of the solvent with lower airflow. Thin-films obtained by this method yielded devices efficiency of over 17%.¹²⁷

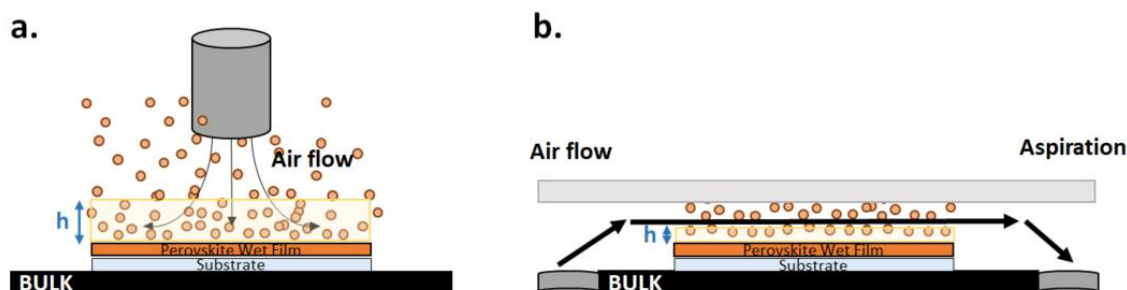


Figure I-17: Air blade drying systems. **a.** Schematic representation of vertical air blow. **b.** Schematic representation of Air Knife Method.

4.3.1.2. Vacuum aspiration

Unlike air blowing, vacuum aspiration removes the solvent by aspiration in a vacuum chamber. The advantage of this technique is the absence of a boundary layer delaying the diffusion and the evacuation of the solvent from the perovskite layer. First, B. Ding *et al.* developed a Gas Pump Method (GPM)¹²⁸ illustrated in **Figure I-18.a.**, which led to the fabrication of perovskite solar cells yielding efficiencies up to 19% on 0,1 cm² and almost 14% on 1,13 cm² area. These excellent results are due to the perfect coverage of the layer and large average grain size (> 400nm). Remarkably, the measured roughness ($S_a = 8\text{nm}$) was equivalent to the roughness reported by L. Gao *et al.* for the

MAK process ($S_a = 5 \text{ nm}$).¹²⁷ However, the quite long depressurization time ($> 30 \text{ sec}$) impacted the speed of evaporation. Then, B. Ding *et al.* improved the pumping method by adding a gas flow in the vacuum chamber, which enhanced small cell performances to 20.44% over a 1.13 cm^2 area.¹²⁹

More recently, X. Li *et al.* developed a quasi-instantaneous evacuation method. A double chamber system allows the chamber containing the substrate to reach 20 Pa in only a few seconds (**Figure I-18.b**). They also introduced a GBL/DMF solvent mix to slow down the crystal growth and prevent layer dewetting. Using the Vacuum-Flash Solution Processing (VASP) method, X. Li *et al.* obtained a PCE of 20.38% on 1 cm^2 aperture area.¹³⁰

Whereas both GPM and VASP have been developed with spin-coating deposition method, F. Guo *et al.* combined vacuum aspiration method with blade-coating deposition (**Figure I-18.c**).¹³¹ They reached over 18% efficiency on 0.09 cm^2 and 11% for $4 \times 4 \text{ cm}^2$ modules. Vacuum drying was associated with MACl addition which enabled obtaining large grain size ($> 1 \mu\text{m}$).

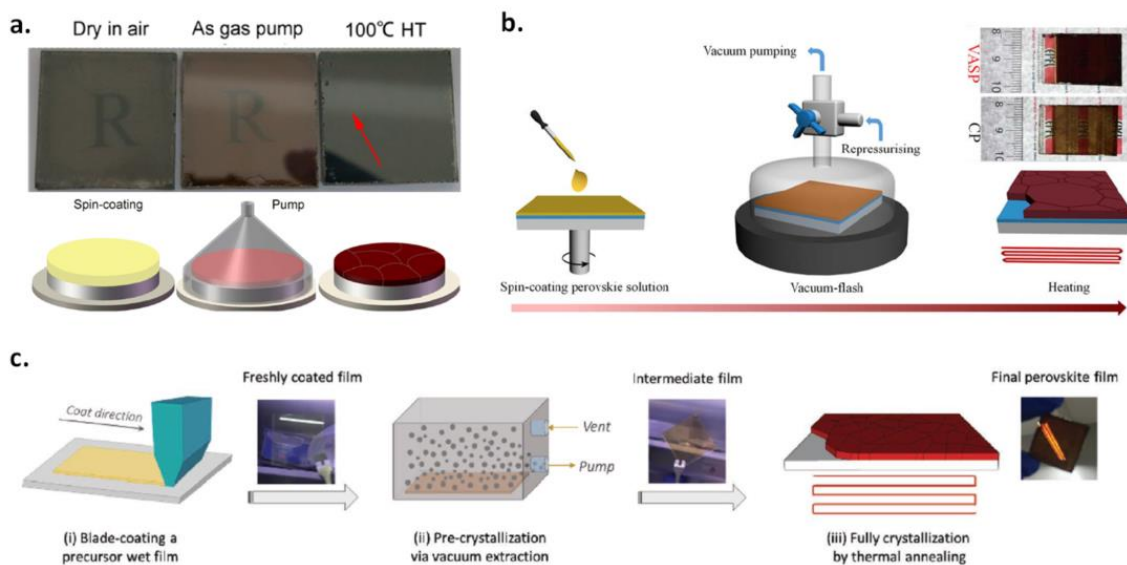


Figure I-18: **a.** Fabrication process steps of GP method and resulting perovskite films. Reproduced from ref. [128]. **b.** Schematic illustration of nucleation/crystallization procedures during the perovskite film formation via vacuum-flash assisted solution processing (VASP). Reproduced from ref. [130]. **c.** Schematic illustration of the one-step deposition of a perovskite film via blade coating, using a vacuum extraction drying system. Reproduced from ref. [131].

4.3.2. Surface heating

4.3.2.1. Hot-casting

Alternatively to a flow-induced method, substrate heating can also fasten the solvent removal. A. Vilayan *et al.* deposited by slot-die a perovskite layer on a pre-heated substrate at 130°C and achieved a 14.5% efficiency for a 0.125cm² aperture area by this method.¹¹³ However, one significant drawback is that the more elevated coating temperature gives rise to a higher surface roughness, which is detrimental to excellent interface quality (**Figure I-19.a.**).

However, Cotella *et al.* diminished this surface roughness from 180nm to 130nm by combining a pre-heated substrate at 65°C with an additional air-knife (**Figure I-19.b.**).¹³² In addition, this method makes it possible to achieve lower crystallization temperatures for lead halide perovskite deposition by selecting highly volatile solvents. For example, this technique has been successfully applied to deposit MAPI perovskite films on the pre-heated substrate at 70°C using methanol and acetonitrile solvent mixture.⁸⁰ As a result, the authors reached as high as 21.38% efficiency for small lab-scale solar cells.

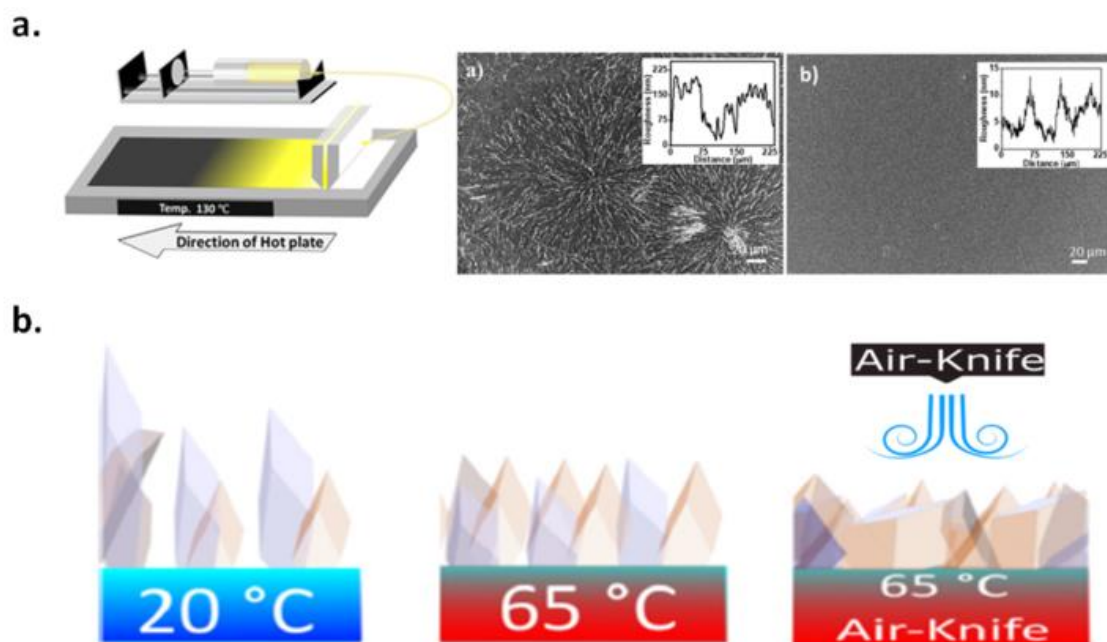


Figure I-19: **a.** Schematic representation of the slot-die coating process and SEM top-view of (a) slot-die-coated film and (b) spin-coated film. The insets show the roughness of the films as measured by profilometry. Reproduced from ref. [113]. **b.** Illustration of the layer differences obtained with the substrate at 20°C, pre-heated to 65 °C and 65 °C with an air knife. Reproduced from ref. [125].

4.3.2.2. Light exposure

Recently, intense pulse light (IPL) or Flash infrared annealing (FIRA) has been developed as a new anti-solvent-free method to dry the perovskite layer efficiently.

IPL delivers a broad spectrum light beam, typically between 150 and 1000 nm, for a few milliseconds duration to rapidly increase the temperature of the layer.¹³⁴ It creates a perovskite film with a more homogeneous profile and smoother surface. However, it requires a fine optimization of the pulsed light parameters (number of pulses and energy density of the radiation (in J/pulse or J/cm²)) to manage the energy delivered during the exposure (**Figure I-20.a**) and avoid the degradation of the film by the temperature. Lavery *et al.* have achieved 12.3% on 0.1cm² combining a spin-coating deposition and an IPL drying.

On the same principle, the FIRA method exposes the perovskite layer to intense NIR radiation within a wavelength ranging from 750-2500 nm. Unlike the IPL, the TCO absorbs most of this energy. The TCO layer is directly heated by the NIR exposition, which indirectly elevates the temperature of the perovskite film (**Figure I-20.b**). Thus, the FIRA method is a substrate-induced crystallization mechanism, as opposed to the IPL causing a bulk-induced crystallization.

Therefore, the NIR exposition can evaporate the solvent while avoiding exposure to UVs which is a source of degradation for the perovskite layer.^{122,123} S. Sanchez *et al.* reported over 20% efficiency for small solar cells and up to 17% on 1.4 cm² area¹³⁷ and B-J. Huang *et al.* achieved 14.3% efficiency on 80x80cm² area module deposited by slot-die technique.¹³⁸

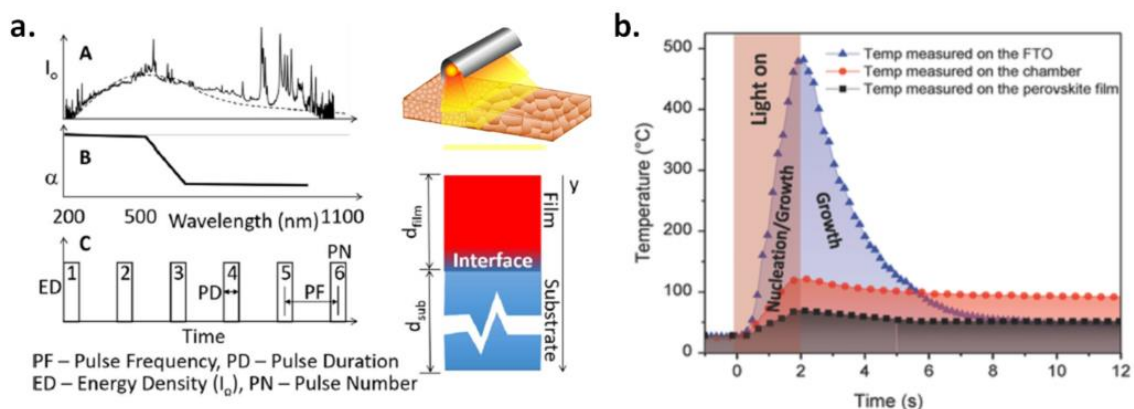


Figure I-20: **a.** Schematic of the parameters involved in the IPL process. Reproduced from ref. [139]. **b.** Temperature measured in the chamber and on the FTO surface with thermocouples and surface temperature of the perovskite film measured by an IR camera. Reproduced from ref. [136].

All these drying approaches played an essential role in raising the efficiency of large-area perovskite solar cells. However, the large efficiency gap remaining between lab devices

to large-area modules is still noticeable, representing one major challenge towards the industrialization of the technology. So far, the announcements of record efficiencies are still mainly realized on small-area devices fabricated by spin-coating.

5. Conclusions

In this chapter, we presented the general context in which this Ph.D. has been conducted. As energy production based on renewable energies increases each year, solar technologies represent an exciting path for future low-carbon energy production. Perovskite especially showed tremendous efficiency increase and demonstrated promising results towards large-scale deployment.

We discussed the fundamentals of the nucleation and crystal growth of perovskites that need to be considered carefully when dealing with larger areas. The underlying crystallization physics enlightened us that suppressing the crystal growth while accelerating the nucleation is essential to form large perovskite grains. However, it is crucial to understand better the crystallization mechanisms involved during the film formation to implement the existing nucleation/growth models and fabricate a high-quality perovskite film on large areas.

Then, we presented the recent progress realized on large-area deposition methods. We especially focused on the slot-die deposition technique, which is at the core of this thesis. We described the associated chemical composition and additives strategies deployed to adapt the perovskite composition to the large-scale deposition constraints.

Finally, we reviewed the different existing drying approaches and emphasized on pros and cons of each method. Given the fundamental differences identified between the crystallization dynamics of the anti-solvent spin-coating system and scalable coating associated with an alternative drying system, it is essential to re-formulate a precursor ink designed explicitly for scalable crystallization.

In the rest of this work, we will develop different additives strategies we elaborated to fabricate our perovskite layers, using a slot-die coating deposition method combined with a vacuum aspiration drying system. The experimental results will be discussed in the following experimental chapters.

6. References

- (1) World Population Prospects - Population Division - United Nations <https://population.un.org/wpp/Download/Standard/CSV/> (accessed 2021 -07 -07).
- (2) World Energy Outlook 2021 – Analysis <https://www.iea.org/reports/world-energy-outlook-2021> (accessed 2021 -11 -19).
- (3) CO2 emissions – Global Energy Review **2021** – Analysis <https://www.iea.org/reports/global-energy-review-2021/co2-emissions> (accessed 2021 -07 -07).
- (4) *BP Statistical Review of World Energy*; 68th edition; **2019**.
- (5) European Union. *Paris Agreement*; Paris, **2015**.
- (6) Solar - Fuels & Technologies <https://www.iea.org/fuels-and-technologies/solar> (accessed 2021 -07 -07).
- (7) Photovoltaic Dreaming 1875--1905: First Attempts At Commercializing PV | CleanTechnica <https://cleantechnica.com/2014/12/31/photovoltaic-dreaming-first-attempts-commercializing-pv/> (accessed 2021 -07 -07).
- (8) International Renewable Energy Agency. *RENEWABLE POWER GENERATION COSTS IN 2019*; Abu Dhabi, **2020**.
- (9) Photovoltaics Report - Fraunhofer ISE <https://www.ise.fraunhofer.de/en/publications/studies/photovoltaics-report.html> (accessed 2021 -09 -03).
- (10) NREL. *Research-Cell Efficiencies Chart*; **2021**.
- (11) Lal, N. N.; Dkhissi, Y.; Li, W.; Hou, Q.; Cheng, Y.-B.; Bach, U. Perovskite Tandem Solar Cells. *Adv. Energy Mater.* **2017**, *7* (18), 1602761. <https://doi.org/10.1002/aenm.201602761>.
- (12) Bremner; Levy, M. Y.; Honsberg, C. B. Analysis of Tandem Solar Cell Efficiencies under {AM1.5G} Spectrum Using a Rapid Flux Calculation Method. *Prog. Photovolt. Res. Appl.* **2008**, *16*, 225–233. <https://doi.org/10.1002/pip.799>.
- (13) Wang, Z.; Song, Z.; Yan, Y.; Liu, S. (Frank); Yang, D. Perovskite—a Perfect Top Cell for Tandem Devices to Break the S–Q Limit. *Adv. Sci.* **2019**, *6* (7), 1801704. <https://doi.org/10.1002/advs.201801704>.
- (14) Kim, D.; Jung, H. J.; Park, I. J.; Larson, B. W.; Dunfield, S. P.; Xiao, C.; Kim, J.; Tong, J.; Boonmongkolras, P.; Ji, S. G.; Zhang, F.; Pae, S. R.; Kim, M.; Kang, S. B.; Dravid, V.; Berry, J. J.; Kim, J. Y.; Zhu, K.; Kim, D. H.; Shin, B. Efficient, Stable Silicon Tandem Cells Enabled by Anion-Engineered Wide-Bandgap

- Perovskites. *Science* **2020**, *368* (6487), 155–160. <https://doi.org/10.1126/science.aba3433>.
- (15) Ehrler, B.; Alarcón-Lladó, E.; Tabernig, S. W.; Veeken, T.; Garnett, E. C.; Polman, A. Photovoltaics Reaching for the Shockley–Queisser Limit. *ACS Energy Lett.* **2020**, *5* (9), 3029–3033. <https://doi.org/10.1021/acsenerylett.0c01790>.
- (16) Chen, B.; Yu, Z. J.; Manzoor, S.; Wang, S.; Weigand, W.; Yu, Z.; Yang, G.; Ni, Z.; Dai, X.; Holman, Z. C.; Huang, J. Blade-Coated Perovskites on Textured Silicon for 26%-Efficient Monolithic Perovskite/Silicon Tandem Solar Cells. *Joule* **2020**, *4* (4), 850–864. <https://doi.org/10.1016/j.joule.2020.01.008>.
- (17) Oxford PV hits new world record for solar cell | Oxford PV <https://www.oxfordpv.com/news/oxford-pv-hits-new-world-record-solar-cell> (accessed 2021 -11 -09).
- (18) Zhu, Z.; Mao, K.; Xu, J. Perovskite Tandem Solar Cells with Improved Efficiency and Stability. *J. Energy Chem.* **2021**, *58*, 219–232. <https://doi.org/10.1016/j.jechem.2020.09.022>.
- (19) Chen, B.; Baek, S.-W.; Hou, Y.; Aydin, E.; De Bastiani, M.; Scheffel, B.; Proppe, A.; Huang, Z.; Wei, M.; Wang, Y.-K.; Jung, E.-H.; Allen, T. G.; Van Kerschaver, E.; García de Arquer, F. P.; Saidaminov, M. I.; Hoogland, S.; De Wolf, S.; Sargent, E. H. Enhanced Optical Path and Electron Diffusion Length Enable High-Efficiency Perovskite Tandems. *Nat. Commun.* **2020**, *11* (1), 1257. <https://doi.org/10.1038/s41467-020-15077-3>.
- (20) Swift Solar - Next generation lightweight and flexible solar technology <https://www.swiftsolar.com/> (accessed 2021 -11 -09).
- (21) Jeong, J.; Kim, M.; Seo, J.; Lu, H.; Ahlawat, P.; Mishra, A.; Yang, Y.; Hope, M. A.; Eickemeyer, F. T.; Kim, M.; Yoon, Y. J.; Choi, I. W.; Darwich, B. P.; Choi, S. J.; Jo, Y.; Lee, J. H.; Walker, B.; Zakeeruddin, S. M.; Emsley, L.; Rothlisberger, U.; Hagfeldt, A.; Kim, D. S.; Grätzel, M.; Kim, J. Y. Pseudo-Halide Anion Engineering for α -FAPbI₃ Perovskite Solar Cells. *Nature* **2021**. <https://doi.org/10.1038/s41586-021-03406-5>.
- (22) Bin, F. The Way to Commercialization; Hangzhou, CHINA, 2019.
- (23) Kojima, A.; Teshima, K.; Shirai, Y.; Miyasaka, T. Organometal Halide Perovskites as Visible-Light Sensitizers for Photovoltaic Cells. *J. Am. Chem. Soc.* **2009**, *131* (17), 6050–6051. <https://doi.org/10.1021/ja809598r>.
- (24) Im, J.-H.; Lee, C.-R.; Lee, J.-W.; Park, S.-W.; Park, N.-G. 6.5% Efficient Perovskite Quantum-Dot-Sensitized Solar Cell. *Nanoscale* **2011**, *3* (10), 4088–4093. <https://doi.org/10.1039/C1NR10867K>.

-
- (25) Kim, H.-S.; Lee, C.-R.; Im, J.-H.; Lee, K.-B.; Moehl, T.; Marchioro, A.; Moon, S.-J.; Humphry-Baker, R.; Yum, J.-H.; Moser, J. E.; Grätzel, M.; Park, N.-G. Lead Iodide Perovskite Sensitized All-Solid-State Submicron Thin Film Mesoscopic Solar Cell with Efficiency Exceeding 9%. *Sci. Rep.* **2012**, *2* (1), 591. <https://doi.org/10.1038/srep00591>.
- (26) Lee, M. M.; Teuscher, J.; Miyasaka, T.; Murakami, T. N.; Snaith, H. J. Efficient Hybrid Solar Cells Based on Meso-Superstructured Organometal Halide Perovskites. *Science* **2012**, *338* (6107), 643–647. <https://doi.org/10.1126/science.1228604>.
- (27) Bett, A. J.; Winkler, K. M.; Bivour, M.; Cojocaru, L.; Kabakli, Ö. S.; Schulze, P. S. C.; Siefer, G.; Tutsch, L.; Hermle, M.; Glunz, S. W.; Goldschmidt, J. C. Semi-Transparent Perovskite Solar Cells with ITO Directly Sputtered on Spiro-OMeTAD for Tandem Applications. *ACS Appl. Mater. Interfaces*. 49th ed. 2019, pp 45796–45804.
- (28) Ahn, N.; Son, D.-Y.; Jang, I.-H.; Kang, S. M.; Choi, M.; Park, N.-G. Highly Reproducible Perovskite Solar Cells with Average Efficiency of 18.3% and Best Efficiency of 19.7% Fabricated via Lewis Base Adduct of Lead(II) Iodide. *J. Am. Chem. Soc.* **2015**, *137* (27), 8696–8699. <https://doi.org/10.1021/jacs.5b04930>.
- (29) Luo, S.; Daoud, W. A. Recent Progress in Organic–Inorganic Halide Perovskite Solar Cells: Mechanisms and Material Design. *J. Mater. Chem. A* **2015**, *3* (17), 8992–9010. <https://doi.org/10.1039/C4TA04953E>.
- (30) Salim, T.; Sun, S.; Abe, Y.; Krishna, A.; Grimsdale, A. C.; Lam, Y. M. Perovskite-Based Solar Cells: Impact of Morphology and Device Architecture on Device Performance. *J. Mater. Chem. A* **2015**, *3* (17), 8943–8969. <https://doi.org/10.1039/C4TA05226A>.
- (31) Yang, W. S.; Noh, J. H.; Jeon, N. J.; Kim, Y. C.; Ryu, S.; Seo, J.; Seok, S. I. High-Performance Photovoltaic Perovskite Layers Fabricated through Intramolecular Exchange. *Science* **2015**. <https://doi.org/10.1126/science.aaa9272>.
- (32) Anaraki, E. H.; Kermanpur, A.; Steier, L.; Domanski, K.; Matsui, T.; Tress, W.; Saliba, M.; Abate, A.; Grätzel, M.; Hagfeldt, A.; Correa-Baena, J.-P. Highly Efficient and Stable Planar Perovskite Solar Cells by Solution-Processed Tin Oxide. *Energy Environ. Sci.* **2016**, *9* (10), 3128–3134. <https://doi.org/10.1039/C6EE02390H>.
- (33) Elumalai, N.; Mahmud, M.; Wang, D.; Uddin, A. Perovskite Solar Cells: Progress and Advancements. *Energies* **2016**, *9* (11), 861. <https://doi.org/10.3390/en9110861>.
- (34) Lee, J.-W.; Dai, Z.; Lee, C.; Lee, H. M.; Han, T.-H.; De Marco, N.; Lin, O.; Choi, C. S.; Dunn, B.; Koh, J.; Di Carlo, D.; Ko, J. H.; Maynard, H. D.; Yang, Y. Tuning Molecular Interactions for Highly Reproducible and Efficient Formamidinium

- Perovskite Solar Cells via Adduct Approach. *J. Am. Chem. Soc.* **2018**, *140* (20), 6317–6324. <https://doi.org/10.1021/jacs.8b01037>.
- (35) Aidarkhanov, D.; Ren, Z.; Lim, C.-K.; Yelzhanova, Z.; Nigmatova, G.; Taltanova, G.; Bapstayev, B.; Liu, F.; Cheung, S. H.; Balanay, M.; Baumuratov, A.; Djurišić, A. B.; So, S. K.; Surya, C.; Prasad, P. N.; Ng, A. Passivation Engineering for Hysteresis-Free Mixed Perovskite Solar Cells. *Sol. Energy Mater. Sol. Cells* **2020**, *215*, 110648. <https://doi.org/10.1016/j.solmat.2020.110648>.
- (36) Li, W.; Lai, X.; Meng, F.; Li, G.; Wang, K.; Kyaw, A. K. K.; Sun, X. W. Efficient Defect-Passivation and Charge-Transfer with Interfacial Organophosphorus Ligand Modification for Enhanced Performance of Perovskite Solar Cells. *Sol. Energy Mater. Sol. Cells* **2020**, *211*, 110527. <https://doi.org/10.1016/j.solmat.2020.110527>.
- (37) Li, Z.; Yang, M.; Park, J.-S.; Wei, S.-H.; Berry, J. J.; Zhu, K. Stabilizing Perovskite Structures by Tuning Tolerance Factor: Formation of Formamidinium and Cesium Lead Iodide Solid-State Alloys. *Chem. Mater.* **2016**, *28* (1), 284–292. <https://doi.org/10.1021/acs.chemmater.5b04107>.
- (38) Gao, X.-X.; Luo, W.; Zhang, Y.; Hu, R.; Zhang, B.; Züttel, A.; Feng, Y.; Nazeeruddin, M. K. Stable and High-Efficiency Methylammonium-Free Perovskite Solar Cells. *Adv. Mater.* **2020**, *32* (9), 1905502. <https://doi.org/10.1002/adma.201905502>.
- (39) Turren-Cruz, S.-H.; Hagfeldt, A.; Saliba, M. Methylammonium-Free, High-Performance, and Stable Perovskite Solar Cells on a Planar Architecture. *Science* **2018**, *362* (6413), 449–453. <https://doi.org/10.1126/science.aat3583>.
- (40) Conings, B.; Drijkoningen, J.; Gauquelin, N.; Babayigit, A.; D’Haen, J.; D’Olieslaeger, L.; Ethirajan, A.; Verbeeck, J.; Manca, J.; Mosconi, E.; Angelis, F. D.; Boyen, H.-G. Intrinsic Thermal Instability of Methylammonium Lead Trihalide Perovskite. *Adv. Energy Mater.* **2015**, *5* (15), 1500477. <https://doi.org/10.1002/aenm.201500477>.
- (41) Lee, J.-W.; Seol, D.-J.; Cho, A.-N.; Park, N.-G. High-Efficiency Perovskite Solar Cells Based on the Black Polymorph of HC(NH₂)₂PbI₃. *Adv. Mater.* **2014**, *26* (29), 4991–4998. <https://doi.org/10.1002/adma.201401137>.
- (42) Lai, M.; Lei, T.; Zhang, Y.; Jin, J.; Steele, J. A.; Yang, P. Phase Transition Dynamics in One-Dimensional Halide Perovskite Crystals. *MRS Bull.* **2020**, 1–7. <https://doi.org/10.1557/mrs.2020.280>.
- (43) Rehman, W.; McMeekin, D. P.; Patel, J. B.; Milot, R. L.; Johnston, M. B.; Snaith, H. J.; Herz, L. M. Photovoltaic Mixed-Cation Lead Mixed-Halide Perovskites: Links between Crystallinity, Photo-Stability and Electronic Properties. *Energy Environ. Sci.* **2017**, *10* (1), 361–369. <https://doi.org/10.1039/C6EE03014A>.

-
- (44) Lee, J.-W.; Kim, D.-H.; Kim, H.-S.; Seo, S.-W.; Cho, S. M.; Park, N.-G. Formamidinium and Cesium Hybridization for Photo- and Moisture-Stable Perovskite Solar Cell. *Adv. Energy Mater.* **2015**, *5* (20), 1501310. <https://doi.org/10.1002/aenm.201501310>.
- (45) Yang, Z.; Zhang, W.; Wu, S.; Zhu, H.; Liu, Z.; Liu, Z.; Jiang, Z.; Chen, R.; Zhou, J.; Lu, Q.; Xiao, Z.; Shi, L.; Chen, H.; Ono, L. K.; Zhang, S.; Zhang, Y.; Qi, Y.; Han, L.; Chen, W. Slot-Die Coating Large-Area Formamidinium-Cesium Perovskite Film for Efficient and Stable Parallel Solar Module. *Sci. Adv.* **2021**, *7* (18), eabg3749. <https://doi.org/10.1126/sciadv.abg3749>.
- (46) Schulze, P. S. C.; Bett, A. J.; Bivour, M.; Caprioglio, P.; Gerspacher, F. M.; Kabaklı, Ö. Ş.; Richter, A.; Stolterfoht, M.; Zhang, Q.; Neher, D.; Hermle, M.; Hillebrecht, H.; Glunz, S. W.; Goldschmidt, J. C. 25.1% High-Efficiency Monolithic Perovskite Silicon Tandem Solar Cell with a High Bandgap Perovskite Absorber. *Sol. RRL* **2020**, *4* (7), 2000152. <https://doi.org/10.1002/solr.202000152>.
- (47) Noh, J. H.; Im, S. H.; Heo, J. H.; Mandal, T. N.; Seok, S. I. Chemical Management for Colorful, Efficient, and Stable Inorganic–Organic Hybrid Nanostructured Solar Cells. *Nano Lett.* **2013**, *13* (4), 1764–1769. <https://doi.org/10.1021/nl400349b>.
- (48) Bush, K. A.; Frohna, K.; Prasanna, R.; Beal, R. E.; Leijtens, T.; Swifter, S. A.; McGehee, M. D. Compositional Engineering for Efficient Wide Band Gap Perovskites with Improved Stability to Photoinduced Phase Segregation. *ACS Energy Lett.* **2018**, *3* (2), 428–435. <https://doi.org/10.1021/acseenergylett.7b01255>.
- (49) Xu, J.; Boyd, C. C.; Yu, Z. J.; Palmstrom, A. F.; Witter, D. J.; Larson, B. W.; France, R. M.; Werner, J.; Harvey, S. P.; Wolf, E. J.; Weigand, W.; Manzoor, S.; van Hest, M. F. A. M.; Berry, J. J.; Luther, J. M.; Holman, Z. C.; McGehee, M. D. Triple-Halide Wide-Band Gap Perovskites with Suppressed Phase Segregation for Efficient Tandems. *Science* **2020**, *367* (6482), 1097–1104. <https://doi.org/10.1126/science.aaz5074>.
- (50) La Mer, V. K. Nucleation in Phase Transitions. *Ind Eng Chem* **1952**, *44* (6), 1270–1277. <https://doi.org/10.1021/ie50510a027>.
- (51) You, H.; Fang, J. Particle-Mediated Nucleation and Growth of Solution-Synthesized Metal Nanocrystals: A New Story beyond the LaMer Curve. *Nano Today* **2016**, *11* (2), 145–167. <https://doi.org/10.1016/j.nantod.2016.04.003>.
- (52) Liu, C.; Cheng, Y.-B.; Ge, Z. Understanding of Perovskite Crystal Growth and Film Formation in Scalable Deposition Processes. *Chem. Soc. Rev.* **2020**, *49* (6), 1653–1687. <https://doi.org/10.1039/C9CS00711C>.
- (53) Ke, L.; Luo, S.; Ren, X.; Yuan, Y. Factors Influencing the Nucleation and Crystal Growth of Solution-Processed Organic Lead Halide Perovskites: A Review. *J. Phys. Appl. Phys.* **2021**, *54* (16), 163001. <https://doi.org/10.1088/1361-6463/abd728>.

- (54) Pascoe, A. R.; Gu, Q.; Rothmann, M. U.; Li, W.; Zhang, Y.; Scully, A. D.; Lin, X.; Spiccia, L.; Bach, U.; Cheng, Y.-B. Directing Nucleation and Growth Kinetics in Solution-Processed Hybrid Perovskite Thin-Films. *Sci. China Mater.* **2017**, *60* (7), 617–628. <https://doi.org/10.1007/s40843-017-9043-y>.
- (55) Baronov, A.; Bufkin, K.; Shaw, D. W.; Johnson, B. L.; Patrick, D. L. A Simple Model of Burst Nucleation. *Phys. Chem. Chem. Phys.* **2015**, *17* (32), 20846–20852. <https://doi.org/10.1039/C5CP01745A>.
- (56) Van Der Heijden, A. E. D. M.; Va Der Eerden, J. P.; Van Rosmalen, G. M. The Secondary Nucleation Rate: A Physical Model. *Chem. Eng. Sci.* **1994**, *49* (18), 3103–3113. [https://doi.org/10.1016/0009-2509\(94\)E0122-7](https://doi.org/10.1016/0009-2509(94)E0122-7).
- (57) Ding, B.; Li, Y.; Huang, S.-Y.; Chu, Q.-Q.; Li, C.-X.; Li, C.-J.; Yang, G.-J. Material Nucleation/Growth Competition Tuning towards Highly Reproducible Planar Perovskite Solar Cells with Efficiency Exceeding 20%. *J. Mater. Chem. A* **2017**, *5* (15), 6840–6848. <https://doi.org/10.1039/C7TA00027H>.
- (58) Li, Y.; Li, X.; Chu, Q.; Dong, H.; Yao, J.; Zhou, Y.; Yang, G. Tuning Nucleation Sites to Enable Monolayer Perovskite Films for Highly Efficient Perovskite Solar Cells. *Coatings* **2018**, *8* (11), 408. <https://doi.org/10.3390/coatings8110408>.
- (59) Jung, M.; Ji, S.-G.; Kim, G.; Seok, S. I. Perovskite Precursor Solution Chemistry: From Fundamentals to Photovoltaic Applications. *Chem. Soc. Rev.* **2019**, *48* (7), 2011–2038. <https://doi.org/10.1039/C8CS00656C>.
- (60) Kim, H.; Hong, J.; Kim, C.; Shin, E.-Y.; Lee, M.; Noh, Y.-Y.; Park, B.; Hwang, I. Impact of Hydroxyl Groups Boosting Heterogeneous Nucleation on Perovskite Grains and Photovoltaic Performances. *J. Phys. Chem. C* **2018**, *122* (29), 16630–16638. <https://doi.org/10.1021/acs.jpcc.8b05374>.
- (61) Hu, H. Nucleation and Crystal Growth Control for Scalable Solution-Processed Organic–Inorganic Hybrid Perovskite Solar Cells. *J. Mater. Chem. A* **2020**, *26*.
- (62) Wang, J.; Luo, S.; Lin, Y.; Chen, Y.; Deng, Y.; Li, Z.; Meng, K.; Chen, G.; Huang, T.; Xiao, S.; Huang, H.; Zhou, C.; Ding, L.; He, J.; Huang, J.; Yuan, Y. Templated Growth of Oriented Layered Hybrid Perovskites on 3D-like Perovskites. *Nat. Commun.* **2020**, *11* (1), 582. <https://doi.org/10.1038/s41467-019-13856-1>.
- (63) Ratke, L.; Voorhees, P. W. *Growth and Coarsening: Ostwald Ripening in Material Processing*; Springer Science & Business Media, 2002.
- (64) Mahmud, M. A.; Elumalai, N. K.; Upama, M. B.; Wang, D.; Puthen-Veetil, B.; Haque, F.; Wright, M.; Xu, C.; Pivrikas, A.; Uddin, A. Controlled Ostwald Ripening Mediated Grain Growth for Smooth Perovskite Morphology and Enhanced Device Performance. *Sol. Energy Mater. Sol. Cells* **2017**, *167*, 87–101. <https://doi.org/10.1016/j.solmat.2017.03.034>.

-
- (65) Hu, Q.; Zhao, L.; Wu, J.; Gao, K.; Luo, D.; Jiang, Y.; Zhang, Z.; Zhu, C.; Schaible, E.; Hexemer, A.; Wang, C.; Liu, Y.; Zhang, W.; Grätzel, M.; Liu, F.; Russell, T. P.; Zhu, R.; Gong, Q. In Situ Dynamic Observations of Perovskite Crystallisation and Microstructure Evolution Intermediated from [PbI₆]⁴⁻ Cage Nanoparticles. *Nat. Commun.* **2017**, *8*, 15688. <https://doi.org/10.1038/ncomms15688>.
- (66) Qin, F.; Wang, Z.; Wang, Z. L. Anomalous Growth and Coalescence Dynamics of Hybrid Perovskite Nanoparticles Observed by Liquid-Cell Transmission Electron Microscopy. *ACS Nano* **2016**, *10* (11), 9787–9793. <https://doi.org/10.1021/acsnano.6b04234>.
- (67) Kim, S.-Y.; Jo, H. J.; Sung, S.-J.; Kim, D.-H. Perspective: Understanding of Ripening Growth Model for Minimum Residual PbI₂ and Its Limitation in the Planar Perovskite Solar Cells. *APL Mater.* **2016**, *4* (10), 100901. <https://doi.org/10.1063/1.4963841>.
- (68) Pascoe, A. R.; Gu, Q.; Rothmann, M. U.; Li, W.; Zhang, Y.; Scully, A. D.; Lin, X.; Spiccia, L.; Bach, U.; Cheng, Y.-B. Directing Nucleation and Growth Kinetics in Solution-Processed Hybrid Perovskite Thin-Films. *Sci. China Mater.* **2017**, *60* (7), 617–628. <https://doi.org/10.1007/s40843-017-9043-y>.
- (69) Kim, D. H.; Park, J.; Li, Z.; Yang, M.; Park, J.-S.; Park, I. J.; Kim, J. Y.; Berry, J. J.; Rumbles, G.; Zhu, K. 300% Enhancement of Carrier Mobility in Uniaxial-Oriented Perovskite Films Formed by Topotactic-Oriented Attachment. *Adv. Mater.* **2017**, *29* (23), 1606831. <https://doi.org/10.1002/adma.201606831>.
- (70) Wang, S.; Li, X.; Wu, J.; Wen, W.; Qi, Y. Fabrication of Efficient Metal Halide Perovskite Solar Cells by Vacuum Thermal Evaporation: A Progress Review. *Curr. Opin. Electrochem.* **2018**, *11*, 130–140. <https://doi.org/10.1016/j.coelec.2018.10.006>.
- (71) Baker, J. A.; Mouhamad, Y.; Hooper, K. E. A.; Burkitt, D.; Geoghegan, M.; Watson, T. M. From Spin Coating to Roll-to-Roll: Investigating the Challenge of Upscaling Lead Halide Perovskite Solar Cells. *IET Renew. Power Gener.* **2017**, *11* (5), 546–549. <https://doi.org/10.1049/iet-rpg.2016.0683>.
- (72) Jeon, N. J.; Noh, J. H.; Kim, Y. C.; Yang, W. S.; Ryu, S.; Seok, S. I. Solvent Engineering for High-Performance Inorganic–Organic Hybrid Perovskite Solar Cells. *Nat. Mater.* **2014**, *13* (9), 897–903. <https://doi.org/10.1038/nmat4014>.
- (73) Higuchi, H.; Negami, T. Largest Highly Efficient 203 × 203 Mm² CH₃NH₃PbI₃ Perovskite Solar Modules. *Jpn. J. Appl. Phys.* **2018**, *57* (8S3), 08RE11. <https://doi.org/10.7567/JJAP.57.08RE11>.
- (74) Deng, Y.; Peng, E.; Shao, Y.; Xiao, Z.; Dong, Q.; Huang, J. Scalable Fabrication of Efficient Organolead Trihalide Perovskite Solar Cells with Doctor-Bladed Active Layers. *Energy Environ. Sci.* **2015**, *8* (5), 1544–1550. <https://doi.org/10.1039/C4EE03907F>.

- (75) Jiang, Y.; Wu, C.; Li, L.; Wang, K.; Tao, Z.; Gao, F.; Cheng, W.; Cheng, J.; Zhao, X.-Y.; Priya, S.; Deng, W. All Electro Spray Printed Perovskite Solar Cells. *Nano Energy* **2018**, *53*, 440–448. <https://doi.org/10.1016/j.nanoen.2018.08.062>.
- (76) Rong, Y.; Ming, Y.; Ji, W.; Li, D.; Mei, A.; Hu, Y.; Han, H. Toward Industrial-Scale Production of Perovskite Solar Cells: Screen Printing, Slot-Die Coating, and Emerging Techniques. *J. Phys. Chem. Lett.* **2018**, *9* (10), 2707–2713. <https://doi.org/10.1021/acs.jpcclett.8b00912>.
- (77) Whitaker, J. B.; Kim, D. H.; Larson, B. W.; Zhang, F.; Berry, J. J.; van Hest, M. F. A. M.; Zhu, K. Scalable Slot-Die Coating of High Performance Perovskite Solar Cells. *Sustain. Energy Fuels* **2018**, *2* (11), 2442–2449. <https://doi.org/10.1039/C8SE00368H>.
- (78) Li, Z.; Klein, T. R.; Kim, D. H.; Yang, M.; Berry, J. J.; van Hest, M. F. A. M.; Zhu, K. Scalable Fabrication of Perovskite Solar Cells. *Nat. Rev. Mater.* **2018**, *3* (4), 18017. <https://doi.org/10.1038/natrevmats.2018.17>.
- (79) Wang, Y.; Duan, C.; Lv, P.; Ku, Z.; Lu, J.; Huang, F.; Cheng, Y.-B. Printing Strategies for Scaling-up Perovskite Solar Cells. *Natl. Sci. Rev.* **2021**, *8* (8). <https://doi.org/10.1093/nsr/nwab075>.
- (80) Xu, F.; Liu, J.; Subbiah, A. S.; Liu, W.; Kang, J.; Harrison, G. T.; Yang, X.; Isikgor, F. H.; Aydin, E.; De Bastiani, M.; De Wolf, S. Potassium Thiocyanate-Assisted Enhancement of Slot-Die-Coated Perovskite Films for High-Performance Solar Cells. *Small Sci.* **2021**, 2000044. <https://doi.org/10.1002/smssc.202000044>.
- (81) Wu, W.-Q.; Rudd, P. N.; Ni, Z.; Van Brackle, C. H.; Wei, H.; Wang, Q.; Ecker, B. R.; Gao, Y.; Huang, J. Reducing Surface Halide Deficiency for Efficient and Stable Iodide-Based Perovskite Solar Cells. *J. Am. Chem. Soc.* **2020**, *142* (8), 3989–3996. <https://doi.org/10.1021/jacs.9b13418>.
- (82) Du, M.; Zhu, X.; Wang, L.; Wang, H.; Feng, J.; Jiang, X.; Cao, Y.; Sun, Y.; Duan, L.; Jiao, Y.; Wang, K.; Ren, X.; Yan, Z.; Pang, S.; Liu, S. (Frank). High-Pressure Nitrogen-Extraction and Effective Passivation to Attain Highest Large-Area Perovskite Solar Module Efficiency. *Adv. Mater.* **2020**, *32* (47), 2004979. <https://doi.org/10.1002/adma.202004979>.
- (83) Microquanta achieves 14.24% efficiency with large-area perovskite solar module <https://www.pv-magazine.com/2019/10/24/microquanta-achieves-14-24-efficiency-with-large-area-perovskite-solar-module/> (accessed 2021 -08 -18).
- (84) China's perovskite solar module efficiency exceeds 20%, setting a new world record_NEWS_Utmost Light <http://utmolight.com/news/117030.html> (accessed 2021 -08 -18).

-
- (85) Green, M.; Dunlop, E.; Hohl-Ebinger, J.; Yoshita, M.; Kopidakis, N.; Hao, X. Solar Cell Efficiency Tables (Version 57). *Prog. Photovolt. Res. Appl.* **2021**, *29* (1), 3–15. <https://doi.org/10.1002/pip.3371>.
- (86) Champion Photovoltaic Module Efficiency Chart <https://www.nrel.gov/pv/module-efficiency.html> (accessed 2021 -08 -18).
- (87) GCL wants a 1 GW perovskite cell production line in place by 2022 <https://www.pv-magazine.com/2019/10/03/gcl-wants-a-1-gw-perovskite-cell-production-line-in-place-by-2022/> (accessed 2021 -08 -18).
- (88) Jung, E. H.; Jeon, N. J.; Park, E. Y.; Moon, C. S.; Shin, T. J.; Yang, T.-Y.; Noh, J. H.; Seo, J. Efficient, Stable and Scalable Perovskite Solar Cells Using Poly(3-Hexylthiophene). *Nature* **2019**, *567* (7749), 511–515. <https://doi.org/10.1038/s41586-019-1036-3>.
- (89) Bu, T.; Liu, X.; Li, J.; Huang, W.; Wu, Z.; Huang, F.; Cheng, Y.-B.; Zhong, J. Dynamic Antisolvent Engineering for Spin Coating of 10×10 Cm² Perovskite Solar Module Approaching 18%. *Sol. RRL* **2020**, *4* (2), 1900263. <https://doi.org/10.1002/solr.201900263>.
- (90) Agresti, A.; Pescetelli, S.; Palma, A. L.; Martín-García, B.; Najafi, L.; Bellani, S.; Moreels, I.; Prato, M.; Bonaccorso, F.; Di Carlo, A. Two-Dimensional Material Interface Engineering for Efficient Perovskite Large-Area Modules. *ACS Energy Lett.* **2019**, *4* (8), 1862–1871. <https://doi.org/10.1021/acseenergylett.9b01151>.
- (91) Uličná, S.; Dou, B.; Kim, D. H.; Zhu, K.; Walls, J. M.; Bowers, J. W.; van Hest, M. F. A. M. Scalable Deposition of High-Efficiency Perovskite Solar Cells by Spray-Coating. *ACS Appl. Energy Mater.* **2018**, *1* (5), 1853–1857. <https://doi.org/10.1021/acsaem.8b00328>.
- (92) Chou, L.-H.; Yu, Y.-T.; Osaka, I.; Wang, X.-F.; Liu, C.-L. Spray Deposition of NiOx Hole Transport Layer and Perovskite Photoabsorber in Fabrication of Photovoltaic Mini-Module. *J. Power Sources* **2021**, *491*, 229586. <https://doi.org/10.1016/j.jpowsour.2021.229586>.
- (93) Heo, J. H.; Lee, M. H.; Jang, M. H.; Im, S. H. Highly Efficient CH₃NH₃PbI₃-xCl_x Mixed Halide Perovskite Solar Cells Prepared by Re-Dissolution and Crystal Grain Growth via Spray Coating. *J. Mater. Chem. A* **2016**, *4* (45), 17636–17642. <https://doi.org/10.1039/C6TA06718B>.
- (94) Li, Z.; Li, P.; Chen, G.; Cheng, Y.; Pi, X.; Yu, X.; Yang, D.; Han, L.; Zhang, Y.; Song, Y. Ink Engineering of Inkjet Printing Perovskite. *ACS Appl. Mater. Interfaces* **2020**, *12* (35), 39082–39091. <https://doi.org/10.1021/acsaami.0c09485>.
- (95) Verma, A.; Martineau, D.; Abdolhosseinzadeh, S.; Heier, J.; Nüesch, F. Inkjet Printed Mesoscopic Perovskite Solar Cells with Custom Design Capability. *Mater. Adv.* **2020**, *1* (2), 153–160. <https://doi.org/10.1039/D0MA00077A>.

- (96) Dai, X.; Deng, Y.; Brackle, C. H. V.; Chen, S.; Rudd, P. N.; Xiao, X.; Lin, Y.; Chen, B.; Huang, J. Scalable Fabrication of Efficient Perovskite Solar Modules on Flexible Glass Substrates. *Adv. Energy Mater.* **2020**, *10* (1), 1903108. <https://doi.org/10.1002/aenm.201903108>.
- (97) Razza, S.; Castro-Hermosa, S.; Di Carlo, A.; Brown, T. M. Research Update: Large-Area Deposition, Coating, Printing, and Processing Techniques for the Upscaling of Perovskite Solar Cell Technology. *APL Mater.* **2016**, *4* (9), 091508. <https://doi.org/10.1063/1.4962478>.
- (98) Fievez, M.; Singh Rana, P. J.; Koh, T. M.; Manceau, M.; Lew, J. H.; Jamaludin, N. F.; Ghosh, B.; Bruno, A.; Cros, S.; Berson, S.; Mhaisalkar, S. G.; Leong, W. L. Slot-Die Coated Methylammonium-Free Perovskite Solar Cells with 18% Efficiency. *Sol. Energy Mater. Sol. Cells* **2021**, *230*, 111189. <https://doi.org/10.1016/j.solmat.2021.111189>.
- (99) Fagiolari, L.; Bella, F. Carbon-Based Materials for Stable, Cheaper and Large-Scale Processable Perovskite Solar Cells. *Energy Environ. Sci.* **2019**, *12* (12), 3437–3472. <https://doi.org/10.1039/C9EE02115A>.
- (100) Di Giacomo, F.; Shanmugam, S.; Fledderus, H.; Bruijnaers, B. J.; Verhees, W. J. H.; Dorenkamper, M. S.; Veenstra, S. C.; Qiu, W.; Gehlhaar, R.; Merckx, T.; Aernouts, T.; Andriessen, R.; Galagan, Y. Up-Scalable Sheet-to-Sheet Production of High Efficiency Perovskite Module and Solar Cells on 6-in. Substrate Using Slot Die Coating. *Sol. Energy Mater. Sol. Cells* **2018**, *181*, 53–59. <https://doi.org/10.1016/j.solmat.2017.11.010>.
- (101) Burkitt, D.; Searle, J.; Worsley, D.; Watson, T. Sequential Slot-Die Deposition of Perovskite Solar Cells Using Dimethylsulfoxide Lead Iodide Ink. *Materials* **2018**, *11* (11), 2106. <https://doi.org/10.3390/ma11112106>.
- (102) Heo, Y.-J.; Kim, J.-E.; Weerasinghe, H.; Angmo, D.; Qin, T.; Sears, K.; Hwang, K.; Jung, Y.-S.; Subbiah, J.; Jones, D. J.; Gao, M.; Kim, D.-Y.; Vak, D. Printing-Friendly Sequential Deposition via Intra-Additive Approach for Roll-to-Roll Process of Perovskite Solar Cells. *Nano Energy* **2017**, *41*, 443–451. <https://doi.org/10.1016/j.nanoen.2017.09.051>.
- (103) Becker, M.; Wark, M. Recent Progress in the Solution-Based Sequential Deposition of Planar Perovskite Solar Cells. *Cryst. Growth Des.* **2018**, *18* (8), 4790–4806. <https://doi.org/10.1021/acs.cgd.8b00686>.
- (104) Binek, A.; Grill, I.; Huber, N.; Peters, K.; Hufnagel, A. G.; Handloser, M.; Docampo, P.; Hartschuh, A.; Bein, T. Control of Perovskite Crystal Growth by Methylammonium Lead Chloride Templating. *Chem. - Asian J.* **2016**, *11* (8), 1199–1204. <https://doi.org/10.1002/asia.201501379>.
- (105) Odysseas Kosmatos, K.; Theofylaktos, L.; Giannakaki, E.; Deligiannis, D.; Konstantakou, M.; Stergiopoulos, T. Methylammonium Chloride: A Key Additive

- for Highly Efficient, Stable, and Up-Scalable Perovskite Solar Cells. *ENERGY Environ. Mater.* **2019**, 2 (2), 79–92. <https://doi.org/10.1002/eem2.12040>.
- (106) Rong, Y.; Hou, X.; Hu, Y.; Mei, A.; Liu, L.; Wang, P.; Han, H. Synergy of Ammonium Chloride and Moisture on Perovskite Crystallization for Efficient Printable Mesoscopic Solar Cells. *Nat. Commun.* **2017**, 8 (1), 14555. <https://doi.org/10.1038/ncomms14555>.
- (107) Williams, S. T.; Zuo, F.; Chueh, C.-C.; Liao, C.-Y.; Liang, P.-W. Role of Chloride in the Morphological Evolution of Organo-Lead Halide Perovskite Thin Films. **2014**, 8 (10), 15.
- (108) Pothiklang, C.; Hongsih, K.; Ruankham, P.; Supabchoopun. Synthesis of Perovskite Film by Using Lead Nitrate as Precursor for Perovskite Solar Cell Applications. *Mater. Today Proc.* **2019**, 17, 1224–1230. <https://doi.org/10.1016/j.matpr.2019.06.002>.
- (109) Lee, D.; Jung, Y.-S.; Heo, Y.-J.; Lee, S.; Hwang, K.; Jeon, Y.-J.; Kim, J.-E.; Park, J.; Jung, G. Y.; Kim, D.-Y. Slot-Die Coated Perovskite Films Using Mixed Lead Precursors for Highly Reproducible and Large-Area Solar Cells. *ACS Appl. Mater. Interfaces* **2018**, 10 (18), 16133–16139. <https://doi.org/10.1021/acsami.8b02549>.
- (110) Deng, Y.; Brackle, C. H. V.; Dai, X.; Zhao, J.; Chen, B.; Huang, J. Tailoring Solvent Coordination for High-Speed, Room-Temperature Blading of Perovskite Photovoltaic Films. *Sci. Adv.* **2019**, 5 (12), eaax7537. <https://doi.org/10.1126/sciadv.aax7537>.
- (111) Hao, F.; Stoumpos, C. C.; Guo, P.; Zhou, N.; Marks, T. J.; Chang, R. P. H.; Kanatzidis, M. G. Solvent-Mediated Crystallization of $\text{CH}_3\text{NH}_3\text{SnI}_3$ Films for Heterojunction Depleted Perovskite Solar Cells. *J. Am. Chem. Soc.* **2015**, 137 (35), 11445–11452. <https://doi.org/10.1021/jacs.5b06658>.
- (112) Subbiah, A. S.; Isikgor, F. H.; Howells, C. T.; De Bastiani, M.; Liu, J.; Aydin, E.; Furlan, F.; Allen, T. G.; Xu, F.; Zhumagali, S.; Hoogland, S.; Sargent, E. H.; McCulloch, I.; De Wolf, S. High-Performance Perovskite Single-Junction and Textured Perovskite/Silicon Tandem Solar Cells via Slot-Die-Coating. *ACS Energy Lett.* **2020**, 5 (9), 3034–3040. <https://doi.org/10.1021/acsenerylett.0c01297>.
- (113) Vijayan, A.; Johansson, M. B.; Svanström, S.; Cappel, U. B.; Rensmo, H.; Boschloo, G. Simple Method for Efficient Slot-Die Coating of MAPbI_3 Perovskite Thin Films in Ambient Air Conditions. *ACS Appl. Energy Mater.* **2020**, 3 (5), 4331–4337. <https://doi.org/10.1021/acsaem.0c00039>.
- (114) Chan, C.-Y.; Wang, Y.; Wu, G.-W.; Wei-Guang Diao, E. Solvent-Extraction Crystal Growth for Highly Efficient Carbon-Based Mesoscopic Perovskite Solar Cells Free of Hole Conductors. *J. Mater. Chem. A* **2016**, 4 (10), 3872–3878. <https://doi.org/10.1039/C6TA00912C>.

- (115) Lee, J.-W.; Kim, H.-S.; Park, N.-G. Lewis Acid–Base Adduct Approach for High Efficiency Perovskite Solar Cells. *Acc. Chem. Res.* **2016**, *49* (2), 311–319. <https://doi.org/10.1021/acs.accounts.5b00440>.
- (116) Nie, W.; Tsai, H.; Asadpour, R.; Blancon, J.-C.; Neukirch, A. J.; Gupta, G.; Crochet, J. J.; Chhowalla, M.; Tretiak, S.; Alam, M. A.; Wang, H.-L.; Mohite, A. D. High-Efficiency Solution-Processed Perovskite Solar Cells with Millimeter-Scale Grains. *Science* **2015**, *347* (6221), 522–525. <https://doi.org/10.1126/science.aaa0472>.
- (117) Yang, W. S.; Park, B.-W.; Jung, E. H.; Jeon, N. J.; Kim, Y. C.; Lee, D. U.; Shin, S. S.; Seo, J.; Kim, E. K.; Noh, J. H. Iodide Management in Formamidinium-Lead-Halide–Based Perovskite Layers for Efficient Solar Cells. *Science* **2017**, *356* (6345), 1376–1379.
- (118) Tsai, C.-M.; Wu, G.-W.; Narra, S.; Chang, H.-M.; Mohanta, N.; Wu, H.-P.; Wang, C.-L.; Diau, E. W.-G. Control of Preferred Orientation with Slow Crystallization for Carbon-Based Mesoscopic Perovskite Solar Cells Attaining Efficiency 15%. *J. Mater. Chem. A* **2017**, *5* (2), 739–747. <https://doi.org/10.1039/C6TA09036B>.
- (119) Qin, Q.; Zhang, Z.; Cai, Y.; Zhou, Y.; Liu, H.; Lu, X.; Gao, X.; Shui, L.; Wu, S.; Liu, J. Improving the Performance of Low-Temperature Planar Perovskite Solar Cells by Adding Functional Fullerene End-Capped Polyethylene Glycol Derivatives. *J. Power Sources* **2018**, *396*, 49–56. <https://doi.org/10.1016/j.jpowsour.2018.05.091>.
- (120) Jeon, N. J.; Noh, J. H.; Kim, Y. C.; Yang, W. S.; Ryu, S.; Seok, S. I. Solvent Engineering for High-Performance Inorganic–Organic Hybrid Perovskite Solar Cells. *Nat. Mater.* **2014**, *13* (9), 897–903. <https://doi.org/10.1038/nmat4014>.
- (121) Cheng, F.; Jing, X.; Chen, R.; Cao, J.; Yan, J.; Wu, Y.; Huang, X.; Wu, B.; Zheng, N. *N*-Methyl-2-Pyrrolidone as an Excellent Coordinative Additive with a Wide Operating Range for Fabricating High-Quality Perovskite Films. *Inorg. Chem. Front.* **2019**, *6* (9), 2458–2463. <https://doi.org/10.1039/C9QI00547A>.
- (122) Zhang, Z.; Xie, L.; Lin, R.; Qin, Q.; Cai, Y.; Zhou, Y.; Liu, H.; Lu, X.; Gao, X.; Shui, L.; Wu, S.; Liu, J.-M. Enhanced Performance of Planar Perovskite Solar Cells Based on Low-Temperature Processed TiO₂ Electron Transport Layer Modified by Li₂SiO₃. *J. Power Sources* **2018**, *392*, 1–7. <https://doi.org/10.1016/j.jpowsour.2018.04.086>.
- (123) Konstantakou, M.; Perganti, D.; Falaras, P.; Stergiopoulos, T. Anti-Solvent Crystallization Strategies for Highly Efficient Perovskite Solar Cells. *Crystals* **2017**, *7* (10), 291. <https://doi.org/10.3390/cryst7100291>.
- (124) Yang, M.; Li, Z.; Reese, M. O.; Reid, O. G.; Kim, D. H.; Siol, S.; Klein, T. R.; Yan, Y.; Berry, J. J.; van Hest, M. F. A. M.; Zhu, K. Perovskite Ink with Wide

- Processing Window for Scalable High-Efficiency Solar Cells. *Nat. Energy* **2017**, *2* (5), 17038. <https://doi.org/10.1038/nenergy.2017.38>.
- (125) Gao, L.-L.; Li, C.-X.; Li, C.-J.; Yang, G.-J. Large-Area High-Efficiency Perovskite Solar Cells Based on Perovskite Films Dried by the Multi-Flow Air Knife Method in Air. *J. Mater. Chem. A* **2017**, *5* (4), 1548–1557. <https://doi.org/10.1039/C6TA09565H>.
- (126) Kim, J.-E.; Jung, Y.-S.; Heo, Y.-J.; Hwang, K.; Qin, T.; Kim, D.-Y.; Vak, D. Slot Die Coated Planar Perovskite Solar Cells via Blowing and Heating Assisted One Step Deposition. *Sol. Energy Mater. Sol. Cells* **2018**, *179*, 80–86. <https://doi.org/10.1016/j.solmat.2018.02.003>.
- (127) Gao, L.-L.; Li, C.-X.; Li, C.-J.; Yang, G.-J. Large-Area High-Efficiency Perovskite Solar Cells Based on Perovskite Films Dried by the Multi-Flow Air Knife Method in Air. *J. Mater. Chem. A* **2017**, *5* (4), 1548–1557. <https://doi.org/10.1039/C6TA09565H>.
- (128) Ding, B.; Gao, L.; Liang, L.; Chu, Q.; Song, X.; Li, Y.; Yang, G.; Fan, B.; Wang, M.; Li, C.; Li, C. Facile and Scalable Fabrication of Highly Efficient Lead Iodide Perovskite Thin-Film Solar Cells in Air Using Gas Pump Method. *ACS Appl. Mater. Interfaces* **2016**, *8* (31), 20067–20073. <https://doi.org/10.1021/acsami.6b05862>.
- (129) Ding, B.; Li, Y.; Huang, S.-Y.; Chu, Q.-Q.; Li, C.-X.; Li, C.-J.; Yang, G.-J. Material Nucleation/Growth Competition Tuning towards Highly Reproducible Planar Perovskite Solar Cells with Efficiency Exceeding 20%. *J. Mater. Chem. A* **2017**, *5* (15), 6840–6848. <https://doi.org/10.1039/C7TA00027H>.
- (130) Li, X.; Bi, D.; Yi, C.; Decoppet, J.-D.; Luo, J.; Zakeeruddin, S. M.; Hagfeldt, A.; Gratzel, M. A Vacuum Flash-Assisted Solution Process for High-Efficiency Large-Area Perovskite Solar Cells. *Science* **2016**, *353* (6294), 58–62. <https://doi.org/10.1126/science.aaf8060>.
- (131) Guo, F.; Qiu, S.; Hu, J.; Wang, H.; Cai, B.; Li, J.; Yuan, X.; Liu, X.; Forberich, K.; Brabec, C. J.; Mai, Y. A Generalized Crystallization Protocol for Scalable Deposition of High-Quality Perovskite Thin Films for Photovoltaic Applications. *Adv. Sci.* **2019**, *6* (17), 1901067. <https://doi.org/10.1002/advs.201901067>.
- (132) Cotella, G.; Baker, J.; Worsley, D.; De Rossi, F.; Pleydell-Pearce, C.; Carnie, M.; Watson, T. One-Step Deposition by Slot-Die Coating of Mixed Lead Halide Perovskite for Photovoltaic Applications. *Sol. Energy Mater. Sol. Cells* **2017**, *159*, 362–369. <https://doi.org/10.1016/j.solmat.2016.09.013>.
- (133) Cotella, G.; Baker, J.; Worsley, D.; De Rossi, F.; Pleydell-Pearce, C.; Carnie, M.; Watson, T. One-Step Deposition by Slot-Die Coating of Mixed Lead Halide Perovskite for Photovoltaic Applications. *Sol. Energy Mater. Sol. Cells* **2017**, *159*, 362–369. <https://doi.org/10.1016/j.solmat.2016.09.013>.

- (134) Lavery, B. W.; Kumari, S.; Konermann, H.; Draper, G. L.; Spurgeon, J.; Druffel, T. Intense Pulsed Light Sintering of $\text{CH}_3\text{NH}_3\text{PbI}_3$ Solar Cells. *ACS Appl. Mater. Interfaces* **2016**, *8* (13), 8419–8426. <https://doi.org/10.1021/acsami.5b10166>.
- (135) Troughton, J.; Charbonneau, C.; Carnie, M. J.; Davies, M. L.; Worsley, D. A.; Watson, T. M. Rapid Processing of Perovskite Solar Cells in under 2.5 Seconds. *J. Mater. Chem. A* **2015**, *3* (17), 9123–9127. <https://doi.org/10.1039/C5TA00568J>.
- (136) Sanchez, S.; Hua, X.; Phung, N.; Steiner, U.; Abate, A. Flash Infrared Annealing for Antisolvent-Free Highly Efficient Perovskite Solar Cells. *Adv. Energy Mater.* **2018**, 1702915. <https://doi.org/10.1002/aenm.201702915>.
- (137) Sánchez, S.; Jerónimo-Rendon, J.; Saliba, M.; Hagfeldt, A. Highly Efficient and Rapid Manufactured Perovskite Solar Cells via Flash InfraRed Annealing. *Mater. Today* **2020**, *35*, 9–15. <https://doi.org/10.1016/j.mattod.2019.11.003>.
- (138) Huang, B.-J.; Guan, C.-K.; Huang, S.-H.; Su, W.-F. Development of Once-through Manufacturing Machine for Large-Area Perovskite Solar Cell Production. *Sol. Energy* **2020**, *205*, 192–201. <https://doi.org/10.1016/j.solener.2020.05.005>.
- (139) Druffel, T.; Dharmadasa, R.; Lavery, B. W.; Ankireddy, K. Intense Pulsed Light Processing for Photovoltaic Manufacturing. *Sol. Energy Mater. Sol. Cells* **2018**, *174*, 359–369. <https://doi.org/10.1016/j.solmat.2017.09.010>.

CHAPTER 2:

Methodology of fabrication of the perovskite device and effect of surfactant addition

1. Introduction

In this chapter, we present the general fabrication protocol of the perovskite solar cells and propose a surfactant-assisted protocol to improve the morphology of the absorber.

First, we describe the fabrication steps of each layer of the perovskite device, from the deposition of the charge transport layers by spin coating to the evaporation of the gold top-electrode.

Following this, we focus on optimizing the key parameters for the slot-die technique to obtain a uniform perovskite layer. Then, the influence of the drying step on the perovskite layer morphology will be discussed.

Finally, we detailed our results on the influence of a surfactant addition into the perovskite precursors solution on the absorber opto-electronic properties. For this study, we investigated two different perovskite compositions: a low bandgap perovskite $\text{Cs}_{0.2}\text{FA}_{0.8}\text{Pb}(\text{I}_{0.95}\text{Br}_{0.05})_3$ ($E_g = 1.58$ eV) and a higher bandgap perovskite $\text{Cs}_{0.17}\text{FA}_{0.83}\text{Pb}(\text{I}_{0.83}\text{Br}_{0.17})_3$ ($E_g = 1.75$ eV).

SUMMARY

1. Introduction	59
2. Device architecture and fabrication protocol	61
3. Perovskite absorber layer by slot-die coating	65
4. Surfactant addition into the precursor's solution	77
5. Conclusion.....	101
6. References.....	102

2. Device architecture and fabrication protocol

This thesis focuses on the deposition of the perovskite absorber layer by using the slot-die technique. Nevertheless, the fabrication of the selective transport and the electrode layers combined with different deposition techniques had to be adjusted for large substrates. The deposition methods were adapted from the baseline process, developed at IPVF lab for spin-coated devices.¹

The slot-die coating requires a leading edge and a trailing edge to start and end the coating, representing around 1 cm on each extremity. Thus, to allow a large enough deposition area, we decided to use 10 x 5 cm² substrates to perform our deposition process and then cut them into small pieces for analysis and device fabrication. The width of the coating substrate was ascribed to the size of the slot-die coating head (5 cm) used during this thesis. It is possible to vary the surface of the coating up to 20 x 20 cm². However, the substrates were mainly kept to this size because it is also small enough to run experiments with multiple annealing conditions, ink composition, and deposition parameters without using too many consumables for material optimization. For all experiments, the environmental temperature was maintained between 19°C and 26°C, and the atmospheric moisture level was between 30 and 55 RH %. In the glovebox, the atmosphere was composed of nitrogen with low levels of H₂O and O₂ (< 15 ppm).

Figure II-1 shows the fabrication process of the perovskite solar cells, from the 10 x 5 cm² substrate to 2 x 2.5 cm² individual cells. This fabrication protocol will then stay identical in the rest of this thesis unless indicated otherwise.

Each fabrication step is described in this part, except the perovskite deposition step that will be detailed more precisely in **part. 3**.

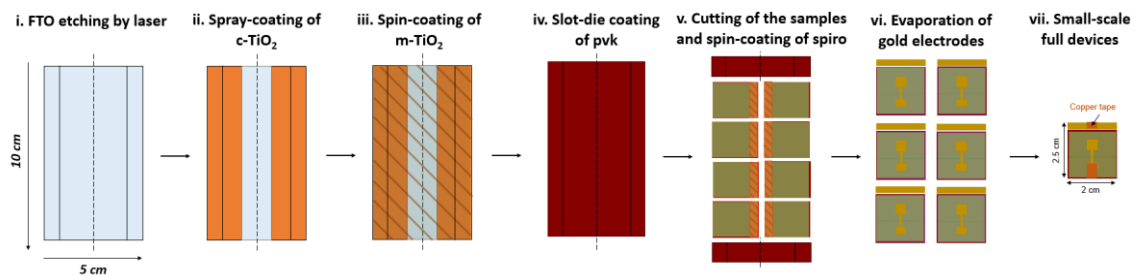


Figure II-1: Main steps of the fabrication process of small-area perovskite solar cells. The deposition of the TiO₂ layers was completed in ambient conditions. The perovskite layer and the HTL were deposited in a N₂-filled glovebox.

2.1. Preparation and etching of the substrates

We used a soda lime glass substrate with a FTO (Fluoride-doped Tin oxide) conductive layer (TEC 7 / 3.1 mm) from Pilkington. The sheet resistance of the FTO layer is around 7-8 Ω/sq , for a thickness of 300 nm.

The patterning of the FTO consisted of two etched lines, 1 cm from the edges throughout the length of the substrate. It created an isolated area to deposit the metallic electrode. This etching is symbolized by the two red lines in **Figure II-2**. First, the patterning of the FTO was performed by chemical etching using a zinc powder and a diluted hydrochloric acid solution (30% in water). Then, this technique was gradually replaced for practical reasons by laser patterning during this Ph.D. This change does not influence the final device characteristics.

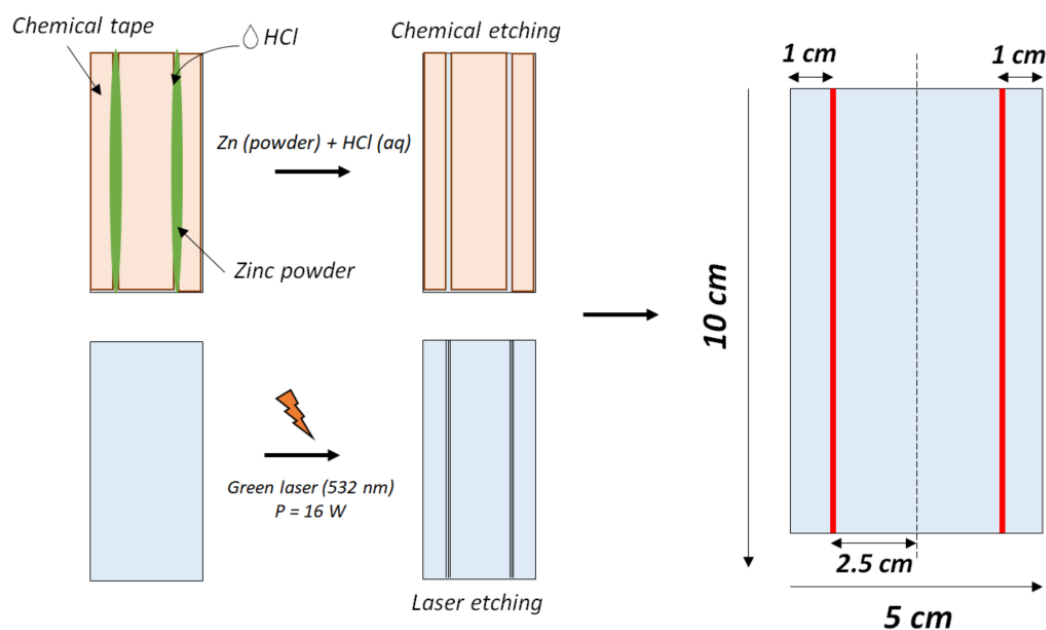


Figure II-2: Schematic description of the different etching techniques.

Following the scribing step, the glass substrates were washed during three successive ultrasound baths. First, the substrate was immersed in a detergent bath (2 vol% RBS™ in deionized water) for 45 minutes. Then, the glass was washed in acetone for 20 minutes and finally in isopropanol (IPA) for 20 minutes.

2.2. TiO₂ bilayer deposition

2.2.1. c-TiO₂ Layer

Once cleaned, the glass was introduced in UV-ozone cleaner for 15 minutes and then transferred on a hotplate for annealing at 500°C for 30 minutes to remove potential

organic residues (**Figure II-3**). Glass slides were deposited in the middle of the substrate to protect a part of the FTO from the spray-coating of the compact TiO₂ (c-TiO₂) layer. After 30 minutes, the hotplate temperature went down and stabilized at 450°C.

To prepare the compact TiO₂ layer, the solution was prepared just before the spray-coating. For a total volume of 50 mL, the solution was composed of 3 mL of titanium diisopropoxide bis(acetylacetonate) (30 vol% TAA precursor in IPA), 2 mL of acetylacetonone in 45 mL of IPA. The nozzle parameters were adjusted before each coating. After 20 deposition steps, the c-TiO₂ thickness is around 20 nm.

The successive moves were made 20 cm above the substrates, bottom to front and front to bottom, along with the red arrows in **Figure II-3**. After the spray-coating, the substrates were kept at 450°C for 15 minutes and then cooled down to room temperature. The substrates were then stored under vacuum until the subsequent layers deposition.

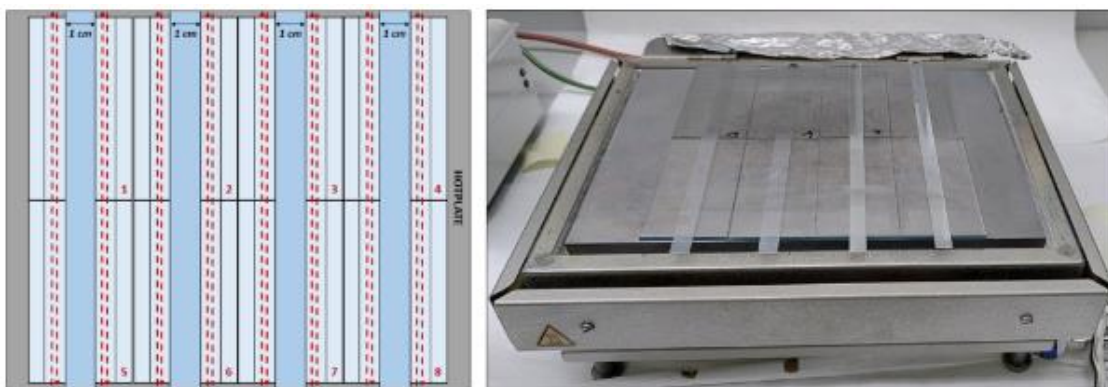


Figure II-3: Disposition of the glass/FTO on the hotplate for the c-TiO₂ deposition by spray pyrolysis. Schematic representation of the disposition of the glass substrates (left) and photo of the glass substrates on the hotplate (right).

2.2.2. Mesoporous deposition

The solution for the deposition of the mesoporous TiO₂ layer was a colloidal solution of TiO₂ nanoparticles (Greatcell Solar Materials, 30 NR-D, titania paste diluted in absolute ethanol). The solution concentration was a (EtOH: TiO₂) mass ratio of (7: 1). The solution was prepared at least 24 hours before the coating and stirred at ambient temperature.

In this step, the m-TiO₂ was deposited on the entire substrate as it was assumed that it was removed during the subsequent perovskite etching. The spin-coating parameters were the same as the baseline: $V_{\text{rotation}} = 4000 \text{ rpm}$, $a_{\text{rotation}} = 2000 \text{ rpm.s}^{-1}$, $T_{\text{rotation}} = 35 \text{ sec}$. A volume of 1.7 μL was deposited on the substrate by static spin-coating. After the deposition, the substrates were placed on a hotplate for annealing. The steps of the

annealing process are displayed in **Table II- 1**. After the coating, the substrate was kept under a vacuum.

Table II- 1: *Parameters of annealing of the mesoporous layer.*

Steps	1	2	3	4	5
Time (min)	5	15	5	5	5
Temperature (°C)	125	325	375	450	500
Ramp (°C/min)	25	13,3	10	15	10
Dwell time (min)	5	5	5	15	15

2.3. HTL deposition and evaporation of the gold electrode

The specific deposition protocol of the perovskite layer by slot-die is detailed in **part. 3**. After the slot-die deposition, the perovskite layer was removed from the glovebox and divided into individual cells of 2 x 2.5 cm² size.

The HTL solution is composed of spiro-OMeTAD powder at C = 11.14 M. The HTM is doped by including 3 oxidizing additives, namely the LiTFSI (lithium bistrifluoromethanesulfonimide) at C = 0.045 mol/L, the FK209 Co(III) (tris[2-(1H-pyrazol-1-yl)-4-tert-butylpyridine cobalt(III) tris bis(trifluoromethylsulfonyl)imide]) at 5.10⁻³ mol/L and commercial solution of 4-tertbutylpyridine (tBP) at C = 0.31 mol/L. Then, the HTL layer was deposited on each cell (V = 30 μL) by dynamic spin-coating inside a glovebox (3000 rpm for 30 seconds).

After, a chemical etching by DMF and DMSO revealed the FTO. Finally, a 100nm-thick gold electrode was evaporated on top of the stack. A metal mask delimited the active area of 0.09 cm². The final stack of the solar cell and the different deposition methods associated with each layer are displayed in **Figure II-4**.

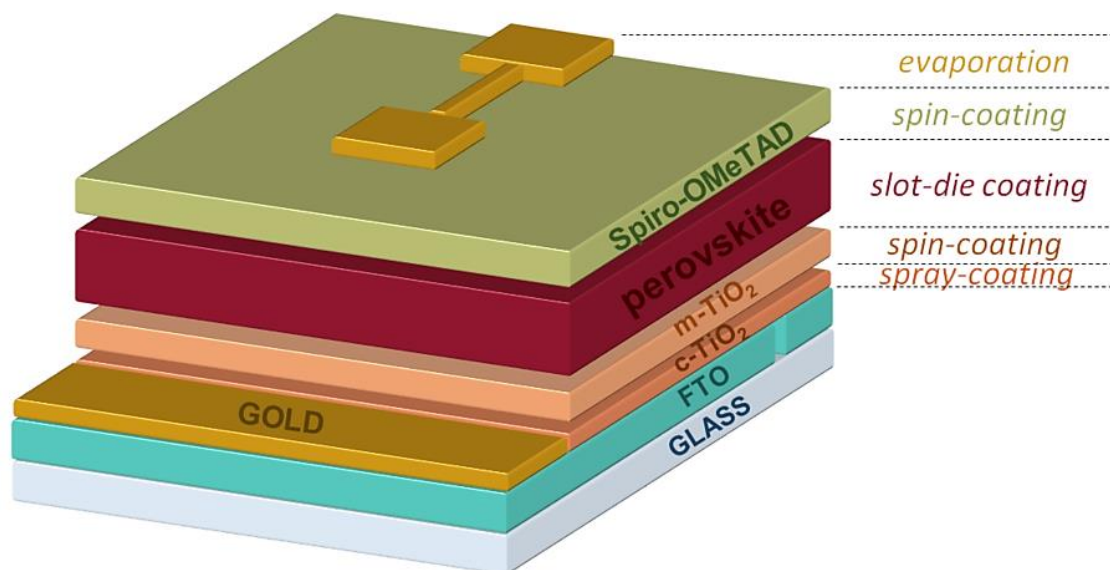


Figure II-4: Stack of a perovskite solar cell. Each layer is displayed with its associated deposition methods.

3. Perovskite absorber layer by slot-die coating

3.1. Presentation of the slot-die configuration

3.1.1. The slot-die setup

During this thesis, we used a nRad slot-die coater from nTact® to deposit the perovskite wet film. The slot-die is enclosed in a specially adapted glovebox from MBraun (**Figure II-5**). The maximum coating size is 20 x 20 cm². The chuck is made of a marble with a vacuum aspiration to ensure the perfect flatness and immobility of the substrate during the coating.

The perovskite precursors solution is pumped from the ink tank by a syringe and then injected into the coating head through the manifold, fixed on the head. The manifold distributes the coating fluid that enters the die and is designed to generate a uniform, streamlined flow of material through the exit slot of the die. The slot-die head can move above the substrate placed on the marble along both the X and Y-axis.

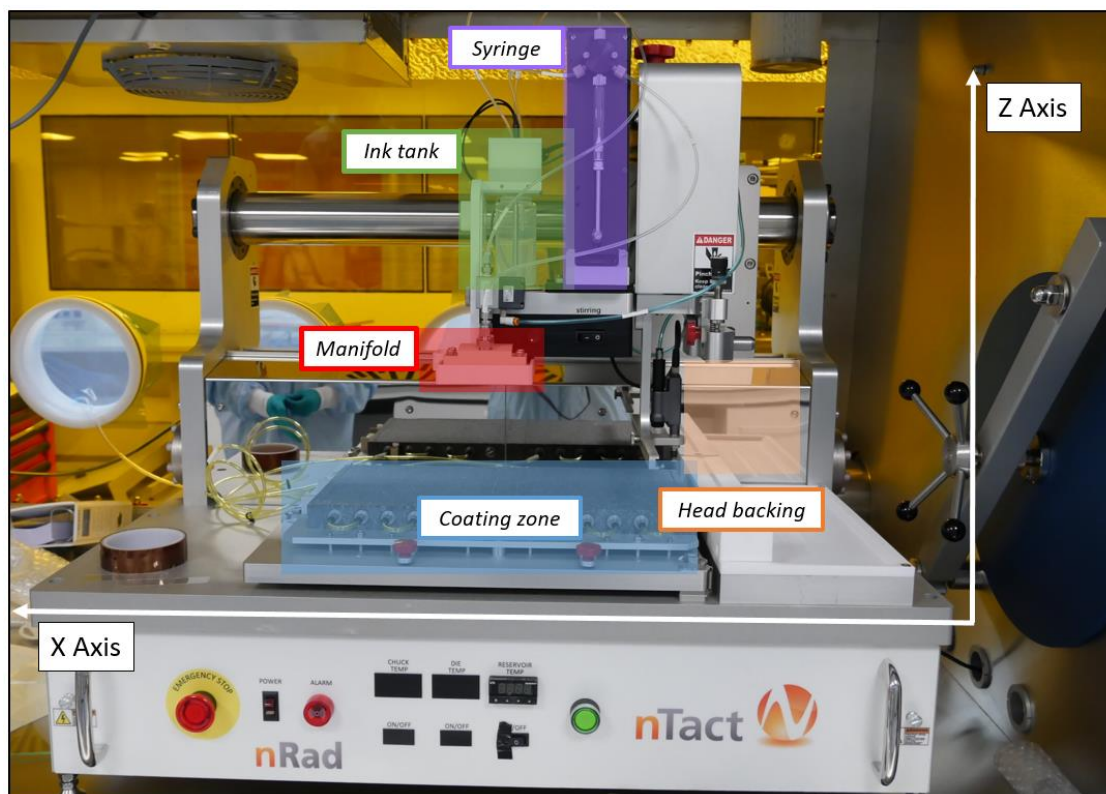


Figure II-5: The slot-die setup inside the glovebox before the building of the coating head. A UV filter protects the inside of the glovebox.

3.1.2. The slot-die coating head

The head is composed of two machined metallic pieces, made of stainless steel 316L to avoid chemical attacks, and is separated by a PEEK mask to control the distance between the two pieces, here around 125 microns. A schematic representation of the slot-die is displayed in **Figure II-6**. The most important parts of the head are the lips, delicate triangle parts, depending on manufacturers, that guide the ink flowing outside the head and form the meniscus.

The head also includes an ink tank to regularize the injection flow. Its size depends on the head size. For the smaller head of 5 cm coatings, the ink tank volume is about 2 mL. In total, the filling of the system (head ink tank + pumping system + syringe) necessitates around 5 mL of solution. For a classical batch of 10 large substrates, 20 mL of perovskite precursors solution was necessary.

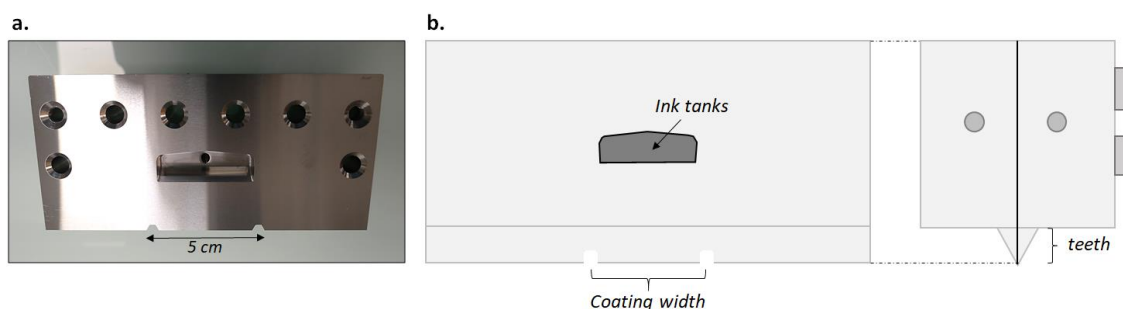


Figure II-6: a. Photo of the slot-die coating head with the ink tank. b. Schematic image of face and side of the slot-die coating head.

3.2. Optimization of the coating parameters

To properly initialize the coating and generate a homogeneous layer, the influence of the coating parameters on the perovskite layer quality has been investigated. The parameter optimization presented in this part has been performed with a double cation perovskite composition $\text{Cs}_{0.2}\text{FA}_{0.8}\text{Pb}(\text{I}_{0.95}\text{Br}_{0.05})_3$. This composition was first developed for slot-die deposition at IMEC (Interuniversity Microelectronics Centre) and transmitted during a training in the EnergyVille center (Leuven, Belgium). Then, this perovskite layer protocol was adapted at the IPVF lab. The first parameters optimization have been carried out on $5 \times 5 \text{ cm}^2$ substrate and then transferred to $5 \times 10 \text{ cm}^2$.

3.2.1. Meniscus formation and coating initialization

The formation of the meniscus is essential to initialize the coating. At the beginning of the deposition, the coating head aligns with the substrate. Then, the head approaches the substrate to form the meniscus by capillarity. This position is called the leading edge gap (L_{LEG}). Then, the head rises to its coating gap position (L_{CG}) and accumulates a volume of solution inside the meniscus to form the coating bed during the ink injection delay. The ink injection delay is the time between the beginning of the ink injection and the moment the coating head starts to move. The main coating steps are displayed in **Figure II-7**.

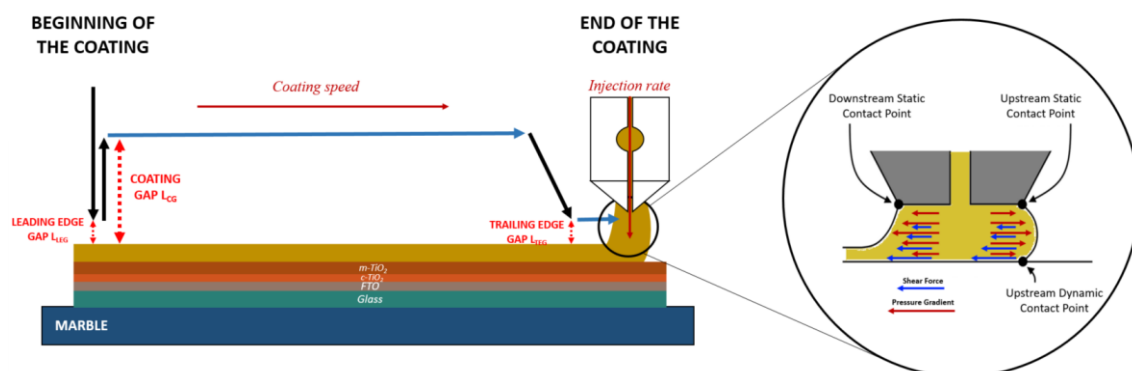


Figure II-7: Slot-die coating deposition parameters and main steps. Schematic representation of the meniscus.



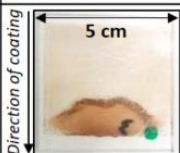



To form a stable coating bed, the combination of the leading edge gap, the coating gap, and the ink injection delay has been optimized. The slot-die coating of the perovskite layers has been first performed on a 5x5 cm² glass/FTO substrate. The results of the different coatings are displayed in **Table II-2**.

First, L_{CG} was fixed at 80 μm , and L_{LEG} was set at 60 μm . In these conditions, no coating was obtained regardless of the ink injection delay. In this case, we found that the gap was too high to maintain the integrity of the meniscus between the coating head and the substrate.

For a lower L_{CG} , namely 60 μm , the meniscus is not formed at the beginning of the coating. Consequently, increasing the ink injection delay up to 7 seconds to obtain a deposition was necessary. However, the deposition only started in the middle of the substrate, indicating that the meniscus was not formed at the beginning of the coating. The ink accumulation on the lips formed a drop that fell during the deposition. If the ink injection delay is further increased, it can overflow the meniscus and thus end up with an inhomogeneous layer.

Finally, L_{LEG} has been lowered to 30 μm . This time, the meniscus is initialized correctly from the beginning. In this case, an ink injection delay as short as 0.5 seconds became sufficient to onset a coating layer. Further increase of the ink injection delay generates an inhomogeneous coating. This observation suggests an important ink accumulation in front of the teeth, similar to a blade-coating mode. Regarding the previous results, the ideal initialization parameters are fixed to L_{CG} of 60 μm , L_{LEG} to 30 μm , and a delay of 2 seconds.

Table II-2: Influence of the leading edge gap and the ink injection delay during the deposition of the perovskite layer by slot-die coating.

Coating gap (μm)	Leading edge gap (μm)	Delay (s)			
		0.5	3	7	10
80	60	No coating	No coating	No coating	No coating
60	60	No coating	No coating		
	30				

3.2.2. Puddle phenomena and end of the coating

After a first optimization of the parameters, the substrates have been enlarged to 10x5 cm². We focused on the following key parameters at the end of the coating :

- The trailing edge gap (L_{TEG}), which brings the lips closer to the substrate at the end of the coating (μm)
- The ink injection offset, which stops the ink injection into the slot-die head before the end of the coating (mm)
- The ink suck back, which evacuates the residual ink inside the coating head to absorb the meniscus

The results are displayed in **Table II-3**.

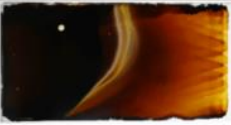





At the end of the coating, the meniscus breaks. The residual ink contained in the coating bed spreads over the end of the coating. It forms an area at the end of the coating with a higher thickness, called “puddle.” When the L_{TEG} is fixed at 70 μm and the ink injection offset at 5 mm, this area covers almost half of the glass substrate (ca. 6 cm).

Increasing the ink injection offset from 5 mm to 10 mm is an efficient way to decrease the puddle area. With the augmentation of the ink injection offset from 5 mm to 10 mm, the puddle area reduces to 3 cm. With an offset of 15 mm, a slight decrease of the puddle, from 3 cm to 2 cm, is observed. However, it is preferable not to use an ink injection offset larger than 15 mm since it induces a gradual diminution of the thickness towards the end of the coating.

Then, L_{TEG} has been gradually decreased from 60 μm to 40 μm to reduce the distance between the teeth and the substrate, hindering the break of the meniscus. A suckback then evacuates the residual ink inside the coating head to absorb the meniscus.

Finally, a combination of an ink injection delay of 15 mm, L_{TEG} of 50 μm , and a suckback of the residual ink into the head successfully allows the deposition of a perovskite layer without a visible puddle.

Table II-3: Influence of the ink injection offset, the ink suckback, and the trailing edge gap on the puddle formation during the deposition of the perovskite layer by slot-die coating.

Ink injection Offset <i>mm</i>	Ink Suck back	Trailing Edge Gap <i>μm</i>	Puddle spread <i>cm</i>	Photos
5	None	60	6	
10	None	60	3	
10	None	50	3	
15	None	50	2	
15	Yes	50	0.75	
15	Yes	40	No Puddle	

3.2.3. Optimization of the perovskite layer thickness and uniformity

Regarding the previous optimization results, the slot-die parameters were fixed at $L_{CG} = 60 \mu\text{m}$, $L_{LEG} = 30 \mu\text{m}$, an ink initialization delay of 2 seconds, $L_{TEG} = 50 \mu\text{m}$, and a final ink injection offset of 15 mm. The coating speed has been fixed at 14 mm/s.

The influence of the main operating parameters on the perovskite layer thickness has been explored:

- Ink injection rate (IIR) of the perovskite precursors solution ($\mu\text{L/s}$)

- Solid content (SC) of the deposited perovskite precursors solution

The SC is calculated as the mass ratio of the precursor on the total mass of the solution (**Eq. 1**).

$$SC_{\text{solution}} = \frac{m(\text{precursors})}{m(\text{precursors})+m(\text{solvent})} \quad (\text{Eq.1})$$

First, we explored the relationship between the thickness of the dry perovskite layer and the IIR. This study have been conducted with two different solution content $SC_1 = 26\%$ and $SC_2 = 33\%$ ($C_1 = 0.6\text{M}$ and $C_2 = 0.8\text{M}$). We fixed a thickness goal of ≈ 470 nm for the perovskite films. The results are displayed in **Figure II-8.a**.

At a solid content of 26% ($C_1 = 0.6\text{M}$), it is necessary to set the IIR up to $10 \mu\text{L/s}$ to obtain a layer thickness of up to 450 nm as determined by cross-section SEM measurements. However, a high IRR can generate a potential accumulation of ink in the meniscus, thus creating thickness heterogeneities on the perovskite layer. The augmentation of the coating speed will destabilize the meniscus. **Figure II-7** illustrates the different forces regulating the coating bed. The shear forces increase with the coating speed, which can generate coating defects call “dripping” that are visible on the substrates as bubbles or surface heterogeneities.² Consequently, the coating speed has to be limited to 13 mm/s.

To characterize the homogeneity of the perovskite layers fabricated with $\text{IIR} = 10 \mu\text{L/s}$ and $\text{SC} = 26\%$, 24 thickness measurements have been performed by profilometry along four measurements lines named e_1 , e_2 , e_3 , and e_4 on $5 \times 10 \text{cm}^2$ substrates (**Figure II-8.b**). These measurements create thickness mapping of the perovskite layer, displayed in **Figure II-8. c**. shows a large distribution of thickness values, from 300nm to 450nm, owing to the meniscus instability generated by the IIR of $10 \mu\text{L/s}$. Thus, the thickness is only 332 nm on average, a value significantly below the targeted thickness of 470 nm.

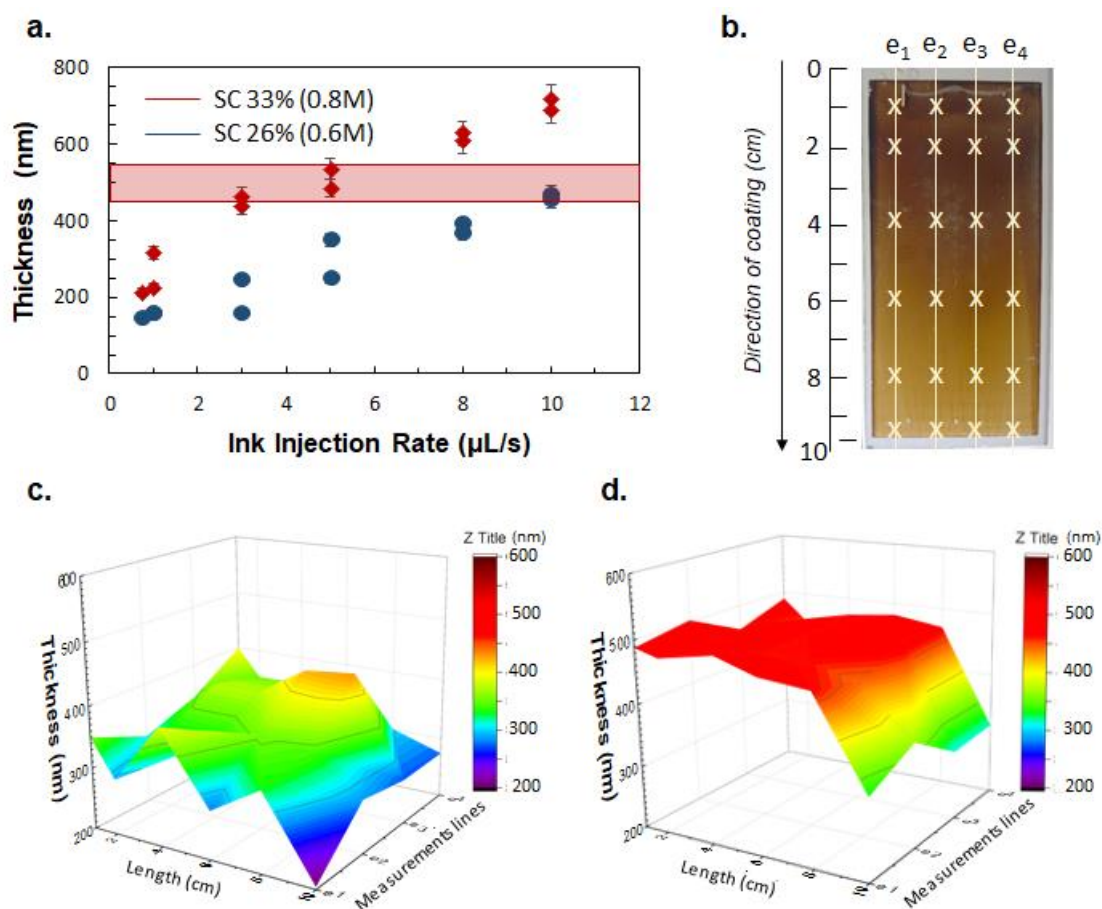


Figure II-8: **a.** Influence of the ink injection rate on the thickness of the perovskite layer deposited by slot-die coating (cross-section SEM measurements). **b.** Perovskite layer mapping. We performed 24 measurements symbolized by the crosses. The measurement lines are separated by 1 cm from each other and 0.5 cm from the edges. **c.** Thickness mapping of the perovskite layer. SC = 26% (0.6M). IIR = 8 $\mu\text{L/s}$. **d.** Thickness mapping of the perovskite layer. SC = 33% (0.8M). IIR = 3 $\mu\text{L/sec}$. The thickness values were determined by profilometer measurements.

At a solid content of 33% ($C_2 = 0.8\text{M}$), a smaller IIR between 3 and 5 $\mu\text{L/sec}$ is necessary to reach a 470nm thick perovskite layer. In addition, the thickness map is displayed in **Figure II-8. d.** displays a more uniform profile with an average thickness of ca. 460 nm. If we exclude the last centimeter of the coating, the standard deviation is reduced from $\sigma = 42$ nm for the following parameters SC = 26% (0.6M) / IIR = 8 $\mu\text{L/sec}$, down to 16 nm for SC= 33% (0.8M) / IIR = 3.5 $\mu\text{L/sec}$.

In both cases, after 9 cm of coating, the map shows a significant decrease in the thickness of the perovskite layer, which is ascribed to the ink injection delay set at 15 mm. Consequently, in the rest of this thesis, the first and the last 1 cm of the substrate will be considered as sacrificial area and thus never used.

Finally, the optimized slot-die deposition parameters used for the fabrication of the perovskite layer during this work are displayed in **Table II-4.**

Table II-4: Optimized slot-die deposition parameters

Meniscus Initialization			Coating			End	
Ink injection delay	L_{EG}	L_{CG}	Coating speed	IIR	SC	L_{TEG}	Ink injection offset
s	μm	μm	mm/s	$\mu\text{L/s}$	%	μm	mm
2	30	60	14	3.5	33	40	15

3.3. The drying step

After the slot-die coating deposition, a wet perovskite layer is obtained. To trigger the nucleation and growth of the crystalline phase, it is essential to extract the solvent. This drying step can be ensured either by slow self-drying or a quenching method.

Traditionally for spin-coating, the solvent is evacuated by the dripping of an anti-solvent on the substrate for the spin-coating process. However, this technique is unsuitable for deposition on large areas and contributes to excessive chemical wastes in the elaboration process, as largely discussed in **Chapter 1**.

Several solvent extraction systems have been compared to the vacuum aspiration method to compare the crystallization paths: Self-drying (**Figure II-9.a**), dipping in anti-solvent (**Figure II-9.b**), vacuum extraction (**Figure II-9.c**), and vacuum extraction combined with simultaneous annealing (**Figure II-9.d**). Then, after the solvent extraction, all the perovskite layers were annealed for 30 minutes at 110°C . In **Figure II-9.e**, the theoretical behavior of La Mer curves under each solvent extraction condition is represented.

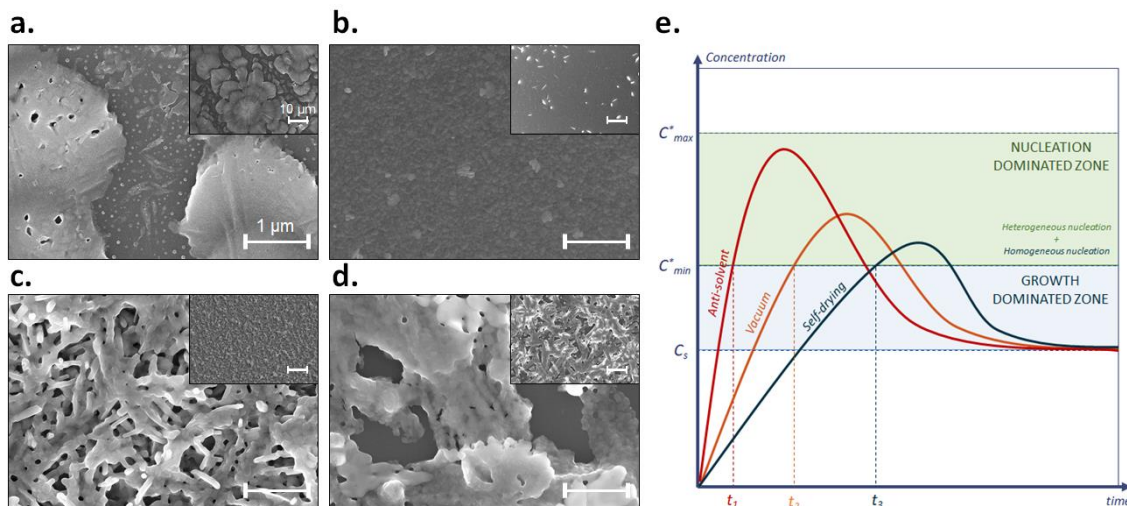


Figure II-9: SEM image of perovskite films deposited on glass/FTO/c-TiO₂ and dried under different conditions. **a.** Self-drying. **b.** Dipping in CB bath for 2 minutes. **c.** Vacuum extraction for 5 minutes and, **d.** Vacuum extraction for 5 minutes at $T = 75^{\circ}\text{C}$. **e.** Influence of the extraction

solvent on the nucleation and growth rate according to the La Mer theory. The value t_x is the time between the beginning of the solvent extraction and the entry in the supersaturation state.

First, a perovskite layer was self-dried in the glovebox filled with nitrogen for 30 minutes. The SEM image (**Figure II-9.a**) shows an uncovering perovskite layer. The c-TiO₂ underlayer is visible. The island-like perovskite morphology is typical of a Volmer-Weber growth model, suggesting that small clusters nucleate directly on the substrate surface and grow into islands of the condensed phase.³ Zheng *et al.* suggested that island-shaped perovskite films are first formed and subsequently coalesce into dense films.⁴ According to the La Mer mechanism, the rate at which a solution enters a supersaturation state is a primary factor in regulating the perovskite nucleation.^{5,6} Considering the unstrained supersaturation state induced by the long solvent evaporation time under self-drying conditions, a limited number of nuclei appear in the precursor's solution.⁷ Therefore, slow self-drying generates a lower amount of nuclei which prevent the coalescence of the perovskite islands and generate an incomplete film's coverage.

Then, the solvent extraction by an anti-solvent dripping has been studied by immersing a perovskite layer in 30 mL of chlorobenzene for 2 minutes. On the SEM image (**Figure II-9.b.**), the perovskite layer exhibits a smooth surface with a complete coverage. On the La Mer curve, we defined t_1 , the time before the solution enters in supersaturation state by anti-solvent dripping, and t_3 , the time before the solution enters in supersaturation state by self-drying. In **Figure II-9.e.**, $t_1 < t_3$ indicates that the level of supersaturation is reached faster in the case of anti-solvent dripping. Consequently, contrary to the self-drying method, anti-solvent dipping triggers faster nucleation and yields uniform growth around these nuclei.

Finally, the third condition investigated is vacuum extraction. A vacuum aspiration plate has been installed inside the glovebox to accommodate upscale processes better (**Fig. II-10**). After the slot-die coating, the wet film is placed inside the vacuum chamber, which can reach one mbar in 4 minutes. The pressure is then maintained at this level of vacuum for one minute. In this case, the final perovskite layer shows a dendritic morphology, with improved coverage compared to self-drying, albeit numerous pinholes and incomplete coverage is still noticed (**Figure II-9.c.**), suggesting an insufficient nuclei density. In addition, we explored the combination between aspiration and simultaneous annealing. As visible on the SEM image (**Figure II-9.d.**), increasing the temperature to 70°C promotes the grain growth in the perovskite film, resulting in denser, though incomplete, perovskite film. The augmentation of the temperature enhances the dissolution of the colloids in the solvent, leading to a quick supersaturation rate. According to M. Bari *et al.*, the high temperature of the system generates a high nucleation rate, causing an abrupt decrease in supersaturation and preventing further crystal growth.⁸ In addition, owing to the thickness of the FTO glass (i.e., 3.1 mm), noticeable thermal inertia exists. As a result, at the beginning of the aspiration, the glass takes a few seconds before reaching the

setpoint temperature of 100°C. Therefore, the annealing is delayed from aspiration and promotes incomplete nucleation.

From these results, it appears very clear that vacuum extraction is a procedure less efficient than anti-solvent dipping to extract the solvent. Therefore, it is necessary to adapt the perovskite precursors solution composition to these new drying conditions.

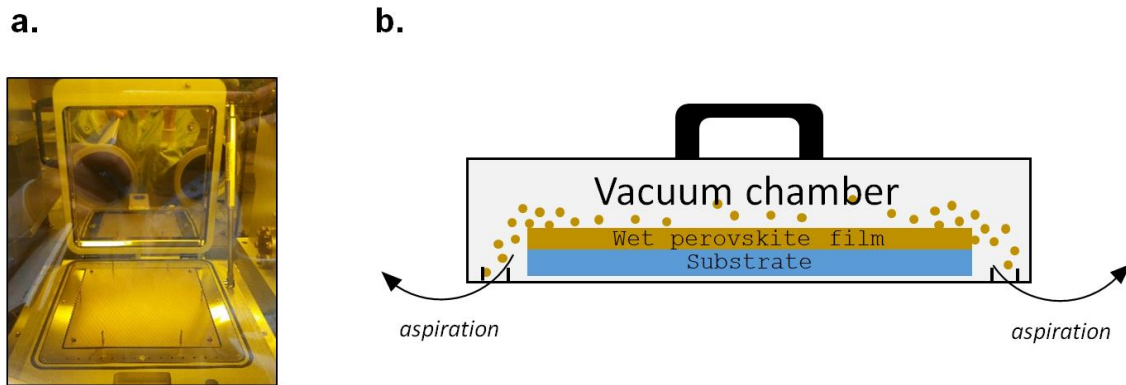


Figure II-10: **a.** Photo of the vacuum chamber used for the solvent extraction of wet perovskite layer after the slot-die deposition. **b.** Schematic description of the vacuum aspiration method.

4. Surfactant addition into the perovskite precursor's solution

Considering La Mer's theory, as discussed in **chapter 1**, for a satisfying perovskite film morphology, it is essential to find the conditions to have fast nucleation and delayed growth. Introducing an additive into the perovskite precursors solution can favor the nucleation versus growth mechanism and efficiently modify the perovskite crystallization kinetic. This approach is at the core of the next part, in which we describe our results in the introduction of a surfactant into the perovskite ink.

4.1. Nucleation theory and surface energy tailoring

The total free energy in solution is given by the sum of the surface free energy and the bulk free energy :

$$\Delta G = \Delta G_s + \Delta G_b = 4\pi r^2\gamma + \frac{4}{3}\pi r^3\Delta G_b \quad (\text{Eq.2})$$

Where r is the radius of a spherical particle and γ is the surface energy.

As shown in **Eq.2**, surface energy γ is a critical factor influencing nucleation behavior, especially in heterogeneous nucleation. To grow a uniform layer of a perovskite film, it is crucial to form heterogeneous nuclei on the substrate rather than homogeneous nuclei or heterogeneous nuclei on colloidal particles.³

During the nucleation phase in a perovskite wet film, the interfacial energy has three components, as shown in **Figure II- 11**. The terms γ_{c-l} , γ_{s-c} , and γ_{s-l} are the interfacial energies between the liquid and crystalline phase, crystalline phase and solid surface, and between the solid surface and liquid, respectively. In experimental conditions, a solid surface can be the substrate as well as impurities existing in the solution. Here, θ is the contact angle of the solution on the solid surface. If θ decreases, the nuclei and active centers exhibit higher affinity, leading to a lower energy barrier for nucleation. This phenomenon can be ascribed to the substantial reduction in the interface energy. Therefore, to promote heterogeneous nucleation on the surface of the substrate, the approach of introducing a surfactant into the precursor solution appears promising.

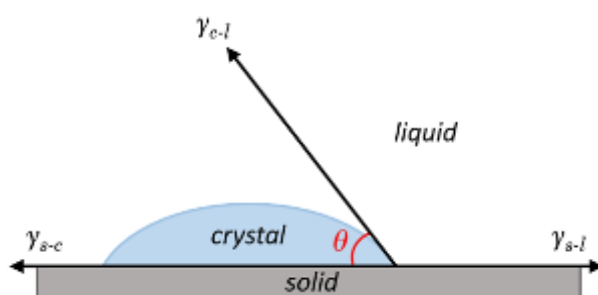


Figure II- 11: Illustration of the contact angle (θ) for heterogeneous nucleation

4.2. Composition and structure of surfactants

Surfactants are molecules that lower the surface tension (or interfacial tension) between either two liquids, a gas and a liquid or a liquid and a solid. Surfactants are usually amphiphilic organic molecules, meaning that they contain both a hydrophobic tail and a hydrophilic head (**Figure II-12. a**). Therefore, a surfactant contains both a water-insoluble (or oil-soluble) component and a water-soluble component.

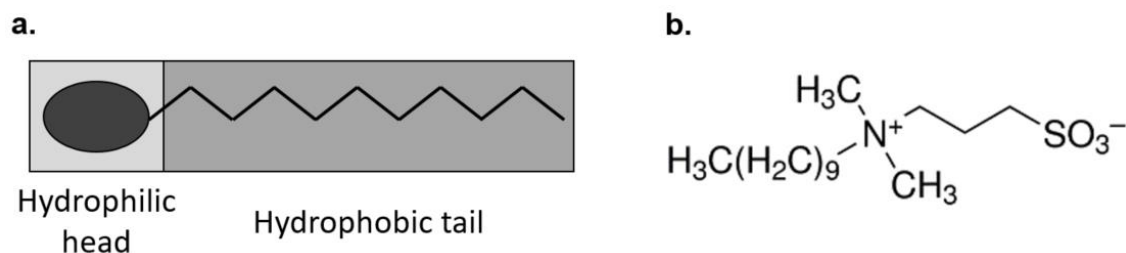


Figure II-12: a. Schematic representation of a surfactant. **b.** Chemical structure of the surfactant: *N-Dodecyl-N,N-dimethyl-3-ammonia-1-propanesulfonate inner salt*

In this part, we selected a zwitterionic surfactant with an anionic sulfonate group and a quaternary ammonium cationic group (**Figure II-12. b**). Several groups highlighted the role of the quaternary ammonium group for the passivation of I⁻ vacancy defects⁹⁻¹¹, combined with either a phosphate or sulfonate anionic group.^{12,13}

Interestingly, X. Zheng *et al.* demonstrated the existence of coordination between PbI_2 and the sulfonate group, which as a consequence, has the potentiality to slow down the perovskite crystal growth, therefore hindering the morphological defects. The authors proposed that a sulfonate-based surfactant can efficiently attach to the surface of the perovskite nucleus' due to the strong affinity of the sulfonate group to bind with lead ions.

4.3. Deposition of $\text{Cs}_{0.2}\text{FA}_{0.8}\text{Pb}(\text{I}_{0.95}\text{Br}_{0.05})_3$ perovskite

4.3.1. Preliminary tests by spin-coating deposition

4.3.1.1. Experimental method

We performed preliminary tests to investigate several concentrations before any slot-die deposition by associating the spin-coating method and our vacuum aspiration system. Therefore, small size substrates glass/FTO/c-TiO₂/m-TiO₂ of 2x2 cm² have been fabricated according to the process detailed in **part. 2**.

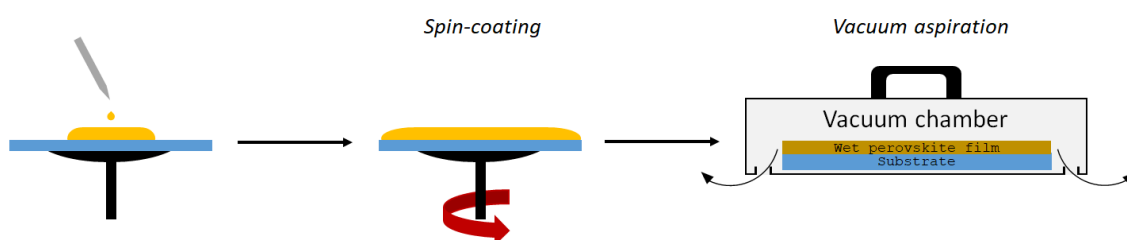


Figure II-13: Spin-test protocol

As specified in **part.3**, the perovskite precursors solution has a solid content of 33% ($C = 0.8\text{M}$) for the slot-die deposition. This concentration is lower than the perovskite precursors solution traditionally used for the baseline deposition by spin-coating. In comparison, at IPVF lab, the baseline solution concentration is 1M, which is in the range of the optimized precursors' concentrations reported in the literature (0.8M - 1.1 M).¹⁴⁻¹⁷

To mimic the upscale process drying conditions and keep a satisfying layer thickness, the spin-coating rotation has been lowered from 6000 rpm to 2000 rpm for 20 seconds. Indeed, a low rotation rate also avoids solvent evaporation during the film's deposition. As a result, the thickness of the perovskite layers deposited by spin-coating is ca. 400 nm. For the same precursor's concentration, the films deposited by slot-die exhibits a thickness of ca. 470 nm (**Figure II-14**). After the deposition, the solvent was evacuated by vacuum aspiration ($P_{\text{min}} = 0.7$ mbar after 5 minutes). Finally, the film is converted into a perovskite structure by post-annealing at 110°C for 30 minutes.

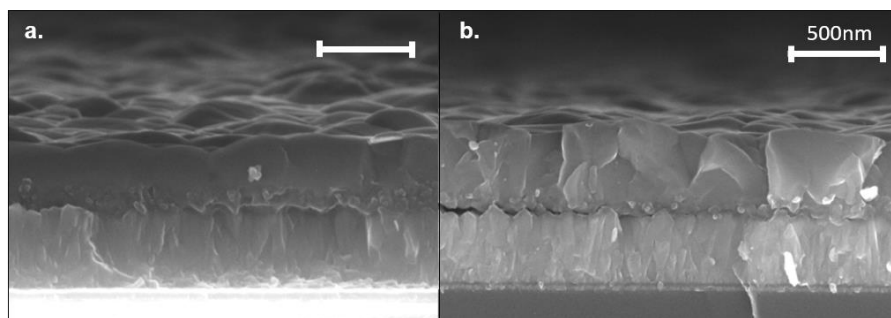


Figure II-14: Cross-section SEM images of a perovskite layer deposited on glass/FTO/c-TiO₂/m-TiO₂ by different deposition methods: **a.** Spin-coating and **b.** Slot-die coating.

4.3.1.2. Morphological characterization

The 3DPS surfactant was directly added into the perovskite precursors solution (FAI, PbI₂, PbBr₂, CsI) in a DMF/NMP mixture (10:1 by vol.), and the surfactant concentration was stepwise increased.

Without surfactant, the perovskite layer exhibits a matt surface aspect, typical of high surface roughness. In **Figure II-15**, the confocal image displays a heterogeneous surface with visible black voids. The SEM measurements show that the perovskite layer is not covering, as illustrated by the visible TiO₂ underlayer. The comparison with the reference sample fabricated by the anti-solvent method evidences the important role of the solvent extraction system over the perovskite crystallization and the final morphology of the film.

With the addition of surfactant, the fabricated perovskite film presents a gradual change of transmission, visible on the images of the backlit perovskite samples. According to the associated confocal and SEM images, the surface heterogeneities are progressively suppressed, and the layer coverage is improved with the surfactant addition. A low surfactant concentration, i.e., 3 and 10 mM, presents significantly fewer visible pinholes than the reference sample obtained without surfactant. The SEM images demonstrate a smooth perovskite layer surface, typical of a mirror-like aspect, for a surfactant concentration up to 30 mM. As a result, one can conclude that introducing the 3DPS surfactant efficiently lowers the interfacial energy barrier to promote nucleation, resulting in a uniform perovskite film with full coverage.

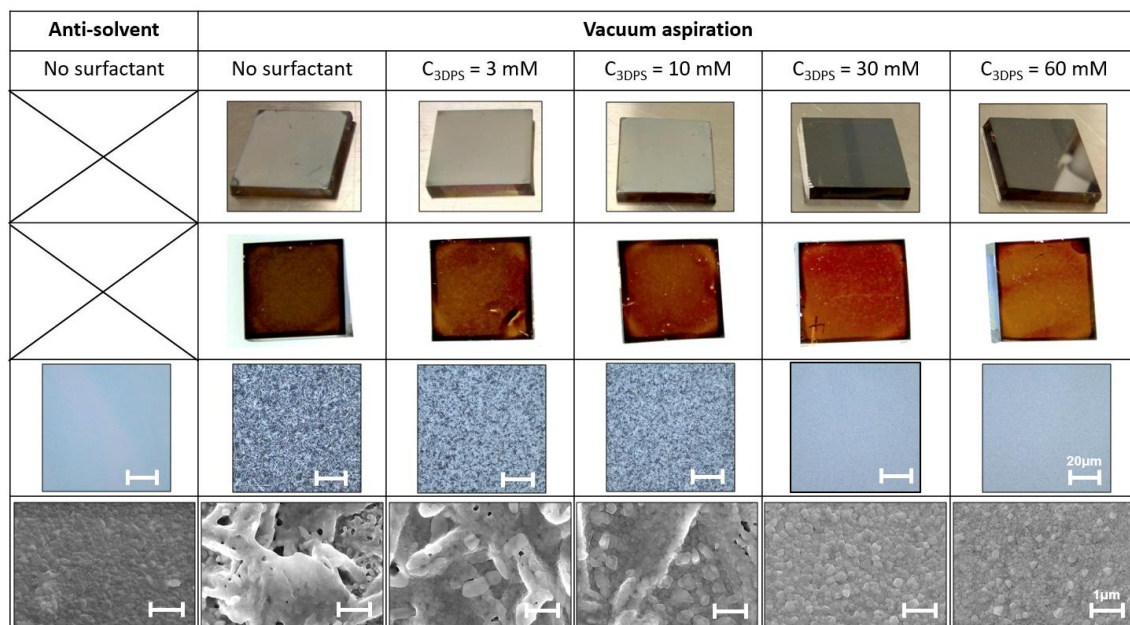


Figure II-15: Pictures, confocal images, and surface SEM images of the perovskite layer deposited by spin-coating on glass/FTO/c-TiO₂/m-TiO₂.

To further investigate the film's morphology, the roughness of the perovskite layer was determined with confocal microscopy by 3D image acquisition of the perovskite surface on a 130 x 130 µm² area. We decided to consider Sa, the calculated difference in height of each point compared to the arithmetical mean of the surface height, as our reference roughness value. To ensure that the results were statistically informative, the scanning location were randomly selected, and each Sa value of **Figure II-16** is a calculated average from three different confocal measurements.

Without surfactant, the perovskite layer presents a surface roughness value of 171 nm. In comparison, a perovskite layer with the same composition fabricated by spin-coating and anti-solvent method displayed a roughness value of 17 nm. As presented in **part 3.3**, the vacuum extraction induces insufficient nucleation leading to non-covering and high-roughness perovskite films. Such high roughness can be detrimental to devices performances due to its high probability of carrier leakage through direct contact between the two selective extraction layers.¹⁸

The surfactant addition leads to a decrease of surface roughness by improving the perovskite film coverage. The perovskite films prepared with a surfactant concentration of 3, 10, 30, and 60 mM showed Sa values of 111 nm, 93 nm, 19 nm, and 17 nm, respectively. Beyond a concentration of 30 mM, the surface roughness seems to stabilize.

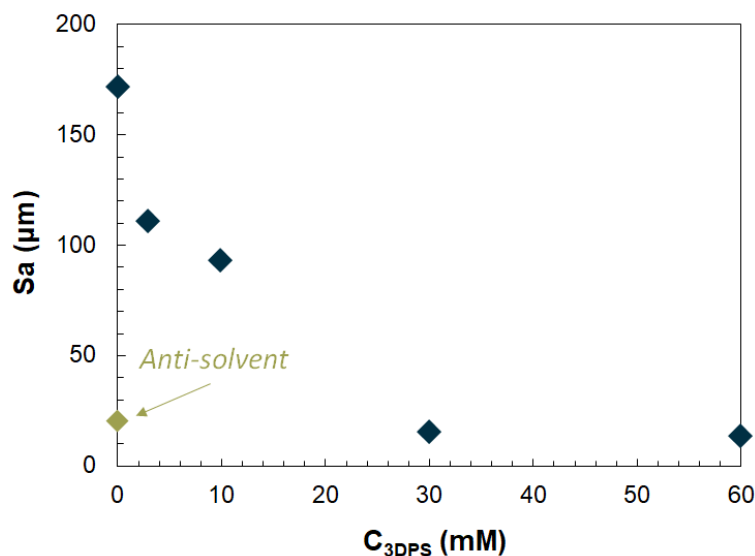


Figure II-16: Surface roughness S_a versus 3DPS surfactant concentration. The S_a values are extracted from the confocal images.

4.3.2. Wetting properties

The effect of surfactant on the film coverage has been characterized by following a de-wetting study. For this, a droplet ($V = 15 \mu\text{L}$) of perovskite precursors solution has been deposited on Glass/FTO/c-TiO₂/m-TiO₂ substrates. During gradual self-drying of the ink droplet under ambient conditions, the wetting angle and the spreading surfaces have been characterized by drop angle measurements (**Figure II-17**). These conditions were kept constant between the different sets of experiments.

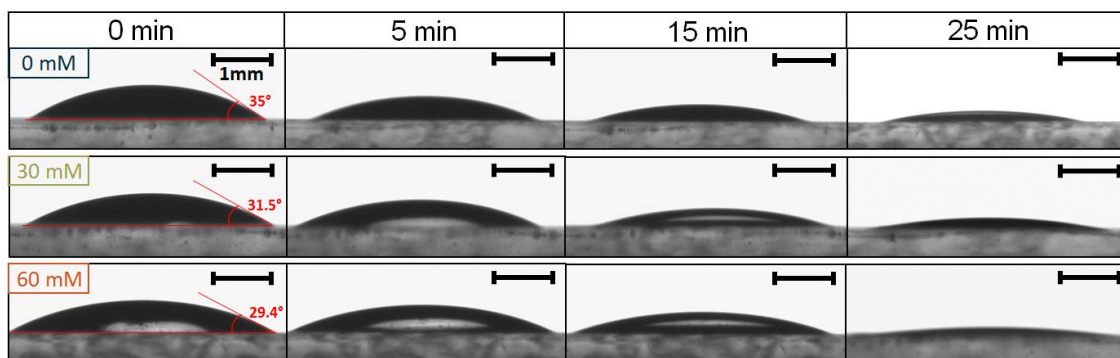


Figure II-17: Droplet angle measurements. ($V_{\text{initial}} = 15 \mu\text{l}$) deposited on Glass/FTO/c-TiO₂/m-TiO₂ substrates under ambient conditions without 3DPS and with 30mM and 60 mM 3DPS. The scale bar is 5 mm.

In **Figure II-17**, we can observe that the surfactant concentration of 30 mM and 60 mM leads to a contact angle θ of 31.5° and 29.4°, respectively. For comparison, a contact angle θ of 35° was determined without surfactant. This result confirms that the

introduction of 3DPS into the precursor's solution affords to modify the surface energy of the perovskite ink and improves its wettability to the underlying substrate. Regarding the contact angles, 3DPS addition can result in a lower energy barrier for the formation of heterogeneous nucleation. It indicates that surfactants modify the ink/substrate interface and improve perovskite ink's wettability on the substrate.

In addition, we monitored the drying of a perovskite ink droplet deposited on the substrate. During solvent evaporation, the droplet volume decreases, and the contact surface of the droplet evolves differently depending on the surfactant content. The droplet coverage is defined as the substrate area covered by the droplet during drying versus the initial surface covered. Without surfactant, the total coverage was reduced from 3.7 cm to 2.9 cm, so a drop of 22% after 25 minutes (**Figure II-18**).

As 3DPS was blended into the perovskite precursors solution, the droplet coverage decreased only from 3.9 cm to 3.6 cm and from 4.2 cm to 4 cm, for 60 mM and 30 mM concentration, respectively. It represents a surface loss of 9% for a concentration of 30 mM and 5% for 60 mM. This "pinning effect" has also been evidenced for another type of surfactants added in the perovskite precursors solution.¹⁹ Considering the existing relationship between the surface tension and the nucleation rate evidenced in part 4.1, the addition of the surfactant represents an efficient way to promote nucleation during perovskite crystallization.

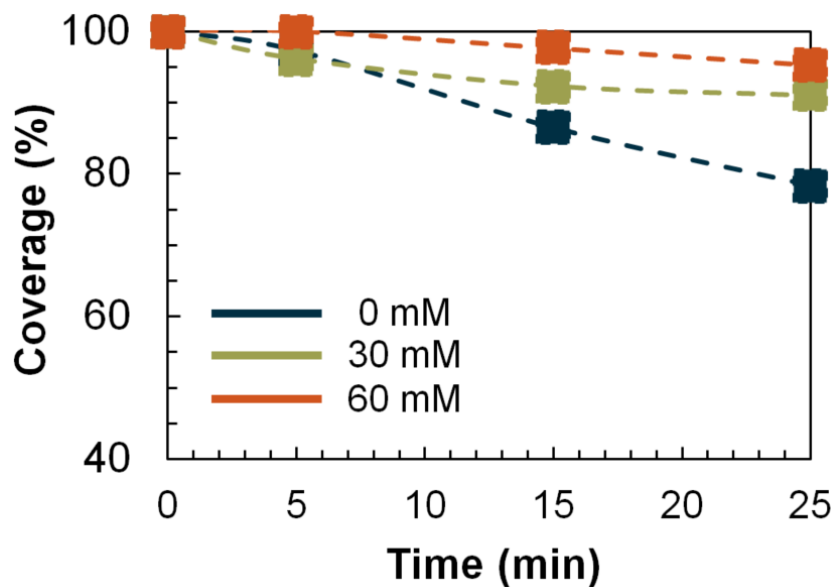


Figure II-18: *The evolution of coverage of perovskite droplets during drying.*

4.3.3. Slot-die deposition of the perovskite layer

After the first evaluation by spin coating, the perovskite films have been deposited on 5 x 10 cm² Glass/FTO/c-TiO₂/m-TiO₂ substrates by slot-die coating. A perovskite film

obtained without surfactant and two films prepared with 30 mM and 60 mM of 3DPS surfactant added in the perovskite precursors solution have been studied. All the films were dried by a vacuum aspiration for 5 minutes and annealed at 110°C for 30 minutes.

4.3.3.1. Morphological characterization

Without surfactant, the surface roughness of the perovskite film deposited by slot-die reached a Sa value of 156 nm (**Figure II-19**). However, the addition of surfactant at a concentration of 30 mM and 60 mM decreased the Sa values to 34 nm and 22 nm, respectively. Besides, the height distribution is significantly reduced, which indicates an improvement of the perovskite film uniformity with the surfactant addition.

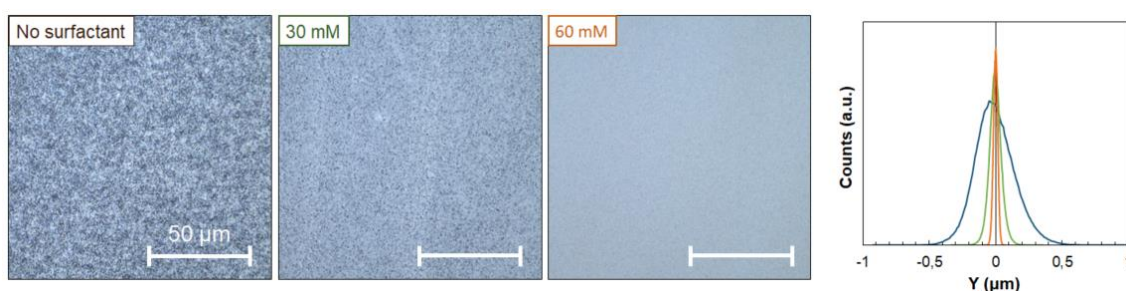


Figure II-19: Confocal images of the perovskite layer deposited by slot-die coating on glass/FTO/c-TiO₂/m-TiO₂ and the associated height distribution of each point compared to the arithmetical mean of the surface.

The difference of absolute Sa value between the spin-coated films and the slot-die films can be attributed to the change of deposition method, which induces a more extended coating window in the case of the slot-die deposition. The window coating represents the time between the coating and the solvent extraction and can impact the nucleation and, thus, the final morphology.²⁰ However, the reduction of the surface roughness by the surfactant addition is confirmed, independently of the deposition method.

The SEM images in **Figure II-21** show that the numerous pinholes create uncovered areas by the perovskite layer without surfactant addition. This is consistent with the previous wettability study, which evidenced the shrinking of the perovskite film upon drying. On the contrary, with the surfactant addition, the affinity of the perovskite film with the substrate increases.

Moreover, the grain size distribution from the SEM images has been extracted with ImageJ software. The average grain size of perovskite film with a surfactant concentration of 30 mM and 60 mM of 3DPS is 127 nm ($\sigma_{30} = 55$ nm) and 105 nm ($\sigma_{60} = 40$ nm), respectively. However, it is smaller than the average particle size without surfactant, which is 251 nm ($\sigma_0 = 118$ nm). Thus, it appears that the surfactant addition homogenizes the grain growth. The gradual diminution of the standard deviation σ illustrates an improved uniformity of the grain size as the 3DPS concentration increases. However,

perovskite films with 3DPS addition present a significantly lower average grain size. Q. Wang *et al.* studied the influence of a similar surfactant addition (1.5 wt. % weight ratio), sulfobetaine zwitterions, in precursors' solution and evidenced a direct link between the reduction of the size of the colloids in solution and the final perovskite grain size. In comparison, a concentration of 30 mM in our solution represents a mass ratio of 2 wt. %; In addition, during the crystallization process, the surfactant molecules were expelled to the grain boundaries (GBs), which may maintain the grain size by impeding further grain growth.²¹ Interestingly, the perovskite grain size was not detrimentally impacted in other recent works, provided that the surfactant concentration was kept below a weight ratio of 0.05 wt%.^{12,19}

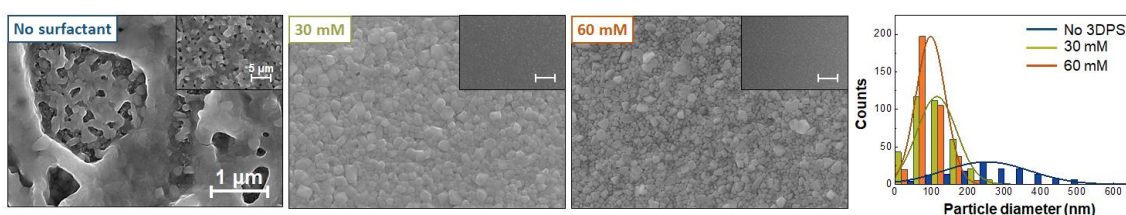


Figure II-20: SEM surface images of the perovskite layer deposited by slot-die coating on glass/FTO/c-TiO₂/m-TiO₂ without and with 30 mM and 60 mM 3DPS introduced into the precursor solution. The associated distribution of particles diameter is also reported.

The compactness of the perovskite film was improved, and the formation of pinholes was suppressed. On the cross-section SEM images, the perovskite films without 3DPS present an unequal vertical growth, whereas the surfactant addition gradually improves the compactness of the perovskite film. Moreover, we can observe that the reduced diameter of the grains (100-130 nm) with the surfactant addition creates multiple grain boundaries perovskite films, resulting in lower device performances.²²⁻²⁴

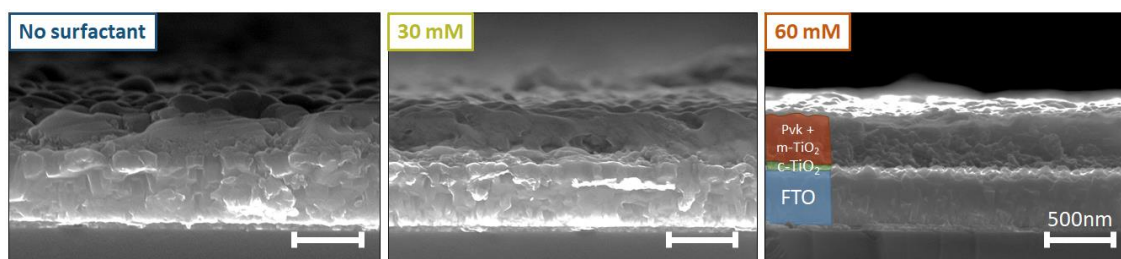


Figure II-21: Cross-section SEM images of the perovskite layer deposited by slot-die coating on glass/FTO/c-TiO₂/m-TiO₂ depending on the surfactant concentration.

4.3.3.2. Structural evolution

In **Figure II-22**, all XRD diffractograms display a pure α -phase, indexed by the cubic Pm-3m space group, independently of the surfactant concentration. The crystallite size, the lattice parameters, and the (100)/(110) intensity ratio are displayed in **Table II-5**.

Depending the surfactant concentration, the (100) characteristic peak position presents a steady position at $\theta = 13.98^\circ$. Consequently, all the films display a lattice parameter of $\approx 6.321 \text{ \AA}$.²⁵ This is consistent with the conclusions of Q. Wang et al. suggesting that the surfactant species migrate towards the grain boundaries without integrating into the crystal structure.²¹

In addition, the peak intensity ratio between the (100) and the (110) increases from 4.1 to 6.1 with the surfactant concentration of 60 mM. This result suggests that the surfactant affects the film crystallinity. It tends to promote a preferential orientation according to the (100) planes parallel to the substrate.

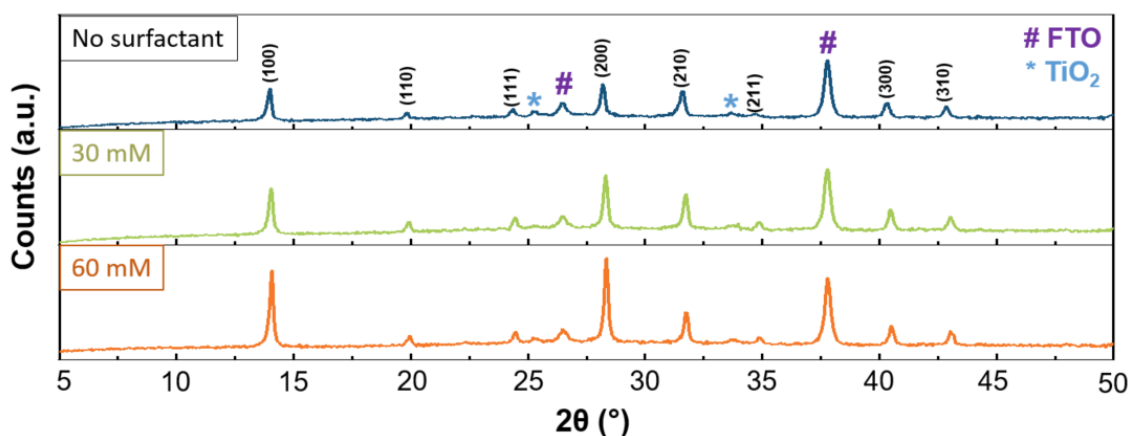


Figure II-22: XRD diffractograms of the perovskite layer deposited by slot-die coating on glass/FTO/c-TiO₂/m-TiO₂ as a function of surfactant concentration.

The crystallite sizes have been calculated using the Williamson-Hall. The method is detailed in **Annex 5**. We approximated our grains as isotropic spherical shapes (shape factor $K = 0.88$), which is a reasonable hypothesis according to the SEM images. The crystallite size gradually decreases while the surfactant concentration increases from 177 nm without surfactant to 100 nm and 91 nm for 30 mM and 60mM. The reduction of the crystallite size follows the same trend as the grain size visualized by SEM.

Finally, the lattice strains decrease from 2.4 for the reference without 3DPS to 1.1 and -0.5 for a surfactant concentration of 30 mM and 60mM. Thus, it indicates the relaxation of the tensile strains induced by the addition of a surfactant.

Table II-5: Parameters calculated from refined diffractograms. Variation of the 3DPS concentration. The crystallite size has been calculated using the Williamson-Hall method.

C_{3DPS} (mM)	D (nm)	a (Å)	(100)/(110)	strains ϵ (10^{-3})
0	106 (9)	6.328 (9)	4.1	2.4
30	103 (9)	6.321 (7)	3.5	1.1
60	79 (6)	6.319 (9)	6.1	-0.5

4.3.3.3. I-V measurements

The perovskite solar cells (PSCs) have been fabricated according to the fabrication proceeding explained in **parts 2 and 3**. The structure of all the devices is a n-i-p architecture: Glass / FTO / c-TiO₂ / m-TiO₂ / Cs_{0.2}FA_{0.8}Pb(I_{0.95}Br_{0.05})₃ / Spiro-OMeTAD / Au. The performances of PSCs made without and with the surfactant are gathered in **Figure II-23**, and all the device characteristics are reported in **Annex 6**.

Looking at the devices statistics based on 10 devices for each surfactant concentration (**Figure II-23**), both the J_{sc} and the V_{oc} are increased, from an average value of 5 mA.cm⁻² and 0.99V for the reference devices to 16.9 mA.cm⁻² and 1.08V for the devices made with a concentration of 30mM. The improvement of the perovskite morphology translates into an enhanced quality of the perovskite interface with the selective extraction layers, thus allowing a better charge extraction.

However, the diminution of the I-V characteristics for a concentration of surfactant of 60 mM points out a limit to its beneficial effect. In fact, the average J_{sc} and V_{oc} are decreasing to 14.15 mA.cm⁻² and 1.01 V, respectively. Moreover, the Fill Factor value displays a continuous decrease from an average of 69% for devices fabricated without surfactant to 66.4% for 30 mM and 64.6% for 60 mM.

One possible explanation is nested in the gradual diminution of the grain size and thus the multiplication of grain boundaries, which are impeding charge collection and favor carriers recombination.²⁶ In another hand, it could also be explained by an excess of 3DPS still present in the film that creates an insulating layer surrounding the perovskite grains and would gradually impact the fill factor.¹²

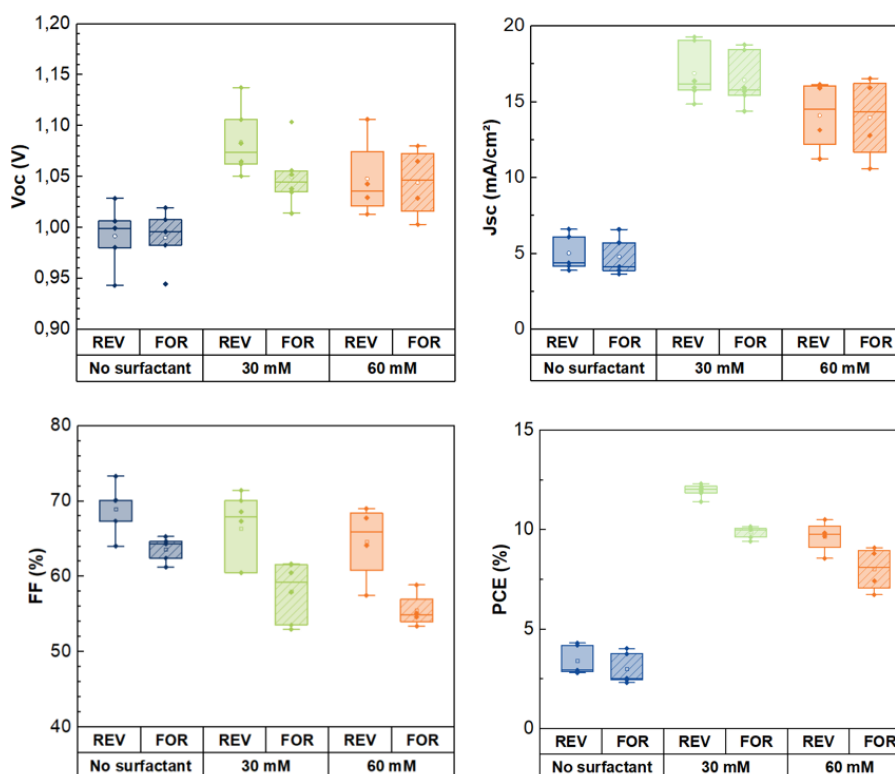


Figure II-23: Device statistics for perovskite solar cells prepared without and with a surfactant concentration of 30 mM and 60 mM. (Each condition is based on 10 cells). The devices present a *n-i-p* architecture Glass/FTO/c-TiO₂/m-TiO₂/Cs_{0.2}FA_{0.8}Pb(I_{0.95}Br_{0.05})₃/Spiro/Au. Reverse scan (plain color) and forward scan (striped).

Figure II-24 displays the I-V curves and MPPT of the best cell with and without surfactant. The best reference device, without surfactant, of 0.09 cm², reached a limited PCE of 4.3% ($V_{oc} = 0.99V / J_{sc} = 6.1 \text{ mA}\cdot\text{cm}^{-2} / FF = 70\%$) in reverse scan, under AM1.5G illumination. As expected from the morphological improvement, devices fabricated with 3DPS showed higher efficiencies than the reference. The champion device reached PCE of 12.3% ($V_{oc} = 1.06V / J_{sc} = 19.3 \text{ mA}\cdot\text{cm}^{-2} / FF = 60.5\%$), stabilized at 10.1%, for a concentration 30 mM. The best device fabricated with a surfactant concentration of 60 mM displayed a lower efficiency at 10.5% ($V_{oc} = 1.03V / J_{sc} = 15.9 \text{ mA}\cdot\text{cm}^{-2} / FF = 64.1\%$). Both devices fabricated with the surfactant display a significant hysteresis phenomenon, whereas this latter is less pronounced for the reference device. Y. Shao *et al.* related the grain size with the I⁻ ion migration in the perovskite layer.²⁷ Consequently, the reduction of the grain diameter induced by 3DPS addition, observed on SEM images, can increase the hysteresis.

To conclude, these results highlight that adding a surfactant in the solution of perovskite precursors is an efficient way to improve the morphology of the perovskite layer and achieve good coverage of the perovskite over the substrate. However, the possible excess of surfactant into the bulk can create multiple recombination sites, decreasing the device's efficiency.

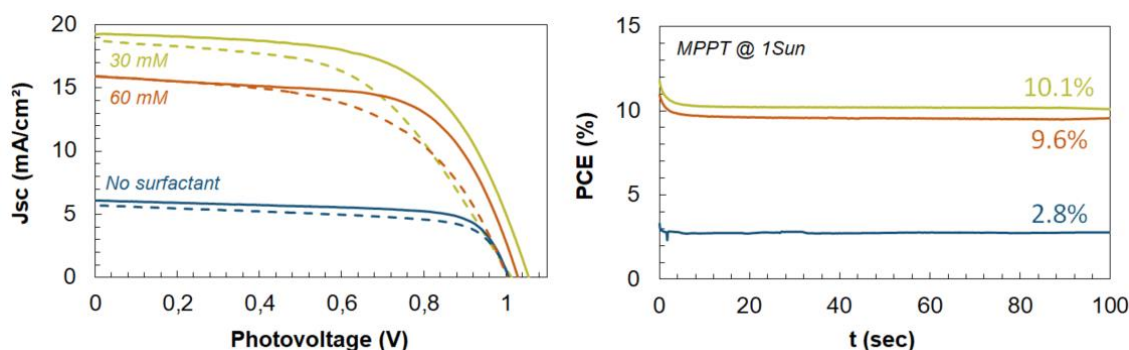


Figure II-24: Best J-V curves of $2 \times 2 \text{ cm}^2$ devices (0.09 cm^2 aperture area) fabricated with surfactant addition and associated stabilized efficiency with time under maximum power point. Reverse scan (plain curves) and forward scan (dotted).

4.4. Deposition of $\text{Cs}_{0.17}\text{FA}_{0.83}\text{Pb}(\text{I}_{0.6}\text{Br}_{0.4})_3$ perovskite

To explore whether 3DPS impacts the PV performance of devices with different perovskite compositions, we fabricated perovskite devices with the following composition $\text{Cs}_{0.17}\text{FA}_{0.73}\text{Pb}(\text{I}_{0.6}\text{Br}_{0.4})_3$. A higher bromide content has been selected to enhance the bandgap value and thus render the composition more suitable for a tandem device ($E_g > 1.7\text{eV}$). In literature, this perovskite composition yields a bandgap value of 1.75 eV .^{28,29}

4.4.1. Preliminary tests by spin-coating deposition

We applied the same spin-coating protocol as previously described in **part 4.3.1.**, i.e., the perovskite layer is spin-coated on TEC7 FTO glass, and the solvent is extracted in a vacuum chamber for 5 minutes, and the resulting film is post-annealed for 30 minutes at 110°C .

In **Figure II-25**, the perovskite samples fabricated with a surfactant concentration lower than 80 mM present a mat surface aspect. This observation correlates with a high surface roughness value of 205 nm for the reference sample (**Figure II-26**). This value gradually decreases to 134 nm , 61 nm , 55 nm , 37 nm , 19 nm , and 20 nm for surfactant concentrations of 10 mM , 30 mM , 60 mM , 80mM , 100 mM , and 120 mM , respectively. A smoother surface is observable for a concentration of 3DPS equal or greater than 80 mM . Beyond this concentration, the visual aspect of the perovskite film is mirror-like, as expected for high-efficiency devices.

Typical SEM images of the perovskite surface layer for the different conditions are displayed in **Figure II-25**. The surface coverage of the perovskite layer without surfactant is incomplete, with numerous pinholes. This aspect is similar to the observations for the previous perovskite composition $\text{Cs}_{0.2}\text{FA}_{0.8}\text{Pb}(\text{I}_{0.95}\text{Br}_{0.05})_3$.

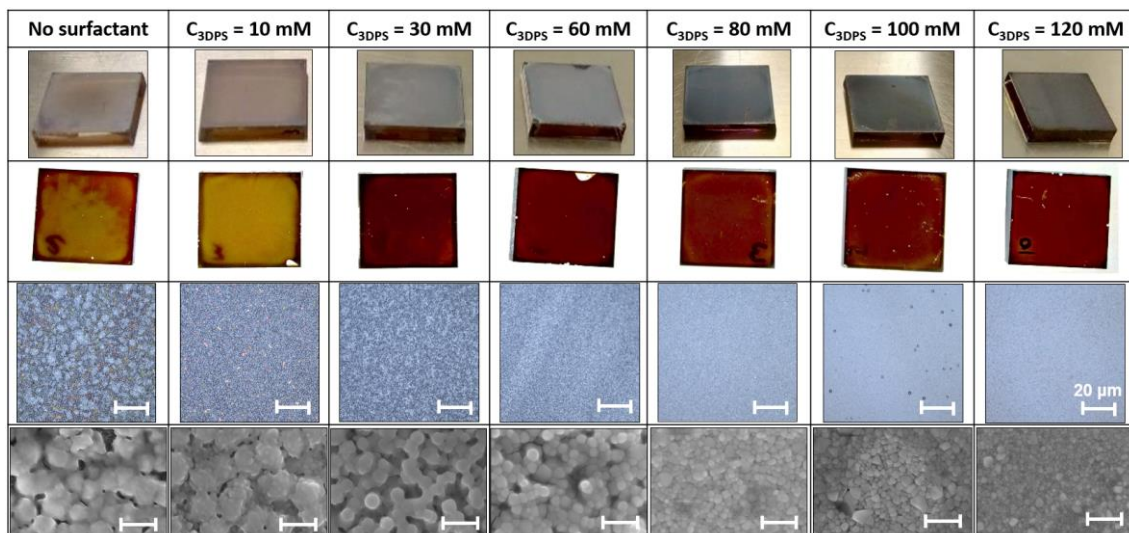


Figure II-25: Photos, confocal images, and surface SEM images of the perovskite layer deposited by spin-coating on glass/FTO/c-TiO₂/m-TiO₂.

The roughness value achieved at a concentration higher than 80 mM is similar to the Sa values achieved for the Cs_{0.2}FA_{0.8}Pb(I_{0.95}Br_{0.05})₃ perovskite composition at 30 mM. This confirms the versatility of the surfactant approach to improve the perovskite morphology. However, the required quantity of surfactant is linked to the perovskite composition. The perovskite composition has a significant impact on the crystallization process. The results support that modifying the bromide/iodide ratio and, to a lesser extent, the cesium/formamidinium ratio changes the crystallization rate and the reaction kinetics.³⁰

Therefore, depending on the perovskite composition, it is necessary to optimize the surfactant concentration to obtain a complete surface coverage and a low surface roughness. In this case, the perovskite layer has a complete coverage at a surfactant concentration of 80 mM, a value significantly higher than in the previous case, for which only 30 mM was needed.

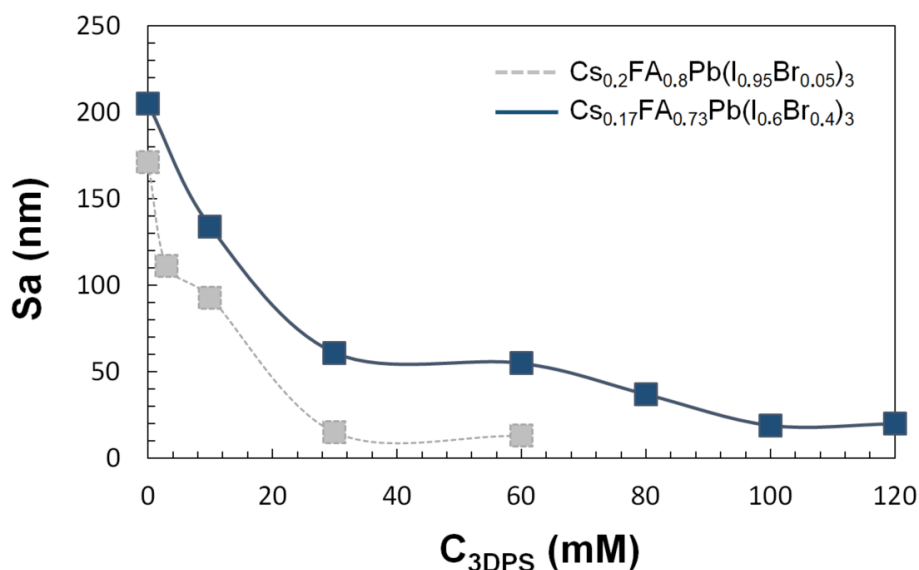


Figure II-26: Surface roughness Sa versus 3DPS surfactant concentration. The Sa values are extracted from the confocal images of Fig. 25.

4.4.2. Slot-die deposition of $Cs_{0.17}FA_{0.73}Pb(I_{0.6}Br_{0.4})_3$ perovskite composition

Based on previous experiments and results, we fabricated using slot-die a reference perovskite sample without surfactant aside from perovskite samples with three different surfactant concentrations: a concentration of 30 mM to compare with the best samples obtained in **part 4.3**, an optimal concentration of 60 mM and a surfactant concentration of 80 mM to study the effect of the excess of surfactant on the optoelectronic properties of the perovskite film.

4.4.2.1. Morphological characterization

The influence of the surfactant concentration on the perovskite surface roughness has been evaluated by confocal measurements. The reference sample exhibits a roughness surface value of 186 nm, with a very broad and multi-modal distribution. (**Figure II-27**), which is three times greater than the previous perovskite composition (**Figure II-19**). This important roughness distribution indicates a high layer heterogeneity. The modification of the perovskite layer final morphology by the halide content has been studied by Wang et al. The replacement of iodide by bromide in the perovskite composition lowers the critical nucleation barrier energy, leading to insufficient generation of nucleation centers during the extraction of the solvent.³¹ In addition, the difference of complexation of Br^- and I^- with Pb^{2+} modifies the coordination rate of precursors.³²

Following the same tendency as the preliminary spin-coating tests, the addition of surfactant in the perovskite precursors solution decreases the surface roughness. The reference sample displayed a surface roughness of 350 nm, whereas the samples with surfactant addition presented to 46 nm, 20 nm, and 13 nm for a 3DPS content of 30 mM, 60 mM, and 80 mM, respectively. Moreover, similarly to the previous perovskite composition (**part. 4.3**), the roughness distribution significantly decreased, which indicates a diminution of the layer heterogeneity.

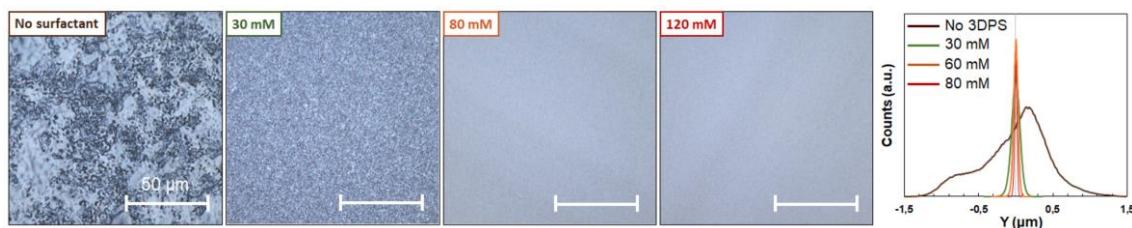


Figure II-27: Confocal images of the $Cs_{0.17}FA_{0.73}Pb(I_{0.6}Br_{0.4})_3$ perovskite layer deposited by slot-die coating on glass/FTO/c-TiO₂/m-TiO₂. Distribution of heights of each point compared to the arithmetical mean of the surface.

On the surface SEM images in **Figure II- 28**, the reference sample presents an incomplete coverage of the perovskite layer with a partial dendritic morphology. Numerous pinholes are visible on the surface of the sample. The addition of the 3DPS surfactant enables to have more uniform films. A surfactant concentration of 30 mM generates an incomplete film coverage and is not enough to totally suppress the pinholes. However, at 60 mM and 80 mM, the surface shows a uniform coverage with small perovskite grains.

The particle size distribution has been determined from the SEM images. The reference sample shows an average particle size of 234 nm, with a standard deviation of 92 nm. This value is slightly higher when adding 30 mM of surfactant, i.e., 272 nm, with a standard deviation of 106 nm. However, at higher concentrations, the average particle size decreases to 135 nm ($\sigma = 38$ nm) and 102 nm ($\sigma = 47$ nm) for surfactant concentrations of 60 mM and 80 mM, respectively. The standard deviation decreased from 38 nm to 47 nm, indicating a more uniform perovskite grains' growth.

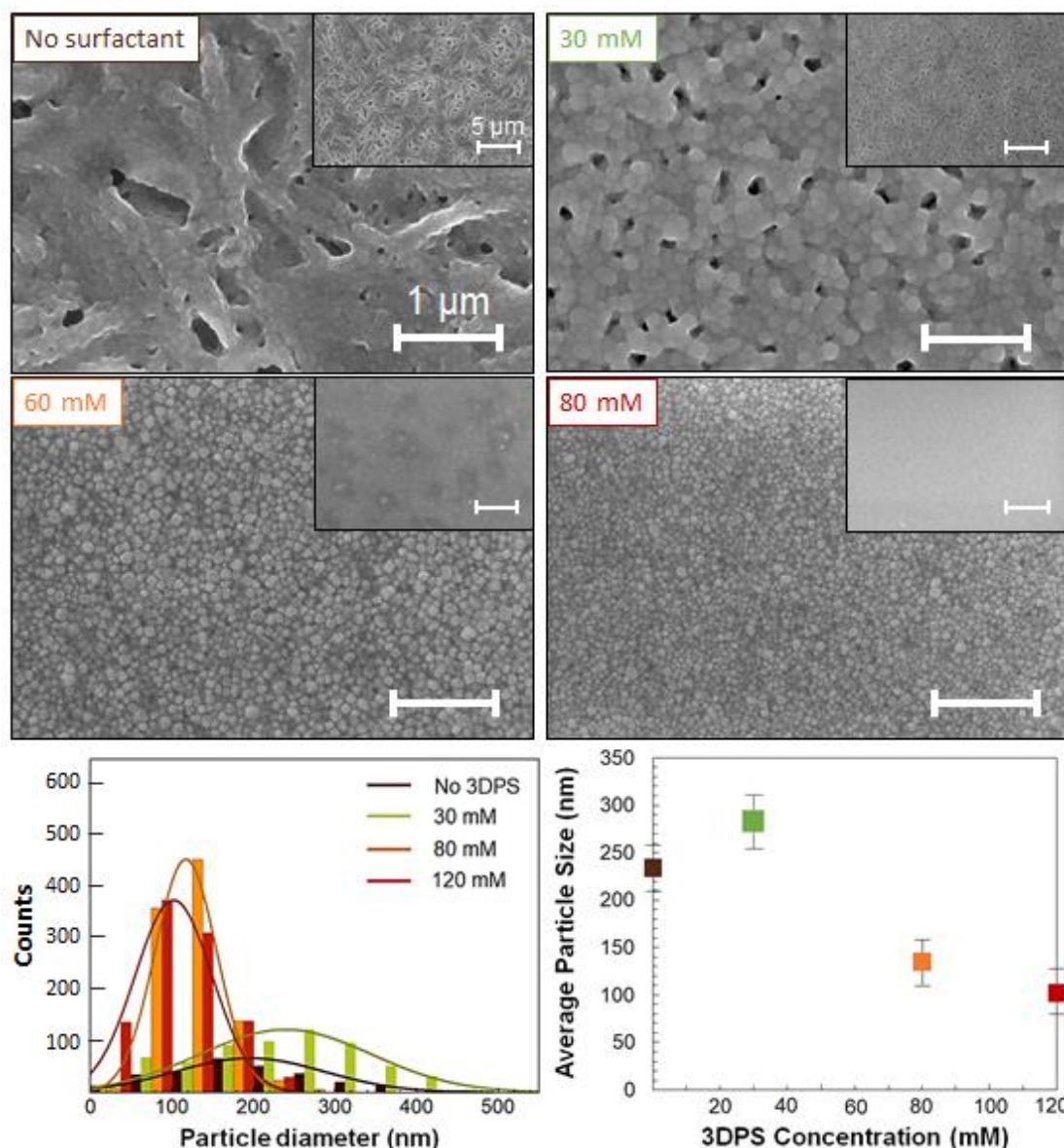


Figure II- 28: SEM surface images of the $Cs_{0.17}FA_{0.73}Pb(I_{0.6}Br_{0.4})_3$ perovskite layer deposited by slot-die on glass/FTO/c-TiO₂/m-TiO₂, associated distributions of particle diameters and average particle size extracted from the SEM images.

The perovskite film's thickness is about 460 nm, comparable to the thickness of the $Cs_{0.2}FA_{0.8}Pb(I_{0.95}Br_{0.05})_3$ film (part 4.3.3.1). The cross-section SEM images in **Figure II- 29** show an important number of pinholes for the reference film obtained without surfactant. The film morphology is slightly improved with a surfactant concentration of 30 mM, though the film still shows many voids in the perovskite layer. At 60 mM, the film appears to have excellent compactness with no visible pinholes. The very low roughness of the film generates a smooth profile with no visible defects on the surface, which would be beneficial for the device's performances.

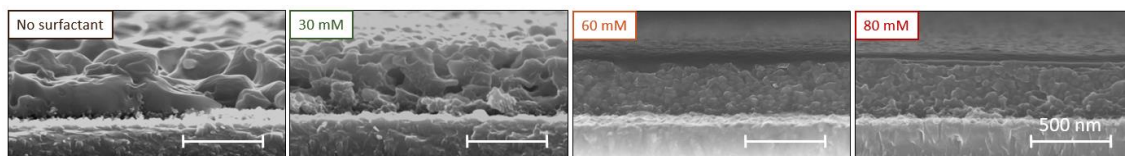


Figure II-29: Cross-section SEM images of the $\text{Cs}_{0.17}\text{FA}_{0.83}\text{Pb}(\text{I}_{0.6}\text{Br}_{0.4})_3$ perovskite layer deposited by slot-die coating on glass/FTO/c-TiO₂/m-TiO₂.

4.4.2.2. Structural evolution

XRD measurements have been performed on the perovskite layer without and with different concentrations of surfactant. All the different films gather the characteristic diffraction peaks of a cubic structure indexed in Pm-3m space group.

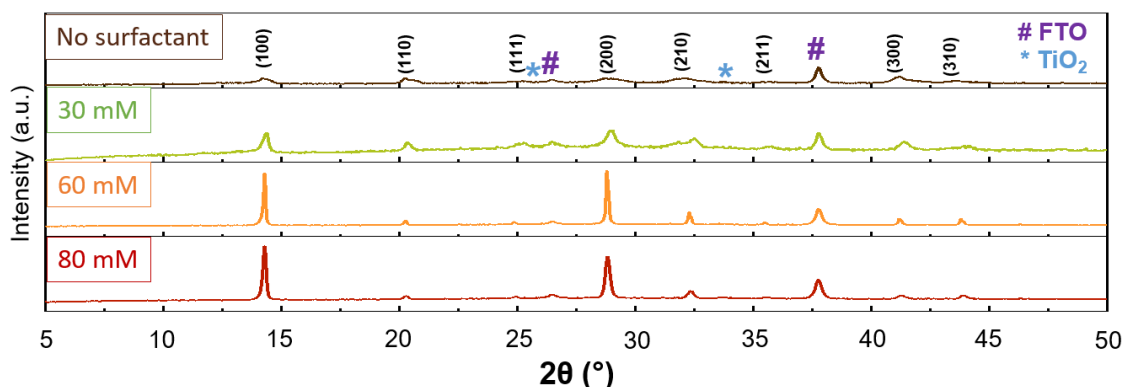


Figure II-30: X-ray diffractograms of the perovskite layer deposited by slot-die coating on glass/FTO/c-TiO₂/m-TiO₂.

Interestingly, for the reference sample and the lower surfactant concentration of 30 mM, the refinement of the XRD diffraction peak (100) shows a shoulder, revealing two contributions at $2\theta \approx 14.1^\circ$ and $\approx 14.4^\circ$ (**Figure II-31**). This phenomenon can be ascribed either to phase segregation induced by the high bromide content in the formulation, leading to the coexistence of a bromide richer perovskite on the one hand and a poor bromide perovskite on the other hand. In fact, for a high bromide content in the halide ratio, the stability of the perovskite α -phase in the Cs/FA. phase may decrease.³³

For higher surfactant concentrations, 60 mM and 80 mM, only one contribution is shown for the (100) diffraction peak at 14.3° . The ratio (100)/(110) increases from 0.7 for the reference to 4.2 and 6.7 for 60 mM and 80 mM concentrations, indicating an enhancement of the preferential orientation along this plane. Rehman *et al.* demonstrated a strong correlation between material crystallinity and stability towards photo-induced halide segregation, which could explain the pure α -phase obtained for the perovskite films fabricated with higher surfactant concentrations.³³ This impact of the surfactant on the crystallinity is similar to for the $\text{Cs}_{0.2}\text{FA}_{0.8}\text{Pb}(\text{I}_{0.95}\text{Br}_{0.05})_3$.

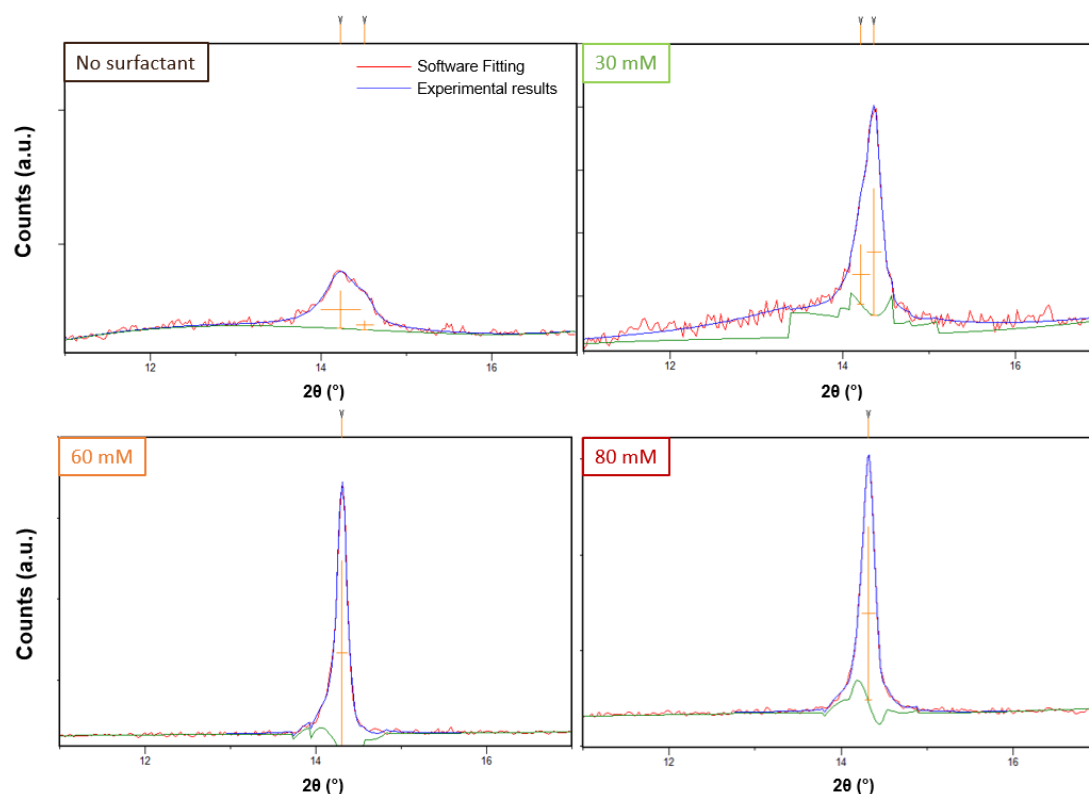


Figure II-31: X-ray diffraction (100) peak from $Cs_{0.17}FA_{0.73}Pb(I_{0.6}Br_{0.4})_3$ perovskite with peak fitting refined by HighScore software.

4.4.2.3. PL measurements

We performed PL measurements on the perovskite films with a green laser at $\lambda = 532$ nm. Results are presented in **Figure II-32.a.** and the detailed data are displayed in **Table II-6.**

The FWHM of the PL band gradually decreases with the surfactant addition from 77 nm for the reference without surfactant to 80 nm, 55 nm, and 42 nm for 30 mM, 60 mM, and 80 mM surfactant concentrations, respectively. This points out the role of the surfactant to decrease the defects density of the perovskite layer. Besides, the PL band of the reference and the 30 mM concentration condition display two emitting contributions with red-shifted maxima, thus indicating the formation of an I-rich lower bandgap.²⁸ This second band tends to disappear when the surfactant concentration is higher than 60 mM.

Moreover, to evaluate the influence of light on the stability of the perovskite absorber, we exposed the films to 1 sun illumination for 5 minutes. We observed a red-shift of the PL from 714 nm to 770 nm and from 717 nm to 768 nm for the reference and the 30 mM samples, whereas the band's position for 60 mM and 80 mM concentrations stayed stable at ≈ 710 nm. A. Gualdron-Reyes *et al.* highlighted an important relationship between the grain size and the “Hoke effect”³⁴, that is, the phase instability under illumination generating rapid halide segregation with the increased bromide content.^{35–37} Limiting the

average grain size in the range or below the carrier's diffusion length was shown to improve illumination stability. In this case, the role of the surfactant in the diminution of the grain size can explain the improved stability at a concentration higher than 60 mM.

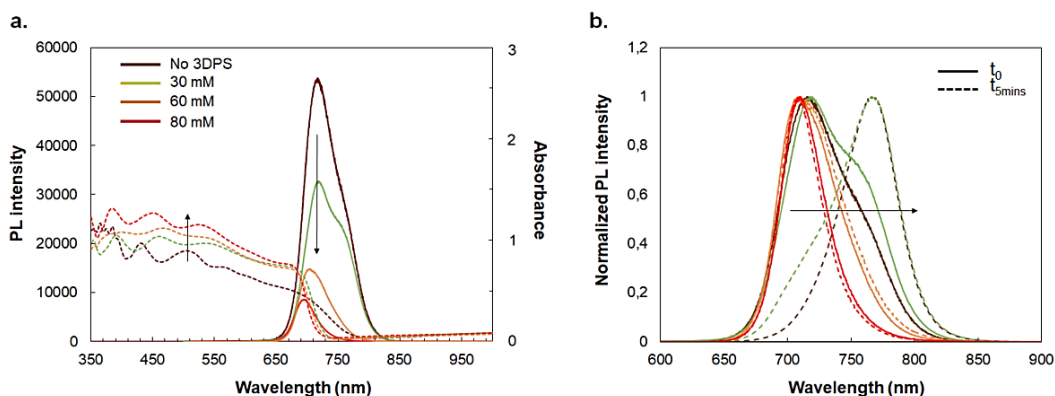


Figure II-32: PL measurements performed on fresh samples (plain line) and associated with the absorbance curve (dotted line). b. Normalized PL curves. The measurements are performed on fresh and aged $\text{Cs}_{0.17}\text{FA}_{0.73}\text{Pb}(\text{I}_{0.6}\text{Br}_{0.4})_3$ perovskite layers exposed 5 minutes to 1 sun illumination.

However, the reference sample displays a PL intensity 1.5 times higher than 30 mM than the sample fabricated with 30 mM of surfactant, four times higher than the sample fabricated with 60 mM of surfactant, and five times higher than the sample fabricated with the 80 mM surfactant. On the other hand, the absorbance curves of the films with surfactants all displayed a better absorbance than the reference film at $\lambda = 532$ nm.

Consequently, the surfactant addition improves the optical properties, characterized by an increase in the film's absorbance. However, it has a detrimental effect on the electronic properties, evidenced by the diminution of the PL response due to the gradual augmentation of the grain boundaries.

Table II-6: PL data from measurements performed on $\text{Cs}_{0.17}\text{FA}_{0.73}\text{Pb}(\text{I}_{0.6}\text{Br}_{0.4})_3$ perovskite samples. The FWHM values are calculated from initial PL peaks displayed in Fig. 32.b.

$\text{C}_{3\text{DPS}}$ (mM)	FWHM	Initial band position	Band position (+5 mins)
	nm	nm	nm
0	77	714	770
30	80	717	768
60	55	708	713
80	42	706	705

4.4.2.4. IV performances

The perovskite solar cells have been fabricated according to the fabrication process displayed in **parts 2 and 3**. The structure of all the devices is Glass/FTO/c-TiO₂/m-TiO₂/Cs_{0.17}FA_{0.73}Pb(I_{0.6}Br_{0.4})₃/Spiro/Au. The I-V parameters of the devices (best cells and average) are displayed in **Annex 7**.

The morphology improvement efficiently enhances the Voc, and the devices fabricated with 30mM of surfactant display satisfying average Voc of 1.12 V compared to 0.99V for the reference devices.

However, the poor efficiency of the devices fabricated with surfactant points out a limit of the involved quantity of 3DPS (**Figure II-33**). As a concentration of 30 mM was not enough to generate a covering morphology, it became necessary to increase the surfactant concentration. After this surfactant concentration, though, the device's current decreased from an average of 16.7 mA/cm² for the reference to 10.7 mA/cm² and 2.02 mA/cm² for 30 mM and 60 mM. As forecasted by the SEM images and the PL curves decreasing intensity, the addition of 3DPS creates multiple grain boundaries, which ends up creating numerous non-radiative recombination centers.

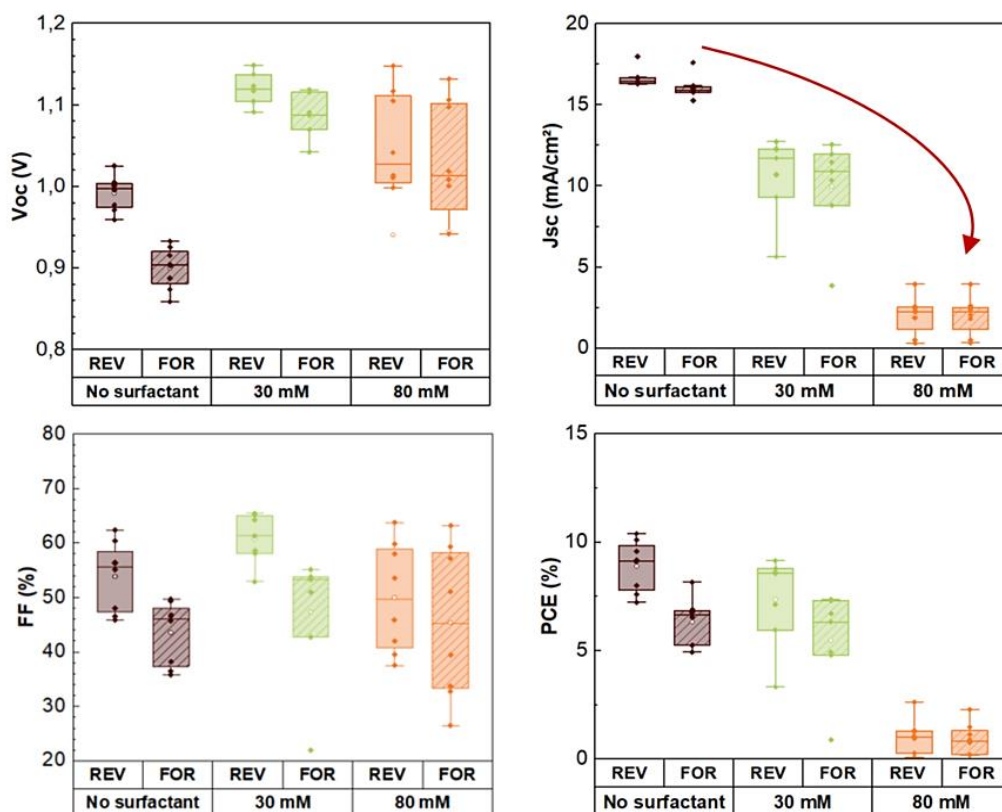


Figure II-33: Device statistics for perovskite solar cells prepared without and with a surfactant concentration of 30 mM and 60 mM (Each condition counts 10 cells). The devices presents a NIP architecture Glass/FTO/c-TiO₂/m-TiO₂/Cs_{0.17}FA_{0.73}Pb(I_{0.6}Br_{0.4})₃/Spiro-OMeTAD/Au. Reverse scan (plain color) and forward scan (stripped).

The best reference device without surfactant reached a PCE of 10.4% ($V_{oc} = 1.03V / J_{sc} = 18 \text{ mA.cm}^{-2} / FF = 56.4\%$), in reverse scan. The performance of the best PSCs made without and with the surfactant-assisted slot-die coating is presented in **Figure II-34**. Unfortunately, devices fabricated with 3DPS displayed lower efficiencies. The surfactant-doped top device reached 9.2% ($V_{oc} = 1.14V / J_{sc} = 12.3 \text{ mA.cm}^{-2} / FF = 9.2\%$), stabilized at 6.5% for a concentration 30 mM. The best device fabricated with a surfactant concentration of 60 mM displayed an even lower efficiency of 2.3% ($V_{oc} = 1.13V / J_{sc} = 3.95 \text{ mA.cm}^{-2} / FF = 51\%$). The devices fabricated with a surfactant concentration of 80mM were all shunted, and no I-V could be measured.

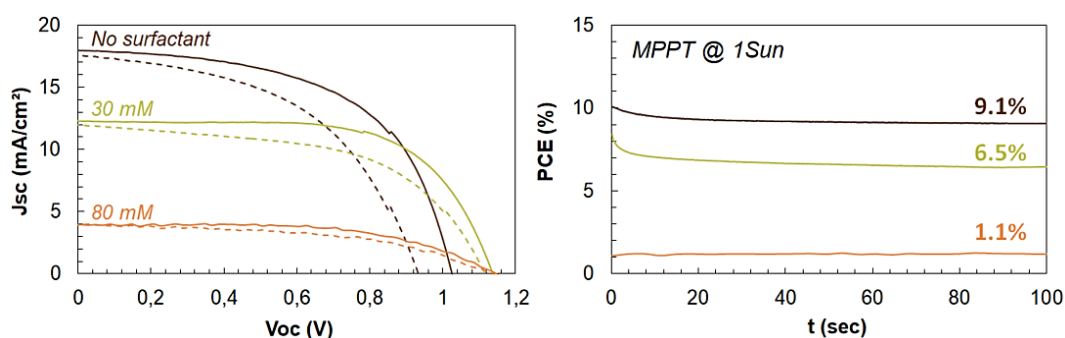


Figure II-34: Best I-V curves of $2 \times 2 \text{ cm}^2$ devices (0.09 cm^2 aperture area) fabricated with surfactant addition and associated MPP tracking. Reverse scan (plain curves) and forward scan (dotted).

Finally, to further understand the drop of the device efficiency, we performed drop angle measurements with Spiro-OMeTAD solution deposited directly on the perovskite layer (**Figure II-35**). On the perovskite layer fabricated without surfactant, the solution displays perfect wettability. Up to a surfactant content of 30 mM, the drop angle stays unmeasurable, evidencing a satisfying wettability of the solution. However, for a surfactant content of 60 mM, the angle displays a value of 15.2° and 37° for a surfactant content of 80mM. Unexpectedly, the surfactant lowers the wettability of the spiro-OMeTAD on the perovskite surface. Therefore, even with a perfectly flat perovskite surface, this phenomenon reduces the interface quality between the HTL and the perovskite layer. This can partially explain the reduction of the perovskite performances we evidenced in the last part.

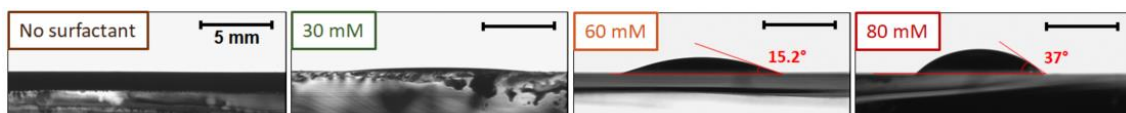


Figure II-35: Wettability of the Spiro-OMeTAD on the perovskite layer surface. Measurements were performed under ambient conditions.

5. Conclusions

In this chapter, we presented the full fabrication process of the small perovskite devices. We especially described the slot-die deposition process of the absorber layer and the associated drying step, carried out by vacuum aspiration. We explored the different deposition parameters and established an optimized fabrication procedure for the rest of this thesis work.

Then, we studied the influence of the addition of a zwitterionic surfactant, namely the N-Dodecyl-N,N-dimethyl-3-ammonio-1-propanesulfonate, on the morphology and the crystallinity of a perovskite layer with a $\text{Cs}_{0,2}\text{FA}_{0,8}\text{Pb}(\text{I}_{0,95}\text{Br}_{0,05})_3$ composition. We showed that adding 30 mM of 3DPS in the perovskite precursors solution enhances the crystallite size while significantly decreasing the surface roughness. We fabricated full perovskite devices with classical n-i-p architecture and a spiro-OMeTAD HTL. The device efficiency yields a champion PCE of 12.3% on a 0.09 cm² aperture area.

In a third part, we fabricated perovskite layers with a different perovskite composition: $\text{Cs}_{0,17}\text{FA}_{0,83}\text{Pb}(\text{I}_{0,6}\text{Br}_{0,4})_3$. We reported a maximum efficiency of 9.2% on 0.09 cm² aperture area for a 30 mM of surfactant in the perovskite precursors solution. However, despite a significant increase of the perovskite layer coverage and a diminution of the surface roughness, we evidenced that a surfactant content higher than 30 mM limits the device efficiency owing to an augmentation of the grains boundaries. This tendency remained identical, independently of the perovskite composition.

To tackle this low-efficiency issue, the next chapter aims to explore another type of additives.

6. References

- (1) Guillemot, T. *Élaboration de Cellules Solaires Nanostructurées à Base de Pérovskite Hybride*, Sorbonne Université, Paris, 2018.
- (2) Ding, X.; Liu, J.; Harris, T. A. L. A Review of the Operating Limits in Slot Die Coating Processes. *AIChE J.* **2016**, *62* (7), 2508–2524. <https://doi.org/10.1002/aic.15268>.
- (3) Jung, M.; Ji, S.-G.; Kim, G.; Seok, S. I. Perovskite Precursor Solution Chemistry: From Fundamentals to Photovoltaic Applications. *Chem. Soc. Rev.* **2019**, *48* (7), 2011–2038. <https://doi.org/10.1039/C8CS00656C>.
- (4) Zheng, Y. C.; Yang, S.; Chen, X.; Chen, Y.; Hou, Y.; Yang, H. G. Thermal-Induced Volmer–Weber Growth Behavior for Planar Heterojunction Perovskites Solar Cells. *Chem. Mater.* **2015**, *27* (14), 5116–5121. <https://doi.org/10.1021/acs.chemmater.5b01924>.
- (5) Ke, L.; Luo, S.; Ren, X.; Yuan, Y. Factors Influencing the Nucleation and Crystal Growth of Solution-Processed Organic Lead Halide Perovskites: A Review. *J. Phys. D: Appl. Phys.* **2021**, *54* (16), 163001. <https://doi.org/10.1088/1361-6463/abd728>.
- (6) You, H.; Fang, J. Particle-Mediated Nucleation and Growth of Solution-Synthesized Metal Nanocrystals: A New Story beyond the LaMer Curve. *Nano Today* **2016**, *11* (2), 145–167. <https://doi.org/10.1016/j.nantod.2016.04.003>.
- (7) Li, Y.; Li, X.; Chu, Q.; Dong, H.; Yao, J.; Zhou, Y.; Yang, G. Tuning Nucleation Sites to Enable Monolayer Perovskite Films for Highly Efficient Perovskite Solar Cells. *Coatings* **2018**, *8* (11), 408. <https://doi.org/10.3390/coatings8110408>.
- (8) Bari, M.; Wu, H.; Bokov, A. A.; Ali, R. F.; Tailor, H. N.; Gates, B. D.; Ye, Z.-G. Room-Temperature Synthesis, Growth Mechanisms and Opto-Electronic Properties of Organic–Inorganic Halide Perovskite $\text{CH}_3\text{NH}_3\text{PbX}_3$ (X = I, Br, and Cl) Single Crystals. *CrystEngComm* **2021**, *23* (18), 3326–3339. <https://doi.org/10.1039/D0CE01690J>.
- (9) Zheng, X.; Chen, B.; Dai, J.; Fang, Y.; Bai, Y.; Lin, Y.; Wei, H.; Zeng, X. C.; Huang, J. Defect Passivation in Hybrid Perovskite Solar Cells Using Quaternary Ammonium Halide Anions and Cations. *Nat Energy* **2017**, *2* (7), 17102. <https://doi.org/10.1038/nenergy.2017.102>.
- (10) Dai, X.; Deng, Y.; Brackley, C. H. V.; Chen, S.; Rudd, P. N.; Xiao, X.; Lin, Y.; Chen, B.; Huang, J. Scalable Fabrication of Efficient Perovskite Solar Modules on Flexible Glass Substrates. *Advanced Energy Materials* **2020**, *10* (1), 1903108. <https://doi.org/10.1002/aenm.201903108>.

- (11) Si, H. Dual-Passivation of Ionic Defects for Highly Crystalline Perovskite. *Nano Energy* **2020**, 10.
- (12) Zheng, X.; Deng, Y.; Chen, B.; Wei, H.; Xiao, X.; Fang, Y.; Lin, Y.; Yu, Z.; Liu, Y.; Wang, Q.; Huang, J. Dual Functions of Crystallization Control and Defect Passivation Enabled by Sulfonic Zwitterions for Stable and Efficient Perovskite Solar Cells. *Adv. Mater.* **2018**, 30 (52), 1803428. <https://doi.org/10.1002/adma.201803428>.
- (13) Liu, K.; Liang, Q.; Qin, M.; Shen, D.; Yin, H.; Ren, Z.; Zhang, Y.; Zhang, H.; Fong, P. W. K.; Wu, Z.; Huang, J.; Hao, J.; Zheng, Z.; So, S. K.; Lee, C.-S.; Lu, X.; Li, G. Zwitterionic-Surfactant-Assisted Room-Temperature Coating of Efficient Perovskite Solar Cells. *Joule* **2020**, 4 (11), 2404–2425. <https://doi.org/10.1016/j.joule.2020.09.011>.
- (14) Alturisa, M. I.; Wira, J.; Mardiyati; Herman; Hidayat, R. Influences of Precursor Solution Concentration and Temperature on CH₃NH₃PbI₃ Perovskite Layer Morphology and the Unconverted PbI₂ Proportion to Their Perovskite Solar Cell Characteristics. *J. Phys.: Conf. Ser.* **2017**, 877, 012046. <https://doi.org/10.1088/1742-6596/877/1/012046>.
- (15) Wang, Y.; Zhong, M.; Chai, L. Effects of the Concentration of PbI₂ and CH₃NH₃I on the Perovskite Films and the Performance of Perovskite Solar Cells Based on ZnO-TiO₂ Nanorod Arrays. *Superlattices and Microstructures* **2018**, 123, 189–200. <https://doi.org/10.1016/j.spmi.2018.07.024>.
- (16) Kim, J.; Park, B.; Baek, J.; Yun, J. S.; Kwon, H.-W.; Seidel, J.; Min, H.; Coelho, S.; Lim, S.; Huang, S.; Gaus, K.; Green, M. A.; Shin, T. J.; Ho-baillie, A. W. Y.; Kim, M. G.; Seok, S. I. Unveiling the Relationship between the Perovskite Precursor Solution and the Resulting Device Performance. *J. Am. Chem. Soc.* **2020**, 142 (13), 6251–6260. <https://doi.org/10.1021/jacs.0c00411>.
- (17) Influence of Precursor Concentration on Printable Mesoscopic Perovskite Solar Cells. *Front. Optoelectron.* **2020**, 13 (3), 256–264. <https://doi.org/10.1007/s12200-020-1013-3>.
- (18) Yu, Y.; Yang, S.; Lei, L.; Cao, Q.; Shao, J.; Zhang, S.; Liu, Y. Ultrasoft Perovskite Film via Mixed Anti-Solvent Strategy with Improved Efficiency. *ACS Appl. Mater. Interfaces* **2017**, 9 (4), 3667–3676. <https://doi.org/10.1021/acsami.6b14270>.
- (19) Deng, Y.; Zheng, X.; Bai, Y.; Wang, Q.; Zhao, J.; Huang, J. Surfactant-Controlled Ink Drying Enables High-Speed Deposition of Perovskite Films for Efficient Photovoltaic Modules. *Nat Energy* **2018**, 3 (7), 560–566. <https://doi.org/10.1038/s41560-018-0153-9>.
- (20) Yang, M.; Li, Z.; Reese, M. O.; Reid, O. G.; Kim, D. H.; Siol, S.; Klein, T. R.; Yan, Y.; Berry, J. J.; van Hest, M. F. A. M.; Zhu, K. Perovskite Ink with Wide

- Processing Window for Scalable High-Efficiency Solar Cells. *Nat Energy* **2017**, *2* (5), 17038. <https://doi.org/10.1038/nenergy.2017.38>.
- (21) Wang, Q.; Zheng, X.; Deng, Y.; Zhao, J.; Chen, Z.; Huang, J. Stabilizing the α -Phase of CsPbI₃ Perovskite by Sulfobetaine Zwitterions in One-Step Spin-Coating Films. *Joule* **2017**, *1* (2), 371–382. <https://doi.org/10.1016/j.joule.2017.07.017>.
- (22) Lee, D. S.; Yun, J. S.; Kim, J.; Soufiani, A. M.; Chen, S.; Cho, Y.; Deng, X.; Seidel, J.; Lim, S.; Huang, S.; Ho-Baillie, A. W. Y. Passivation of Grain Boundaries by Phenethylammonium in Formamidinium-Methylammonium Lead Halide Perovskite Solar Cells. *ACS Energy Lett.* **2018**, *3* (3), 647–654. <https://doi.org/10.1021/acsenergylett.8b00121>.
- (23) Bi, Z.; Liang, Z.; Xu, X.; Chai, Z.; Jin, H.; Xu, D.; Li, J.; Li, M.; Xu, G. Fast Preparation of Uniform Large Grain Size Perovskite Thin Film in Air Condition via Spray Deposition Method for High Efficient Planar Solar Cells. *Solar Energy Materials and Solar Cells* **2017**, *162*, 13–20. <https://doi.org/10.1016/j.solmat.2016.12.032>.
- (24) Xu, W.; Lei, G.; Tao, C.; Zhang, J.; Liu, X.; Xu, X.; Lai, W.-Y.; Gao, F.; Huang, W. Precisely Controlling the Grain Sizes with an Ammonium Hypophosphite Additive for High-Performance Perovskite Solar Cells. *Adv. Funct. Mater.* **2018**, *28* (33), 1802320. <https://doi.org/10.1002/adfm.201802320>.
- (25) McMeekin, D. P.; Sadoughi, G.; Rehman, W.; Eperon, G. E.; Saliba, M.; Hörantner, M. T.; Haghighirad, A.; Sakai, N.; Korte, L.; Rech, B.; Johnston, M. B.; Herz, L. M.; Snaith, H. J. A Mixed-Cation Lead Mixed-Halide Perovskite Absorber for Tandem Solar Cells. *Science* **2016**, *351* (6269), 151–155. <https://doi.org/10.1126/science.aad5845>.
- (26) An, Q.; Paulus, F.; Becker-Koch, D.; Chansoon, C. Small Grains as Recombination Hot Spots in Perovskite Solar Cells. **2021**, *4* (5), 1442–1445. <https://doi.org/doi.org/10.1016/j.matt.2021.02.020>.
- (27) Shao, Y.; Fang, Y.; Li, T.; Wang, Q.; Dong, Q.; Deng, Y.; Yuan, Y.; Wei, H.; Wang, M.; Gruverman, A.; Shield, J.; Huang, J. Grain Boundary Dominated Ion Migration in Polycrystalline Organic–Inorganic Halide Perovskite Films. *Energy Environ. Sci.* **2016**, *9* (5), 1752–1759. <https://doi.org/10.1039/C6EE00413J>.
- (28) Bush, K. A.; Frohna, K.; Prasanna, R.; Beal, R. E.; Leijtens, T.; Swifter, S. A.; McGehee, M. D. Compositional Engineering for Efficient Wide Band Gap Perovskites with Improved Stability to Photoinduced Phase Segregation. *ACS Energy Lett.* **2018**, *3* (2), 428–435. <https://doi.org/10.1021/acsenergylett.7b01255>.
- (29) Bett, A. J.; Schulze, P. S. C.; Winkler, K. M.; Kabakli, Ö. S.; Ketterer, I.; Mundt, L. E.; Reichmuth, S. K.; Siefer, G.; Cojocaru, L.; Tutsch, L.; Bivour, M.; Hermle, M.; Glunz, S. W.; Goldschmidt, J. C. Two-terminal Perovskite Silicon Tandem Solar Cells with a High-Bandgap Perovskite Absorber Enabling Voltages over 1.8

- V. *Prog Photovolt Res Appl* **2020**, 28 (2), 99–110. <https://doi.org/10.1002/pip.3208>.
- (30) Yang, J. Crystallization Tailoring of Cesium/Formamidinium Double-Cation Perovskite for Efficient and Highly Stable Solar Cells. *Journal of Energy Chemistry* **2020**, 9.
- (31) Wang, L.; Yuan, G. D.; Duan, R. F.; Huang, F.; Wei, T. B.; Liu, Z. Q.; Wang, J. X.; Li, J. M. Tunable Bandgap in Hybrid Perovskite $\text{CH}_3\text{NH}_3\text{Pb}(\text{Br}_{3-y}\text{X}_y)$ Single Crystals and Photodetector Applications. *AIP Advances* **2016**, 6 (4), 045115. <https://doi.org/10.1063/1.4948312>.
- (32) Yoon, S. J.; Stamplecoskie, K. G.; Kamat, P. V. How Lead Halide Complex Chemistry Dictates the Composition of Mixed Halide Perovskites. *J. Phys. Chem. Lett.* **2016**, 7 (7), 1368–1373. <https://doi.org/10.1021/acs.jpcclett.6b00433>.
- (33) Rehman, W.; McMeekin, D. P.; Patel, J. B.; Milot, R. L.; Johnston, M. B.; Snaith, H. J.; Herz, L. M. Photovoltaic Mixed-Cation Lead Mixed-Halide Perovskites: Links between Crystallinity, Photo-Stability and Electronic Properties. *Energy Environ. Sci.* **2017**, 10 (1), 361–369. <https://doi.org/10.1039/C6EE03014A>.
- (34) Hoke, E. T.; Slotcavage, D. J.; Dohner, E. R.; Bowring, A. R.; Karunadasa, H. I.; McGehee, M. D. Reversible Photo-Induced Trap Formation in Mixed-Halide Hybrid Perovskites for Photovoltaics. *Chem. Sci.* **2014**, 6 (1), 613–617. <https://doi.org/10.1039/C4SC03141E>.
- (35) Gualdrón-Reyes, Andrés. F.; Yoon, S. J.; Barea, E. M.; Agouram, S.; Muñoz-Sanjosé, V.; Meléndez, Á. M.; Niño-Gómez, M. E.; Mora-Seró, I. Controlling the Phase Segregation in Mixed Halide Perovskites through Nanocrystal Size. *ACS Energy Lett.* **2019**, 4 (1), 54–62. <https://doi.org/10.1021/acsenergylett.8b02207>.
- (36) Brennan, M. C.; Ruth, A.; Kamat, P. V.; Kuno, M. Photoinduced Anion Segregation in Mixed Halide Perovskites. *Trends in Chemistry* **2020**, 2 (4), 282–301. <https://doi.org/10.1016/j.trechm.2020.01.010>.
- (37) Hu, L.; Guan, X.; Chen, W.; Yao, Y.; Wan, T.; Lin, C.-H.; Pham, N. D.; Yuan, L.; Geng, X.; Wang, F.; Huang, C.-Y.; Yuan, J.; Cheong, S.; Tilley, R. D.; Wen, X.; Chu, D.; Huang, S.; Wu, T. Linking Phase Segregation and Photovoltaic Performance of Mixed-Halide Perovskite Films through Grain Size Engineering. *ACS Energy Lett.* **2021**, 1649–1658. <https://doi.org/10.1021/acsenergylett.1c00213>.

CHAPTER 3:

Addition of methylammonium chloride

In this chapter, we introduced methylammonium chloride in the perovskite's precursors solution. This additive aroused great interest, notably because it can improve the diffusion length of the carriers in the perovskite layer as a result of enhanced optoelectronic properties.^{1,2}

Lately, the challenges introduced by larger area deposition methods brought back the need for tailoring the perovskite precursors solution. In this chapter, we focused on the perovskite composition $\text{Cs}_{0.17}\text{FA}_{0.83}\text{Pb}(\text{I}_{0.83}\text{Br}_{0.17})_3$, which displays a bandgap value of 1.64 eV, compatible with future tandem applications.³ We decide to reduce the bromide content to avoid possible phase segregation, as seen in the previous chapter.

In the first part, we present the preliminary tests realized on perovskite layers produced by spin-coating. We study the intermediate formation by XRD and optimize the concentration of the MAI additive.

The second part describes the transfer of the ink formulation to the slot-die deposition process. Fine refining of the MAI concentration and the annealing conditions are carried out as a last-step optimization.

Then, we focus on the performances of the solar devices. We measured the J-V curves of small-scale solar cells and selected the best conditions for the fabrication of the first modules of 12cm².

Lastly, the stability of the solar cells devices has been characterized. An encapsulation process is detailed, and the device degradation is discussed based on STEM technique to monitor the morphological evolution of the perovskite and the HTL layer upon aging.

SUMMARY

1. Preliminary spin-tests	102
2. Optimization of the slot-die deposition conditions	108
3. Full devices performances	117
4. Stability tests.....	122
5. Conclusions	131
6. References	132

1. Preliminary spin-tests

1.1. Differences between anti-solvent and vacuum aspiration solvent extraction methods

1.1.1. Intermediate phases characterization by XRD measurements

For the spin-test samples, we deposited the perovskite layer by traditional spin-coating technique. After deposition, the solvent was either evacuated by the anti-solvent method with chlorobenzene or by vacuum aspiration.

Just after the vacuum aspiration step, the as-deposited films are taken out from the glovebox. XRD measurements were performed less than 3 minutes after the end of the quench, and the scan duration was 10 minutes. Particular attention has been paid to this procedure to reduce the presumed instability of the pre-annealed films in ambient air condition. However, at the end of the scan, the films presented a visible difference of colour between the beginning of the measurement and the ending.

This section aims to underline the film's differences depending on the solvent evacuation method, i.e. anti-solvent dripping as conventionally associated with the spin-coating technique and solvent extraction under vacuum. However, contrary to the anti-solvent dripping method, which can evacuate the solvent almost instantaneously, the vacuum aspiration has a slower extraction rate.

First, we can observe in **Figure III-1** that, despite the absence of any thermal annealing, the perovskite photoactive α -phase is already formed, as showed by the diffraction peak at $2\theta = 14.1^\circ$ corresponding to the (100) direction.

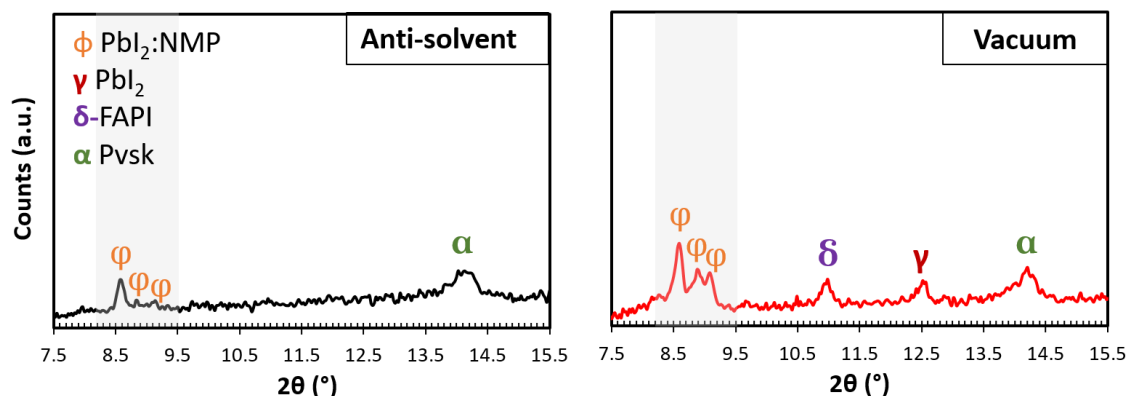


Figure III-1: Structure of the « as-deposited » films by x-ray diffraction analysis on glass/c-TiO₂/m-TiO₂.

Interestingly, regardless of the solvent extraction method, we noticed the presence of several diffraction peaks which cannot be ascribed to the expected α -phase, at $2\theta = 8.6^\circ$ and two close peaks at 8.9° and 9.1° . These peaks, noted φ , can be attributed to an intermediate phase forming between the solvent and PbI_2 , PbI_2 -NMP, as identified by F. Cheng *et al.*⁴

In the case of vacuum aspiration, the film structure is different. Indeed, we also identified the presence of the transparent perovskite δ -phase at $2\theta = 11.0^\circ$ and a small peak of PbI_2 at $2\theta = 12.6^\circ$.

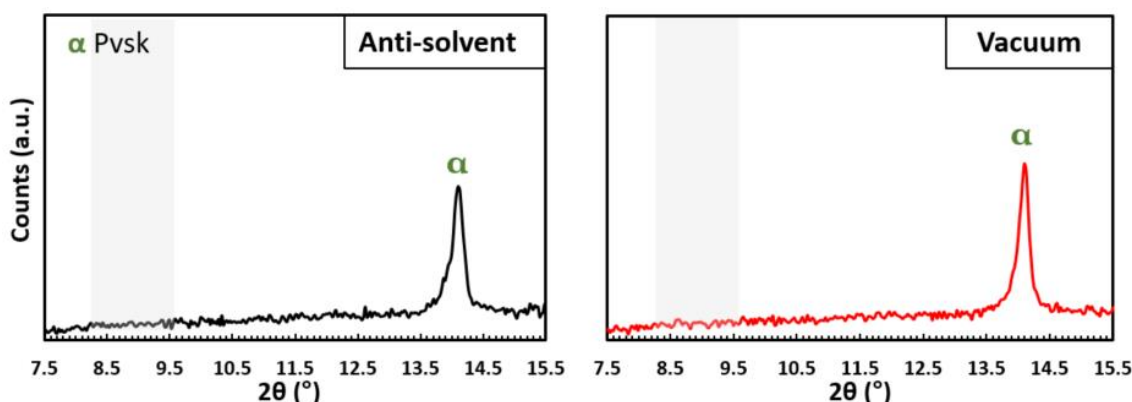


Figure III-2: XRD measurements of spin-coated “final” perovskite layers after two different quench methods. Black curve: Anti-solvent, chlorobenzene dripping. Red curve: Vacuum aspiration in a vacuum chamber.

After a thermal treatment at 110°C for 30 minutes, all the diffraction peaks assigned to the PbI_2 -solvent complexes, δ phase, and PbI_2 have disappeared, leading to a film of pure α -phase for both solvent extraction techniques (**Figure III-2**).

1.1.2. Morphological characterization

SEM analysis was carried out on the post-annealed perovskite film to analyze the effect of the quenching method on the film’s morphology. In **Figure III-3**, we can see that the anti-solvent dripping method generates a smoother and denser perovskite film compared to the vacuum quench method. The layer obtained employing vacuum aspiration exhibits a non-compact morphology with multiple pinholes. This result stresses that the film’s morphology is significantly influenced by the quench method, which leads to a poor morphology

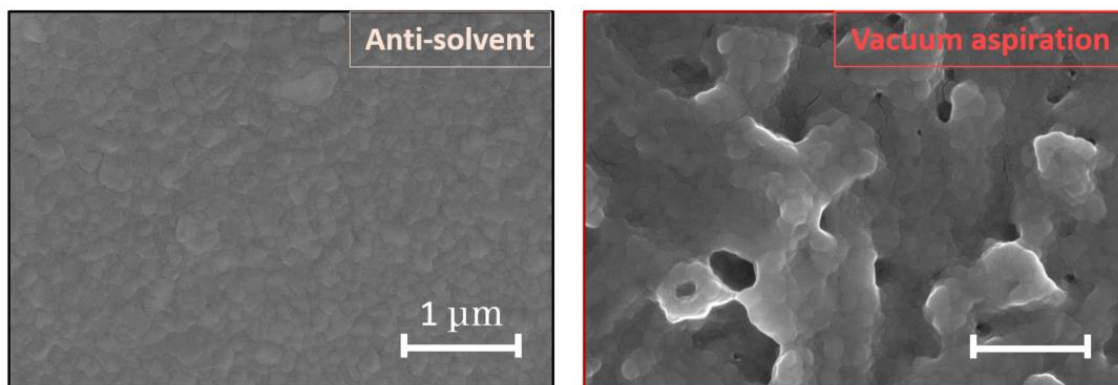


Figure III-3: Top-view SEM images of post-annealed perovskite layer after anti-solvent dripping or a vacuum aspiration quench.

To better quantify the film's roughness, this latter was determined more precisely by confocal microscopy. The perovskite film fabricated by anti-solvent dripping technique displays a Sa value of 18 nm, whereas the roughness value increases to 74 nm for vacuum aspiration. These results point out the vital role of the solvent extraction method for grain growth and the final perovskite film morphology.

Therefore, in order to use a vacuum aspiration system combined with the slot-die deposition, we decided to add MACl in the perovskite precursors solution.

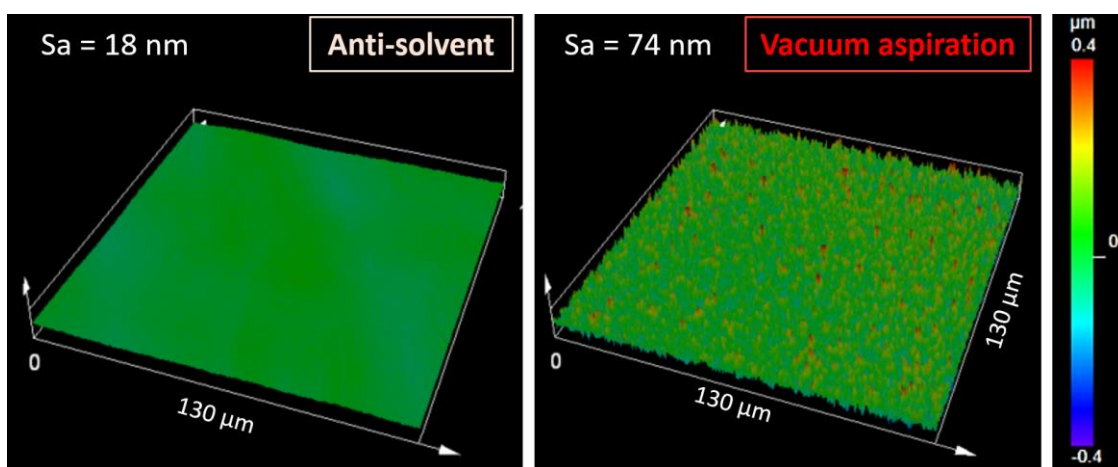


Figure III-4: 3D mapping and Sa value of a spin-coating perovskite layer in which solvent was extracted by anti-solvent (left) and vacuum aspiration (right).

1.2. Influence of the MACl addition

1.2.1. Intermediate phases characterization by XRD measurements

To improve the film's the film coverage and final morphology, we gradually added MACl in the perovskite precursors solution. The MACl content is calculated as a

molar ratio between MACl and FAI in the precursor solution (MACl: FAI). The ink is stirred overnight at 60°C to allow a good dissolution of the MACl salt, which has poor solubility in the solvent mix used in this work (DMF.:NMP volume ratio of (10:1)). After deposition, the film was placed in a vacuum chamber for 5 minutes or washed by anti-solvent dripping. Finally, all the films were annealed at 110°C for 30 minutes.

To analyze the impact of MACl on the perovskite crystallization, we varied the MACl: FAI ratio in the precursor's solution. Then, XRD measurements have been accordingly to the aforementioned conditions for the two solvent extraction methods.

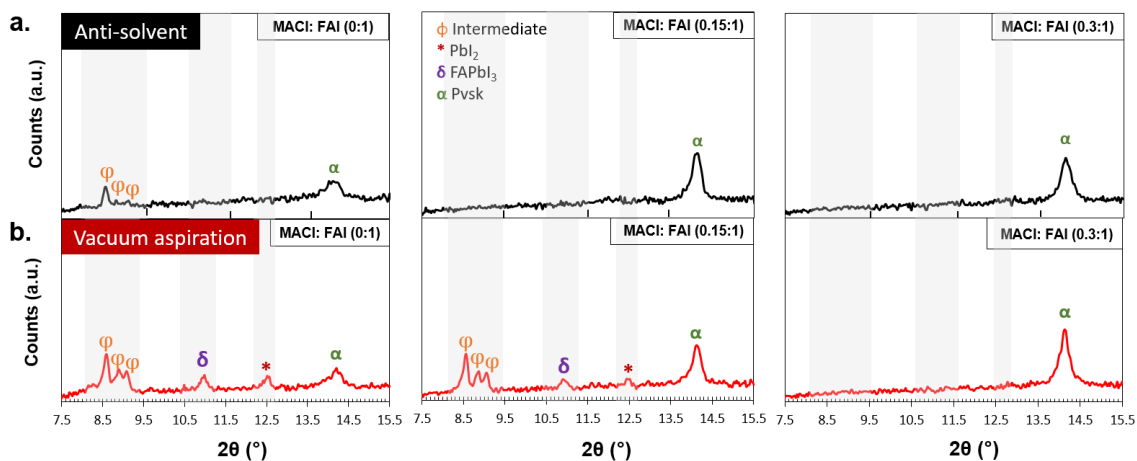


Figure III-5: XRD measurements of the spin-coated as-deposited layers with different MACl concentrations. **a.** after dripping of the anti-solvent. **b.** after vacuum aspiration of the solvent.

First, we performed XRD measurements on as-deposited perovskite films. In the case of an anti-solvent dripping method, we observed that the intermediates are only formed without MACl additives (**Figure III-5.a**). This ϕ -peaks, identified at $\theta = 8.6^\circ$, $\theta = 8.9^\circ$ and $\theta = 9.1^\circ$ can be ascribed to the same solvent adduct previously mentioned, NMP-PbI₂. However, once we introduced a small concentration of MACl into the precursor solution, these diffractions peaks are not visible anymore, suggesting a modification of the crystallization route.

In the case of vacuum aspiration, the same intermediates peaks are also visible on the x-ray diffractograms in **Figure III-5.b**. Nevertheless, as for the above technique, the gradual addition of MACl delays the formation of the PbI₂-solvent intermediates. The latter is not visible on the spectra for a MACl: FAI molar ratio of 0.3:1, independently of the drying technique.

MACl decomposes into MA⁺ and Cl⁻. Cl⁻ anions have been monitored by M. Kim *et al.* and can coordinate either with FA⁺ to form FAcI or with Pb²⁺ to form PbCl₂. The temporary substitution of I⁻ by Cl⁻ delays the formation of the FAPI structure. On the other hand, an excess of MA⁺ during the first stage of nucleation has been proved to be an effective way to promote ion exchange in the perovskite precursors solution.⁵ Such a phenomenon has already been reported by Li *et al.*⁶, in the case of the double-cation

MA_xFA_{1-x} perovskite deposited by spin-coating. Then, during the annealing stage, The Cl⁻ and MA⁺ ions then fade away during the thermal annealing stage.⁷

Combined with the co-solvent NMP, which creates a solvent adduct, it successfully regulates crystal growth and opens the window coating. It also prevents the formation of the δ phase and PbI₂.

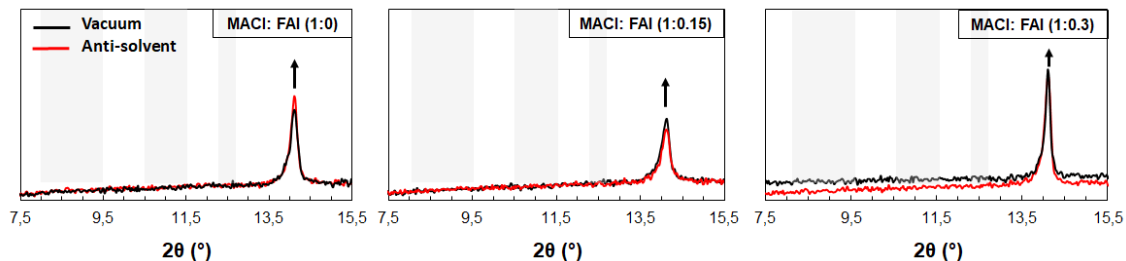


Figure III-6: XRD measurements of the spin-coated “intermediates” layers with different MACl concentrations, after vacuum aspiration of the solvent and an annealing at 110°C for 30 minutes.

After the annealing, the identified PbI₂-NMP adducts peaks fade away, indicating the complete conversion of the film into an α -Cs_xFA_{1-x} perovskite phase.

From the refined x-ray diffractograms, we calculated the crystallite size by the Williamson-hall method. The results are displayed in **Table 1**. Independently of the solvent extraction system, the crystal size grows with the addition of MACl. For the anti-solvent system, the crystal increases from 41 nm without MACl to 65 nm and 78 nm for MACl: FAI molar ratios of (0.15: 1) and (0.3:1), respectively. For the vacuum aspiration system, the crystal increases from 66 nm without MACl to 72 nm and 82 nm for MACl: FAI molar ratios of (0.15: 1) and (0.3:1), respectively.

In addition, the MACl addition also promotes a preferential orientation along (100 plan). In the case of a vacuum aspiration system, the $I_{(100)}/I_{(110)}$ ratio increases from 2.6 to 4.5. It has been shown in recent reports in the literature that additives, such as MACl, have a strong effect on the thin-film preferential orientation, which enhances the device performances.^{8,9}

Table 1: XRD calculated parameters are extracted from refined diffractograms of perovskite films after an annealing of 30 minutes at 110°C.

	MACl: FAI	C (nm)	a (Å)	$I_{(100)}/I_{(110)}$
Anti-solvent	No MACl	41 (2)	6.276	2.7
Vacuum aspiration		66 (4)	6.275	2.6
Anti-solvent	MACl: FAI (0.15:1)	65 (6)	6.273	2.1
Vacuum aspiration		72 (5)	6.274	2.2
Anti-solvent	MACl: FAI (0.3:1)	78 (8)	6.276	3.4
Vacuum aspiration		82 (15)	6.274	4.5

1.2.2. Morphology analysis

The modification of the intermediates formed before the film's crystallization and the MACl addition influences the final film's morphology. **Figure III-7** represents the top-view SEM images of final perovskite films. In the case of a vacuum quench, the addition of MACl in the precursor solution affords to enhance the film's morphology. The latter becomes denser, smoother, and presents a better coverage which are important characteristics for having good device performances.

Kosmatos *et al.* suggested for a MAPbI₃ composition that MAI and PbI₂ perovskite precursors are coordinating and forming a colloidal framework in solution.¹⁰ It has been demonstrated that crystal evolution can be correlated with the coordination between the precursor solute and solvent.¹¹ Both the size and the structure of the aggregated colloids determine the morphology of the final perovskite film.

In the presence of MACl, such a colloidal framework becomes more stable due to the preferential coordination of Cl⁻ with Pb²⁺ than I⁻.¹² The delayed perovskite crystal growth and the stabilization of the precursor's colloids lead to denser morphologies and larger grains and thus enhanced device performances. Moreover, the influence of the MACl addition on the perovskite film morphology has also been observed on FA-based perovskite composition, suggesting the possible versatility of such mechanism in the case of a PbI₂-FAI framework.⁵

In the case of our vacuum aspiration process, we identified the molar ratio of MACl: FAI (0.3:1) as the best concentration in perovskite precursors solution since it displays a good coverage of the perovskite layer.

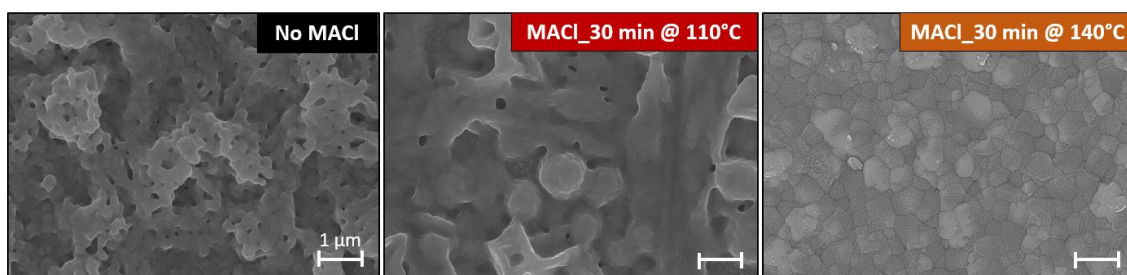


Figure III-7: Top-view SEM images of post-annealed perovskite films after a vacuum aspiration quench followed by a 110°C annealing for 30 minutes.

2. Optimization of the slot-die deposition conditions

Based on the above results, we transferred the ink formulation to the slot-die coating technique and performed a more detailed material analysis on the influence of MACl additive using this larger area deposition method.

A slot-die coating system deposits the perovskite layer within a glovebox in a nitrogen atmosphere. Then, the wet film is placed in a vacuum chamber and quenched for 5 minutes ($P_{\min} = 0.7$ mbar). As suggested in the previous section, we obtained an as-deposited film containing a PbI_2 -solvent complex of general composition $\text{FAI} \cdot \text{PbI}_2 \cdot \text{MACl} \cdot \text{NMP}/\text{DMF}$. According to Dualeh *et al.*, the MACl is decomposed into methylamine (CH_3NH_2) and hydrogen chloride (HCl) as gas products after annealing.¹³ The complete deposition route is depicted in **Figure III-8**.

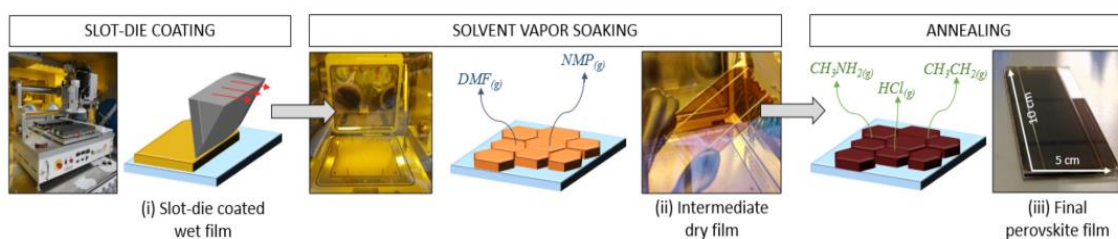


Figure III-8: Schematic deposition route and associated perovskite crystallization step using a slot-die technique.

2.1. Effect of the MACl on the crystal structure

Figure III-9.a. shows the evolution of the x-ray diffractograms as a function of MACl content. We can notice that the characteristic diffraction peaks of the perovskite are present for all the films regardless of MACl addition, without any traces neither of PbI_2 nor non-photoactive δ -phase.

The X-ray diffractograms have been refined by using the software Highscore. The calculated lattice cell parameters are gathered in **Table III-1**, and the refined profiles of (100) peaks are displayed in **Figure III-9.b**. It confirms the formation of a pure α -phase for all conditions, with the refinement of the (100) XRD peak. All the reflections can be indexed by a cubic unit cell with Pm-3m space group, thus confirming the absence of impurities in the film

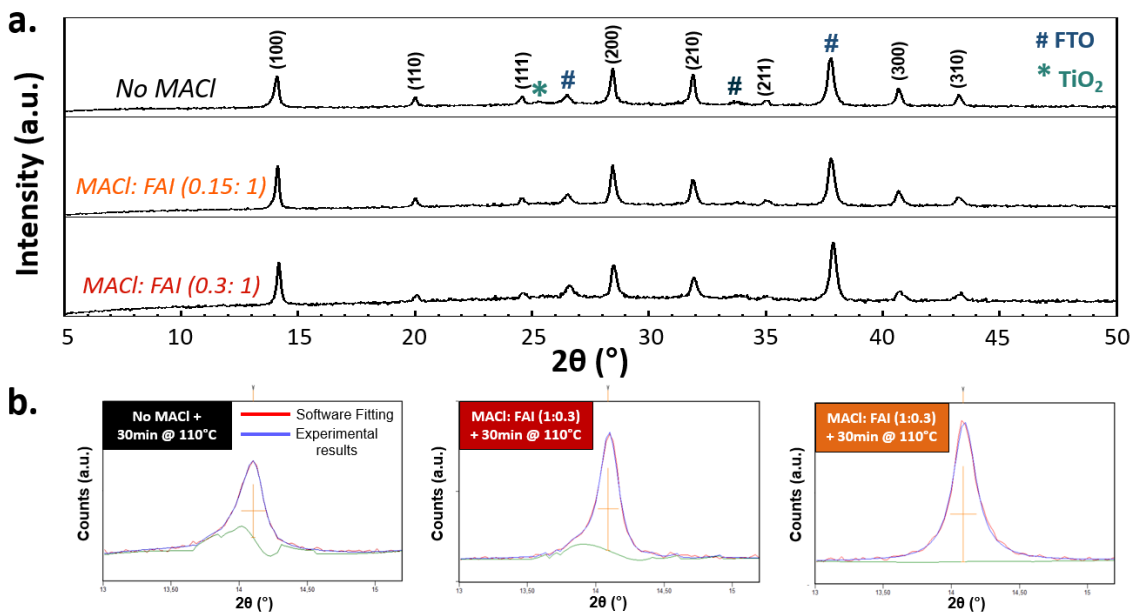


Figure III-9: X-ray diffractograms of perovskite film deposited on FTO/c-TiO₂/m-TiO₂ with different MACl contents: No MACl (Black curve), 15% MACl (Blue curve), and 30% MACl (Red curve). The two diffraction peaks at $2\theta = 26.5^\circ$ and 37.8° correspond to the FTO layer from the glass.

A more pronounced preferential orientation along the (100) direction compared to the (110) is observed upon MACl addition, as illustrated by the gradual increase of the (100)/(110) ratio from 2.4 to 7.6. This suggests that this latter not only favors the crystal's growth but also influences the crystal orientation during the growth. However, it appears that MACl has no effect on the lattice cell parameter, $6.277(9) \text{ \AA}$ is determined for MACl-free film, and $6.284(7) \text{ \AA}$ and $6.284(9) \text{ \AA}$ is determined for the films prepared with 0.15 and 0.3 molar ratio of MACl, respectively. This result indicates that neither MA⁺ nor Cl⁻ ions are introduced into the perovskite lattice.

The average crystallite size has been calculated using the Williamson-Hall method. Consequently, we can observe that the crystallite size increases from $76 \pm 6 \text{ nm}$ (No MACl) to 137 nm (0.15:1 MACl: FAI ratio) before it decreases to $114 \pm 9 \text{ nm}$ for 0.30:1 MACl: FAI ratio. Thus, a larger crystallite size upon the addition of MACl is in agreement with the literature.¹¹ Interestingly, the larger crystallite size is obtained for a ratio of 0.15:1. However, as aforementioned, this ratio was not further investigated owing to the poor film's coverage compared to the samples prepared with a 0.30:1 molar ratio (**Figure III-10**).

Moreover, the change of microstrains in the perovskite lattice has also been investigated. The strain values, calculated by the Williamson-Hall method, reveal small compressive strains (-0.84) when no MACl is added. However, as soon as MACl is added in the perovskite precursors solution, the strain value increases to 1.92 (for MACl: FAI (0.15:1) molar ratio) and 1.64 (MACl: FAI (0.15:1) molar ratio). It points out the ability of the

additive to relax the residual strains. Reducing residual strains in the crystal is particularly crucial as it can increase the phase conversion nucleation barrier.¹⁴

Table III-1: XRD calculated parameters are extracted from refined diffractograms.

MACl: FAI	C (nm)	a (Å)	I ₍₁₀₀₎ /I ₍₁₁₀₎	ϵ (10 ⁻³)
0:1	76 (1)	6.277 (9)	2.4	-0.84
0.15:1	137 (15)	6.284 (7)	4.3	1.92
0.30:1	111 (10)	6.284 (9)	7.6	1.64

2.2. Influence of the MACl addition on the perovskite morphology

We followed the morphological change of the perovskite film upon the addition of MACl by SEM. As we can easily observe in **Figure III-10**, at a (MACl: FAI) molar ratio of (0.15:1), the coverage is better than without MACl, but there are still numerous pinholes. When we increased the (MACl: FAI) molar ratio at (0.3:1), it induced the formation of a uniform layer, without pinholes, in good agreement with the previous results obtained by the spin-coating technique.

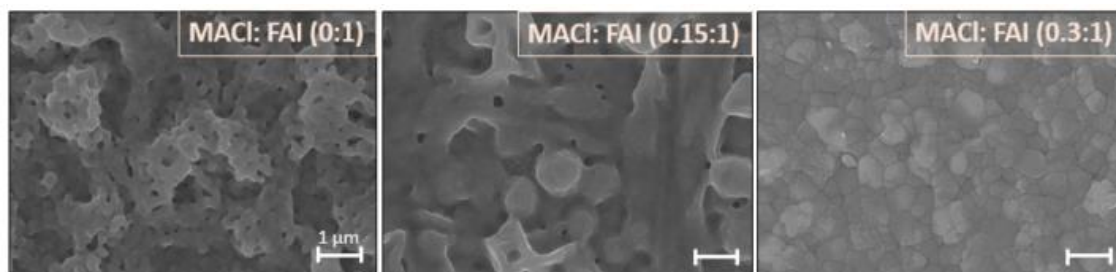


Figure III-10: Evolution of the top-view SEM images of slot-die coated post-annealed perovskite film after vacuum quench without and with MACl addition.

We marked out the sample's surface with a red line on the cross-section SEM pictures reported in **Figure III-11**. For the MACl-free perovskite film, the incomplete coverage generates numerous pinholes. The surface layer aspect is compliant with the SEM images of the perovskite films fabricated by spin-coating, confirming that vacuum aspiration influences perovskite morphology. Interestingly, Whitaker *et al.* used MACl to fabricate a MAPbI₃ perovskite layer by blade-coating combined with a vacuum extraction system and noticed a similar significant enhancement of the grain size.¹⁵

With MACl addition, the perovskite morphology is visibly improved due to surface roughness, a decrease in the film's porosity, reduction of the number of grain boundaries, and larger size particles. Consequently, the grain size of the perovskite appears to be

controlled by the MACl additive, which could effectively reduce the grain boundaries of the perovskite film. It is believed that the enlarged grain size and reduced grain boundaries could decrease the trap density of the perovskite film, beneficial to the photovoltaic performance.^{16–18} In addition, the faster growth kinetics along preferential $\langle 100 \rangle$ in the presence of Cl has been explained by a recent computational study, which showed that Cl at the MAPbI₃/TiO₂ interface reinforces the binding of (001) planes of MAPbI₃ with the TiO₂ underlayer.¹⁹

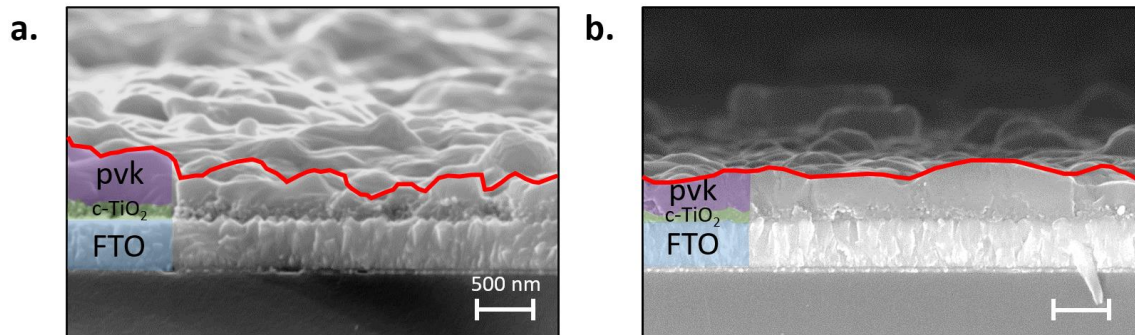


Figure III-11: Cross-section SEM images of the slot-die coated post-annealed perovskite film after vacuum quench without (left picture) and with a MACl: FAI ratio of (0.3: 1) (right).

The reduction of the film's roughness is in good agreement with confocal microscopy experiments showing an important reduction of the roughness Sa value deduced from the measured height distribution, from 124 nm down to 56 nm for MACl: FAI ratio of 0.3:1 (**Figure III-12**). These measurements were performed directly on the perovskite film deposited on Glass/FTO/c-TiO₂/m-TiO₂ stack.

This trend is consistent with the morphological evolution observed on SEM images. Moreover, the reference sample, i.e., without MACl addition, presents a wide distribution of measured heights, indicating the presence of numerous dots on the film's surface, pinholes, and surface defects, by contrast to the (0.3:1) ratio, which exhibits a much narrower distribution.

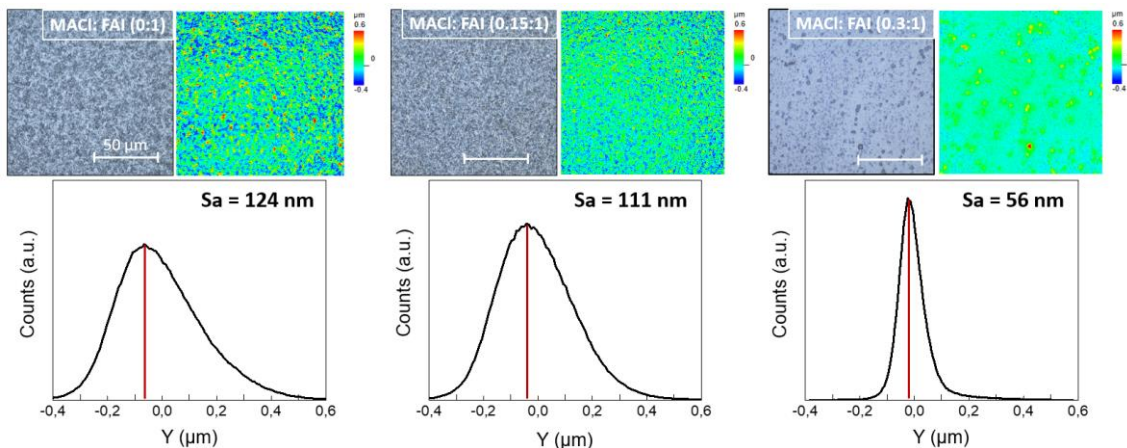


Figure III-12: Microscope confocal measurements of slot-die coated annealed perovskite layer after a vacuum aspiration quench, followed by a 30 mins annealing at 110°C for 30 minutes. The black curve represents the distribution of height measurements extracted from surface roughness mapping.

2.3. Influence of the annealing conditions on the perovskite film properties

The annealing temperature has been proven to affect the film's morphology. Dualeh *et al.*¹³ studied the influence of annealing time and temperature up to 200°C associated with a lead chloride (PbCl₂) precursor. Interestingly, the authors directly related the perovskite coverage to the annealing conditions. Moreover, Kim *et al.* proposed a flash high-temperature post-annealing, i.e., 400°C for 4 seconds, and observed greater grain size.²⁰ Based on these results, our approach was to study the annealing temperature and time to improve both the film's crystallinity and morphology of our slot-die coated perovskite film using MAcl: FAI ratio of 0.3:1. We investigated two standard annealing treatments for 30 minutes, one at 110°C and a second at 140°C, and two "flash" post-treatments for 5 minutes at 170°C and 200°C.

2.3.1. Evolution of the film's crystallinity

We can see on **Figure III-13** that each annealing condition led to a pure α -phase, except at 200°C for which a small diffraction peak at $2\theta = 12.6^\circ$ is observed, ascribed to PbI₂ impurities arising from the onset of the perovskite decomposition by temperature.

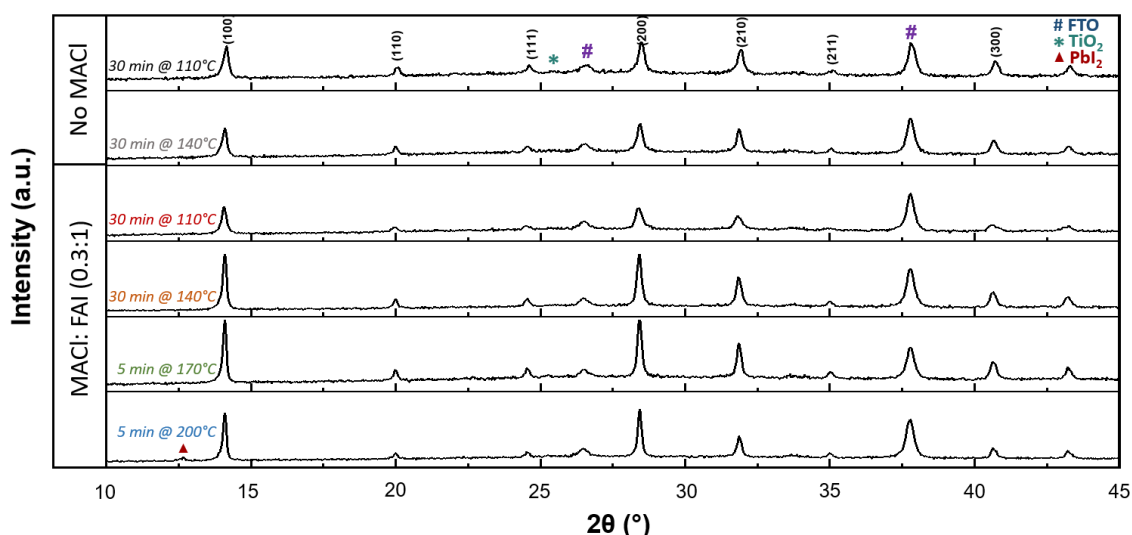


Figure III-13: X-ray diffractograms of six perovskite films deposited on glass/FTO/c-TiO₂/m-TiO₂. The two reference samples were fabricated without MAcl additive and annealed at 110°C and 140°C for 30 minutes. The four other samples were prepared with a MAcl: FAI molar ratio of 0.3:1 and were annealed under different conditions.

The lattice parameter for all annealing conditions is reported in **Table III-2**. Regardless of the conditions, no noticeable modification of the lattice cell parameter is observed, indicating that the film's stoichiometry and bulk point defects are comparable between the different conditions. It shows only a very small increase for the 110°C annealing (less than 0.01 Å of variation).

Under higher annealing temperatures, though, the lattice value a stays identical to the associated references without chloride ($\approx 6,280$ Å). This indicates that neither change of stoichiometry nor MAcl inclusion is expected when varying the annealing conditions. This latter should have led to a lattice shrinkage due to the smaller size of the MA-cation compared to the FA-cation as pointed out by Nie *et al.*²¹ It thus suggests that MA⁺ and Cl⁻ are not incorporated in the lattice for all the conditions

The annealing temperature induces a gradual increase of the crystallite size, as one could expect. The crystal size increases from 46 nm at 110°C to 110 nm at 140°C without MAcl additive and, from 152 nm to 187 nm with MAcl additive. In addition, 5 minutes of flash annealing at 170°C afford to reach a crystallite size as large as 225 nm before decreasing to 149 nm when increasing the temperature to 200°C. This decrease can be related to the perovskite film's thermal degradation, leading to organic gas releases and PbI₂.

Table III-2: Evolution of crystallite size determined by the Williamson-Hall formalism, lattice cell parameter, and intensity ratio between (100) and (110) diffraction peak depending on the post-annealing conditions.

	Annealing conditions	C (nm)	a (Å)	I ₍₁₀₀₎ /I ₍₁₁₀₎	ϵ (10 ⁻³)
No MAcl	30 min @ 110°C	42 (4)	6.276 (8)	3.6	-0.20
	30 min @ 140°C	44 (5)	6.283 (9)	4.0	-0.18
MAcl: FAI (0.3:1)	30 min @ 110°C	109 (21)	6.287 (9)	5.8	3.30
	30 min @ 140°C	156 (29)	6.280 (8)	5.4	1.75
	5 min @ 170°C	133 (18)	6.283 (9)	7.2	1.46
	5 min @ 200°C	72 (2)	6.279 (7)	11.2	0.71

2.3.2. Impact on the morphology of the perovskite layer

First, we studied the influence of the annealing condition without MAcl addition on the grain size distribution. In **Figure III-14**, we can observe that the perovskite film presents small perovskite grains, and the mean size doesn't vary significantly when we increase the annealing temperature from 110° to 140°C (255 nm to 261 nm, respectively).

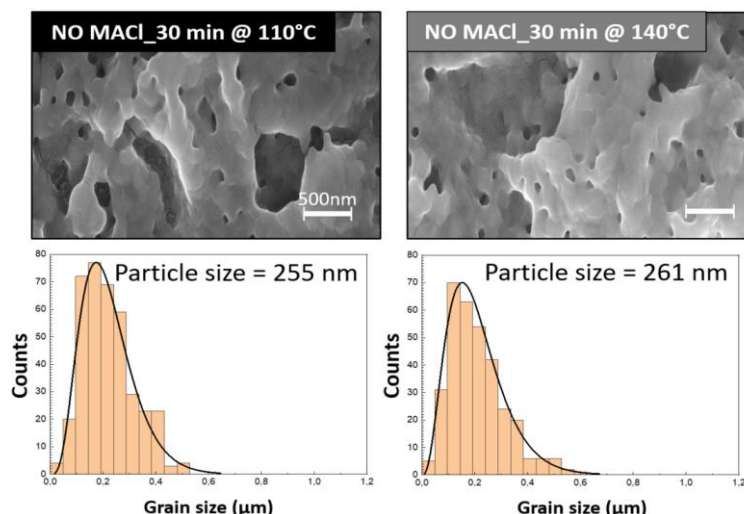


Figure III-14: SEM image and associated grain size distribution of the perovskite film without MACl addition post-annealed either at 110°C or 140°C.

Second, when MACl is added, the grain size increases with the annealing temperature (**Figure III-15**). At 110°C with a MACl additive, the average particle size increases from 255 nm to 354 nm. This particle's growth is also well visible on the top-view SEM images. It reaches a maximum of 486 nm on average when the film is post-annealed at 170°C for 5 minutes. However, the distribution of the particles size becomes broader with the temperature owing to the apparition of large grains (> 600nm in diameter) for annealing temperatures of 140°C and 170°C. This evolution is consistent with crystallite size growth, as discussed above. Nevertheless, the size of the crystallites and the grain size determined from the SEM images are different. This result can indicate that the grain growth is controlled by the coalescence of primary grains leading to polycrystalline grains.²²

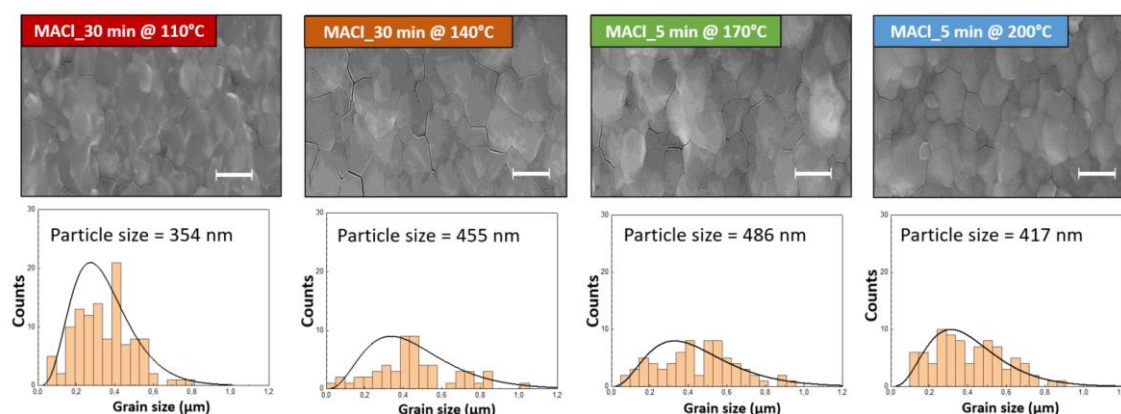


Figure III-15: SEM images and associated grain size distribution in the perovskite film prepared with a MACl: FAI ratio of 0.3:1 under different annealing conditions: Two classical annealing during 30 minutes at 110°C (red) and 140°C (orange), and two flash annealings during 5 minutes at 170°C (green) and 200°C (blue).

2.3.3. Opto-electronic properties of the perovskite film depending on annealing conditions

The transmission spectra presented in **Figure III-6. a.** show that the transmission for wavelengths above the bandgap (i.e., > 750 nm) significantly increases from 45% for the reference sample to 65% with MACl addition. The excessive pinholes can explain this feature in the film without MACl, which contributes to light scattering according to Mie scattering theory.²³

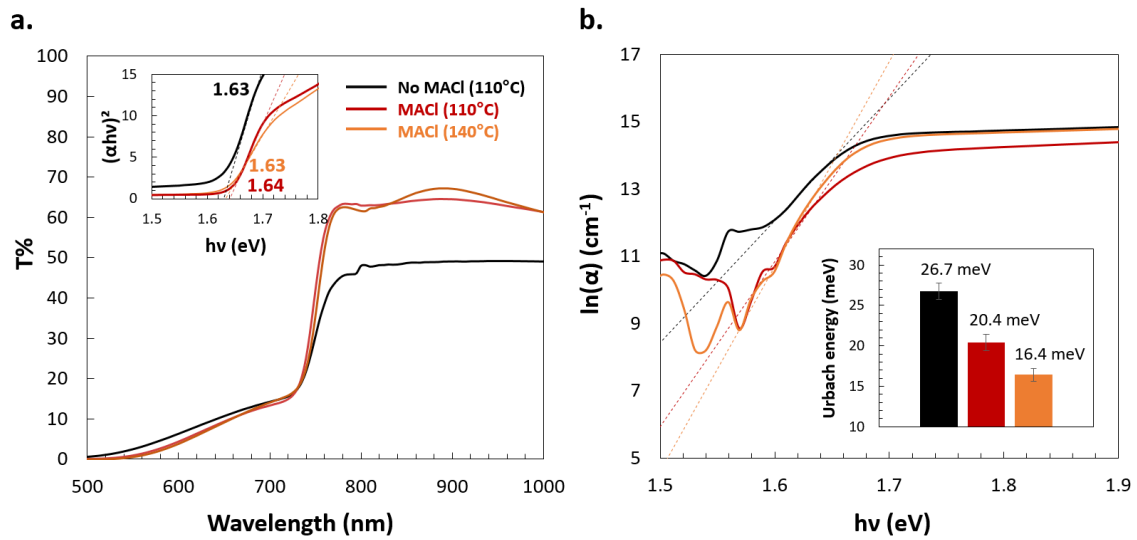


Figure III-16: **a.** Evolution of the transmission spectra of the perovskite film (the tauc plot is represented in inset). **b.** Urbach energy of perovskite films. The perovskite films are deposited on glass/FTO/c-TiO₂/m-TiO₂ and prepared with different annealing conditions.

For wavelengths below 500 nm, a higher magnified inset in **Figure III-16.a.** reveals that the transmission for the MACl samples reaches zero by contrast to the sample MACl-free for which a slight optical transmission persists owing to the poorer film's coverage. **Figure III-16. b.** shows the Urbach plot, derived from the absorption curve, i.e., $\ln(\alpha)$, as a function of photon energy.

The Urbach energy, which can be determined from the slope of the Urbach plot using the below equation, describes the electronic disorder at the bandgap threshold:

$$\ln(\alpha) = \frac{h\nu}{E_u} + \ln(\alpha_0) \quad (\text{Eq. 1})$$

Where α is the absorption coefficient, $h\nu$ is the photon energy, and E_u is the Urbach energy.

The reference sample has an $E_u = 26.7$ meV, whereas the samples with MACl exhibit lower Urbach energy, $E_u = 20.4$ meV for 110°C post-annealing and $E_u = 16.4$ meV for 140°C post-annealing. These values are respectively 24% and 39% lower than the reference, indicating that the MACl addition and a higher annealing temperature helps to lower electronic disorder and defects close to the band edges of the perovskite films.²⁴

We performed photoluminescence and cathodo-luminescence measurements, presented in **Figure III-17**, on three samples prepared with different conditions: a reference sample without MACl additive and post-annealed at 110°C, and two samples prepared with a MACl: FAI ratio of (0.3:1), post-annealed at 110°C and 140°C respectively. All the measurements have been performed on half-cells where the perovskite is deposited on glass/c-TiO₂/m-TiO₂).

To extract the optical bandgap from the PL measurement, we fitted the curve using the model proposed by Katahara *et al.*^{25,26} Independently of the MACl addition and annealing conditions, the optical bandgap of the perovskite is $E_g = 1.64$ eV.^{3,27} In addition, a single emission band at ca. 750 nm is observed by cathodo-luminescence regardless of the sample (**Figure III-17.b**).

In the case of a MAPbI₃ perovskite crystal, W. Kaiser *et al.* point out that chlorine can be incorporated at a relatively low concentration level below 3–4% without significantly affecting the bandgap.²⁸ However, in the case of our protocol, the invariability of the lattice parameters combined with the bandgap measurements excludes the possibility of a chloride inclusion.

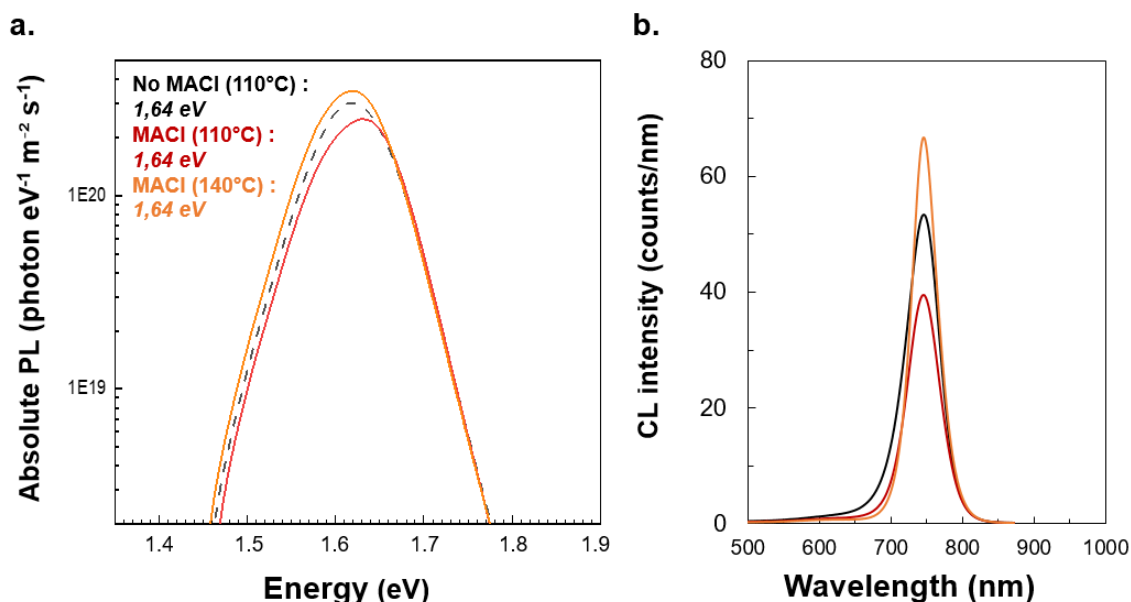


Figure III-17: **a.** Photoluminescence measurements: The PL acquisition was conducted using a microscope, a 2D band-pass filtering system with 2 nm resolution, and finally a 1Mpix silicon-based charged-coupled device camera PCO1300. The sample was illuminated at $\lambda = 532$ nm and **b.** Cathodo-luminescence curves. CL measurements were carried out using an Attolight Chronos

quantitative CL microscope at room temperature with 3 kV acceleration voltage and a dose lower than $10^{20} e^{-1} cm^{-2}$.

Although MAI has no effect at first sight, closer looking shows that the addition of the latter associated with an annealing temperature of 140°C contributes to a narrowing of the CL emission band, for which the FWHM goes from 56 nm to 44 nm. It also reduces the emission band asymmetry, in particular the raising tail above 600 nm. The PL values are displayed in **Table III-3**. These results point out the enhancement in the optical quality of the perovskite film upon the addition of MAI.^{29,30} Diab *et al.* ascribed an evolution of the PL intensity to a reduction of point defects, strains, and composition fluctuation.³¹ This is consistent with the suppression of the compressive strains by the MAI addition and the reduction of the tensile strains by the annealing temperature highlighted in **part 2.3.1**.

Thus, the annealing temperature of 140°C combined with MAI addition reduces the defects density in the perovskite layer.

Table III- 3: Values extracted from cathodo-luminescence measurements

MAI: FAI	Annealing temperature °C	E _g (CL) eV	FWHM CL nm
(0:1)	110	1.63	56 (1)
(0.3:1)	110	1.64	54 (1)
(0.3:1)	140	1.64	44 (1)

In summary, we investigated the MAI addition effects on the perovskite films. As a result, we achieved high-quality pure α -phase perovskite material. In addition, the surface morphology, crystallographic properties, optical absorption, and photo-luminescence properties were enhanced. The repeatable effect of the MAI addition, from spin-coating sample to slot-die coating, confirms that the beneficial effect of MAI is directly transferable to scalable printing.

3. Full devices performances

3.1. Small-cells performances

The fabrication protocol of the full solar devices has been extensively described in **Chapter 2. in parts 3 and 4**. The IV parameters of the best solar cells and the average of each parameter are displayed in **Annex 7**.

As one could anticipate from the film's morphology, **Figure III-19** shows that MAI addition with a 0.3: 1 ratio compared to FAI affords a significant increase in the cell photovoltage from 1.00 V to 1.14 V. This cell photovoltage is not affected by the post-

annealing temperature. This enhancement can be interpreted as reducing non-radiative shallow trap defects in the perovskite layer in agreement with the lower Urbach energy.
24

The cell photocurrent is also significantly enhanced, thanks to the MACl additive, from 14.2 to 19.8 mA/cm² for a post-annealing at 110°C and from 16.1 to 20.3 mA/cm² for a post-annealing at 140°C. This improvement is ascribed to the better film quality, i.e., improved coverage, larger grain size, and smoother surface when MACl is added.

However, despite a significant increase in the grain size as aforementioned, the flash annealing approach did not translate to any improvement in the device performances (**Figure III-18**). This is mainly due to a loss of the cell photovoltage. One possible explanation is the creation of surface defects such as iodide vacancies due to the high temperature and the onset of PbI₂ formation for the 200°C sample.

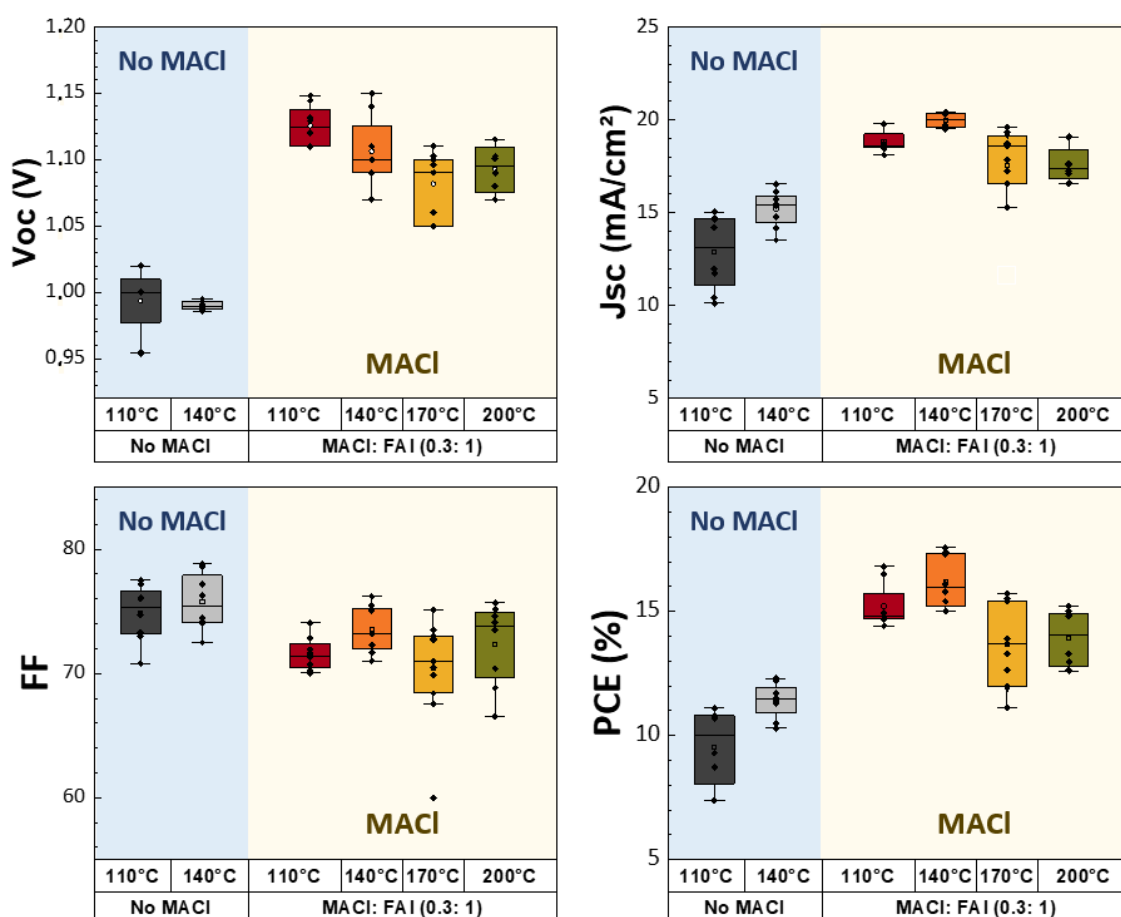


Figure III-18: Device statistics for perovskite solar cells prepared with a molar ratio MACl: FAI (0.3:1). Each annealing condition counts 6 cells. Reverse scan (plain color) and forward scan (stripped).

The best power conversion efficiency (PCE) obtained is 16.8 % in reverse scan for a perovskite film crystallized at 110°C ($V_{oc} = 1.15$ V, $J_{sc} = 19.8$ mA/cm², FF = 74.1 %) and shows 16.7 % stable PCE under maximum power point condition (MPP). Increasing the temperature to 140°C is beneficial for the device's performance.

A record PCE of 17.4% is reached in reverse scan ($V_{oc} = 1.14$ V, $J_{sc} = 20.3$ mA/cm², FF = 75%) (**Figure III-19.b**) and 17.5 % stable PCE under MPP condition. This performance is a very encouraging result. To date, the best solar cells performances fabricated by slot-die have been reached by Z. Yang *et al.* with a 18.2% efficiency on 0.09 cm² active area.

Interestingly, one can notice the very low hysteresis in these cases, which is directly related to the degree of crystallinity and the size of the crystalline domains as reported by Tripathi *et al.*³² Moreover, the MACl addition have been extensively proved to passivate the surface defects allowing hysteresis-free perovskite devices.^{33,34}

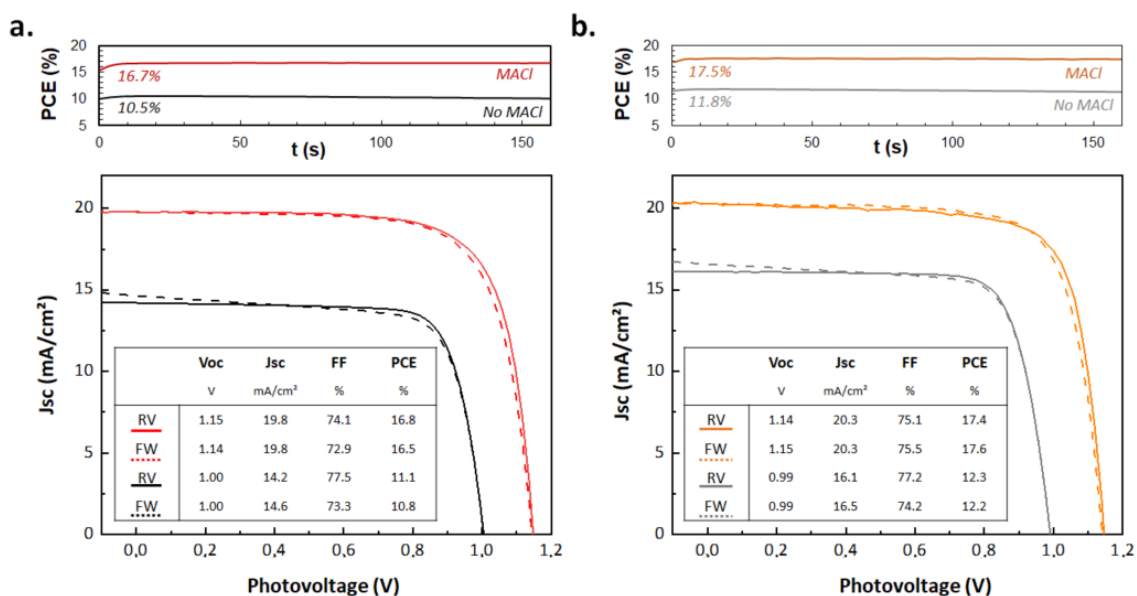


Figure III-19: *J-V performances under A.M.1.5G conditions for the best cells without and with MACl addition: a. post-annealed at 110°C for 30 minutes, b. post-annealed at 140°C for 30 minutes.*

As a first attempt to evaluate the homogeneity of our coating, we displayed a map of the efficiency of 8 individual cells from one 5 x 10 cm² substrate. Almost all the cells display efficiencies over 15%. We noticed that the efficiency of the cells located near the end of the coating demonstrates lower PCE due to a thinner perovskite layer.

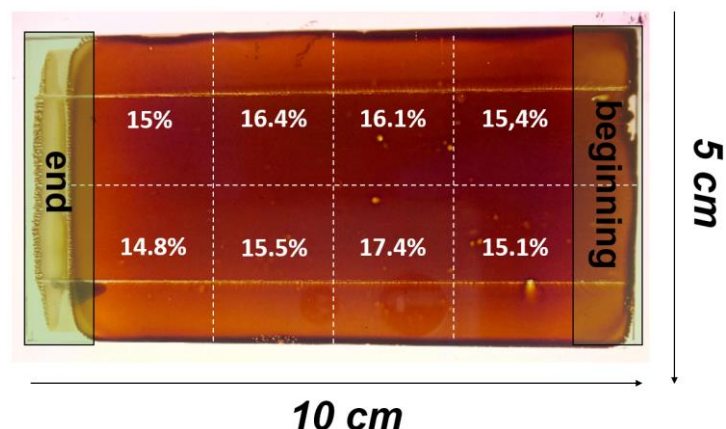


Figure III-20: PCE mapping of 8 devices ($2 \times 2.5 \text{ cm}^2$) produced from one $5 \times 10 \text{ cm}^2$ substrate with a slot-die coated perovskite layer, with a MAI:FAI (0.3:1) molar ratio (reverse scans). The green areas are sacrificial areas ($1 \times 5 \text{ cm}^2$).

3.2. Modules

To further investigate the homogeneity and performance of the slot-die coated perovskite layers over a larger surface, mini-modules with an aperture area of 12 cm^2 were fabricated.

The mini-modules consist of 6 individual cell stripes with 2 cm^2 each, connected in series with an average geometrical fill factor of around 90%. The width of the subcells was set to 0.5 cm, minimizing the loss arising from series resistance in relation to the dead area as reported previously.³⁵ Laser scribing of the perovskite modules was performed using an Innolas ILS LT laser system equipped with a UV laser (355 nm) and a green laser (532 nm) delivering monochromatic pulses of 10 ps at 400 kHz. P1 scribing on $5 \text{ cm} \times 10 \text{ cm}$ FTO substrates was performed using the UV laser at maximum power. P2 and P3 were done using a green laser with powers of 12.7 W and 0.5 W, respectively. Images of the fabricated mini-modules are shown in **Figure III-21**.

For the perovskite layer, we chose the fabrication conditions displaying the best results for small-scale solar cells: a MAI:FAI molar ratio of (0.3: 1) and a 30 minutes annealing at 140°C were selected.

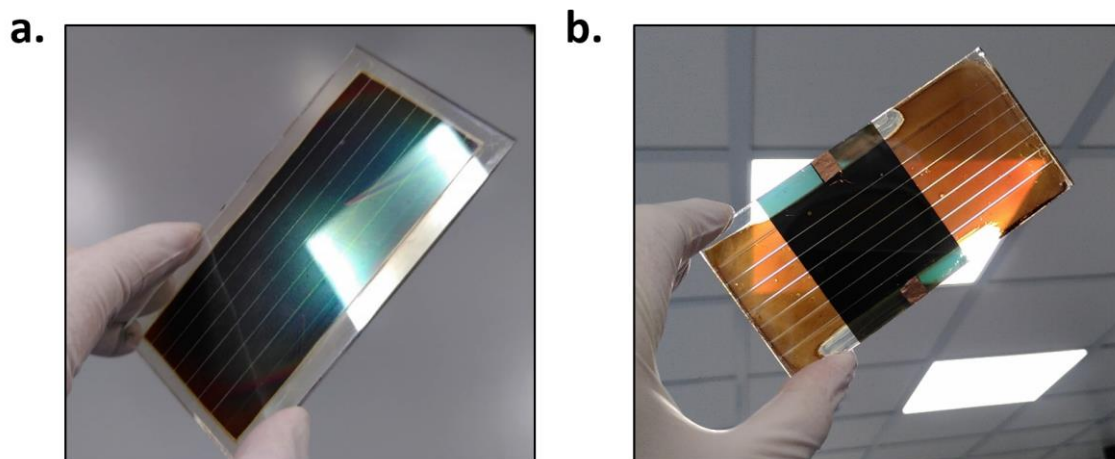


Figure III-21: **a.** Perovskite module before the deposition of the gold electrode and the P3 laser patterning. **b.** 12cm² module delimited by the gold electrode.

The distribution of the module's efficiencies is displayed in **Figure III-30.a**. The PCE statistics of 15 mini-modules showed an average value of 13.6%. The lowest modules demonstrated an efficiency of 11.3%, while the best module reached an efficiency of 15.7% (15.6% stabilized).

The IV curve and the MPP tracking of the champion device are shown in **Figure III-22. b. and c.** Carefully tuning the laser power during the P2 scribe was crucial to entirely remove the ETL layer without damaging the underlying FTO, resulting in a high V_{oc} for the champion device of almost 7V.

So far, only a few modules devices with a perovskite absorber deposited by a one-step slot-die process have been reported. D. Lee *et al.* used a combination of $PbCl_2$ with $PbAc_2$ to delay the crystallization by Cl^- incorporation. Coupled with a “gas-assisted” approach to promote rapid nucleation, a pinhole-free and large-grain perovskite film were obtained, leading to a 10 cm² module with a PCE of 8.3%.³⁶ In addition, a scalable sheet-to-sheet slot-die coating process for perovskite devices was realized by Galagan *et al.*, where large-area modules of 12.5 x 13.5 cm² and 10% efficiency were deposited on 6 in. x 6 in. substrates.³⁷ More recently, Z. Yang *et al.* realized a record module of 16.63% on 20 cm² by combining two co-solvents in the perovskite ink in addition to DMF, NMP, and DMSO.

Therefore, the fabrication of these modules validates our deposition protocol's potential for the fabrication of perovskite over large surfaces. However, some optimization work is still necessary to keep up with the state of the art, both in terms of material quality and uniformity.

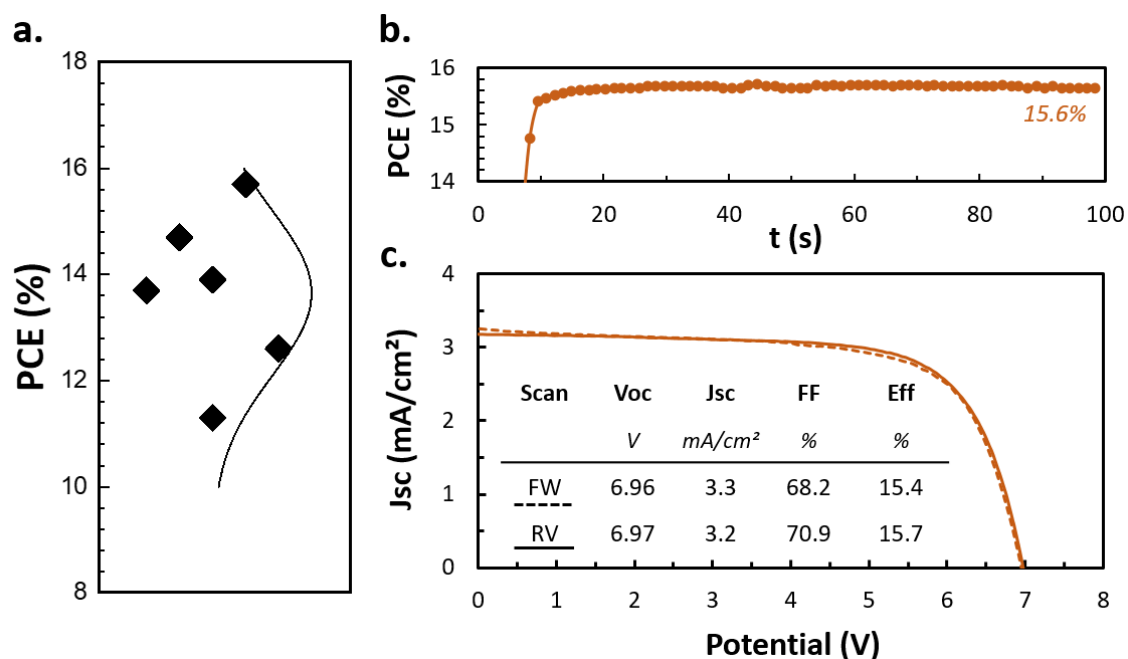


Figure III-22: **a.** Distribution of modules performances. **b.** MPP tracking of the best module, and **c.** J-V curve of the best module. The efficiency is calculated for a 12 cm² area.

4. Stability Tests

4.1. Encapsulation of perovskite solar cells

We tried to evaluate the stability of the fabricated devices. To do so, the cells prepared under different post-annealing conditions were encapsulated as described in **Figure III-23**. We started by edge sealing the active area with a thermoplastic Surlyn polymer and added on top of the polymer a 3 mm-thick glass. The assembly is placed in a press and heated for two minutes to melt the polymer film. Then, we completed the sealing by adding Loctite glue on the edges, and the latter was cured under UV exposition for 1 minute. During this process, the perovskite is protected from the UVs by placing an opaque tape upon the active area. Finally, copper tape is added to enhance the electrical contacts. Crocodile clips ensure the connection with the stability bench.

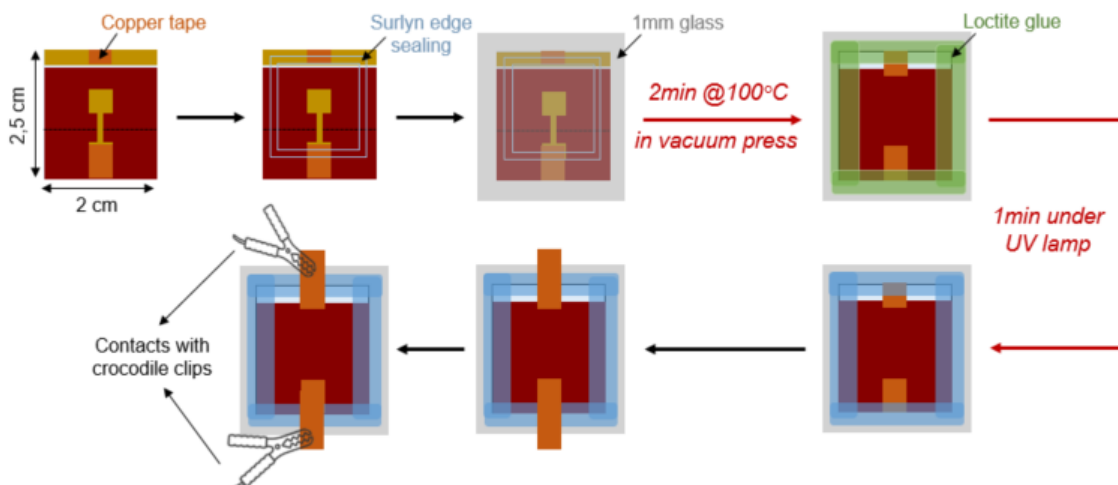


Figure III-23: Full devices contact and encapsulation process. The encapsulation is done in a glovebox for the Surlyn edge sealing and in an ambient atmosphere for the Loctite glue.

4.2. Encapsulation impact on the performances of the device

The encapsulation process involves a heating step at 100°C. We measured the device performances before and just after the encapsulation process to ascertain that the Spiro-OMeTAD has not been degraded by the above heating step (**Figure III-24**). The IV parameters of the solar cells are displayed in **Annex 8**.

As a result, we conclude that only a relatively small impact due to the encapsulation has been observed, which affords to validate this process. All the cells showed a loss of V_{oc} , except for the 140°C annealing condition with the MACl additive. The loss of V_{oc} is probably due to a slight degradation of the HTM or the doping effectiveness by the heating. This issue is actually addressed at IPVF Lab by replacing the Spiro-OMeTAD with a PTAA layer for spin-coating devices. The replacement of Spiro-OMeTAD by PTAA for slot-die devices will be further described in **Chapter 4**.

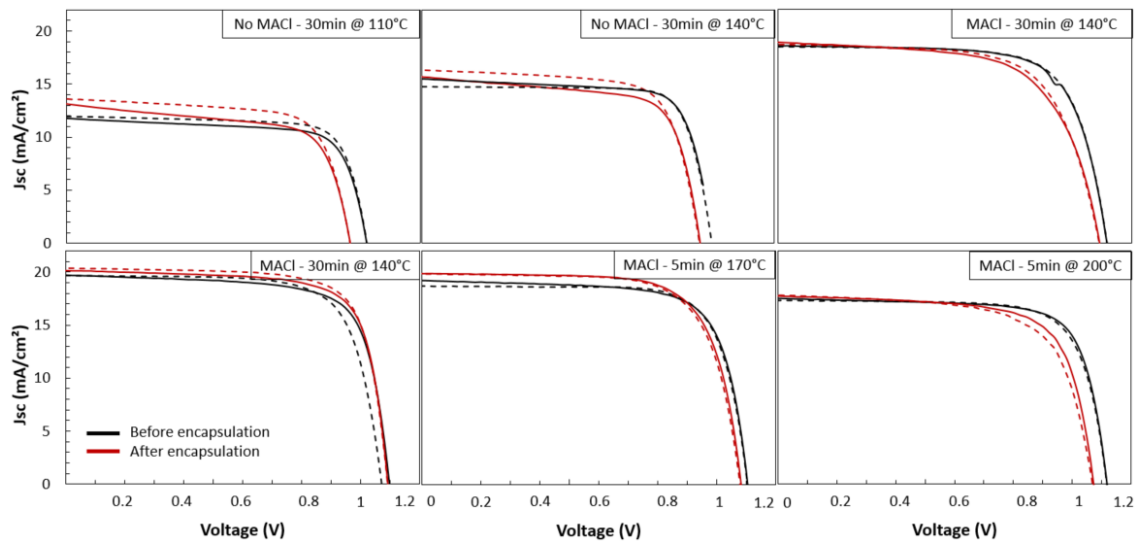


Figure III-24: J - V curves of the solar cells under A.M.1.5G conditions before (black curves) and after the encapsulation process (red curves). The reverse scans are indicated in plain lines and the forward scan in dotted lines.

4.3. Impact of annealing conditions on full devices stability

We encapsulated solar cells of each condition and followed the evolution of their performance under constant illumination (0.7 sun - LED illumination without UV). The performances of the cells were systematically measured at maximum power point (MPP) regardless of the annealing conditions. The **Figure III-25.b** shows the normalized efficiency evolution over 300 hours ageing. Due to contact failure, the device annealed at 200°C has been discarded.

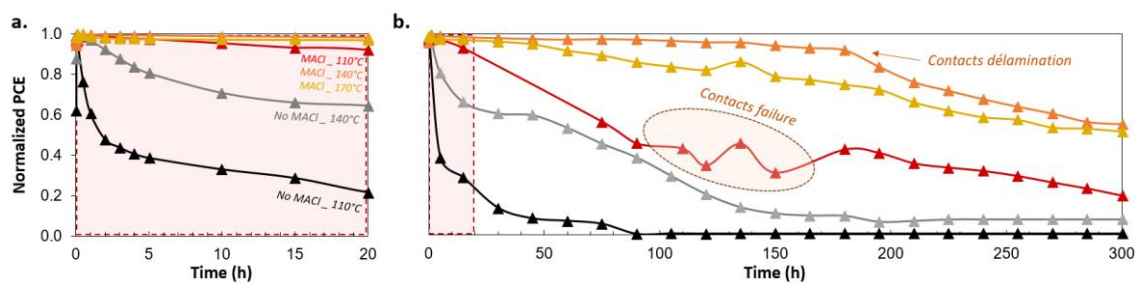


Figure III-25: Stability data of encapsulated devices exposed under constant illumination under MPP conditions. **a.** First 20 hours of ageing. **b.** Stability over 300 hours.

We defined T_{80} , the time the device retains over 80% of its initial efficiency, and T_{50} , the time the device retains 50% of its initial efficiency. All the values are displayed in **Table III-4**.

The efficiency of the devices without MA₂Cl dropped very quickly. T_{80} is under 4 hours for both annealing conditions. The 140°C post-annealing condition affords to prolong a bit the stability compared to the 110°C counterpart, $T_{50} = 66\text{h}$ and $T_{50} = 2\text{h}$ respectively. This indicates that the annealing temperature plays an important role in the stability of the device.

In addition, when MA₂Cl is added to the perovskite precursors solution, the devices exhibit superior stability. At 110°C, the T_{80} is 36 hours, and the T_{50} is 85 hours. This represents only a small gain compared to the T_{50} of the reference cell without MA₂Cl annealed at 140°C.

When we increased the annealing temperature, the devices displayed higher stability. For a post-annealing at 140°C, which showed the best PCE, $T_{80} = 200$ hours, whereas the post-annealing at 170°C reached T_{80} after 150 hours. At the end of the 300 hours stability test, all conditions fell below the T_{50} limit, except for the devices annealed at 140°C and 170°C.

A first inspection of the devices after the ageing indicates that the decrease observable on the stability curve for our best devices is partially due to the way the metallic contact is taken in our device. In fact, we used copper tape, which tends to delaminate over time, mainly because of the heat due to continuous illumination. Regarding the stability curves and the experimental observations, the delamination phenomena seem to impact the measurements after 200 hours directly. Optimization of the cell design is ongoing to replace the copper tape with welded wires.

Table III-4: Influence of the MA₂Cl addition and the annealing conditions on the device stability. Stability datas of the encapsulated devices aged under illumination for 300 hours.

(MA ₂ Cl: FAI)	Annealing conditions	T_{80}	T_{50}
(0:1)	30 mins at 110°C	1h	2h
	30 mins at 140°C	4h	66h
(0.3:1)	30 mins at 110°C	36h	85h
	30 mins at 140°C	200h	>300h
	5 mins at 170°C	150h	>300h

4.4. Post-mortem characterization of aged devices

To identify some degradation paths and understand the efficiency loss of the encapsulated devices, Scanning Transmission Electron Microscopy (STEM) and High Annular Angle Dark Field (HAADF) have been performed on the devices' cross-section. We aimed to characterize the evolution of the perovskite morphology, quality of the

interfaces, and elemental analysis to provide more insights into the main degradation mechanisms. We selected three device conditions:

- A reference cell. The perovskite layer was fabricated without MACl and annealed at 110°C for 30 minutes;
- Two devices, which the perovskite layer was fabricated with MACl and annealed at 110°C for 30 minutes or at 140°C for 30 minutes.

The characterizations were performed before ageing on non-encapsulated devices and after ageing on encapsulated devices.

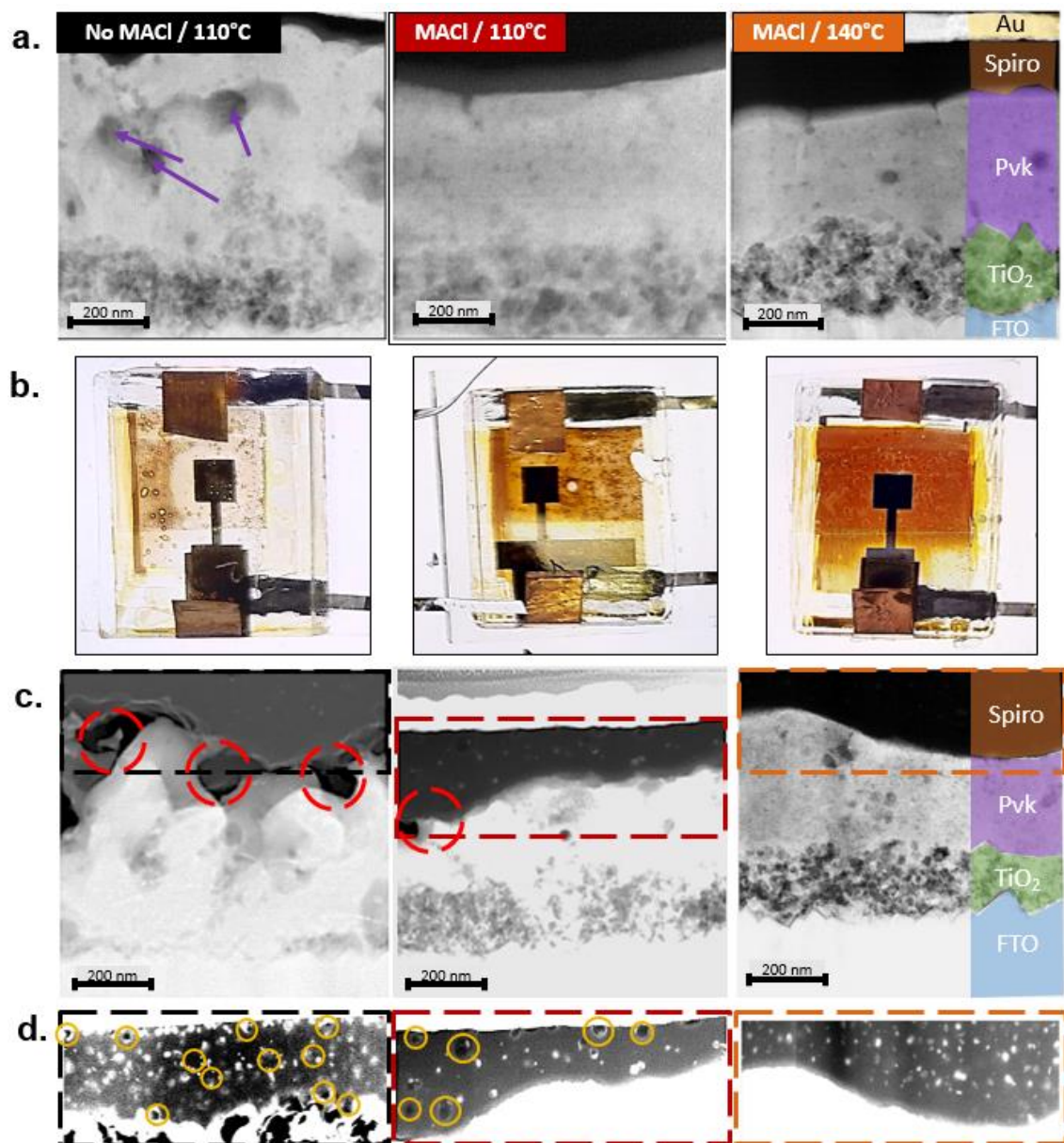


Figure III-26: **a.** STEM-HAADF images of fresh devices. **b.** Images of the aged encapsulated solar cell after 350h under continuous illumination. **c.** STEM-HAADF images of devices aged

under continuous illumination during 350 hours. **d.** Contrasted STEM-HAADF images showing the Spiro-OMeTAD layer. The perovskite layer was fabricated without or with a MACl additive, the reference was annealed at 110°C, and the other devices were annealed at two different temperatures, 110°C, and 140°C.

Figure III-26.a. represent the cross-sections of the fresh devices. Each PSC constitutive layers are visible on the images. The reference device, without MACl additive, exhibits internal pores as indicated by the purple arrows, in accordance with previous top-view SEM observations. Also, in this case, we can observe that the film roughness decreases upon MACl addition.

Then, the same devices have been characterized after ageing under continuous 1-sun illumination. **Figure III-26.b.** represents the encapsulated devices after ageing, and **Figure III-26.c.** displays the cross-sections of these devices. The important change of colour visible in **Figure III-26.b** already marks a clear different state of progress of the degradation of the three devices. In addition, The HAADF images show apparent damages of the interfaces for the device prepared without MACl, particularly at the interface between the perovskite and the HTM leading to voids formed upon ageing as indicated by the red circles (**Figure III-26.c**). These voids seem promoted by the initial high roughness of the film's surface since they can be avoided if the film is prepared with MACl additive and crystallized at 140°C to reach the smoothest surface. Lee *et al.* evidenced that the poor adhesion at the Spiro-OMeTAD/perovskite interface is due to weak interactions as well as a hardening of the film by an accumulation of additives at this interface.³⁸ Moreover, Wei *et al.* observed a photo-degradation of the chemical contact between Spiro-OMeTAD and Au at the interface under continuous illumination.³⁹

By adjusting the contrast on the HAADF images (**Figure III-26.d**) the presence of pinholes is also detected in the Spiro-OMeTAD layer after ageing (yellow circles). This indicates degradations in the bulk of the HTL. S. Cacovich *et al.* related the presence of such defects due to the gold diffusion during the device's ageing.⁴⁰ Consequently, the HTL undergoing such severe morphological deformations can decrease the charge-carriers collection by forming energy barriers chapter.^{41,42} Interestingly, no voids are observed for the 140°C annealing condition, which can be at the origin of the improved device stability.

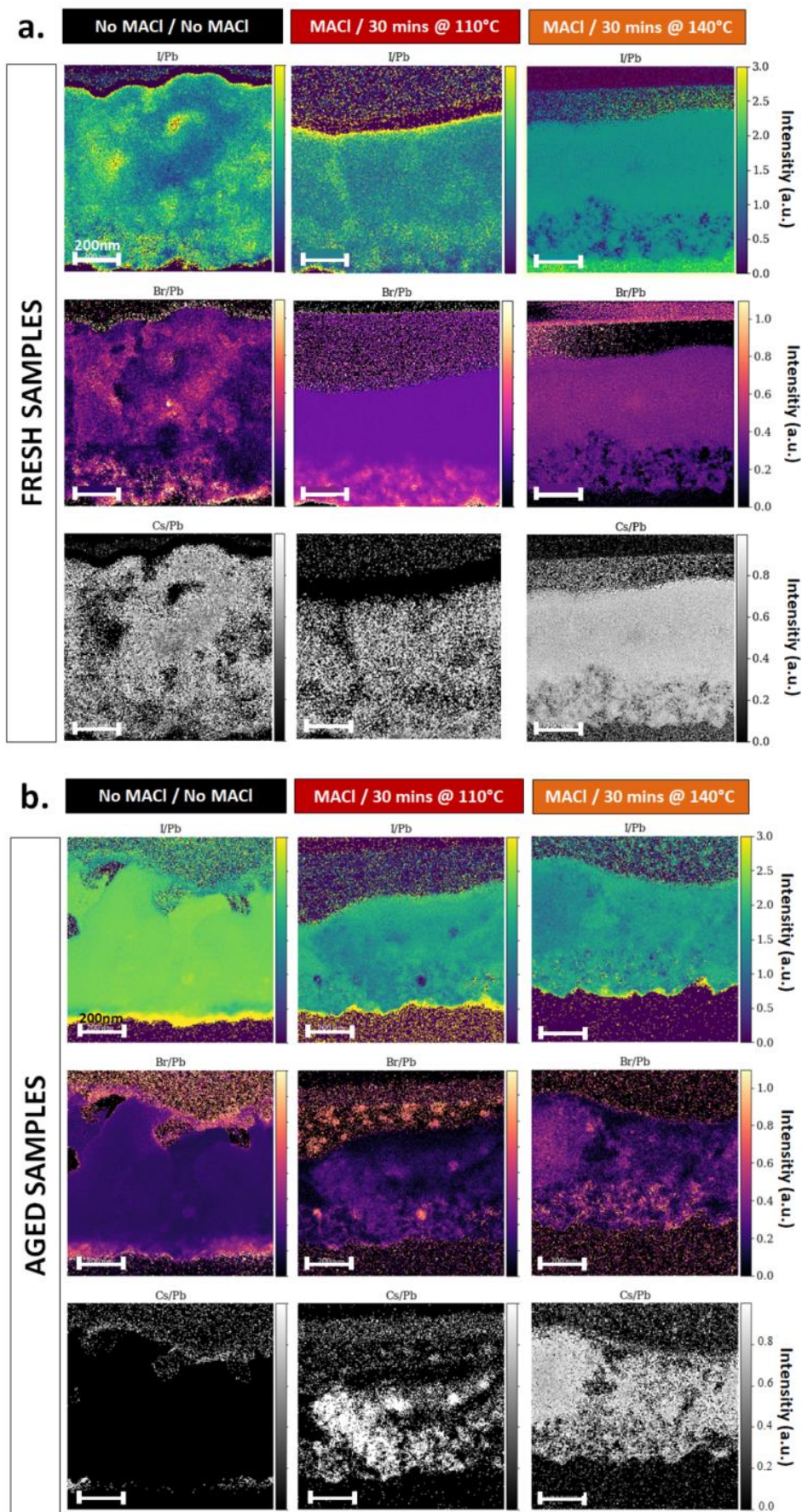


Figure III-27: Characterisation of the perovskite layer in a complete device by STEM-HAADF with MACl addition. The scale represents the normalized intensity **a.** Images of fresh devices. **b.** Images of the device after 300 hours of ageing under illumination. For the measurements, the acceleration voltage was kept at 200 kV, and the current was kept < 500 pA during EDS and HAADF acquisition.

The elemental distribution in the perovskite absorber layer of the best performing cell before and after ageing has been carried out by Energy Dispersive X-ray Spectroscopy (EDS) in STEM mode (**Figure III-27**).

The results on fresh samples, presented in **Figure III-27.a**, show a homogeneous elemental distribution of halides to lead ratio, which remains fairly constant across the thickness for the devices fabricating with MACl. However, the fresh reference device already presents heterogeneities in iodide, bromide, and cesium distributions.

After the ageing under illumination, new STEM-HAADF measurements have been carried out on the encapsulated samples (**Figure III-27.b**). This time, both I rich and Br rich regions in the perovskite layer are detected for all devices, suggesting an elemental segregation⁴³ also visible by X-ray diffraction showing the formation of new phases as indicated by new diffraction peaks (**Figure III-28**).

The variation of iodine intensity for the aged reference device suggests the degradation of the perovskite layer into PbI_2 . The XRD peaks of the PbI_2 are visible on the x-ray diffractograms displayed in **Figure III-28** for both the reference sample without MACl and the MACl sample annealed at 110°C. Though, it is not visible for the sample annealed at 140°C. In addition, it is possible to observe I-rich region at the interface between the perovskite and TiO_2 for all conditions, suggesting a preferential iodide migration phenomena to this interface.⁴⁴

On the contrary, some local bromide-rich regions are visible principally in the bulk of the perovskite layer on the STEM-HAADF images. Phase segregation induced by light is a phenomenon reported in the literature and ascribed to the metastability of multi-cations / multi-anions composition in the perovskite structure.⁴⁵⁻⁵¹ The wider bandgap regions in the bromide-rich phase may affect the V_{OC} and charge transport⁵², inducing a significant drop in the device efficiency, similar to the one observed in the previous **part 4.3**. However, the average low intensity of the Br/Pb signal instead suggests an overall depletion of bromide content in the layer.

On the x-ray diffractograms performed on fresh devices and aged devices (**Figure III-28**), new peaks at $2\theta = 25.1^\circ$, $2\theta = 25.5^\circ$, and $2\theta = 26.9^\circ$ and 27.3° have been ascribed to CsPbI_3 .⁵³ Interestingly, the intensity of XRD peaks attributed to the perovskite structure $\text{Cs}_{0.17}\text{FA}_{0.83}\text{Pb}(\text{I}_{0.83}\text{Br}_{0.17})_3$ has drastically decreased in intensity in the case of the reference sample. The peak at $2\theta = 14.1^\circ$ corresponding to the (100) direction has almost disappeared after ageing. In addition, the STEM-HAADF signal intensity associated with Cs content is very low for the reference sample, suggesting the diffusion or the evaporation of the inorganic components of the perovskite. This is consistent with the low intensity of the XRD peaks of CsPbI_3 . The diminution of the intensity of the XRD peaks

attributed to the perovskite structure is also visible for the samples prepared with MACl, however, to a lower extent. It points out the significant role of both the annealing temperature and the MACl addition to stabilize the α -phase.⁵⁴

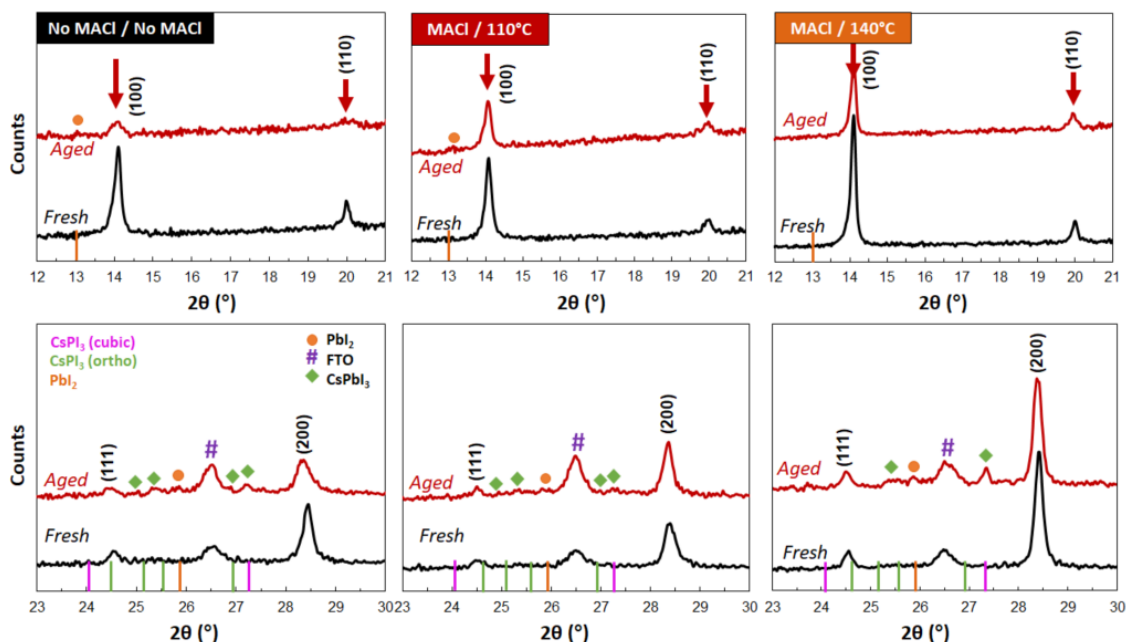


Figure III-28: Comparison of X-ray diffractograms of fresh (black curves) and aged (red curves) perovskite devices. The X-ray measurements on the fresh devices have been performed on half cell (glass/FTO/c-TiO₂/m-TiO₂/pvk) and collected two days after the deposition. The measurements on aged devices were performed on full devices (glass/FTO/c-TiO₂/m-TiO₂/pvk/spiro-OMeTAD/Au) after the end of ageing.

After refining the diffractograms, we noticed a slight increase of the lattice parameters highlighted by the left shift of the XRD peaks, from 6.277 Å to 6.292 Å for the reference sample without MACl, from 6.287 Å to 6.302 Å for the sample with MACl annealed at 110°C and from 6.280 Å to 6.295 Å for the sample with MACl annealed at 140°C (**Table III-5**). This result suggests a change in the perovskite stoichiometry after ageing.

Such morphological and compositional changes were already observed by S. Kundu *et al.*⁵⁵ and were directly related to a light and moisture-induced decomposition of the perovskite layer. These results suggest that the encapsulation process needs to be optimized to isolate the perovskite devices properly.

Table III-5: XRD calculated parameters from fitted XRD diffractograms. With and without MACl, before and after the ageing

	MACl: FAI	Annealing	a (Å)	(100)/(110)
Fresh	0	110°C	6.276 (9)	3.6
	0.3		6.287 (9)	5.8
	0.3	140°C	6.280 (8)	5.4
Aged	0	110°C	6.292 (7)	2.2
	0.3		6.302 (3)	4.9
	0.3	140°C	6.295 (7)	5.3

5. Conclusions

To conclude this chapter, we highlighted in our study the major difference between two different solvent extraction methods: a traditional anti-solvent dripping and a vacuum quench. We demonstrated that the quench method has a significant impact on the final film's morphology and thus that the ink composition must be tailored accordingly. For this reason, we developed an ink composition containing methylammonium chloride as an additive into the perovskite precursor solution.

We explored different MACl concentrations and annealing conditions for optimizing the performances. The impact of these parameters on the opto-electronic properties of the perovskite film have been thoroughly investigated. This approach led us to reach a stabilized PCE of 17.5 % on a small-scale device fabricated with slot-die coating.

By selecting a (MACl: FAI) molar ratio of (0.3: 1) combined with annealing at 140°C for 30 minutes, we achieved an efficiency of 15.7% for a module of 12cm². However, this encouraging result must be mitigated due to the large distribution of the modules' efficiency, pointing out the need for further optimizations.

Stability is also an important characteristic for large-scale applications. We encapsulated the fabricated devices and monitored the PCE evolution during 300 hours under continuous illumination and at maximum power point. Our study underlines the beneficial impact of MACl addition on devices stability. The degradation of the perovskite stack was further investigated by STEM technique and allowed us to identify some degradation paths, notably the spiro-OMeTAD bulk degradation and the depletion of Cesium during the aging. The replacement of the spiro-OMeTAD for a PTAA layer could address this issue and enhance the stability of the device. This aspect will be discussed in the next chapter.

Overall, this work unveils the potential of one-step slot-die-coated perovskite as a means of upscaling PSCs using industry-compatible techniques.

6. References

- (1) Williams, S. T.; Zuo, F.; Chueh, C.-C.; Liao, C.-Y.; Liang, P.-W. Role of Chloride in the Morphological Evolution of Organo-Lead Halide Perovskite Thin Films. *2014*, *8* (10), 15.
- (2) Colella, S.; Mosconi, E.; Fedeli, P.; Listorti, A.; Gazza, F.; Orlandi, F.; Ferro, P.; Besagni, T.; Rizzo, A.; Calestani, G.; Gigli, G.; Angelis, F. D.; Mosca, R. MAPbI₃-xCl_x Mixed Halide Perovskite for Hybrid Solar Cells: The Role of Chloride as Dopant on the Transport and Structural Properties. *Chem Mater* **2013**, *6*.
- (3) Song, Z.; Chen, C.; Li, C.; Awni, R. A.; Zhao, D.; Yan, Y. Wide-Bandgap, Low-Bandgap, and Tandem Perovskite Solar Cells. *Semicond. Sci. Technol.* **2019**, *34* (9), 093001. <https://doi.org/10.1088/1361-6641/ab27f7>.
- (4) Cheng, F.; Jing, X.; Chen, R.; Cao, J.; Yan, J.; Wu, Y.; Huang, X.; Wu, B.; Zheng, N. *N*-Methyl-2-Pyrrolidone as an Excellent Coordinative Additive with a Wide Operating Range for Fabricating High-Quality Perovskite Films. *Inorg. Chem. Front.* **2019**, *6* (9), 2458–2463. <https://doi.org/10.1039/C9QI00547A>.
- (5) Li, C.; Zhou, Y.; Wang, L.; Chang, Y.; Zong, Y.; Etgar, L.; Cui, G.; Padture, N. P.; Pang, S. Methylammonium-Mediated Evolution of Mixed-Organic-Cation Perovskite Thin Films: A Dynamic Composition-Tuning Process. *Angew. Chem. Int. Ed.* **2017**, *56* (26), 7674–7678. <https://doi.org/10.1002/anie.201704188>.
- (6) Li, Y.; Zhang, T.; Xu, F.; Wang, Y.; Li, G.; Yang, Y.; Zhao, Y. CH₃NH₃Cl Assisted Solvent Engineering for Highly Crystallized and Large Grain Size Mixed-Composition (FAPbI₃)_{0.85}(MAPbBr₃)_{0.15} Perovskites. *Crystals* **2017**, *7* (9), 272. <https://doi.org/10.3390/cryst7090272>.
- (7) Mateen, M.; Arain, Z.; Yang, Y.; Liu, X.; Ma, S.; Liu, C.; Ding, Y.; Ding, X.; Cai, M.; Dai, S. MAcl-Induced Intermediate Engineering for High-Performance Mixed-Cation Perovskite Solar Cells. *ACS Appl. Mater. Interfaces* **2020**, *12* (9), 10535–10543. <https://doi.org/10.1021/acsami.9b22719>.
- (8) Chen, A. Z.; Choi, J. J. Crystallographic Orientation and Layer Impurities in Two-Dimensional Metal Halide Perovskite Thin Films. *J. Vac. Sci. Technol. A* **2020**, *38* (1), 010801. <https://doi.org/10.1116/1.5126738>.
- (9) Bouchard, M.; Hilhorst, J.; Pouget, S.; Alam, F.; Mendez, M.; Djurado, D.; Aldakov, D.; Schüllli, T.; Reiss, P. Direct Evidence of Chlorine-Induced Preferential Crystalline Orientation in Methylammonium Lead Iodide Perovskites

- Grown on TiO₂. *J. Phys. Chem. C* **2017**, *121* (14), 7596–7602. <https://doi.org/10.1021/acs.jpcc.6b11529>.
- (10) Odysseas Kosmatos, K.; Theofylaktos, L.; Giannakaki, E.; Deligiannis, D.; Konstantakou, M.; Stergiopoulos, T. Methylammonium Chloride: A Key Additive for Highly Efficient, Stable, and Up-Scalable Perovskite Solar Cells. *ENERGY Environ. Mater.* **2019**, *2* (2), 79–92. <https://doi.org/10.1002/eem2.12040>.
- (11) Guo, F.; Qiu, S.; Hu, J.; Wang, H.; Cai, B.; Li, J.; Yuan, X.; Liu, X.; Forberich, K.; Brabec, C. J.; Mai, Y. A Generalized Crystallization Protocol for Scalable Deposition of High-Quality Perovskite Thin Films for Photovoltaic Applications. *Adv. Sci.* **2019**, *6* (17), 1901067. <https://doi.org/10.1002/advs.201901067>.
- (12) Fan, L.; Ding, Y.; Luo, J.; Shi, B.; Yao, X.; Wei, C.; Zhang, D.; Wang, G.; Sheng, Y.; Chen, Y.; Hagfeldt, A.; Zhao, Y.; Zhang, X. Elucidating the Role of Chlorine in Perovskite Solar Cells. *J. Mater. Chem. A* **2017**, *5* (16), 7423–7432. <https://doi.org/10.1039/C7TA00973A>.
- (13) Dualeh, A.; Tétreault, N.; Moehl, T.; Gao, P.; Nazeeruddin, M. K.; Grätzel, M. Effect of Annealing Temperature on Film Morphology of Organic-Inorganic Hybrid Perovskite Solid-State Solar Cells. *Adv. Funct. Mater.* **2014**, *24* (21), 3250–3258. <https://doi.org/10.1002/adfm.201304022>.
- (14) Lee, J.-W.; Tan, S.; Han, T.-H.; Wang, R.; Zhang, L.; Park, C.; Yoon, M.; Choi, C.; Xu, M.; Liao, M. E.; Lee, S.-J.; Nuryyeva, S.; Zhu, C.; Huynh, K.; Goorsky, M. S.; Huang, Y.; Pan, X.; Yang, Y. Solid-Phase Hetero Epitaxial Growth of α -Phase Formamidinium Perovskite. *Nat. Commun.* **2020**, *11* (1), 5514. <https://doi.org/10.1038/s41467-020-19237-3>.
- (15) Guo, F.; Qiu, S.; Hu, J.; Wang, H.; Cai, B.; Li, J.; Yuan, X.; Liu, X.; Forberich, K.; Brabec, C. J.; Mai, Y. A Generalized Crystallization Protocol for Scalable Deposition of High-Quality Perovskite Thin Films for Photovoltaic Applications. *Adv. Sci.* **2019**, *6* (17), 1901067. <https://doi.org/10.1002/advs.201901067>.
- (16) Guo, Y.; Yuan, S.; Zhu, D.; Yu, M.; Wang, H.-Y.; Lin, J.; Wang, Y.; Qin, Y.; Zhang, J.-P.; Ai, X.-C. Influence of the MA₂Cl Additive on Grain Boundaries, Trap-State Properties, and Charge Dynamics in Perovskite Solar Cells. *Phys. Chem. Chem. Phys.* **2021**, *23* (10), 6162–6170. <https://doi.org/10.1039/D0CP06575G>.
- (17) Nishimura, K.; Hirotsu, D.; Kamarudin, M. A.; Shen, Q.; Toyoda, T.; Iikubo, S.; Minemoto, T.; Yoshino, K.; Hayase, S. Relationship between Lattice Strain and Efficiency for Sn-Perovskite Solar Cells. *ACS Appl. Mater. Interfaces* **2019**, *11* (34), 31105–31110. <https://doi.org/10.1021/acsami.9b09564>.

- (18) Kim, G.; Min, H.; Lee, K. S.; Lee, D. Y.; Yoon, S. M.; Seok, S. I. Impact of Strain Relaxation on Performance of α -Formamidinium Lead Iodide Perovskite Solar Cells. *Science* **2020**, *370* (6512), 108–112. <https://doi.org/10.1126/science.abc4417>.
- (19) Lee, B.; Hwang, T.; Lee, S.; Shin, B.; Park, B. Microstructural Evolution of Hybrid Perovskites Promoted by Chlorine and Its Impact on the Performance of Solar Cell. *Sci. Rep.* **2019**, *9* (1), 4803. <https://doi.org/10.1038/s41598-019-41328-5>.
- (20) Kim, M.; Kim, G.-H.; Oh, K. S.; Jo, Y.; Yoon, H.; Kim, K.-H.; Lee, H.; Kim, J. Y.; Kim, D. S. High-Temperature–Short-Time Annealing Process for High-Performance Large-Area Perovskite Solar Cells. *ACS Nano* **2017**, *11* (6), 6057–6064. <https://doi.org/10.1021/acsnano.7b02015>.
- (21) Xie, F. Vertical Recrystallization for Highly Efficient and Stable Formamidinium-Based Inverted-Structure Perovskite Solar Cells. *Environ. Sci.* **2017**, *8*.
- (22) You, H.; Fang, J. Particle-Mediated Nucleation and Growth of Solution-Synthesized Metal Nanocrystals: A New Story beyond the LaMer Curve. *Nano Today* **2016**, *11* (2), 145–167. <https://doi.org/10.1016/j.nantod.2016.04.003>.
- (23) Schade, H.; Smith, Z. E. Mie Scattering and Rough Surfaces. *Appl. Opt.* **1985**, *24* (19), 3221–3226. <https://doi.org/10.1364/AO.24.003221>.
- (24) Rajagopal, A.; Liang, P.-W.; Chueh, C.-C.; Yang, Z.; Jen, A. K.-Y. Defect Passivation via a Graded Fullerene Heterojunction in Low-Bandgap Pb–Sn Binary Perovskite Photovoltaics. *ACS Energy Lett.* **2017**, *2* (11), 2531–2539. <https://doi.org/10.1021/acseenergylett.7b00847>.
- (25) Katahara, J. K.; Hillhouse, H. W. Quasi-Fermi Level Splitting and Sub-Bandgap Absorptivity from Semiconductor Photoluminescence. *J. Appl. Phys.* **2014**, *116* (17), 173504. <https://doi.org/10.1063/1.4898346>.
- (26) Cacovich, S.; Messou, D.; Bercegol, A.; Béchu, S.; Yaiche, A.; Shafique, H.; Rousset, J.; Schulz, P.; Bouttemy, M.; Lombez, L. Light-Induced Passivation in Triple Cation Mixed Halide Perovskites: Interplay between Transport Properties and Surface Chemistry. *ACS Appl. Mater. Interfaces* **2020**, *12* (31), 34784–34794. <https://doi.org/10.1021/acсами.0c06844>.
- (27) Wang, R.; Huang, T.; Xue, J.; Tong, J.; Zhu, K.; Yang, Y. Prospects for Metal Halide Perovskite-Based Tandem Solar Cells. *Nat. Photonics* **2021**, *15* (6), 411–425. <https://doi.org/10.1038/s41566-021-00809-8>.

- (28) Kaiser, W.; Radicchi, E.; Mosconi, E.; Kachmar, A.; De Angelis, F. Iodide vs Chloride: The Impact of Different Lead Halides on the Solution Chemistry of Perovskite Precursors. *ACS Appl. Energy Mater.* **2021**, *4* (9), 9827–9835. <https://doi.org/10.1021/acsaem.1c01874>.
- (29) Xiao, C.; Li, Z.; Guthrey, H.; Moseley, J.; Yang, Y.; Wozny, S.; Moutinho, H.; To, B.; Berry, J. J.; Gorman, B.; Yan, Y.; Zhu, K.; Al-Jassim, M. Mechanisms of Electron-Beam-Induced Damage in Perovskite Thin Films Revealed by Cathodoluminescence Spectroscopy. *J Phys Chem C* **2015**, *8*.
- (30) Paul, T.; Chatterjee, B. K.; Maiti, S.; Sarkar, S.; Besra, N.; Das, B. K.; Panigrahi, K. J.; Thakur, S.; Ghorai, U. K.; Chattopadhyay, K. K. Tunable Cathodoluminescence over the Entire Visible Window from All-Inorganic Perovskite CsPbX₃ 1D Architecture. *J. Mater. Chem. C* **2018**, *6* (13), 3322–3333. <https://doi.org/10.1039/C7TC05703B>.
- (31) Diab, H.; Arnold, C.; Lédée, F.; Trippé-Allard, G.; Delport, G.; Vilar, C.; Bretenaker, F.; Barjon, J.; Lauret, J.-S.; Deleporte, E.; Garrot, D. Impact of Reabsorption on the Emission Spectra and Recombination Dynamics of Hybrid Perovskite Single Crystals. *J. Phys. Chem. Lett.* **2017**, *8* (13), 2977–2983. <https://doi.org/10.1021/acs.jpcclett.7b00998>.
- (32) Tripathi, N.; Yanagida, M.; Shirai, Y.; Masuda, T.; Han, L.; Miyano, K. Hysteresis-Free and Highly Stable Perovskite Solar Cells Produced via a Chlorine-Mediated Interdiffusion Method. *J. Mater. Chem. A* **2015**, *3* (22), 12081–12088. <https://doi.org/10.1039/C5TA01668A>.
- (33) Aidarkhanov, D.; Ren, Z.; Lim, C.-K.; Yelzhanova, Z.; Nigmatova, G.; Taltanova, G.; Bapayev, B.; Liu, F.; Cheung, S. H.; Balanay, M.; Baumuratov, A.; Djurišić, A. B.; So, S. K.; Surya, C.; Prasad, P. N.; Ng, A. Passivation Engineering for Hysteresis-Free Mixed Perovskite Solar Cells. *Sol. Energy Mater. Sol. Cells* **2020**, *215*, 110648. <https://doi.org/10.1016/j.solmat.2020.110648>.
- (34) Hanmandlu, C.; Swamy, S.; Singh, A.; Chen, H.-A.; Liu, C.-C.; Lai, C.-S.; Mohapatra, A.; Pao, C.-W.; Chen, P.; Chu, C.-W. Suppression of Surface Defects to Achieve Hysteresis-Free Inverted Perovskite Solar Cells via Quantum Dot Passivation. *J. Mater. Chem. A* **2020**, *8* (10), 5263–5274. <https://doi.org/10.1039/C9TA12904A>.
- (35) Moon, S.; Yum, J.; Löfgren, L.; Walter, A.; Sansonnens, L.; Benkhaira, M.; Nicolay, S.; Bailat, J.; Ballif, C. Laser-Scribing Patterning for the Production of Organometallic Halide Perovskite Solar Modules. *IEEE J. Photovolt.* **2015**, *5* (4), 1087–1092. <https://doi.org/10.1109/JPHOTOV.2015.2416913>.

- (36) Lee, D.; Jung, Y.-S.; Heo, Y.-J.; Lee, S.; Hwang, K.; Jeon, Y.-J.; Kim, J.-E.; Park, J.; Jung, G. Y.; Kim, D.-Y. Slot-Die Coated Perovskite Films Using Mixed Lead Precursors for Highly Reproducible and Large-Area Solar Cells. *ACS Appl. Mater. Interfaces* **2018**, *10* (18), 16133–16139. <https://doi.org/10.1021/acsami.8b02549>.
- (37) Di Giacomo, F.; Shanmugam, S.; Fledderus, H.; Bruijnaers, B. J.; Verhees, W. J. H.; Dorenkamper, M. S.; Veenstra, S. C.; Qiu, W.; Gehlhaar, R.; Merckx, T.; Aernouts, T.; Andriessen, R.; Galagan, Y. Up-Scalable Sheet-to-Sheet Production of High Efficiency Perovskite Module and Solar Cells on 6-in. Substrate Using Slot Die Coating. *Sol. Energy Mater. Sol. Cells* **2018**, *181*, 53–59. <https://doi.org/10.1016/j.solmat.2017.11.010>.
- (38) Yun, J. H.; Lee, I.; Kim, T.-S.; Ko, M. J.; Kim, J. Y.; Son, H. J. Synergistic Enhancement and Mechanism Study of Mechanical and Moisture Stability of Perovskite Solar Cells Introducing Polyethylene-Imine into the CH₃NH₃PbI₃/HTM Interface. *J. Mater. Chem. A* **2015**, *3* (44), 22176–22182. <https://doi.org/10.1039/C5TA06008G>.
- (39) Wei, D.; Wang, T.; Ji, J.; Li, M.; Cui, P.; Li, Y.; Li, G.; Mbengue, J. M.; Song, D. Photo-Induced Degradation of Lead Halide Perovskite Solar Cells Caused by the Hole Transport Layer/Metal Electrode Interface. *J. Mater. Chem. A* **2016**, *4* (5), 1991–1998. <https://doi.org/10.1039/C5TA08622A>.
- (40) Cacovich, S. Electron Microscopy Studies of Hybrid Perovskite Solar Cells. Thesis, University of Cambridge, 2018. <https://doi.org/10.17863/CAM.24048>.
- (41) Kim, S.; Bae, S.; Lee, S.-W.; Cho, K.; Lee, K. D.; Kim, H.; Park, S.; Kwon, G.; Ahn, S.-W.; Lee, H.-M.; Kang, Y.; Lee, H.-S.; Kim, D. Relationship between Ion Migration and Interfacial Degradation of CH₃NH₃PbI₃ Perovskite Solar Cells under Thermal Conditions. *Sci. Rep.* **2017**, *7* (1), 1200. <https://doi.org/10.1038/s41598-017-00866-6>.
- (42) Jena, A. K.; Numata, Y.; Ikegami, M.; Miyasaka, T. Role of Spiro-OMeTAD in Performance Deterioration of Perovskite Solar Cells at High Temperature and Reuse of the Perovskite Films to Avoid Pb-Waste. *J. Mater. Chem. A* **2018**, *6* (5), 2219–2230. <https://doi.org/10.1039/C7TA07674F>.
- (43) Rehman, W.; McMeekin, D. P.; Patel, J. B.; Milot, R. L.; Johnston, M. B.; Snaith, H. J.; Herz, L. M. Photovoltaic Mixed-Cation Lead Mixed-Halide Perovskites: Links between Crystallinity, Photo-Stability and Electronic Properties. *Energy Environ. Sci.* **2017**, *10* (1), 361–369. <https://doi.org/10.1039/C6EE03014A>.

- (44) Divitini, G.; Cacovich, S.; Matteocci, F.; Cinà, L.; Di Carlo, A.; Ducati, C. In Situ Observation of Heat-Induced Degradation of Perovskite Solar Cells. *Nat. Energy* **2016**, *1* (2), 15012. <https://doi.org/10.1038/nenergy.2015.12>.
- (45) Hoke, E. T.; Slotcavage, D. J.; Dohner, E. R.; Bowring, A. R.; Karunadasa, H. I.; McGehee, M. D. Reversible Photo-Induced Trap Formation in Mixed-Halide Hybrid Perovskites for Photovoltaics. *Chem. Sci.* **2015**, *6* (1), 613–617. <https://doi.org/10.1039/C4SC03141E>.
- (46) Bischak, C. G.; Hetherington, C. L.; Wu, H.; Aloni, S.; Ogletree, D. F.; Limmer, D. T.; Ginsberg, N. S. Origin of Reversible Photoinduced Phase Separation in Hybrid Perovskites. *Nano Lett.* **2017**, *17* (2), 1028–1033. <https://doi.org/10.1021/acs.nanolett.6b04453>.
- (47) Yoon, S. J.; Draguta, S.; Manser, J. S.; Sharia, O.; Schneider, W. F.; Kuno, M.; Kamat, P. V. Tracking Iodide and Bromide Ion Segregation in Mixed Halide Lead Perovskites during Photoirradiation. *ACS Energy Lett.* **2016**, *1* (1), 290–296. <https://doi.org/10.1021/acsenergylett.6b00158>.
- (48) Draguta, S.; Sharia, O.; Yoon, S. J.; Brennan, M. C.; Morozov, Y. V.; Manser, J. S.; Kamat, P. V.; Schneider, W. F.; Kuno, M. Rationalizing the Light-Induced Phase Separation of Mixed Halide Organic–Inorganic Perovskites. *Nat. Commun.* **2017**, *8* (1), 200. <https://doi.org/10.1038/s41467-017-00284-2>.
- (49) Bush, K. A.; Frohna, K.; Prasanna, R.; Beal, R. E.; Leijtens, T.; Swifter, S. A.; McGehee, M. D. Compositional Engineering for Efficient Wide Band Gap Perovskites with Improved Stability to Photoinduced Phase Segregation. *ACS Energy Lett.* **2018**, *3* (2), 428–435. <https://doi.org/10.1021/acsenergylett.7b01255>.
- (50) Kumar, V.; Schmidt, W. L.; Schileo, G.; Masters, R. C.; Wong-Stringer, M.; Sinclair, D. C.; Reaney, I. M.; Lidzey, D.; Rodenburg, C. Nanoscale Mapping of Bromide Segregation on the Cross Sections of Complex Hybrid Perovskite Photovoltaic Films Using Secondary Electron Hyperspectral Imaging in a Scanning Electron Microscope. *ACS Omega* **2017**, *2* (5), 2126–2133. <https://doi.org/10.1021/acsomega.7b00265>.
- (51) Duong, T.; Mulmudi, H. K.; Wu, Y.; Fu, X.; Shen, H.; Peng, J.; Wu, N.; Nguyen, H. T.; Macdonald, D.; Lockrey, M.; White, T. P.; Weber, K.; Catchpole, K. Light and Electrically Induced Phase Segregation and Its Impact on the Stability of Quadruple Cation High Bandgap Perovskite Solar Cells. *ACS Appl. Mater. Interfaces* **2017**, *9* (32), 26859–26866. <https://doi.org/10.1021/acsami.7b06816>.

- (52) Hentz, O.; Zhao, Z.; Gradečak, S. Impacts of Ion Segregation on Local Optical Properties in Mixed Halide Perovskite Films. *Nano Lett.* **2016**, *16* (2), 1485–1490. <https://doi.org/10.1021/acs.nanolett.5b05181>.
- (53) Jain, A.; Ong, S. P.; Hautier, G.; Chen, W.; Richards, W. D.; Dacek, S.; Cholia, S.; Gunter, D.; Skinner, D.; Ceder, G.; Persson, K. A. Commentary: The Materials Project: A Materials Genome Approach to Accelerating Materials Innovation. *APL Mater.* **2013**, *1* (1), 011002. <https://doi.org/10.1063/1.4812323>.
- (54) Haque, F.; Yi, H.; Duan, L.; Zhang, Y.; Wright, M.; Conibeer, G.; Uddin, A. Optimisation of Annealing Temperature for Low Temperature Processed Inverted Structure Caesium Formamidinium Lead Triiodide Perovskite Solar Cells. *Mater. Sci. Semicond. Process.* **2019**, *102*, 104580. <https://doi.org/10.1016/j.mssp.2019.06.015>.
- (55) Kundu, S.; Kelly, T. L. In Situ Studies of the Degradation Mechanisms of Perovskite Solar Cells. *EcoMat* **2020**, *2* (2), e12025. <https://doi.org/10.1002/eom2.12025>.

CHAPTER 4:

Synergic action of surfactant and MAcl addition

In the previous chapters, we focused on the influence of two different additives, namely the surfactant 3DPS and MAcl, which were used separately.

In **Chapter 2**, we highlighted the beneficial influence of the zwitterionic 3DPS surfactant to improve the film's morphology and coverage. Following this, in **Chapter 3**, we optimized the MAcl concentration into the precursor solution and reached up to 17% efficiency for small-scale solar cells. In this chapter, we simultaneously introduce these two additives in the perovskite precursor's solution.

In the first part, a MAcl: FAI molar ratio of (0.3:1) is selected, as it is the optimal ratio identified in **Chapter 3**. Then, the concentration of the surfactant into the precursor's solution is gradually increased. The influence of the synergic effect of these additives on the surface roughness, perovskite layer morphology, and crystallinity will be explored.

Perovskite devices with a n-i-p architecture FTO / c-TiO₂ / m-TiO₂ / Cs_{0.17}FA_{0.83}Pb(I_{0.83}Br_{0.17})₃ / HTL / Au are fabricated. We evaluate the device performance and stability and compare two different HTL, the conventional Spiro-OMeTAD layer, and PTAA.

The third part is dedicated to the fabrication of semi-transparent solar cells using either Spiro-OMeTAD or PTAA. Their performance and stability are evaluated.

Finally, we evaluate the potential of our ST cell integrated in a tandem architecture.

The fabrication of the semi-transparent perovskite solar cells, the deposition of the ITO (Indium Tin Oxide) semi-transparent electrode layer by sputtering and the integration process of large perovskite filters in a tandem stack, the work presented in this part has been carried out in close collaboration with several members of IPVF lab.

SUMMARY

1. Morphological and structural analysis.....	141
2. Full devices performances	149
3. Integration in semi-transparent perovskite cells architecture	157
4. Tandem performances projection.....	165
5. Conclusions.....	168
6. References.....	170

1. Morphological and structural analysis

We fabricated two different perovskite samples as control. For the first one (C1), the perovskite layer was fabricated without MACl or 3DPS addition. The second one (C2) was made with a MACl: FAI molar ratio of 0.3:1 without 3DPS. For the other samples, the 3DPS molar ratio was gradually increased, to 0.7 mM, 1.5 mM, 2.3 mM, and 4.6 mM, to find an optimum in conjunction with the MACl.

The MACl and the surfactant were directly added into the perovskite precursor's solution. Then, all the perovskite layers were deposited on Glass/FTO/c-TiO₂/m-TiO₂ by slot-die deposition and dried by vacuum aspiration and subsequent annealing.

1.1. Grain size analysis

The influence of the surfactant addition on the grain size has been evaluated. Top-view SEM images of the different perovskite layers fabricated with and without additives are presented in **Figure IV-1**.

In this batch of samples, the average grain size increases from 215 nm without any additives to 387 nm with a MACl: FAI molar ratio of (0.3:1). This is in good accordance with the results presented in **Chapter 3**. However, the size distribution shows a wide standard variation ($\sigma_{C2} = 180$ nm), thus indicating a high heterogeneity in the grain growth.

A very small quantity of surfactant (0.7 mM) added to MACl does not have any visible impact on the average grain size. The surfactant content is calculated as a molar concentration (0 mM, 0.7 mM, 1.5 mM, 2.3 mM, and 4.6 mM). In both cases, with and without surfactant, the perovskite films showed in **Figure IV-1.b.**, and **c.** show almost the average same grain size of ≈ 380 nm. However, the standard deviation of the films prepared with the surfactant is significantly lower ($\sigma_{0.7\text{mM}} = 116$ nm), thus suggesting a more homogeneous crystal growth owing to a better controlled repartition of the nuclei.

When the surfactant concentration is increased into the perovskite precursors solution, the grain average size increases from 405 nm for a concentration of 1.5 mM to 543 nm for 2.3 mM and 516 nm for 4.6 mM. Interestingly, when no surfactant is added, only 2% of perovskite grains show a diameter larger than 600 nm. This tendency shows a constant augmentation with 3DPS addition. Almost 12% of perovskite grains diameters are larger than 600 nm for 0.7 mM, 14% for 1.5 mM and 42% for 2.3 mM of 3DPS. However, the proportion of large grains decreases to 29% when the surfactant concentration is 4.6 mM. This result highlights the existence of a combined action between MACl and 3DPS, yielding to the formation of larger and uniform perovskite grains.

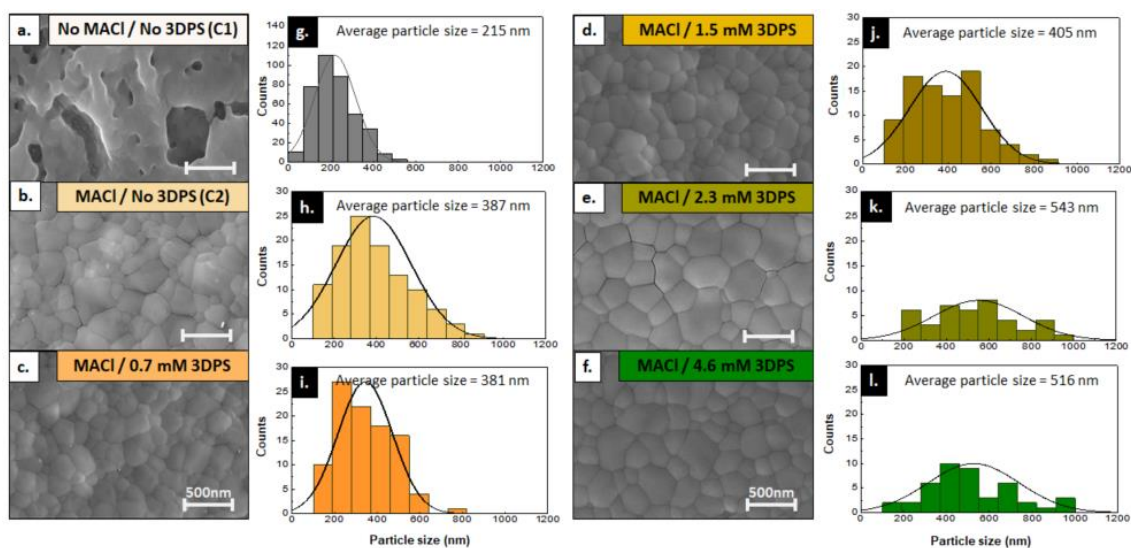


Figure IV-1: a-f. Top-view SEM images of a $CS_{0.17}FA_{0.83}Pb(I_{0.83}Br_{0.17})_3$ perovskite layer deposited on FTO/c-TiO₂/m-TiO₂, with gradual augmentation of surfactant 3DPS concentration. **g-l.** Particle size distributions.

1.2. Surface roughness analysis

The confocal image of the control sample C1, displayed in **Figure IV-2.a**, shows a very rough surface. The 3D capture of the surface highlights the presence of numerous pinholes (blue areas) on the whole surface (**Figure IV-2.g**).

In **Chapter 3**, we saw that the surface homogeneity was significantly enhanced with the addition of MACl. However, the perovskite layer still showed numerous surface “dots” important local surface roughness, visible as black points on the confocal image of sample C2 (**Figure IV-2.b**) and highlighted by red circles on confocal images. The 3D acquisition in **Figure IV-2.h** confirms that the dots are high-intensity points, with a height of a few hundred nanometers.

With the gradual addition of surfactant, the perovskite surface presents a more homogeneous and smoother aspect, visible in **Figure IV-2.c-f**. Neither blue area, characteristic of pinholes presence nor particles appear on the surface when the surfactant concentration is higher than 1.5 mM.

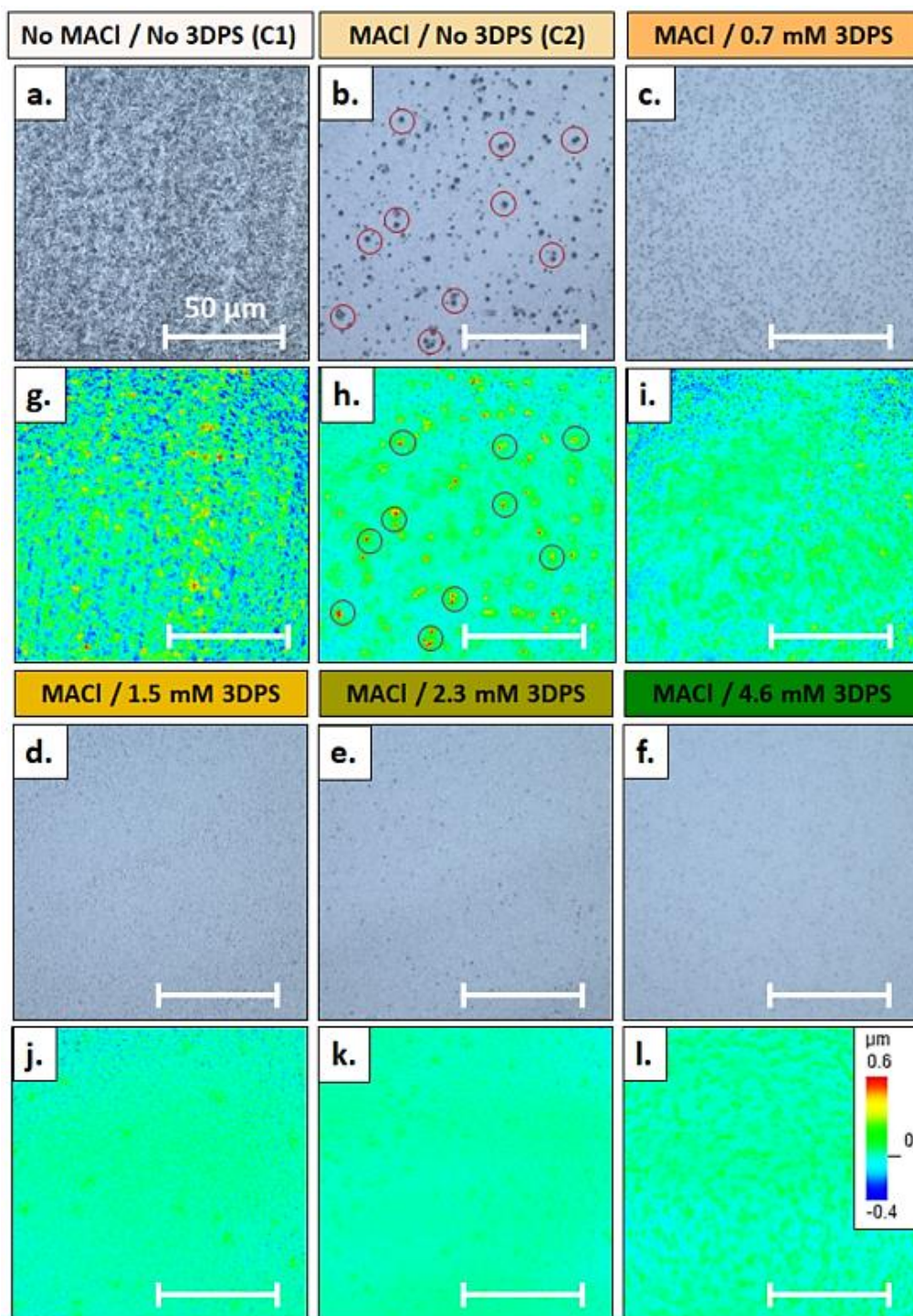


Figure IV-2: a-f. Confocal images of the perovskite surface. g-l. 3D acquisition of the surface roughness.

To assess the homogeneity of the layers, the distribution of the roughness heights and the Sa values were extracted from the 3D surface acquisition image (**Figure IV-3.a and b.**). For the C1 control sample, the distribution is very broad due to the heterogeneity of the perovskite film. The calculated average surface roughness (Sa_{C1}) is 124 nm.

If we compare with the effect of MACl addition alone explored in the previous chapter, this value is significantly lowered to $S_{aC2} = 56$ nm. The standard deviation of height distribution decrease concomitantly from $\sigma_{C1} = 0.12$ μm to $\sigma_{C2} = 0.046$ μm , indicating an improvement of the surface homogeneity together with the roughness decrease.

Interestingly, with the surfactant addition, surface roughness together with the standard deviations continues to decrease from $S_{a0.7\text{mM}} = 51$ nm ($\sigma_{0.7\text{mM}} = 0.046$ nm) to $S_{a2.3\text{mM}} = 22$ nm ($\sigma_{2.3\text{mM}} = 0.026$ μm), indicating a continuous improvement of the surface homogeneity. This roughness value lies now very close to the surface roughness of the laboratory baseline, $S_a = 17$ nm, when using the spin-coating technique.

However, when the surfactant concentration increases further in the perovskite precursors solution, the final perovskite film displays a $S_{a4.6\text{mM}}$ value of 29 nm. It suggests that the surface roughness diminution induced by surfactant addition meets a threshold at $C_{3\text{DPS}} > 2.3$ mM.

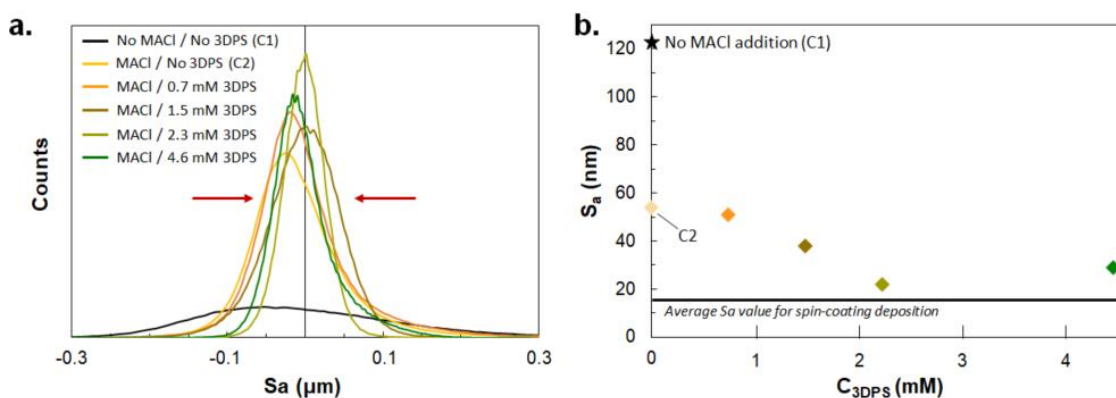


Figure IV-3: a. Distribution of the surface height measurements and, b. Average surface roughness value depending on the concentration of 3DPS surfactant.

The evolution of the perovskite morphology and compactness is observed on cross-section SEM images (**Figure IV-4**). Without additive, the film presents a high porosity inducing numerous pinholes. In **Chapter 3**, we discussed that MACl addition improved the perovskite layer compactness by promoting the growth of larger perovskite grains. However, the “dots” previously observed on the confocal surface images are also herein visible and highlighted by red arrows in **Figure IV-4.b-c**. By measuring the roughness profile of the perovskite layer, dots height can be estimated between 180 nm and up to 500 nm, in comparison to the perovskite layer thickness, which is around $470 \text{ nm} \pm 15$ nm. Their formation can be attributed to the migration of perovskite solutes around the primary nuclei during the island-like growth. As described in **Chapter 1, part. 1.2.**, the formation of nuclei can be promoted by the presence of micro-impurities on the substrate, which creates surface tension gradients and promotes a rapid accumulation of precursors.¹

When the surfactant is combined with MACl, the dots tend to disappear from the perovskite surface gradually. At a surfactant concentration higher than 1.5 mM, no dots are visible on confocal images (Figure IV-2.d-f) or cross-sections images (Figure IV-4. d-f). The associated roughness profiles display flat profiles with low roughness values of $R_a < 35$ nm. According to Y. Deng *et al.*, a small concentration of surfactants can prevent the migration flux of precursors toward the nuclei, avoiding a local over-accumulation of solutes and suppressing the formations of dots.¹ Consequently, the perovskite films fabricated with MACl and surfactant exhibit a smoother surface and improved compactness.

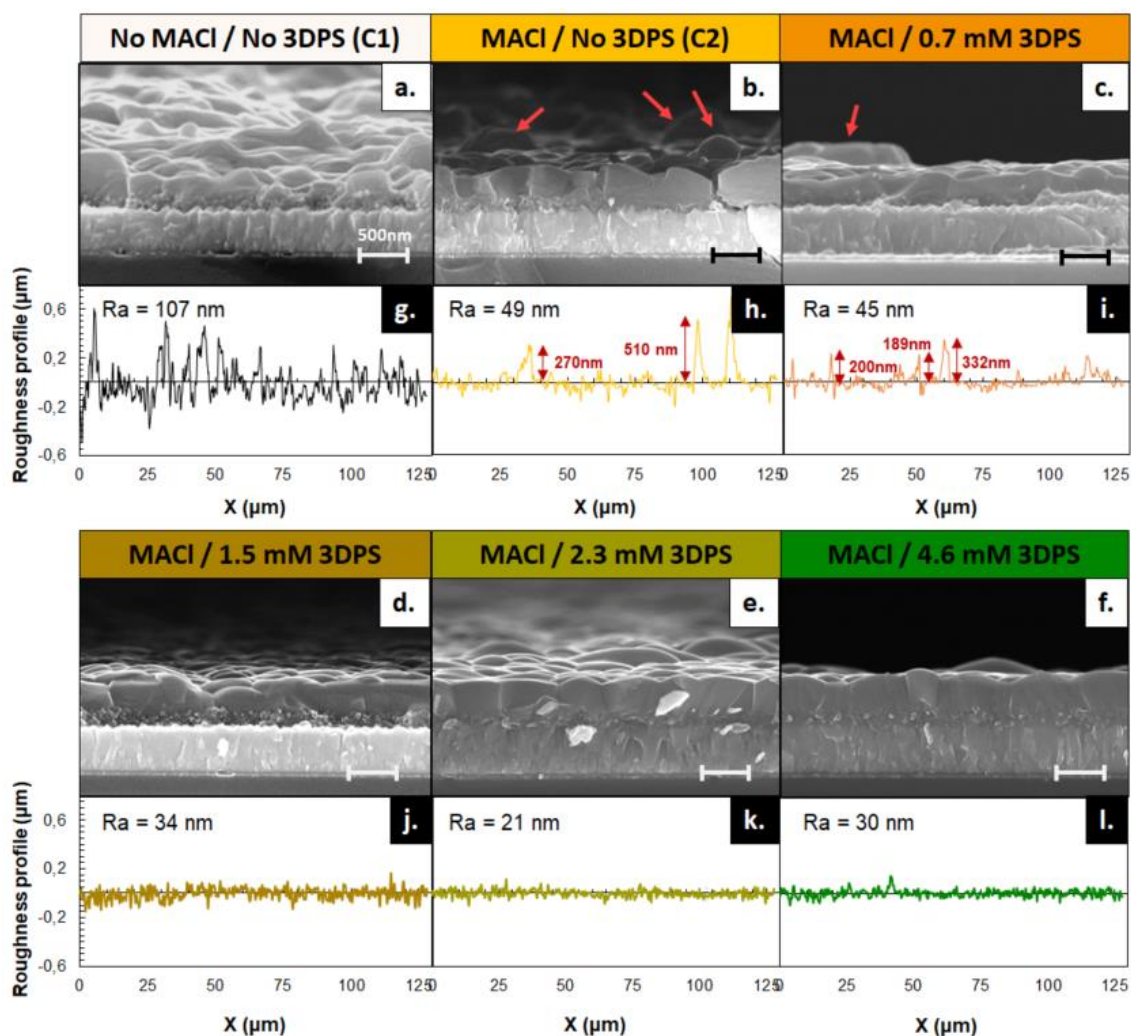


Figure IV-4: a-f. Cross-section SEM images of slot-die coated perovskite layer deposited on FTO/c-TiO₂/m-TiO₂, with different surfactant concentrations, and g-l. Associated roughness profile measured by confocal microscopy.

1.3. Structural analysis of the perovskite films

XRD measurements were performed to investigate the role of the combined utilization of MACl and 3DPS on the perovskite crystallization and grain orientation. The resulting diffractograms are displayed in **Figure IV-5**.

The diffractograms show the pure photoactive α -phase regardless of the ink composition. All the diffraction peaks are indexed by the cubic lattice of Pm-3m space group. All the samples display the characteristic perovskite peaks of (100) and (110) at $2\theta = 14.1^\circ$ and 19.98° , respectively. The surfactant addition induces an increase of the (100) peak intensity. The ratio of (100) and (110) peak intensities for all the conditions explored are reported in **Figure IV-6. a**. For a 3DPS content ranging from 0 to 4.6 mM, the peak intensity ratio increases from 4.9 to 6.7, suggesting that the surface assists an anisotropic particle's growth to privilege a preferential along the (100) crystal plane.

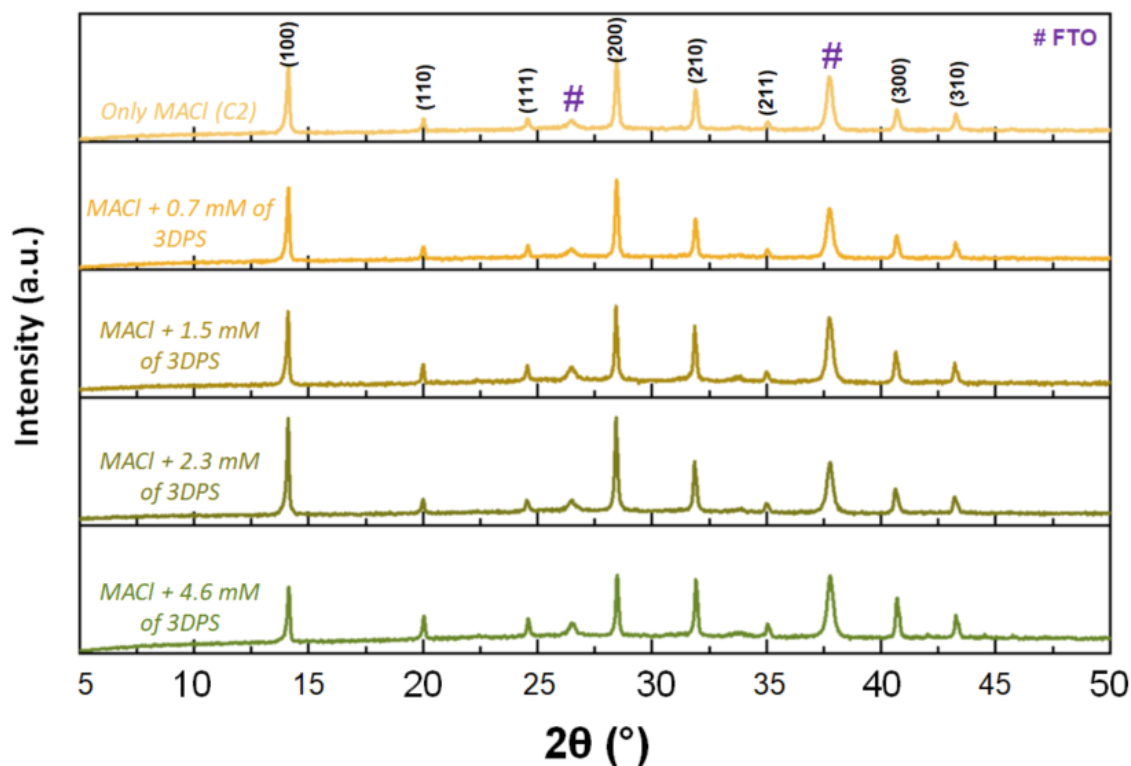


Figure IV-5: X-ray diffractograms measured on perovskite films deposited on FTO/c-TiO₂/m-TiO₂, with different surfactant concentrations.

In addition, on the refined XRD, the FWHM of the (100) peaks was calculated to be 0.12° for C2 perovskite films and 0.08° for a surfactant content of 2.3 mM. A higher 3DPS content of 4.6 mM leads to a broader FWHM of 0.10° . This broadening indicates that smaller coherence domains are formed within the perovskite grains when an excessive amount of 3DPS is introduced. It thus reduces the crystal growth rate and also the preferential orientation. This reduction of the crystallite size is consistent with the diminution of the grain size characterized in **part 1.1**.

The crystallite size is estimated to be 151 ± 10 nm for the sample C2, using Williamson-Hall (W-H) formalism. The addition of surfactant increases the crystallite size to 191 ± 6 nm, 248 ± 18 nm, 244 ± 21 nm, and 225 ± 8 nm for 0.7 mM, 1.5 mM, 2.3 mM, and 4.6 mM of 3DPS, respectively (**Figure IV-6. b**). Moreover, the perovskite films demonstrated a preferential orientation along the (100) plane, along with the augmentation of the average grain size. This preferential orientation has been proved to be beneficial for perovskite electronic properties.²

In addition, we observe a diminution of the tensile lattice micro-strains, from $\epsilon_{C2} = 3.1 \cdot 10^{-3}$ MPa to $\epsilon_{4.6mM} = 0.9 \cdot 10^{-3}$ MPa (**Figure IV-6. b**), suggesting that MACl and 3DPS addition leads to a relaxation of the perovskite film.

Combining XRD and SEM observations, we noticed that the increase in the grain size goes along with the crystallites. For a 3DPS concentration of 4.6 mM, the crystallite size decreases to 225 nm. This threshold is consistent with the SEM and confocal observations and sets a concentration limit for the beneficial effects of surfactant and MACl combined.

The average grain size seems to remain larger than the calculated crystallites, suggesting polycrystalline domains. However, this result has to be considered carefully though. The W-H method considers perfectly anisotropic spheres, which is not strictly compliant with perovskite particles. This can generate an approximation for the final perovskite crystallite size calculation.

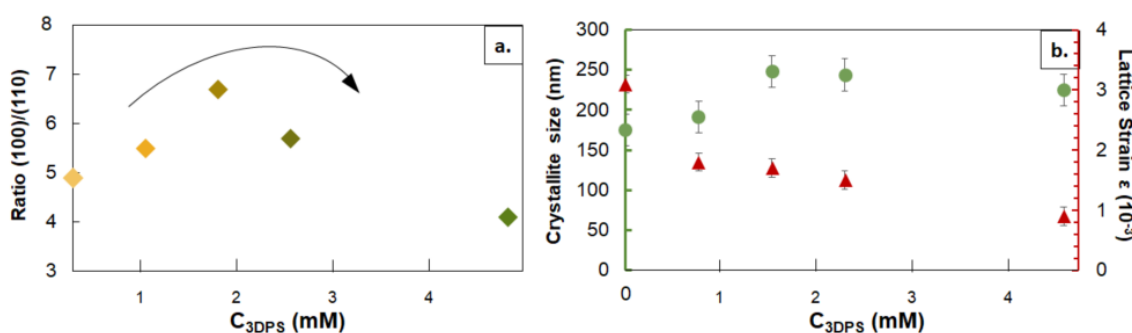


Figure IV-6: a. Evolution of the peak intensity ratio (100)/(110) orientation plans, depending on the surfactant concentration. b. Crystallite size and micro-strains depending on the surfactant concentration, calculated by W-H method.

1.4. Optical properties

The optical properties of the perovskite films deposited on FTO/c-TiO₂/m-TiO₂ have been measured by (UV/Vis) spectrophotometry.

We notice an enhancement in the absorption of the perovskite films with the surfactant addition, compared to the absorption of the reference sample C2 on a wavelength range between 500 and 750nm. The results are displayed in the inset of **Figure IV-7.a**. The absorption shows a continuous increase of 1.5%, 4.8%, 7.6%, and 11% with the 3DPS content.

Since the thickness of the perovskite films stays close regardless of the surfactant concentration, as confirmed by the cross-section SEM images in **Figure IV-4**, this absorption enhancement at short wavelengths is mainly due to the improvement of the perovskite layer morphology, which modifies the optical response of the film. The transmission curves for higher concentrations of surfactant (>2.3 mM) display wavy profiles in the near IR range, indicating optical interferences characteristic of very smooth films.

Moreover, on transmission and absorption spectra, no visible shift of the absorption onset is visible, which indicates that the bandgap value (1.64 eV) is not impacted by the additives.

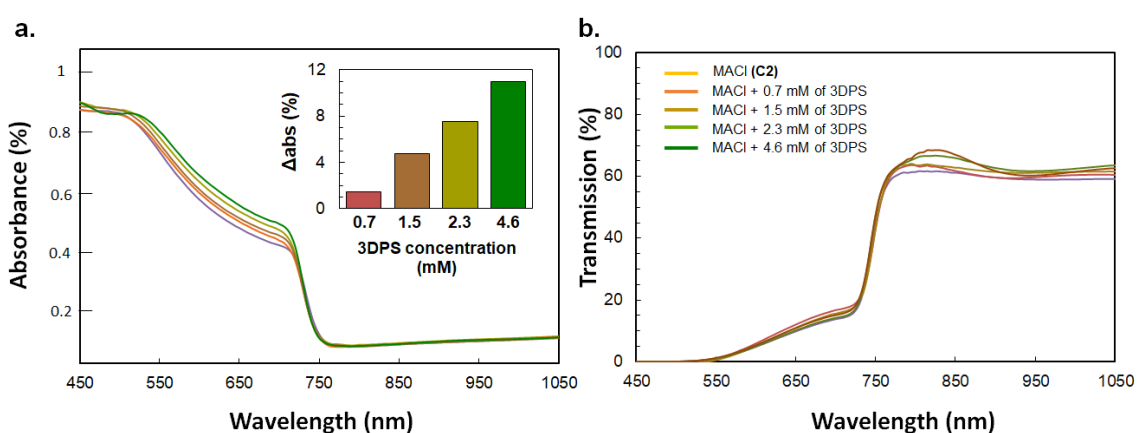


Figure IV-7: **a.** Absorbance spectra. Inset: relative improvement of the absorbance measured between 450 and 700 nm compared to the reference sample C2. **b.** Transmission curves, depending on the surfactant concentration. Measurements performed on perovskite films deposited on FTO/c-TiO₂/m-TiO₂.

1.5. Rationalization of the crystallization process results

In the previous chapters, we studied the independent influence of the two additives. We displayed our observations conducted on the film morphology and resulting conclusions in **Figure IV-8**.

Without any additives, we faced a poor covering perovskite film, with a dendritic structure and a high surface roughness. According to the crystallization theories, we concluded that the poor morphology was due to a poor nuclei density.

Then, in **chapter 2**, we concluded that the surfactant enhanced the nuclei density by promoting the heterogeneous nucleation. However, this behavior induced the lowering of the perovskite grain size, which can be detrimental to the electronic properties of the perovskite layer.

In **chapter 3**, we demonstrated that MACl could reduce the crystal growth rate by creating an intermediate with PbI₂. The resulting perovskite films showed large grains and enhanced crystallite size.

Finally, in this chapter, we displayed the combined action of the two additives on the perovskite morphology. The presence of surfactant allowed the formation of a sufficient nuclei density while promoting heterogeneous nucleation phenomena. As discussed in **chapter 1**, heterogeneous nucleation favors the fabrication of smooth perovskite films. In parallel, the introduction of MACl reduces the growth rate, resulting in a more homogeneous and larger perovskite grain growth. Finally, it enables the fabrication of smooth and well-covering perovskite film.

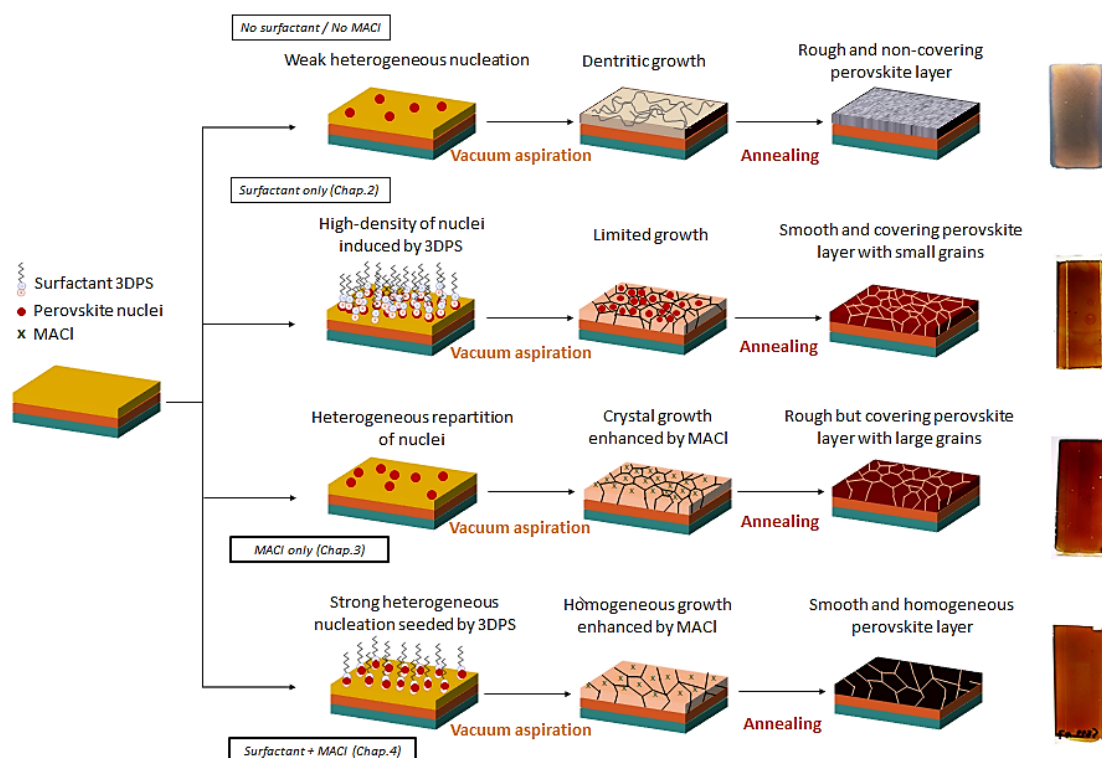


Figure IV-8: Illustration of the proposed crystallization mechanisms during perovskite film formation without additives, with surfactant only, with MACl only, and the synergic action between MACl and 3DPS.

2. Full devices performances

The deposition of the different extraction and electrodes layers was made accordingly to the procedure detailed in **Chapter 2, part.2, and part.3**.

The perovskite precursor's solution was prepared the day before the deposition of the absorber. The perovskite absorber was deposited by slot-die and dried by vacuum aspiration, according to the fabrication protocol detailed in **Chapter 2, part. 4**. Then, all the wet films were annealed for 30 minutes at 140°C.

2.1. Spiro-OMeTAD as Hole Transporting Layer

First, Spiro-OMeTAD was used as a hole transporting layer. The devices statistics are displayed in **Figure IV-8**. The detailed performance of the best devices and average performances for every growth condition herein investigated are presented in **Annex 9**.

The reference devices C₂ display an average value of J_{sc} of 19.0 mA.cm⁻² (in reverse scan). Then, a gain of J_{sc} can be obtained by the addition of MACl and 3DPS simultaneously. The J_{sc} increases to 19.8 mA.cm⁻² (+4%), 19.5 mA.cm⁻² (+3%), 20.3 mA.cm⁻² (+7%) and even to 20.8 mA.cm⁻² (+8.7%) with a surfactant content of 0.7 mM, 1.5 mM, 2.3 mM and 4.6 mM respectively. The increase of the J_{sc} is in the same order of magnitude as the improvement of the film's absorption detailed in **Figure IV-7. a**.

The open-circuit voltage V_{oc} is not affected by the surfactant addition. It stays at around 1.10V. Only a surfactant concentration of 2.3 mM leads to a slight improvement of the average V_{oc} to 1.12V. In addition, The FF value also remains stable, around 74 % for all surfactant content ≤ 2.3 mM.

In **Chapter 2**, we observed that the surfactant addition results in numerous grain boundaries that can be detrimental to the device's efficiency. However, its addition in smaller concentrations, combined with MACl, improves film morphology and enhances performance.

However, when a surfactant content of 4.6 mM is incorporated, it induces a significant drop of the average FF to 62.1 % (**Figure IV-9**). A drop of the FF without a noticeable impact on the V_{oc} can point out problems of charges extraction. Notably, K. Liu *et al.* reported that an accumulation of a zwitterionic surfactant in the perovskite bulk could impact the charge mobility due to the excess of alkyl chains assembled at the surface and in the grain boundaries of perovskite films.³ This limit of the surfactant addition is consistent with the observation of previous works, pointing out the migration surfactant species in the GBs during the annealing.⁴ The increasing number of grain boundaries arising from the diminution of the grain size induced by a surfactant concentration ≥ 4.6 mM can also impact the FF.

The control devices based on perovskite fabricated with only MACl exhibited an average efficiency of 15.7% (reverse scan), while it goes up to 17.2% on average for a surfactant concentration condition of 2.3 mM.

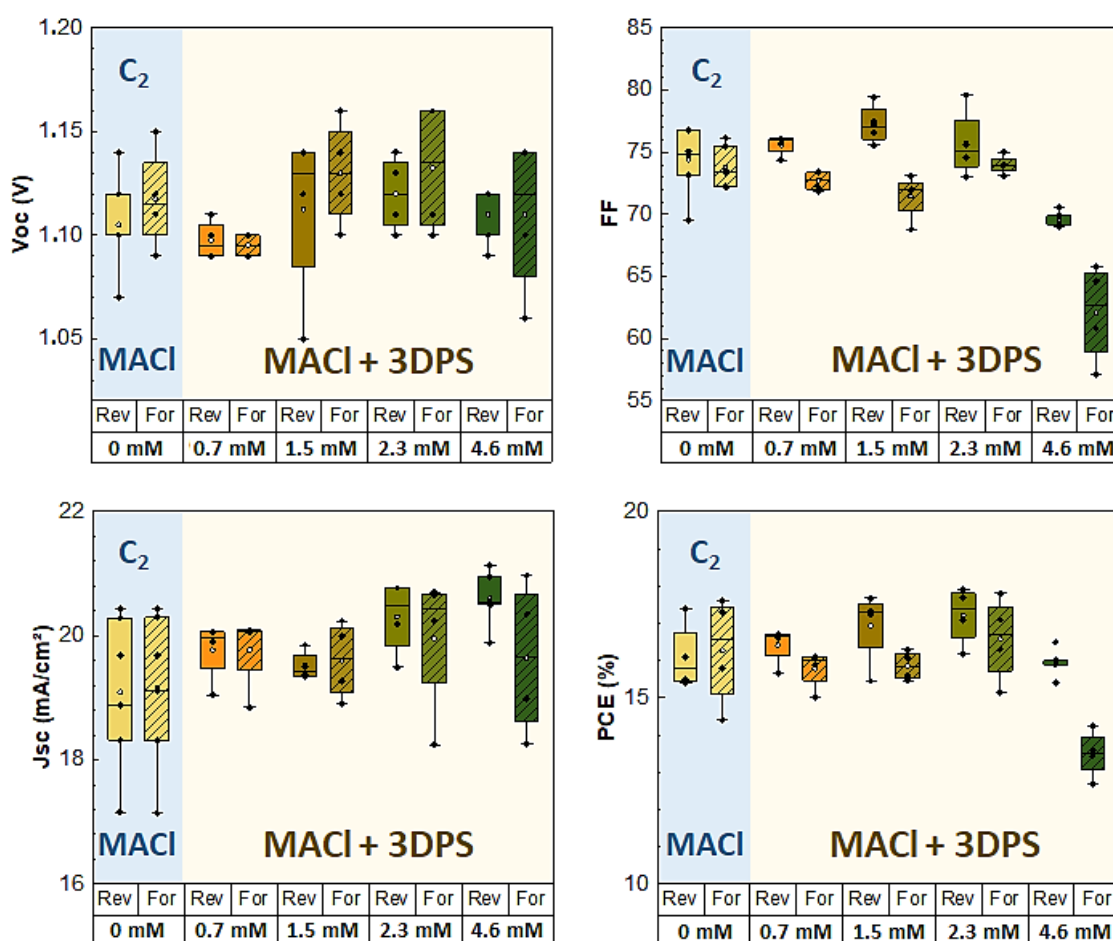


Figure IV-9: Influence of the surfactant addition on J-V parameters with a Spiro-OMeTAD as Hole Transport Layer. Device statistics for perovskite solar cells were prepared with a molar ratio MACl: FAI (0.3:1) and a gradual augmentation of surfactant concentration (Each condition counts ten cells). The devices present a NIP architecture glass/FTO/c-TiO₂/m-TiO₂/CS_{0.17}FA_{0.83}Pb(I_{0.83}Br_{0.17})₃/Spiro-OMeTAD/Au. Reverse scan (plain color) and forward scan (stripped).

Figure IV-10 displays the J-V curves and MPP of the best cell, fabricated only with MACl, and with the combination of MACl and 3DPS (2.3 mM).

The best reference cell yields 17.3% ($V_{oc} = 1.08\text{V}$, $J_{sc} = 20.4\text{ mA}\cdot\text{cm}^{-2}$, $FF = 74.6\%$), while we obtained a top cell of over 17.8% ($V_{oc} = 1.14\text{V}$, $J_{sc} = 20.7\text{ mA}\cdot\text{cm}^{-2}$, $FF = 75.6\%$) efficiency and stabilized at 17.5%, with a 2.3 mM 3DPS content, with a lower hysteresis. This result is the best efficiency obtained in this work, which thus underlines the added value and the synergy obtained with this double additive strategy.

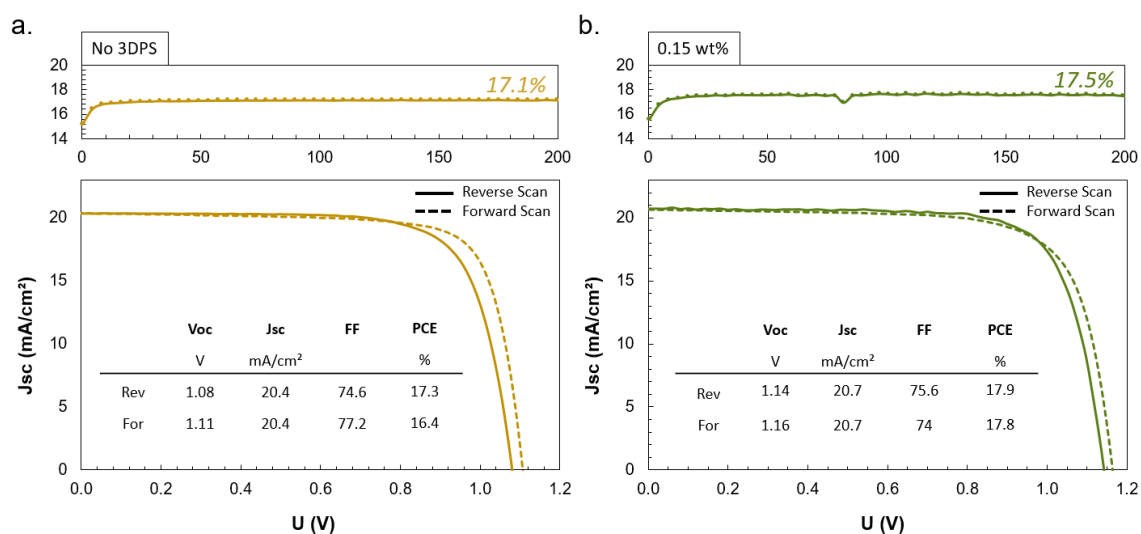


Figure IV-10: *J-V and MPP of best perovskite cells. a. No 3DPS (yellow curves). b. 3DPS content of 2.3 mM (green curves). Both cells were measured one week after deposition.*

2.2. PTAA as Hole Transporting Layer

Spiro-OMeTAD is a reference HTL for PSCs. Numerous studies investigated physical characteristics, electronic properties, optimization, and stability with this HTL.⁴⁻⁶ One of the most significant issues is the requirement for a high doping level to reach sufficiently high hole mobility for reaching high charge collection efficiency owing to the hopping type of the hole conduction. This doping is generally achieved by adding both lithium bis(trifluoromethylsulfonyl)amide (LiTFSI) and 4-*tert*-butylpyridine (tBP), in combination with a Cobalt-based complex as an additional *p*-type dopant. Unfortunately, these dopants often hurt the device's stability.^{7,8}

An alternative material, PTAA (Poly(triarylamine)), has been proposed because of its favorable highest occupied molecular orbital (HOMO) energy level position (-5.2 eV). Interestingly, the optimal concentrations of dopants for PTAA-based perovskite devices are about four times lower than the conventional concentrations of LiTFSI, and tBP added to spiro-OMeTAD.⁵ In addition, Co(III) complexes are generally not used to dope PTAA. Consequently, when incorporated into a perovskite device, it offers remarkable photovoltaic efficiency and enhanced stability thanks to the lower thickness needed, requiring a lower doping content.¹⁰ In addition, compared to spiro-OMeTAD, PTAA has a higher glass transition and melting temperature. Kim *et al.* found that PTAA is more stably amorphous than doped spiro-OMeTAD upon thermal stressing at both 65 °C and 85 °C, but pinhole formation was observed in both doped spiro-OMeTAD and PTAA films upon thermal stressing and ascribed to tBP evaporation.^{11,12} In addition, as HTLs provide the main barrier between the perovskite layer and the environment, their response to moisture strongly affects perovskite solar cell stability. Spiro-OMeTAD has been shown to crack upon exposure to moisture, allowing water to degrade the perovskite

directly, while PTAA only forms small holes, enabling better coverage and slower degradation of the perovskite film.¹³

We fabricated complete devices by replacing the spiro-OMeTAD layer with PTAA. **Figure IV-10** shows the statistic of the cell characteristics of the following devices:

- The two reference devices, either with Spiro-OMeTAD or PTAA. The perovskite layer benefited only of MACl addition.
- The same four different growth conditions as presented before, with combined MACl and surfactant.

Detailed performances of best cells and average performances for every tested condition are presented in **Annex 10**.

Looking at the reference cells without 3DPS, replacing the Spiro-OMeTAD by PTAA induces a severe loss of J_{sc} , decreasing from $19.0 \text{ mA}\cdot\text{cm}^{-2}$ to only $13.2 \text{ mA}\cdot\text{cm}^{-2}$. In addition, the average V_{oc} also shows a significant loss of 0.1 V , and the FF value decreases from 74% to 66% . Due to the lower thickness of the PTAA layer (ca. 20 nm) compared to Spiro-OMeTAD (ca. 200 nm), the important roughness of the absorber, as shown in **Figure IV-4** ($S_a = 56 \text{ nm}$), may create a poor coverage of the PTAA layer onto the perovskite. Consequently, direct contact between the gold electrode and the perovskite layer will take place. This poor interface quality is thus detrimental to final performances, resulting in an average PCE of 8.8% , compared to 15.7% with Spiro-OMeTAD. As a result, diminishing the surface roughness of the perovskite layer is one key to improving the performance of the PTAA cells.

With gradual increase of the surfactant concentration, the average J_{sc} value of the PTAA devices raise up to $19.0 \text{ mA}\cdot\text{cm}^{-2}$ (0.7 mM), $20.3 \text{ mA}\cdot\text{cm}^{-2}$ (1.5 mM), $19.5 \text{ mA}\cdot\text{cm}^{-2}$ (2.3 mM) and $18.9 \text{ mA}\cdot\text{cm}^{-2}$ (4.6 mM) with 3DPS addition. The V_{oc} also showed an important improvement, from an average value of 1.01 V for the reference PTAA device to 1.1 V (0.7 mM), 1.15 V (1.5 mM), 1.12 V (2.3 mM) and finally 1.1 V (4.6 mM). The reference PTAA devices exhibited an average efficiency of 8.8% (reverse scan), while it goes up to 16.1% on average for a surfactant concentration condition of 1.5 mM and 16.4% for 2.3 mM 3DPS content.

The overall improvement of the device performances is directly related to reducing the surface roughness by the addition of 3DPS. Indeed, as previously discussed, the latter affords to decrease the number of morphological defects, particularly the so-called “dots.” Note that a slightly higher hysteresis was observed in the case of the PTAA compared to Spiro-OMeTAD. This hysteresis gradually decreases with the addition of the surfactant, which is in agreement with the improvement of the interface quality. However, as observed with Spiro-OMeTAD devices, the beneficial effect of surfactant addition meets a limit when the 3DPS content is higher than 2.3 mM .

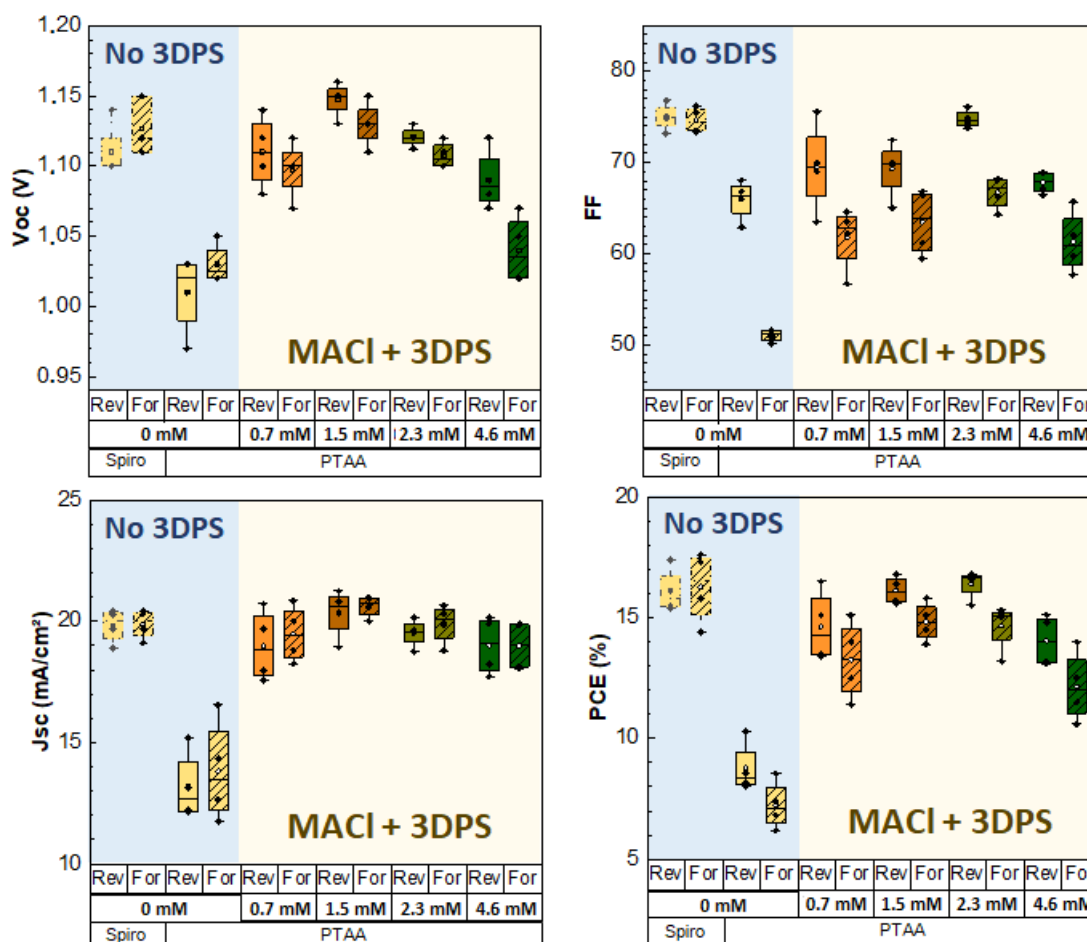


Figure IV-11: Influence of the surfactant addition on J-V parameters with a PTAA as Hole Transporting Layer. Device statistics for perovskite solar cells were prepared with a molar ratio MACl: FAI (0.3:1) and a gradual augmentation of surfactant concentration (Each condition counts for five cells). The devices present a n-i-p architecture glass/FTO/c-TiO₂/m-TiO₂/Cs_{0.17}FA_{0.83}Pb(I_{0.83}Br_{0.17})₃/PTAA/Au. Reverse scan (plain color) and forward scan (stripped).

Figure IV-12 compares the J-V curves of the best devices for the conditions without surfactant (yellow curves) and the devices with a surfactant content of 2.3 mM (green curves). The best reference cell yields 10.3% (15.2 mA.cm⁻², 1.03V, 66.0), while we obtained a top cell of 16.8% (19.6 mA.cm⁻², 1.12V, 76.1) of efficiency and stabilized at 15.6%, with a 2.3 mM 3DPS content. Interestingly, the PTAA devices show their best performances five days after the fabrication.

Although this efficiency represents a significant improvement in the efficiency of the PTAA devices compared to a protocol without surfactant, the best PTAA-based device still displays a 5% lower average efficiency (16.4%) than their spiro-OMeTAD counterparts (17.2%), pointing out the need for further optimizations.

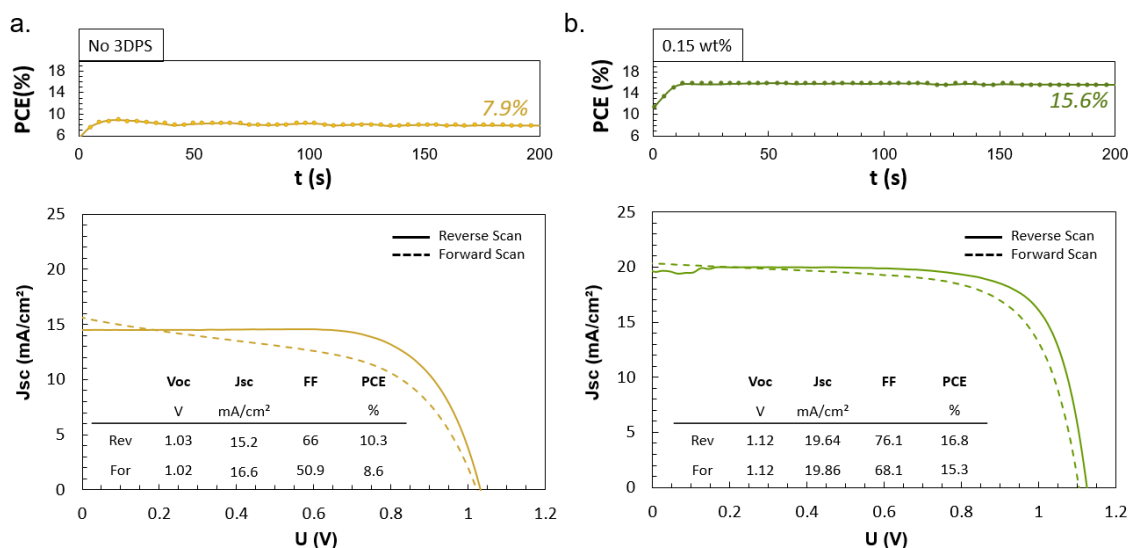


Figure IV-12: *J-V of best perovskite cells. a. Perovskite layer fabricated only with MACl and without 3DPS (yellow curves). b. Perovskite layer fabricated with MACl and a surfactant content of 2.3 mM (green curves). Both cells were measured one week after the fabrication of the full stack.*

2.3. Aging in dark conditions

To evaluate the impact of the HTL layer on the stability, we compared the evolution of the I-V parameters during 45 days for the best four cells of each ink formulation (**Figure IV- 13**). The devices were stored under vacuum in the dark and only taken out for the I-V measurements under one sun illumination. The average J-V parameters of aged devices are displayed in **Annex 11**.

The performances of the Spiro-OMeTAD devices remain stable during the first ten days, with only a 4% loss of the initial efficiency, mainly due to the FF. However, after two weeks, the performances start to degrade more quickly. In particular, the Voc decreases from 1.11 V to 1.05 V, which points out the degradation of the interface perovskite/HTL. This loss of performance is consistent with the degradation path of the HTL, as evidenced previously. The device's aging results in a significant morphological modification, like the generation of pinholes and delamination of the HTL layer, as evidenced in **Chapter 3**.

On the contrary, the PTAA devices show only small variations of the J-V characteristics. On average, after 45 days, the spiro-OMeTAD devices lose around 20 % of their initial PCE, whereas PTAA-based devices remained very stable with a PCE retention as high as 98 %. Therefore, the PTAA layer as HTL represents an exciting way to enhance the stability of the solar cells.

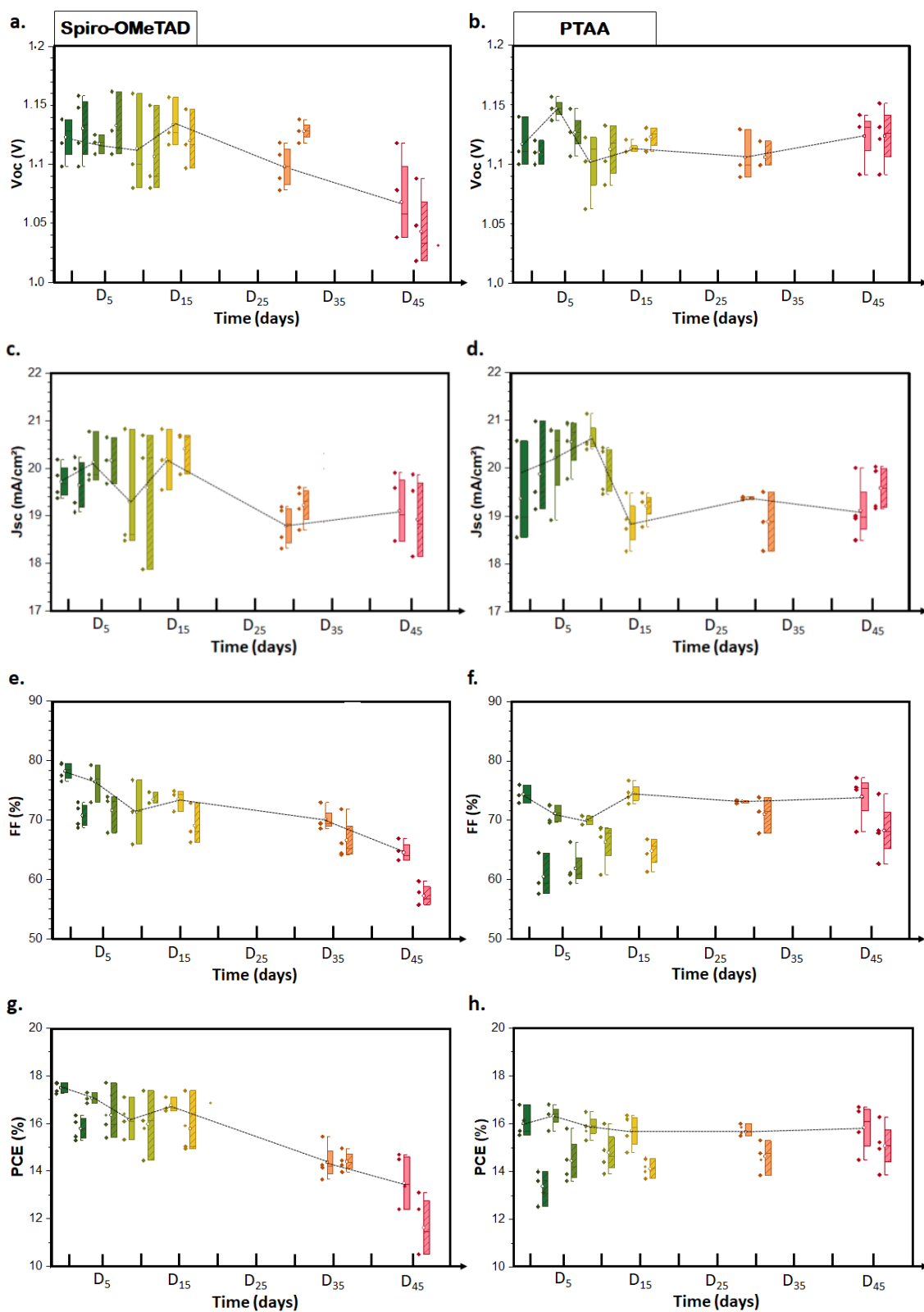


Figure IV- 13: Ageing of solar cells stored in the dark and under vacuum conditions. **a.** Perovskite solar cells fabricated with Spiro-OMeTAD or **b.** with PTAA.

3. Integration in semi-transparent perovskite cells architecture

As discussed in **Chapter 1**, perovskite solar cells have been proven to be very promising top-cell for multi-junction solar cells due to their tunable bandgap, easy fabrication, and potential low-cost fabrication.^{13–16} Then, in **part. 1 and 2.** of this chapter, we focused on fabricating a high-performance perovskite device with a slot-die coating perovskite material with a high bandgap of 1.64 eV. This bandgap is compatible with tandem requirements.^{17,18}

However, to fabricate efficient Si/perovskite tandem devices, it is necessary to elaborate a semi-transparent (ST) perovskite top-cell. Various materials have been investigated in the literature to replace the traditional opaque gold electrode layer, for a n-i-p architecture, with a transparent TCO. Among them, AZO (Aluminium-doped Zinc Oxide), IZO (indium-doped zinc oxide), and ITO material represent the most promising candidates due to their excellent average visible transmittance (>80%), their low sheet resistance (~10 Ω /sq), and their high color rendering index (>75%).^{19,20} However, sputtered ITO stays the industry's current standard commercial TCO in optoelectronic devices and has been the most reported top TCO in semi-transparent and tandem perovskite photovoltaics.²¹

This part focus on the fabrication, optimization, and characterization of semi-transparent devices with a transparent bi-layer ITO top-electrode. The development and the deposition of the transparent ITO have been carried out by Emilie Raoult (Ph.D. student at IPVF).

3.1. ITO deposition and fabrication of the solar cells

The fabrication conditions of the c-TiO₂, m-TiO₂, perovskite, and HTL layers remain identical to the previous chapters. The complete deposition methods for each layer have been detailed in **Chap. 2, part. 2 and 3.**

For the perovskite deposition, we used a surfactant content of 2.3mM combined with a (MACl: FAI) molar ratio of (0.3: 1) in the perovskite precursors solution. The perovskite layer is coated onto a large 5 x 10 cm² substrate. It is then divided into 2 x 2.5 cm² individual cells and then covered by the HTL (either PTAA or Spiro-OMeTAD have been investigated). A sputtered ITO layer as transparent conductive contact is sheltering the HTL. Finally, the cell is terminated by a fork-like gold contact evaporated around the ITO layer to ease the lateral carrier transport to the external electrical circuit. It allows a better contact for IV measurements without covering the transparent ITO. The detailed ITO deposition protocol developed by E. Raoult is displayed in **Annex 13.** The full stack of the fabricated semi-transparent solar cells is sketched in **Figure IV-14.**

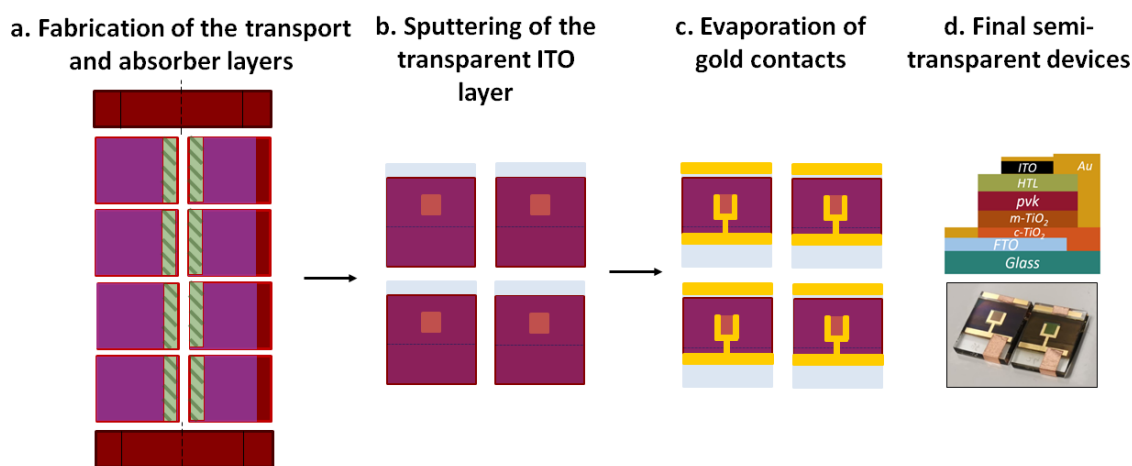


Figure IV-14: Main steps of the fabrication process of semi-transparent small-area solar cells **a.** a large slot-die coated perovskite sample ($10 \times 5 \text{ cm}^2$) is divided into individual semi-transparent solar cells of $2 \times 2.5 \text{ cm}^2$. **b.** Sputtering of the ITO layer, **c.** evaporation of the gold contact, and **d.** Architecture and picture of the final ST perovskite devices.

3.2. Morphological characterization

Figure IV-15. a. and b. show the confocal images of the ITO layer morphology deposited on Spiro-OMeTAD and PTAA, respectively. The ITO layer grown on a PTAA layer presents a smooth surface, whereas important wrinkles are formed when the ITO layer is deposited on top of a Spiro-OMeTAD. According to confocal 3D images, the wrinkles can be as high as $4 \mu\text{m}$, suggesting significant delamination. The cross-section SEM images (**Figure IV-15.c.**) confirm that the wrinkles visible on the ITO layer deposited on Spiro-OMeTAD are due to delamination of the ITO layer. On the contrary, the ITO keeps perfect adhesion on the PTAA layer.

The devices can be subjected to high temperatures generated by the plasma during the ITO deposition by sputtering. This represents a major difference with the gold evaporation, which does not submit the samples to a temperature variation. The exact temperature reached by the cells during the deposition remains unknown, but a measure on the samples after the withdrawal from the sputtering vacuum chamber indicated 45°C . Since the cells stay 30 minutes in the sputtering chamber after the end of the deposition, the actual temperature reached by the samples during the process is probably higher. A. J. Bett *et al.* demonstrated that a sputtering temperature $> 50^\circ\text{C}$ during the deposition can degrade the performances of ST devices fabricated with a Spiro-OMeTAD HTL.²³ Indeed, an important mismatch exists between the thermal expansion coefficient (CTE) of the ITO ($\text{CTE} \approx 5\text{-}6.3 \cdot 10^{-6} \text{ K}^{-1}$) and the Spiro-OMeTAD ($\text{CTE} \approx 300\text{-}450 \cdot 10^{-6} \text{ K}^{-1}$). The latter is lower in the case of the PTAA ($\text{CTE} = 50\text{-}100 \cdot 10^{-6} \text{ K}^{-1}$). Consequently, when exposed to the sputtering process temperature, the Spiro-OMeTAD tends to dilate more than the ITO, inducing its delamination upon cooling. This creates a loss of electrical contact between the Spiro-OMeTAD and the electrode.

In addition, the Spiro-OMeTAD can be damaged due to bombardment with high energetic ions.²³ Consequently, the ITO layer is deposited following a two-step process, starting with a low energy step during which the plasma is kept at 10W for 30 mins.

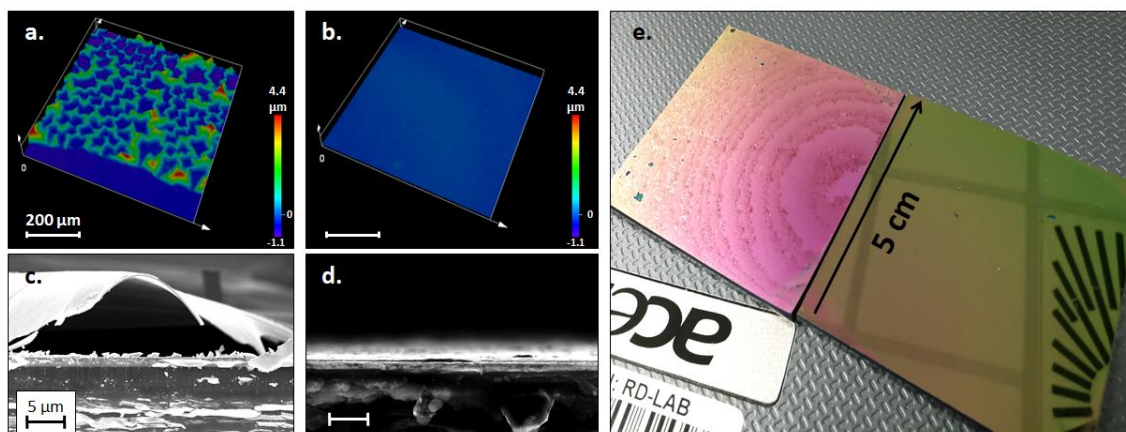


Figure IV-15: Confocal images (x20 magnification) of ITO deposited on: **a.** spiro-OMeTAD and **b.** PTAA. Cross-section SEM images of perovskite stack with different HTL. ITO deposited on **c.** spiro-OMeTAD, and **d.** ITO deposited on PTAA. **e.** Picture of ITO deposited on Spiro-OMeTAD (pink sample, left) and PTAA (green sample, right).

3.3. Optical properties

We performed ellipsometry measurements on the filters and calculated the refractive index n and the extinction coefficient k to characterize the perovskite deposited by slot-die. The measurements were performed using a spectroscopic ellipsometer (J.A. Woollam M-2000VI).

We compared the results for a triple cation perovskite fabricated by spin-coating and a double cation perovskite fabricated by slot-die. For the slot-die perovskite layer, the roughness was modeled by adding a mix sub-layer bulk/void (86% bulk/14% void).

We noted a very similar ellipsometric response between slot-die and spin-coating perovskite layers. It is possible to observe the absorption peaks of the perovskite layer (black arrows), visible in the UV-Visible spectral region. Between 300 and 800 nm, we observed a slight variation of energetic levels due to the different bandgaps: 1.58 eV for the baseline and 1.64 eV for the slot-die coated perovskite films.

The PTAA shows a higher refractive index (~ 1.7) and lower extinction coefficient than spiro-OMeTAD (~ 1.6).^{25,26} When compared to the refractive index of the perovskite layer (~ 2.2), calculated by ellipsometry (**Figure IV-16.a.**), the better matching of the refractive index between PTAA and the perovskite layer allows to lower the reflection losses and reduce parasitic absorption.

Figure IV-16.b. shows the absorbance, the reflection, and the transmission curves measured by UV-vis spectro-photometry on the stack: Glass/FTO/c-TiO₂/m-TiO₂/perovskite/Spiro-OMeTAD or PTAA/ITO. Between 550 nm and 700 nm, the PTAA stack shows a slightly lower absorbance (-3.1%), correlated with a higher transmission of this HTL compared to the Spiro-OMeTAD in the same wavelength range. This difference can be attributed to a phenomenon of light re-absorption at the interface perovskite/Spiro-OMeTAD due to the thicker HTL. In addition, between 900 nm and 1100 nm, the Spiro-OMeTAD layer absorbs more in the NIR than a PTAA layer due to the more important dopant content.

The difference between refractive index and HTL thickness is visible on the final ITO color (**Figure IV-15.e**).

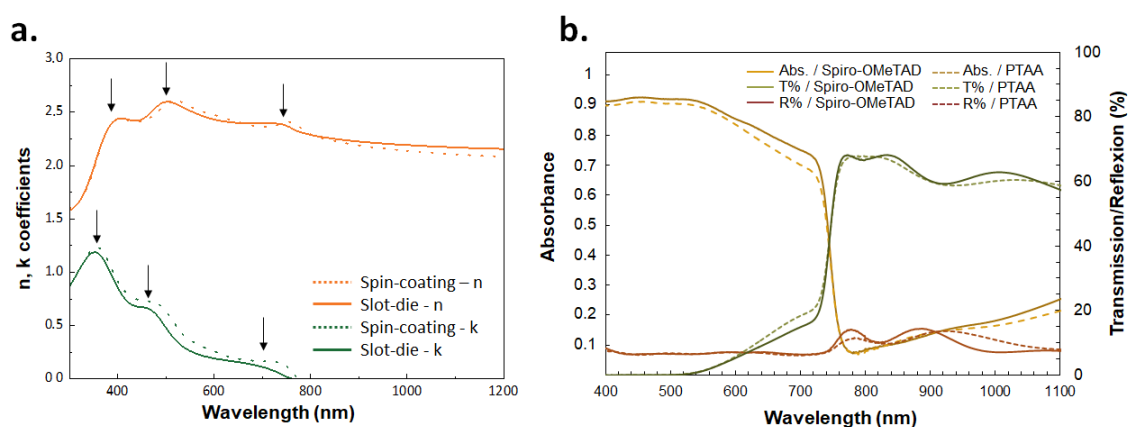


Figure IV-16: a. UV-vis Spectro-photometry measurements performed on the *n-i-p* stack Glass/FTO/c-TiO₂/m-TiO₂/perovskite/Spiro-OMeTAD or PTAA/ITO. Absorbance curves (yellow), Transmission curves (green), and reflection curves (orange). **b.** Ellipsometry measurements were performed on Glass/FTO/c-TiO₂/m-TiO₂/perovskite. The absorber layer MAFACs ($E_g = 1.56\text{eV}$) have been deposited by spin-coating (dotted curves), and the absorber layer FACs ($E_g = 1.64\text{eV}$) have been deposited by spin-coating (plain curves).

3.4. Semi-transparent solar cells performances

Figure IV-17 shows the electrical parameters statistic of the semi-transparent perovskite devices fabricated with Spiro-OMeTAD or PTAA. The detailed performances of the best cells and the related average performances are presented in **Annex 13**.

The semi-transparent solar cells exhibit a lower efficiency than their gold counterparts. The semi-transparent Spiro-OMeTAD devices display an average J_{sc} of $19.2\text{ mA}\cdot\text{cm}^{-2}$ (-5.4%), and the PTAA an average J_{sc} of $18.1\text{ mA}\cdot\text{cm}^{-2}$ (-7.2%). It can be partially explained by the difference in electrode materials. In the case of an opaque cell, the light entering the cell is reflected by the gold contact and comes back inside the absorber, increasing the light absorption. On the contrary, in the case of a semi-transparent layer, a part of the light is transmitted through the cell, inducing a lower current generation. In addition, the

lower FF value of the semi-transparent devices can be due to the higher resistivity of the ITO layer (16 ohm/sq) compared to a gold electrode ($\sim 10^{-5}$ ohm/sq).²⁶

On average, the Spiro-OMeTAD devices lead to higher efficiencies than PTAA devices. The day of the fabrication, the devices with Spiro-OMeTAD exhibit an average V_{oc} of 1.11V, $J_{sc} = 19.2 \text{ mA.cm}^{-2}$ and $FF = 72.3$, compared to a average $V_{oc} = 1.05V$, $J_{sc} = 18.1 \text{ mA.cm}^{-2}$ and $FF = 62.9$ for PTAA devices (reverse scans). However, this difference is gradually reduced with the aging of the cells. On average, the cells with PTAA as hole transport layers yield their best efficiency a week after the deposition. and present a maximum average efficiency 13% lower (PCE = 13.1%) than their Spiro-OMeTAD counterparts (15.3%). This difference is consistent with the tendency identified for the opaque solar cells previously in **part 2**.

Even in the literature, it exists a significant efficiency gap between both HTL materials. To date, the best semi-transparent efficiency is 19.4% on 0.05cm^2 and 16.5% on 1 cm^2 for a n-i-p planar architecture with a Spiro-OMeTAD HTL, a MoO_3 buffer layer, and a transparent AZO top electrode.²⁷ In comparison, the best-reported device using a PTAA layer and an ITO transparent top-electrode in a n-i-p architecture reached 15.4% efficiency.²⁸ Interestingly, to tackle this problem, a lot of teams chose a p-i-n architecture, offering better stability and potentially better efficiencies.^{20,29,30}

Nevertheless, we noted that the deposition of the ITO layer on Spiro-OMeTAD gives rise to a lack of reproducibility from batch to batch, this material being susceptible to the stresses undergone during the sputtering process. For example, for all the cells presented in this study, 5 devices over 18 were damaged and demonstrated a PCE lower than 2% after the ITO deposition, representing almost a 30% loss. By replacing the Spiro-OMeTAD with PTAA, a significant gain in reproducibility was obtained. Consequently, it significantly decreased the cells loss after the TCO deposition. On 14 semi-transparent devices fabricated with PTAA, only one cell displayed an efficiency lower than 2% after the sputtering deposition.

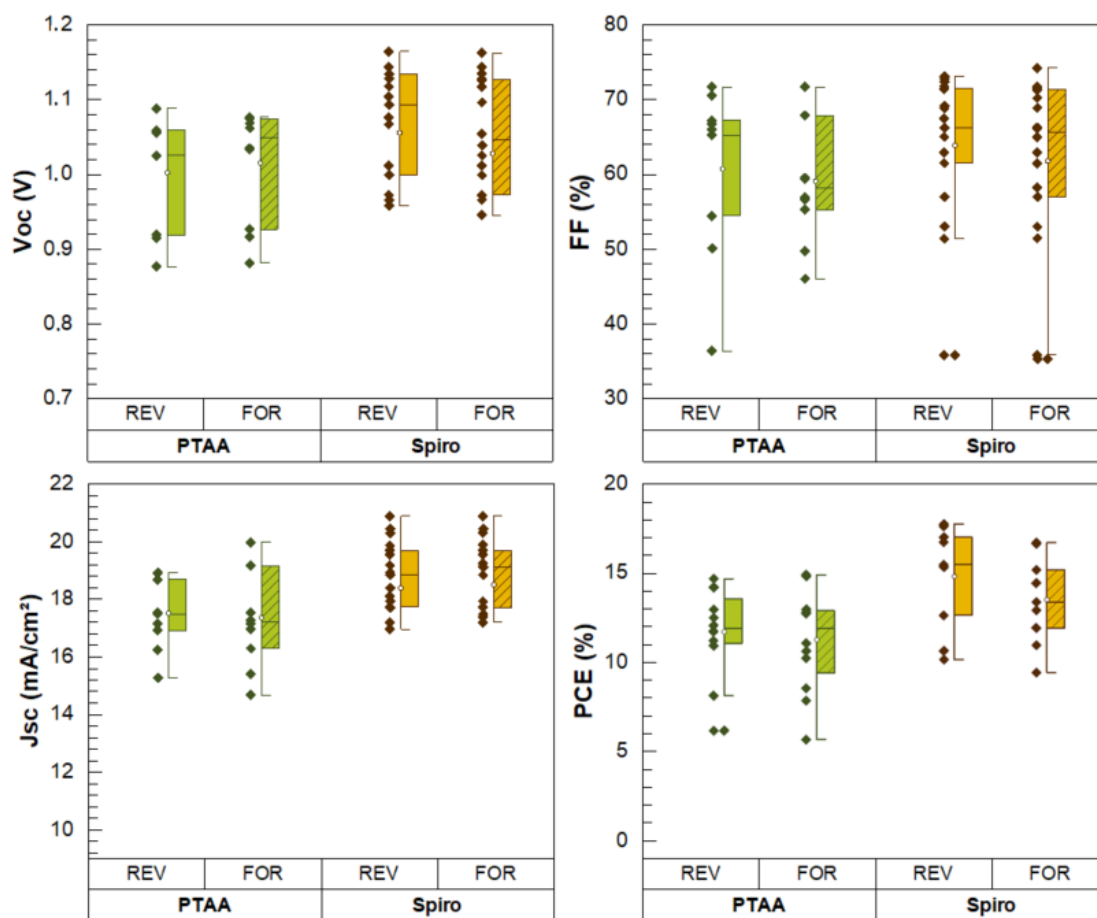


Figure IV-17: Influence of the HTL on J-V parameters. Device statistics for semi-transparent perovskite solar cells at D+1. The devices present a NIP architecture glass/FTO/c-TiO₂/m-TiO₂/Cs_{0.17}FA_{0.83}Pb(I_{0.83}Br_{0.17})₃/PTAA/Au. Reverse scan (plain color) and forward scan (striped). They were measured one week after deposition.

The J-V curves of the best fabricated ST solar cells are displayed in **Figure IV-18**. The best ST cell with Spiro-OMeTAD displayed an efficiency of 16.7% (reverse scan) ($V_{oc} = 1.13\text{V}$ / $J_{sc} = 20.3\text{ mA}\cdot\text{cm}^{-2}$ / $FF = 71.8\%$), without hysteresis for a Spiro-OMeTAD perovskite device. In comparison, the best PTAA device reached a maximum efficiency of 14.8% (reverse scan) ($V_{oc} = 1.07\text{V}$ / $J_{sc} = 19.1\text{ mA}\cdot\text{cm}^{-2}$ / $FF = 72.7\%$) as PTAA is used as HTL. Recently, S.H. Lim *et al.* reported a 15.72% efficiency with an IZTO (Indium Zinc-Thin Oxide) transparent top-electrode.²⁰ To date, the best reported semi-transparent perovskite solar cell with a sputtered ITO top-electrode layer directly on the HTL yields an efficiency of 15.4%.²⁸

Regardless of the HTL, the EQE curve indicates a conversion loss for longer wavelengths than 500 nm. This phenomenon is common to both Spiro-OMeTAD and PTAA devices and points out an insufficient thickness of the absorber layer, which penalizes the conversion of lower-lying energy photons close to the bandgap. During this thesis, the deposition parameters have been optimized for a reproducible perovskite layer thickness of $\approx 470 \pm 15\text{ nm}$.

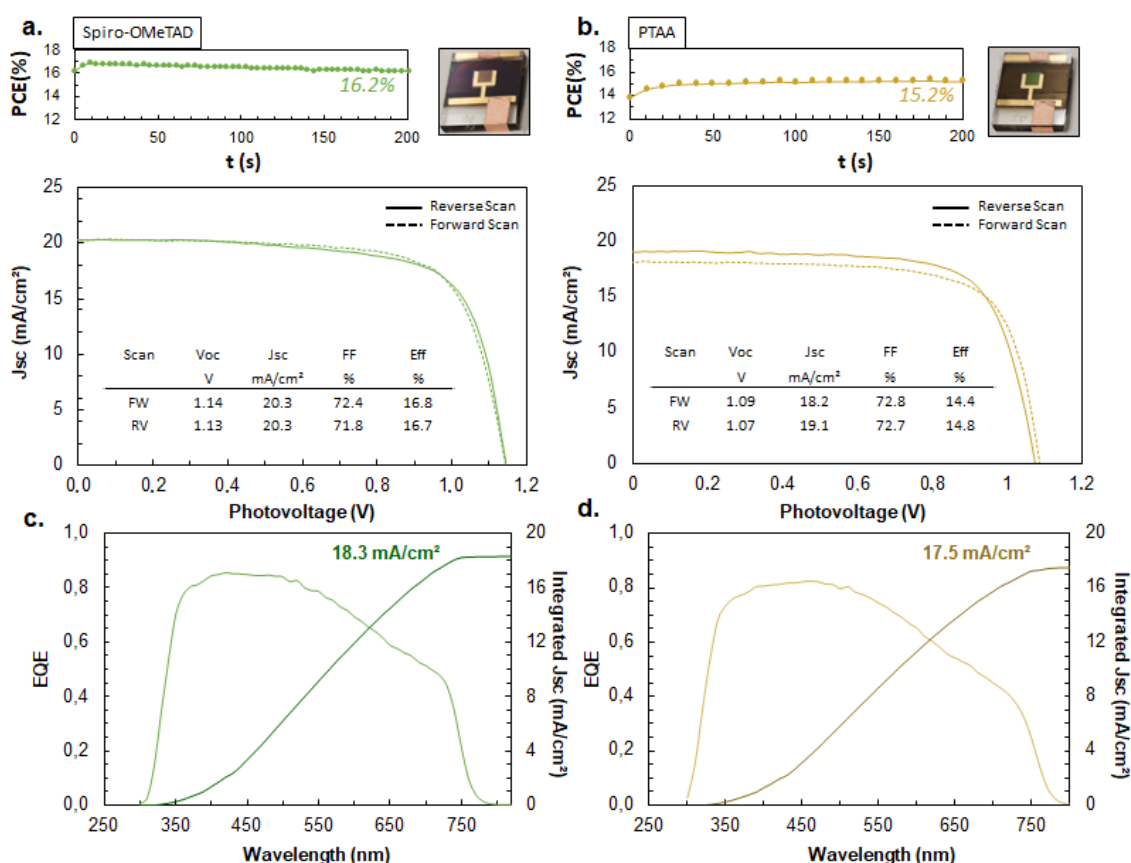


Figure IV-18: **a.** *J-V* curve of best Spiro-OMeTAD device, measured D+1 after deposition. **b.** *I-V* curve of best PTAA device measured D+10 after deposition. **c.** EQE curve of best Spiro-OMeTAD device measured D+1 after deposition. **d.** EQE curve of best PTAA device measured D+10 after deposition.

3.5. Aging in dark conditions

Similarly to **part 3.3**, the stability of the perovskite devices has been studied over 45 days (4 cells for each condition) (**Figure IV-19**). The devices were stored under vacuum in dark conditions and only taken out for the I-V measurements under one sun illumination. The detailed J-V parameters of aged devices are displayed in **Annex 13**.

Spiro-OMeTAD devices have a higher initial average efficiency than PTAA devices. However, after ten days, the efficiency of the PTAA devices went from 11.8% to 12.8%, which represents an increase of 8.6%. In the meantime, the Spiro-OMeTAD devices lost 11.7 % of their initial efficiency. At the end of the 45 days following, we can see that the PTAA devices retained 88% of their initial performances and Spiro-OMeTAD devices retained only 48% of their initial performances.

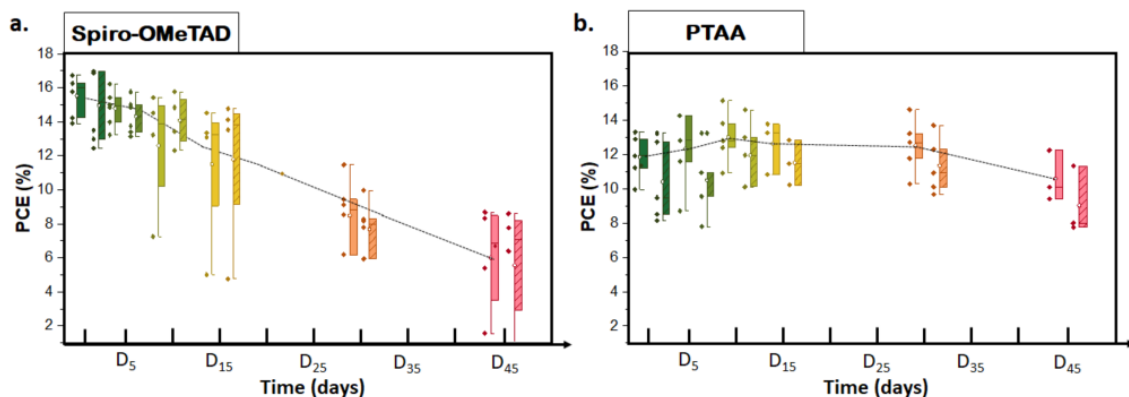


Figure IV-19: Ageing of solar cells stored in the dark and under vacuum conditions (Each condition counts for four cells). **a.** Perovskite solar cells fabricated with Spiro-OMeTAD or **b.** with PTAA. The devices present a *n-i-p* architecture glass/FTO/c-TiO₂/m-TiO₂/Cs_{0.17}FA_{0.83}Pb(I_{0.83}Br_{0.17})₃/HTL/ITO/Au. Reverse scan (plain color) and forward scan (stripped).

The Spiro-OMeTAD cells J-V parameters demonstrate an important loss on the J_{sc} on **Figure IV-20**, from an average of 20.1 mA.cm⁻² to 15.0 mA.cm⁻². It could indicate a possible degradation of the absorber layer, as observed in **Chap.3**.

The J-V curves also show an increase of the resistance losses, conducting to a diminution of the FF. Looking at the average J-V results in **Annex 13**, it also indicates a severe V_{oc} loss for most of the aged devices.

On the contrary, the PTAA champion device (**Figure IV-20. b**) displays a stable behavior. In this case, the gradual diminution of the V_{oc} and J_{sc} values represents a loss of only 3.7% and 4.1%, respectively. This is consistent with the average values.

The decline of the ST PTAA device's efficiency after 45 days (-12%) is consistent with the tendency identified in **part 3.3**. for opaque cells (-2%). On the contrary, the Spiro-OMeTAD devices display a much more important PCE loss after 45 days (-62%) than the equivalent opaque solar cells (-22.3%). Therefore, it is possible that, even in working solar cells, the Spiro-OMeTAD suffers a preliminary degradation during the sputtering, resulting in accelerated degradation of the devices.

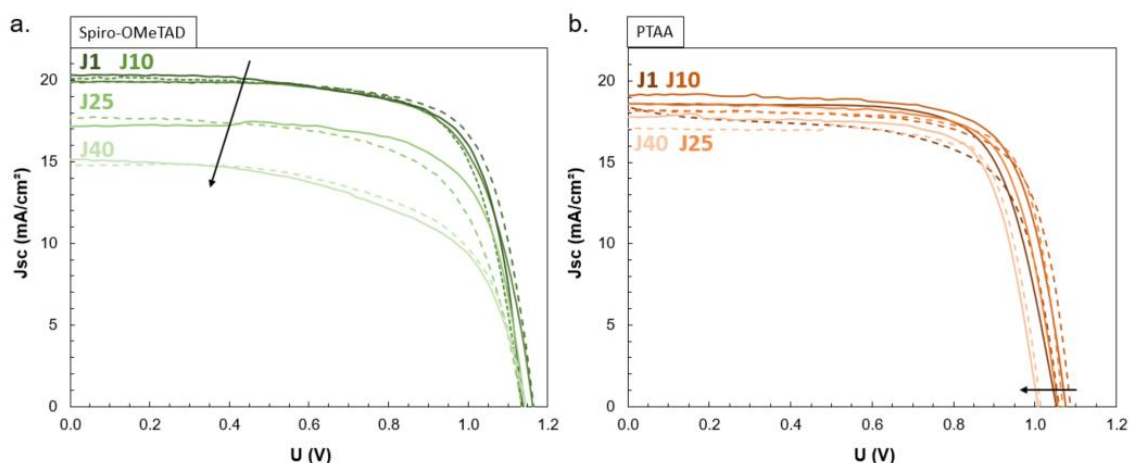


Figure IV-20: Ageing of the two best semi-transparent solar cells. **a.** Spiro-OMeTAD as hole transporting layer (green curve) and **b.** PTAA as hole transport layer (pink curve). The solar cells were stored under a vacuum in dark conditions.

4. Tandem performances projection

Great progress has been made in developing high-efficiency perovskite-Si tandem solar cells since, in 2016, Albrecht *et al.* reported the first demonstration of a perovskite-Si tandem reaching an 18% efficiency with a heterojunction silicon bottom cell.³¹ Since then, the successful integration of perovskite cells with silicon cells to form a tandem solar device has shown tremendous potential for outperforming the state-of-the-art single-junction silicon devices.

Therefore, in the final part of this chapter and this thesis, we decided to fabricate a tandem stacking to evaluate the potential of our ST solar cells in a tandem configuration.

First, the J-V performances of the silicon bottom cells were measured under 1 Sun (AAA Simulator) in a 4-wires configuration. The J-V curves are displayed in **Figure IV-21. c.**

Then, the pseudo-tandem devices were assembled as follow (the detailed integration protocol, developed by T. Guillemot, Ph.D. is displayed in **Annex 14**):

- A bottom-cell, which is a n-PERT c-Si cell supplied by ISC Konstanz, is encapsulated with a polyolefin film (PO). The Si cell has a stringed active surface area of 16 cm² (**Figure IV-21. a.**).
- A top-cell, which is a full ST perovskite device stack (5x5cm²), is directly put on the Si bottom cell, without electrical connections (**Figure IV-21. b.**). This part, called a “filter,” is placed above the bottom cell to measure the electrical response of the filtered Si cell. The J-V curves of the filtered Si cells are displayed in **Figure IV-21. c.**

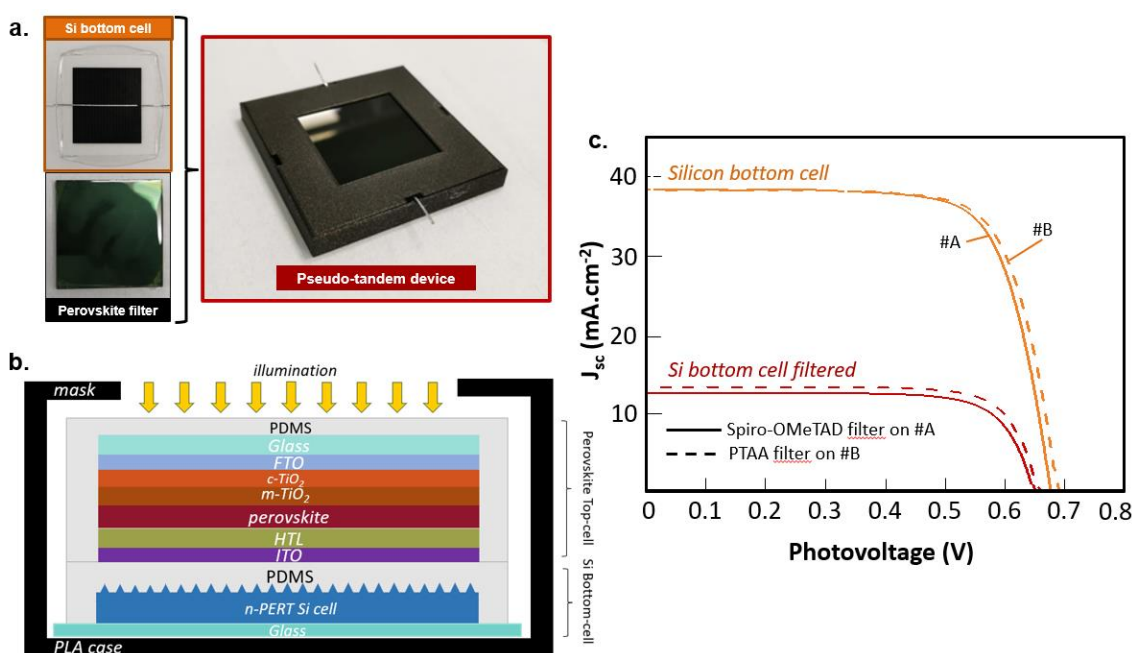


Figure IV-21: a. Pseudo-tandem device b. Architecture of the pseudo-tandem device and, c. J-V curves of Si bottom cells filtered and unfiltered.

Since the top and bottom cells are not electrically connected, the device is called a “pseudo-tandem.” To evaluate the efficiency of the pseudo-tandem, we associated the efficiency of the filtered Si bottom-cells with the efficiencies of the best semi-transparent perovskite cell obtained in **part 2**. The devices fabricated by slot-die were compared with devices fabricated by spin-coating with the same architecture but different bandgaps. We considered several different configurations:

- Pseudo-tandem #A: This device is composed of a-Si bottom cell and a top-cell filter, with a Spiro-OMETAD HTL and a perovskite layer fabricated by slot-die displaying a high bandgap (1.64eV). For the pseudo-tandem performances projection, we considered the ST perovskite top cell of 16.7% efficiency.
- Pseudo-tandem #B: This device is composed of a-Si bottom cell and a top-cell filter, with a PTAA HTL and a perovskite layer fabricated by slot-die and displaying a high bandgap (1.64eV). For the pseudo-tandem performances projection, we considered the ST perovskite top cell of 14.8% efficiency.
- Pseudo-tandem #C: This device is composed of a-Si bottom cell and a top-cell filter, with a Spiro-OMETAD HTL and a perovskite layer fabricated by spin-coating and displaying a low bandgap (1.56eV). For the pseudo-tandem performances projection, we considered the ST perovskite top cell of 17.7% efficiency.
- Pseudo-tandem #D: This device is composed of a-Si bottom cell and a top-cell filter, with a PTAA HTL and a perovskite layer fabricated by spin-coating and displaying a low bandgap (1.56eV). For the pseudo-tandem performances projection, we considered the ST perovskite top cell of 17.3% efficiency.

The efficiency of all c-Si bottom cells was similar, with only minor variations of their electrical properties, as shown in **Figure IV-21.c.** and **Table IV-1.** The c-Si cell #B presents a higher FF (75%) than the others (73-74%). However, the c-Si cell #C has the best efficiency (19.9%) with the highest J_{sc} (39.3 mA.cm⁻²). The c-Si cell #D shows the lower electrical properties, with an efficiency of 19.1%.

The performances measured on the filtered c-Si cells are 6.4% for the Spiro-OMeTAD (#A) and 6.6% for the PTAA (#B) devices fabricated by slot-die and displays 5.7% for the Spiro-OMeTAD (#C) and 5.6% for the PTAA (#D) devices fabricated by spin-coating. Compared with their equivalents by spin-coating, the slot-die devices show an improved efficiency of +11% between #A and #C and +15% between #C and #D. This gain can be attributed to the broader bandgap of the perovskite (1.64 eV) fabricated by slot-die, compared to the spin-coating baseline smaller bandgap (1.56eV). These results present encouraging perspectives for tandem application with a large bandgap perovskite fabricated by slot-die.

The rebuilt tandem efficiencies yield up to 23.1% (16.7% + 6.4%) for the Spiro-OMeTAD device (#A) and 21.4% (14.8% + 6.6%) for the PTAA device (#B). The rebuilt tandem efficiencies for spin-coating devices demonstrate 24.2% (17.7% + 5.7%) for the Spiro-OMeTAD device (#C) and 22.9% (17.3%+5.6%) for the PTAA device (#D). The slot-die-based pseudo-tandem devices show lower efficiencies. This difference can be attributed to the lower average performances of the initial semi-transparent solar cells fabricated by slot-die compared to the spin-coating device. Notably, the efficiency of the PTAA devices, with an absorber layer fabricated by slot-die, are widely dependant on the perovskite roughness and further optimization of the perovskite/PTAA interface is crucial to reach higher efficiencies.

Our results are comparable to the reconstructed tandem performances achieved with a ST perovskite cell (Spiro-OMeTAD HTL and ITO transparent electrode) presented by A. J. Bett *et al.* who achieved efficiencies of up to 24.2% efficiency.²² In their publication, they added a MGF₂ antireflection coating to reduce the optical losses, which allowed an efficiency gain of 2.4%. Though, when compared to the literature^{22,32} our solar cells suffer from a lower current, which impacts its final efficiency in single-junction and tandem configuration. This loss might be reduced by an increase in the perovskite absorber layer thickness.

However, these tandem efficiencies only represent preliminary results based on the optical characterization of the possible tandem stack. Notably, the semi-transparent efficiencies are issued from small-scale solar cells where spin-coating deposition is the most efficient fabrication process. For larger devices, though, slot-die represent a more promising path, which would result in more homogeneous deposition and higher efficiencies, as reported in **Chapter 1.**

Table IV-1: *Electrical properties of semi-transparent perovskite cells, silicon cells, and pseudo-tandem device.*³³

#Device	Perovskite deposition method	Cells	PCE	J_{sc}	V_{oc}	FF
			%	$mA.cm^{-2}$	V	%
A	Slot-die	Best Psk cell (Spiro-OMeTAD)	16.7	19.9	1.16	73
		c-Si bottom cell	19.3	38.2	0.67	75
		Filtered Psk (Spiro)/c-Si/PDMS	6.4	12.7	0.65	76
		Pseudo-tandem efficiency (%)	23.1			
B	Slot-die	Best Psk Cell (PTAA)	14.8	18.9	1.06	71
		c-Si bottom cell	19.7	38.0	0.69	75
		Filtered Psk (PTAA)/c-Si/PDMS	6.6	13.1	0.65	77
		Pseudo-tandem efficiency (%)	21.4			
C	<i>Spin-coating (Baseline)</i>	<i>Best Psk cell (Spiro-OMeTAD)</i>	17.7	21.5	1.08	76
		<i>c-Si bottom cell</i>	19.9	39.3	0.68	74
		<i>Filtered Psk (Spiro)/c-Si/PDMS</i>	5.7	11.2	0.66	77
		Pseudo-tandem efficiency (%)	24.2			
D	<i>Spin-coating (Baseline)</i>	<i>Best Psk Cell (PTAA)</i>	17.3	21.7	1.08	74
		<i>c-Si bottom cell</i>	19.1	37.8	0.69	73
		<i>Filtered Psk (PTAA)/c-Si/PDMS</i>	5.6	11.6	0.65	75
		Pseudo-tandem efficiency (%)	22.9			

5. Conclusions

In this chapter, we presented the added value of the combined addition of MACl and a zwitterionic surfactant 3DPS to improve the morphology and the crystallinity of the perovskite layer. We showed that an optimized ratio of 2.5 mM of 3DPS with a (MACl: FAI) molar ratio of (0.3: 1) enhances the grain size, from 387 nm to 543 nm, while significantly decreasing the surface roughness, from $Sa = 56$ nm to $Sa = 22$ nm.

Based on this optimization, we fabricated full devices with classical n-i-p architecture and Spiro-OMeTAD as a HTL. The best perovskite cell, fabricated with MACl and 3DPS, reached up to 17.8% efficiency, which is the best efficiency for an opaque solar cell reported in this work. However, the adverse effect of parasitic absorption shown by Spiro-OMETAD is quite significant and cannot be ignored. Therefore, we tested perovskite devices fabricated with PTAA instead of Spiro-OMeTAD as a HTL. The best PTAA-based devices reached a PCE of 16.8% and stabilized at 15.5%. The evolution of the efficiency of the devices during 45 days evidenced the added value of the PTAA to enhance the device stability under dark and vacuum deposition conditions.

To further improve the efficiency and stability, the introduction of a buffer layer between the perovskite and the HTL could be interesting and can be seen as a perspective of this work. Indeed, in the literature, several groups have studied the role of interlayers such as PMMA³⁴, MoO₃²⁷, or PCBM³⁵, suggesting it can passivate the perovskite surface and improve the affinity with the HTL.

In addition, for future optimizations of the semi-transparent devices, it could be relevant to increase the thickness of the absorber to limit the absorption losses. By simulation studies, Zhao *et al.* proposed the optimal thickness of the perovskite layer in a tandem configuration to be 600-700 nm, to reduce optical losses without a significant cost of absorbance in the silicon bottom cell.³⁶

Finally, we fabricated semi-transparent perovskite solar cells by replacing gold with a transparent ITO layer as the top electrode. We obtained a maximum efficiency of 16.7% with a Spiro-OMeTAD device and 14.8% with a PTAA device. However, even if the PTAA-based devices exhibited a lower efficiency on average compared to Spiro-OMeTAD, the PTAA displayed a better resistance to the sputtering conditions and also afforded a better reproducibility. We evaluated the potential of our semi-transparent architecture integrated into a pseudo-tandem stack, combining the best results obtained for a semi-transparent cell and associated filtered silicon solar cells. We reached over 23.1% for the spiro-OMeTAD-based device and 21.4% for the PTAA-based device.

6. References

- (1) Deng, Y.; Zheng, X.; Bai, Y.; Wang, Q.; Zhao, J.; Huang, J. Surfactant-Controlled Ink Drying Enables High-Speed Deposition of Perovskite Films for Efficient Photovoltaic Modules. *Nat. Energy* **2018**, *3* (7), 560–566. <https://doi.org/10.1038/s41560-018-0153-9>.
- (2) Lee, B.; Hwang, T.; Lee, S.; Shin, B.; Park, B. Microstructural Evolution of Hybrid Perovskites Promoted by Chlorine and Its Impact on the Performance of Solar Cell. *Sci. Rep.* **2019**, *9* (1), 4803. <https://doi.org/10.1038/s41598-019-41328-5>.
- (3) Liu, K.; Liang, Q.; Qin, M.; Shen, D.; Yin, H.; Ren, Z.; Zhang, Y.; Zhang, H.; Fong, P. W. K.; Wu, Z.; Huang, J.; Hao, J.; Zheng, Z.; So, S. K.; Lee, C.-S.; Lu, X.; Li, G. Zwitterionic-Surfactant-Assisted Room-Temperature Coating of Efficient Perovskite Solar Cells. *Joule* **2020**, *4* (11), 2404–2425. <https://doi.org/10.1016/j.joule.2020.09.011>.
- (4) Wang, Q.; Zheng, X.; Deng, Y.; Zhao, J.; Chen, Z.; Huang, J. Stabilizing the α -Phase of CsPbI₃ Perovskite by Sulfobetaine Zwitterions in One-Step Spin-Coating Films. *Joule* **2017**, *1* (2), 371–382. <https://doi.org/10.1016/j.joule.2017.07.017>.
- (5) Hawash, Z.; Ono, L. K.; Qi, Y. Recent Advances in Spiro-MeOTAD Hole Transport Material and Its Applications in Organic–Inorganic Halide Perovskite Solar Cells. *Adv. Mater. Interfaces* **2018**, *5* (1), 1700623. <https://doi.org/10.1002/admi.201700623>.
- (6) Rombach, F. M.; Haque, S. A.; Macdonald, T. J. Lessons Learned from Spiro-OMeTAD and PTAA in Perovskite Solar Cells. *Energy Environ. Sci.* **2021**. <https://doi.org/10.1039/D1EE02095A>.
- (7) Yang, Y.; Hoang, M. T.; Yao, D.; Pham, N. D.; Tiong, V. T.; Wang, X.; Wang, H. Spiro-OMeTAD or CuSCN as a Preferable Hole Transport Material for Carbon-Based Planar Perovskite Solar Cells. *J. Mater. Chem. A* **2020**, *8* (25), 12723–12734. <https://doi.org/10.1039/D0TA03951A>.
- (8) Jena, A. K.; Numata, Y.; Ikegami, M.; Miyasaka, T. Role of Spiro-OMeTAD in Performance Deterioration of Perovskite Solar Cells at High Temperature and Reuse of the Perovskite Films to Avoid Pb-Waste. *J. Mater. Chem. A* **2018**, *6* (5), 2219–2230. <https://doi.org/10.1039/C7TA07674F>.
- (9) Tumen-Ulzii, G.; Qin, C.; Matsushima, T.; Leyden, M. R.; Balijipalli, U.; Klotz, D.; Adachi, C. Understanding the Degradation of Spiro-OMeTAD-Based Perovskite Solar Cells at High Temperature. **2020**, *8*.

- (10) Ko, Y.; Kim, Y.; Lee, C.; Kim, Y.; Jun, Y. Investigation of Hole-Transporting Poly(Triarylamine) on Aggregation and Charge Transport for Hysteresisless Scalable Planar Perovskite Solar Cells. *ACS Appl. Mater. Interfaces* **2018**, *10* (14), 11633–11641. <https://doi.org/10.1021/acsami.7b18745>.
- (11) Kim, J.; Park, N.; Yun, J. S.; Huang, S.; Green, M. A.; Ho-Baillie, A. W. Y. An Effective Method of Predicting Perovskite Solar Cell Lifetime—Case Study on Planar CH₃NH₃PbI₃ and HC(NH₂)₂PbI₃ Perovskite Solar Cells and Hole Transfer Materials of Spiro-OMeTAD and PTAA. *Sol. Energy Mater. Sol. Cells* **2017**, *162*, 41–46. <https://doi.org/10.1016/j.solmat.2016.12.043>.
- (12) Mesquita, I.; Andrade, L.; Mendes, A. Temperature Impact on Perovskite Solar Cells Under Operation. *ChemSusChem* **2019**, *12* (10), 2186–2194. <https://doi.org/10.1002/cssc.201802899>.
- (13) Yang, J.; Siempelkamp, B. D.; Liu, D.; Kelly, T. L. Investigation of CH₃NH₃PbI₃ Degradation Rates and Mechanisms in Controlled Humidity Environments Using in Situ Techniques. *ACS Nano* **2015**, *9* (2), 1955–1963. <https://doi.org/10.1021/nn506864k>.
- (14) Lal, N. N.; Dkhissi, Y.; Li, W.; Hou, Q.; Cheng, Y.-B.; Bach, U. Perovskite Tandem Solar Cells. *Adv. Energy Mater.* **2017**, *7* (18), 1602761. <https://doi.org/10.1002/aenm.201602761>.
- (15) Bremner; Levy, M. Y.; Honsberg, C. B. Analysis of Tandem Solar Cell Efficiencies under {AM1.5G} Spectrum Using a Rapid Flux Calculation Method. *Prog. Photovolt. Res. Appl.* **2008**, *16*, 225–233. <https://doi.org/10.1002/pip.799>.
- (16) Wang, Z.; Song, Z.; Yan, Y.; Liu, S. (Frank); Yang, D. Perovskite—a Perfect Top Cell for Tandem Devices to Break the S–Q Limit. *Adv. Sci.* **2019**, *6* (7), 1801704. <https://doi.org/10.1002/advs.201801704>.
- (17) Kim, D.; Jung, H. J.; Park, I. J.; Larson, B. W.; Dunfield, S. P.; Xiao, C.; Kim, J.; Tong, J.; Boonmongkolras, P.; Ji, S. G.; Zhang, F.; Pae, S. R.; Kim, M.; Kang, S. B.; Dravid, V.; Berry, J. J.; Kim, J. Y.; Zhu, K.; Kim, D. H.; Shin, B. Efficient, Stable Silicon Tandem Cells Enabled by Anion-Engineered Wide-Bandgap Perovskites. *Science* **2020**, *368* (6487), 155–160. <https://doi.org/10.1126/science.aba3433>.
- (18) Chen, B.; Yu, Z.; Liu, K.; Zheng, X.; Liu, Y.; Shi, J.; Spronk, D.; Rudd, P. N.; Holman, Z.; Huang, J. Grain Engineering for Perovskite/Silicon Monolithic Tandem Solar Cells with Efficiency of 25.4%. *Joule* **2019**, *3* (1), 177–190. <https://doi.org/10.1016/j.joule.2018.10.003>.

- (19) Jäger, K.; Sutter, J.; Hammerschmidt, M.; Schneider, P.-I.; Becker, C. Prospects of Light Management in Perovskite/Silicon Tandem Solar Cells. *Nanophotonics* **2020**, *10* (8), 1991–2000. <https://doi.org/10.1515/nanoph-2020-0674>.
- (20) Challali, F.; Mendil, D.; Touam, T.; Chauveau, T.; Bockelée, V.; Sanchez, A. G.; Chelouche, A.; Besland, M.-P. Effect of RF Sputtering Power and Vacuum Annealing on the Properties of AZO Thin Films Prepared from Ceramic Target in Confocal Configuration. *Mater. Sci. Semicond. Process.* **2020**, *118*, 105217. <https://doi.org/10.1016/j.mssp.2020.105217>.
- (21) Lim, S.-H.; Seok, H.-J.; Kwak, M.-J.; Choi, D.-H.; Kim, S.-K.; Kim, D.-H.; Kim, H.-K. Semi-Transparent Perovskite Solar Cells with Bidirectional Transparent Electrodes. *Nano Energy* **2021**, *82*, 105703. <https://doi.org/10.1016/j.nanoen.2020.105703>.
- (22) Park, H. H. Transparent Electrode Techniques for Semitransparent and Tandem Perovskite Solar Cells. *Electron. Mater. Lett.* **2021**, *17*, 18–32. <https://doi.org/10.1007/s13391-020-00259-4>.
- (23) Bett, A. J.; Winkler, K. M.; Bivour, M.; Cojocaru, L.; Kabakli, Ö. S.; Schulze, P. S. C.; Siefer, G.; Tutsch, L.; Hermle, M.; Glunz, S. W.; Goldschmidt, J. C. Semi-Transparent Perovskite Solar Cells with ITO Directly Sputtered on Spiro-OMeTAD for Tandem Applications. *ACS Appl. Mater. Interfaces*. 49th ed. 2019, pp 45796–45804.
- (24) Fu, F.; Feurer, T.; Jäger, T.; Avancini, E.; Bissig, B.; Yoon, S.; Buecheler, S.; Tiwari, A. N. Low-Temperature-Processed Efficient Semi-Transparent Planar Perovskite Solar Cells for Bifacial and Tandem Applications. *Nat. Commun.* **2015**, *6* (1), 8932. <https://doi.org/10.1038/ncomms9932>.
- (25) Santbergen, R.; Mishima, R.; Meguro, T.; Hino, M.; Uzu, H.; Blanker, J.; Yamamoto, K.; Zeman, M. Minimizing Optical Losses in Monolithic Perovskite/c-Si Tandem Solar Cells with a Flat Top Cell. *Opt. Express* **2016**, *24* (18), A1288–A1299. <https://doi.org/10.1364/OE.24.0A1288>.
- (26) Jiang, Y.; Almansouri, I.; Huang, S.; Young, T.; Li, Y.; Peng, Y.; Hou, Q.; Spiccia, L.; Bach, U.; Cheng, Y.-B.; Green, M. A.; Ho-Baillie, A. Optical Analysis of Perovskite/Silicon Tandem Solar Cells. *J. Mater. Chem. C* **2016**, *4* (24), 5679–5689. <https://doi.org/10.1039/C6TC01276K>.
- (27) Sambles, J. R.; Elsom, K. C.; Jarvis, D. J. The Electrical Resistivity of Gold Films. *Philos. Trans. R. Soc. Lond. Ser. Math. Phys. Sci.* **1982**, *304* (1486), 365–396.
- (28) Chen, B.; Baek, S.-W.; Hou, Y.; Aydin, E.; De Bastiani, M.; Scheffel, B.; Proppe, A.; Huang, Z.; Wei, M.; Wang, Y.-K.; Jung, E.-H.; Allen, T. G.; Van Kerschaver,

- E.; García de Arquer, F. P.; Saidaminov, M. I.; Hoogland, S.; De Wolf, S.; Sargent, E. H. Enhanced Optical Path and Electron Diffusion Length Enable High-Efficiency Perovskite Tandems. *Nat. Commun.* **2020**, *11* (1). <https://doi.org/10.1038/s41467-020-15077-3>.
- (29) Duong, T.; Wu, Y.; Shen, H.; Peng, J.; Fu, X.; Jacobs, D.; Wang, E.-C.; Kho, T. C.; Fong, K. C.; Stocks, M.; Franklin, E.; Blakers, A.; Zin, N.; McIntosh, K.; Li, W.; Cheng, Y.-B.; White, T. P.; Weber, K.; Catchpole, K. Rubidium Multication Perovskite with Optimized Bandgap for Perovskite-Silicon Tandem with over 26% Efficiency. *Adv. Energy Mater.* **2017**, *7* (14), 1700228. <https://doi.org/10.1002/aenm.201700228>.
- (30) Xu, Y.; Wang, J.; Sun, L.; Huang, H.; Han, J.; Huang, H.; Zhai, L.; Zou, C. Top Transparent Electrodes for Fabricating Semitransparent Organic and Perovskite Solar Cells. *J. Mater. Chem. C* **2021**, *9* (29), 9102–9123. <https://doi.org/10.1039/D1TC02413B>.
- (31) Akhil, S.; Akash, S.; Pasha, A.; Kulkarni, B.; Jalalah, M.; Alsaiani, M.; Harraz, F. A.; Balakrishna, R. G. Review on Perovskite Silicon Tandem Solar Cells: Status and Prospects 2T, 3T and 4T for Real World Conditions. *Mater. Des.* **2021**, *211*, 110138. <https://doi.org/10.1016/j.matdes.2021.110138>.
- (32) Albrecht, S.; Saliba, M.; Baena, J. P. C.; Lang, F.; Kegelmann, L.; Mews, M.; Steier, L.; Abate, A.; Rappich, J.; Korte, L.; Schlattmann, R.; Nazeeruddin, M. K.; Hagfeldt, A.; Grätzel, M.; Rech, B. Monolithic Perovskite/Silicon-Heterojunction Tandem Solar Cells Processed at Low Temperature. *Energy Environ. Sci.* **2016**, *9* (1), 81–88. <https://doi.org/10.1039/C5EE02965A>.
- (33) Jaysankar, M.; Qiu, W.; van Eerden, M.; Aernouts, T.; Gehlhaar, R.; Debucquoy, M.; Paetzold, U. W.; Poortmans, J. Four-Terminal Perovskite/Silicon Multijunction Solar Modules. *Adv. Energy Mater.* **2017**, *7* (15), 1602807. <https://doi.org/10.1002/aenm.201602807>.
- (34) Raoult, S.; Guillemot, T.; Bernard, S.; Provost, M.; Daniau, V.; Yaiche, A.; Schneider, N.; Coutencier, D.; Bodeux, R.; Collin, S.; Rousset, J.; Jutteau, S. Toward a Highly Efficient Large Surface Perovskite Silicon 4-Terminal Tandem Module; 2021.
- (35) McKenna, B.; Troughton, J. R.; Watson, T. M.; Evans, R. C. Enhancing the Stability of Organolead Halide Perovskite Films through Polymer Encapsulation. *RSC Adv.* **2017**, *7* (52), 32942–32951. <https://doi.org/10.1039/C7RA06002E>.
- (36) Qiu, W.; Bastos, J. P.; Dasgupta, S.; Merckx, T.; Cardinaletti, I.; Jenart, M. V. C.; Nielsen, C. B.; Gehlhaar, R.; Poortmans, J.; Heremans, P.; McCulloch, I.; Cheyns,

- D. Highly Efficient Perovskite Solar Cells with Crosslinked PCBM Interlayers. *J. Mater. Chem. A* **2017**, 5 (6), 2466–2472. <https://doi.org/10.1039/C6TA08799J>.
- (37) Zhao, P.; Yue, M.; Lei, C.; Lin, Z.; Su, J.; Chen, D.; Zhang, C.; Zhang, J.; Chang, J.; Hao, Y. Device Simulation of Organic–Inorganic Halide Perovskite/Crystalline Silicon Four-Terminal Tandem Solar Cell With Various Antireflection Materials. *IEEE J. Photovolt.* **2018**, 8 (6), 1685–1691. <https://doi.org/10.1109/JPHOTOV.2018.2869743>.

General conclusion and perspectives

In this work, we focused on developing a reliable fabrication process of a perovskite absorber by slot-die. The main goal was to introduce a new competence within the IPVF laboratory to fabricate large-area perovskite-based devices.

The first chapter presented the general context of the study, with a growing part of the photovoltaic technology in the energy production landscape. The bibliography work outlined the main technological advances in the field of perovskite-based PV technologies. It appears that upscaling remains one of the biggest challenges to ensure an industrial future for perovskite solar devices. To better understand the nucleation and growth mechanisms taking place during the deposition of the perovskite layer, we detailed the different existing theoretical models. This approach of fundamental crystallization theory allowed us, on the one hand, to highlight the main parameters influencing the growth of perovskite layers and, on the other hand, identify the still existing blind spots. Then, we reviewed the different upscale deposition methods and the associated solvent extraction systems. Finally, we decided to use a vacuum aspiration system combined with the slot-die deposition to fabricate the perovskite absorber on $5 \times 10 \text{ cm}^2$ substrates.

In the second chapter, we detailed the main fabrication steps of a complete perovskite-based solar device. On a first hand, we developed a n-i-p architecture composed of a bi-layer of TiO_2 for the ETL, spiro-OMeTAD for the HTL, a perovskite absorber layer, and a gold top electrode. According to the literature review, the tailoring of the perovskite ink appeared to be an interesting path to adapt to the new constraints of the large-scale deposition method and allow a fine control of the crystallization steps. Consequently, we studied the influence of a surfactant addition on the perovskite properties. We fabricated a perovskite layer with two different compositions: the first one $\text{Cs}_{0.17}\text{FA}_{0.83}\text{Pb}(\text{I}_{0.83}\text{Br}_{0.17})_3$ presenting a low bandgap of $E_g = 1.58 \text{ eV}$. And a second one $\text{Cs}_{0.17}\text{FA}_{0.73}\text{Pb}(\text{I}_{0.6}\text{Br}_{0.4})_3$, presenting a high bandgap of $E_g = 1.7 \text{ eV}$. The surfactant had very interesting effects on the perovskite morphology, improving the film coverage and drastically reducing the surface roughness. With the addition of 30 mM of surfactant in the perovskite solution, we obtained a maximum PCE of 12.3% and 9.2% on 0.09 cm^2 aperture area, for low bandgap and high bandgap compositions, respectively. However, in both cases, the surfactant addition met a concentration threshold, after which the surfactant ended up being detrimental to the devices' efficiency. It appeared that this strategy had severe limitations for the fabrication of high-efficiency perovskite devices.

In the third chapter, we changed the additive and selected MACl as identified in the literature as an efficient complexing agent. Moreover, in the previous chapter, we noticed that the perovskite composition $\text{Cs}_{0.17}\text{FA}_{0.73}\text{Pb}(\text{I}_{0.6}\text{Br}_{0.4})_3$ presented a significant instability under illumination due to its important bromide content. Therefore, in this part, we decided to work on a perovskite composition $\text{Cs}_{0.17}\text{FA}_{0.83}\text{Pb}(\text{I}_{0.83}\text{Br}_{0.17})_3$ with an intermediate bandgap ($E_g = 1.64$ eV) and a lower bromide content. Different MACl concentrations and annealing conditions have been explored, and their impact on the optoelectronic properties of the perovskite film has been thoroughly investigated. We identified a MACl: FAI molar ratio of (0.3:1) followed by a 30 minutes annealing at 140°C as the optimal combination. This approach led us to reach a stabilized PCE of 17.5 % on a small-scale device fabricated with slot-die coating. After that, we encapsulated the fabricated devices and monitored the PCE evolution during 300 hours under continuous illumination and at the maximum power point. Our study underlined the beneficial effect of MACl addition on the device's stability. The degradation of the perovskite stack was further investigated by STEM technique and allowed us to identify the main degradation paths of the spiro-OMeTAD layer and the absorber. Finally, 12 cm^2 modules have been fabricated and reached up to 15% efficiency, which proved the compatibility of the developed process on larger surfaces.

Finally, in the fourth chapter, we presented the influence of the combined addition of MACl and the zwitterionic surfactant on the morphology and the crystal structure of the perovskite layer. We showed that an optimized ratio of 2.3 mM of 3DPS combined with a (MACl: FAI) molar ratio of (0.3: 1) enhances the crystal size and significantly decreases the surface roughness. We fabricated full perovskite devices with a classical NIP architecture and a spiro-OMeTAD HTL layer, and the best device reached up to 17.8% efficiency, which is the best efficiency reported in this work. The main challenge during this study has been to find a proper trade-off between the two additives without impacting the performances of the final devices.

Then, perovskite devices have been fabricated with a PTAA HTL. The best PTAA devices reached a PCE of 16.8% and stabilized at 15.5%. The evolution of the device's efficiency during 45 days evidenced a significantly enhanced stability for the devices with PTAA compared to the devices with spiro-OMeTAD. Then, we fabricated semi-transparent perovskite solar cells by depositing a transparent ITO layer as the top electrode. We obtained a maximum efficiency of 16.7% with a spiro-OMeTAD device and 14.8% with a PTAA device. However, even if the PTAA devices presented a lower efficiency on average than spiro-OMeTAD, the PTAA displayed a better resilience to the sputtering process and allowed a better reproducibility from batch to batch.

Finally, in the literature review, we highlighted that tandem configuration was one of the most promising paths for future industrial application of the perovskite solar cells. Therefore, we wanted to evaluate the potential of our semi-transparent architecture integrated into a pseudo-tandem stack. We combined the best results obtained for a semi-transparent cell and measured the performance of filtered silicon solar cells. As a result, we obtained a calculated pseudo-tandem efficiency of 23.1% with our spiro-OMeTAD

stack and 21.4% efficiency with our PTAA stack. Even if there is some room for improvements, it represents encouraging results and validates the compatibility of the developed semi-transparent architecture with tandem configurations.

To conclude, in this Ph.D. work, we designed and optimized a complete fabrication process of the perovskite absorber layer by slot-die. We explored different perovskite compositions to explore large bandgaps compatible with tandem applications. Starting from small-scale devices of 2 x 2.5 cm², we successfully transferred this process to 12cm² modules.

In this work, we chose to focus on a chemical approach to address the modification of nucleation and growth mechanisms during crystallization. The use of additives is an easy-going method, with various promising candidates. Moreover, from an industrial perspective, the use of additives can represent a flexible way to adapt to a wide range of perovskite compositions, depositions methods, or production throughputs. However, as illustrated in the bibliography review, vacuum aspiration is not the only solvent extraction method compatible with large-scale deposition processes. An air-blade or intense-light exposure can open large possibilities for further optimizations in the future.

In addition, this work mainly focused on the synthesis of the perovskite absorber layer. However, from now on, work on the transport layers seems necessary to improve the stability and upscale compatibility of future devices. In the literature, planar architectures (with SnO₂ as ETL layer, for example) represent an interesting path for large-area perovskite modules. Planar HTL reduces the complexity of the fabrication process and is more reproducible than mesoporous TiO₂.

Finally, it could be interesting to investigate the insertion of interlayers. Then, the encapsulation process has to be developed for large-area modules to enhance the stability of the fabricated devices. Finally, many additives, such as acetate-based precursors, have shown promising results and could be experimented with for slot-die fabrication.

We are still at an early stage of understanding and addressing the challenges of scaling up perovskite devices, with respect to the myriad perovskite composition and device architectures. However, the rapid development towards scaling up at a relevant performance level coupled with the low-cost manufacturing capability has already attracted substantial industrial interest worldwide. If the remaining challenges for efficiency and stability can be addressed, the potential for PSCs, compared with other PV technologies, to have an impact on global energy production at the terawatt scale is unrivalled.

Appendix

- **Annex 1:** *Photovoltaic Effect*
- **Annex 2:** *Silicon and Thin-film PV Technologies*
- **Annex 3:** *Best Research-Cell Efficiencies of NREL*
- **Annex 4:** *Champion Modules Efficiencies of NREL*
- **Annex 5:** *Determination of crystal size and strains by Williamson-Hall method*
- **Annex 6:** *J-V parameters (best cells and average) of solar cell devices of NIP architecture: Glass/FTO/c-TiO₂/m-TiO₂/Cs_{0.2}FA_{0.8}Pb(I_{0.95}Br_{0.05})₃/Spiro-OMeTAD /Au.*
- **Annex 7:** *J-V parameters (best cells and average) of solar cell devices of NIP architecture: Glass/FTO/c-TiO₂/m-TiO₂/Cs_{0.17}A_{0.83}Pb(I_{0.6}Br_{0.4})₃/ Spiro-OMeTAD/Au.*
- **Annex 8:** *J-V parameters before and after encapsulation of perovskite solar cells selected for the aging test.*
- **Annex 9:** *J-V parameters (best cells and average) of solar cell devices of NIP architecture: Glass/FTO/c-TiO₂/m-TiO₂/Cs_{0.17}FA_{0.83}Pb(I_{0.83}Br_{0.17})₃/Spiro-OMeTAD /Au.*
- **Annex 10:** *J-V parameters (best cells and average) of solar cell devices of NIP architecture: Glass/FTO/c-TiO₂/m-TiO₂/Cs_{0.17}FA_{0.83}Pb(I_{0.83}Br_{0.17})₃/PTAA /Au.*
- **Annex 11:** *J-V parameters of aged perovskite devices fabricated with spiro-OMeTAD or PTAA HTL layer.*
- **Annex 12:** *Deposition process of the ITO transparent electrode.*
- **Annex 13:** *J-V parameters of fresh and aged semi-transparent perovskite devices of NIP architecture: Glass/FTO/c-TiO₂/m-TiO₂/Cs_{0.17}FA_{0.83}Pb(I_{0.83}Br_{0.17})₃/Spiro-OMeTAD or PTAA /ITO/Au.*
- **Annex 14:** *Fabrication process of pseudo-tandem devices*

Annex 1: Photovoltaic Effect

A solar cell is generally a semiconductor device that converts light energy into electrical energy. Certain specificities exist depending on the different photovoltaic technologies, but the basic principle remains unchanged. The key material in a solar cell is the absorber material which absorbs the incident light and generates an electron-hole pair, illustrated in **Figure 1. a**. The electrons and holes are separated within the semiconductor or at a PN junction and collected at their respective electrodes.

Semiconductor materials are characterized by the existence of an energy band forbidden for electrons whose defined width, also called gap, separates two bands of permitted energies (**Figure 1. b**): the valence band below, whose levels are practically completely occupied (the electrons involved constituting the chemical bonds between atoms), and the conduction band above, whose levels are almost empty at equilibrium.

When subjected to luminous flux, semiconductors can absorb photons whose energy is equal to or greater than the gap. The absorption of a photon by the material generates the excitation of an electron of the valence band, causing migration of the latter in the conduction band. It creates a hole in the valence band, thus forming an electron-hole pair within the absorber material.

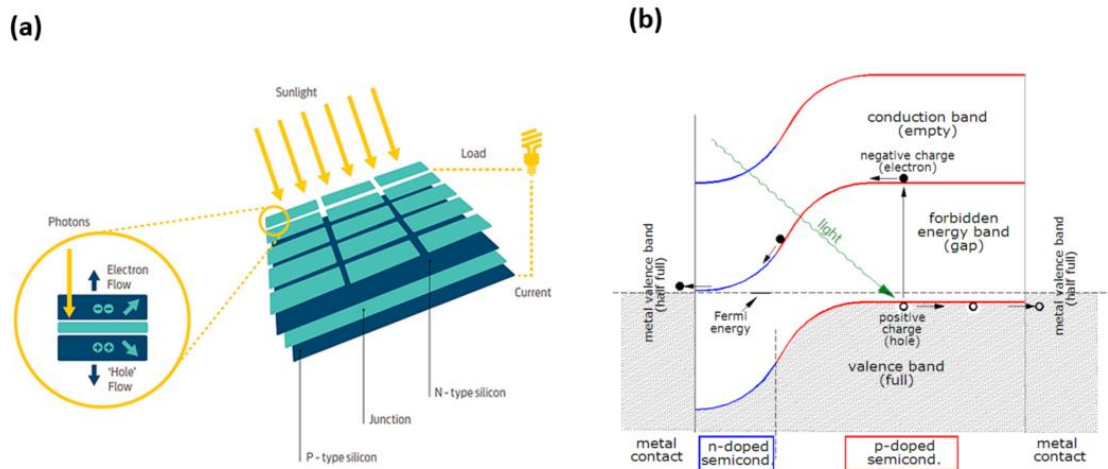


Figure 1: Theory of solar cells. a. Schematic representation of a single junction silicon solar cell. Reproduced from ref. [3]. b. Band diagram of a solar cell, corresponding to horizontal Fermi level. Reproduced from ref. [4].

Annex 2: Silicon and Thin-film PV Technologies

1. Silicon

Crystalline silicon (c-Si), structured with a single p-n junction, is the most prevalent bulk material for solar cells and constitutes 90% of the current market. Bulk silicon is separated into several categories, depending on the crystallinity and crystal size in the resulting ingot, ribbon, or wafer.

Mono-crystalline Silicon

Monocrystalline silicon (mono-Si) solar cells feature a single-crystal composition grown by the Czochralski process, enabling electrons to move more freely than in a multi-crystal configuration. The high quality of the Si absorber material minimizes losses. It offers the highest yields in the sector, with a maximum of 26.1% for a mono-junction device developed by the Institute of Solar Energy Research in Hamelin (ISFH)⁵.

Polycrystalline Silicon

Polycrystalline silicon or multi-crystalline silicon (multi-Si) cells are the products of a simplified fabrication process to reduce fabrication costs. It induces the formation of small crystals, giving the material its typical metal flake effect. The polysilicon cells are the most common type used in photovoltaics but are also less efficient than those made from monocrystalline silicon. The maximum efficiency for a mono-junction device is 23.2%, achieved by Jinko Solar⁶.

Silicon technologies profits from fifty years of research and development, and the sector is moving towards a phase of technological maturity. However, the silicon purification processes, the growth of ingots at high temperatures, losses associated with cutting, and the number of manufacturing steps remain limitations for this technology. Besides, the maximum efficiencies draw near the maximum theoretical limits predicted by the Shockley-Queisser limit⁷, which creates the need to develop alternative photovoltaic technologies and materials.

2. Thin films technologies

Amorphous Si

Historically, amorphous silicon is the first Si technology developed for solar cell applications. Thin-film cells are deposited by chemical vapor deposition (typically plasma-enhanced, PE-CVD) on glass substrates. Amorphous silicon (a-Si) solar cells are composed of non-crystalline or microcrystalline silicon and have a higher bandgap (1.7 eV) than crystalline silicon. However, it displays much lower solar cells efficiencies, with a recorded maximum efficiency of 14%⁸.

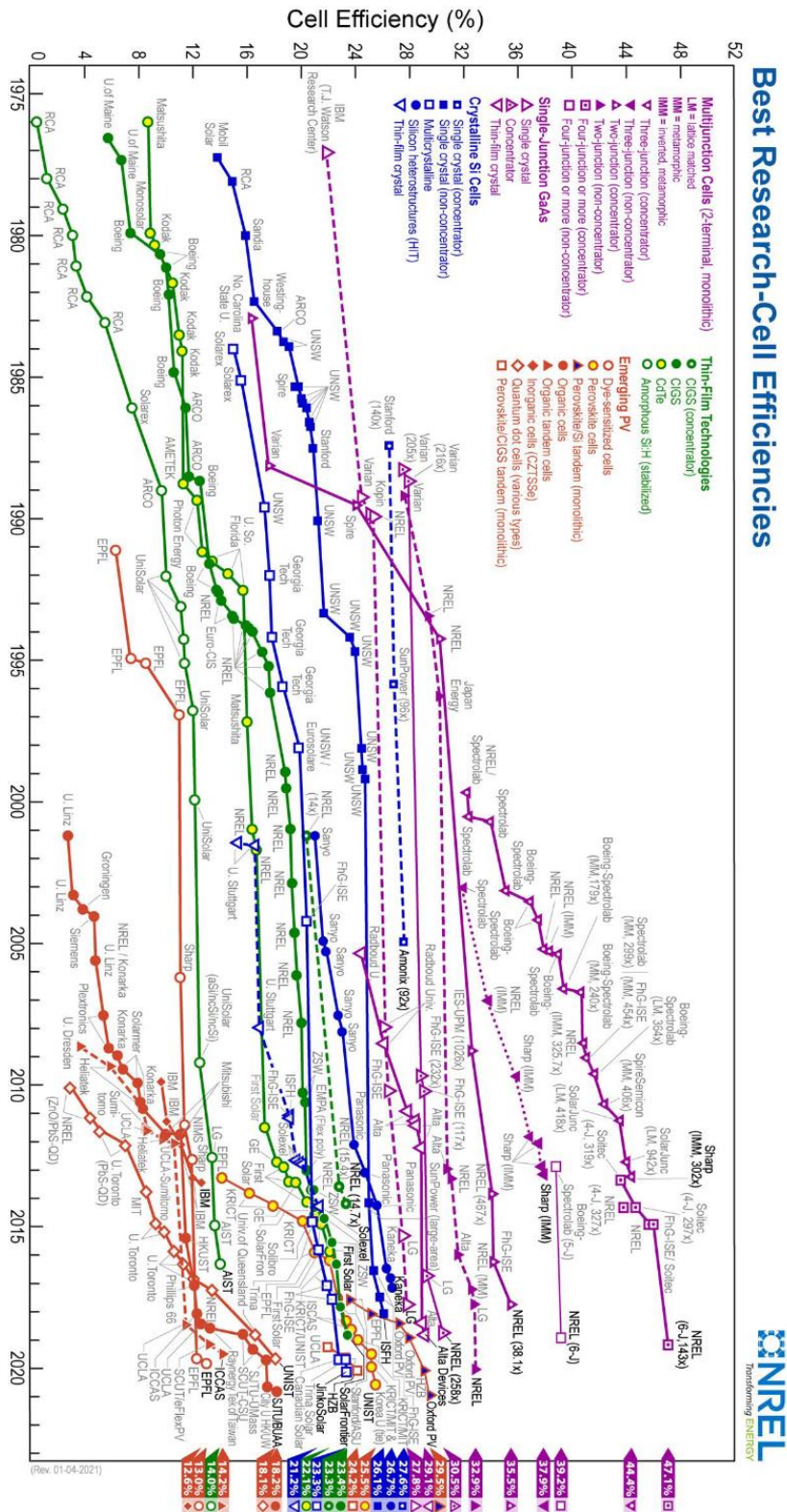
Cadmium Tellurium

With its direct gap of 1.45 eV and excellent semiconductor properties, cadmium telluride (CdTe) provides a maximum efficiency of 22.1%, achieved by First Solar in 2016⁹. However, cadmium present in the cells is highly toxic, and the overall supplies are limited, urging the emergence of less polluting alternatives.

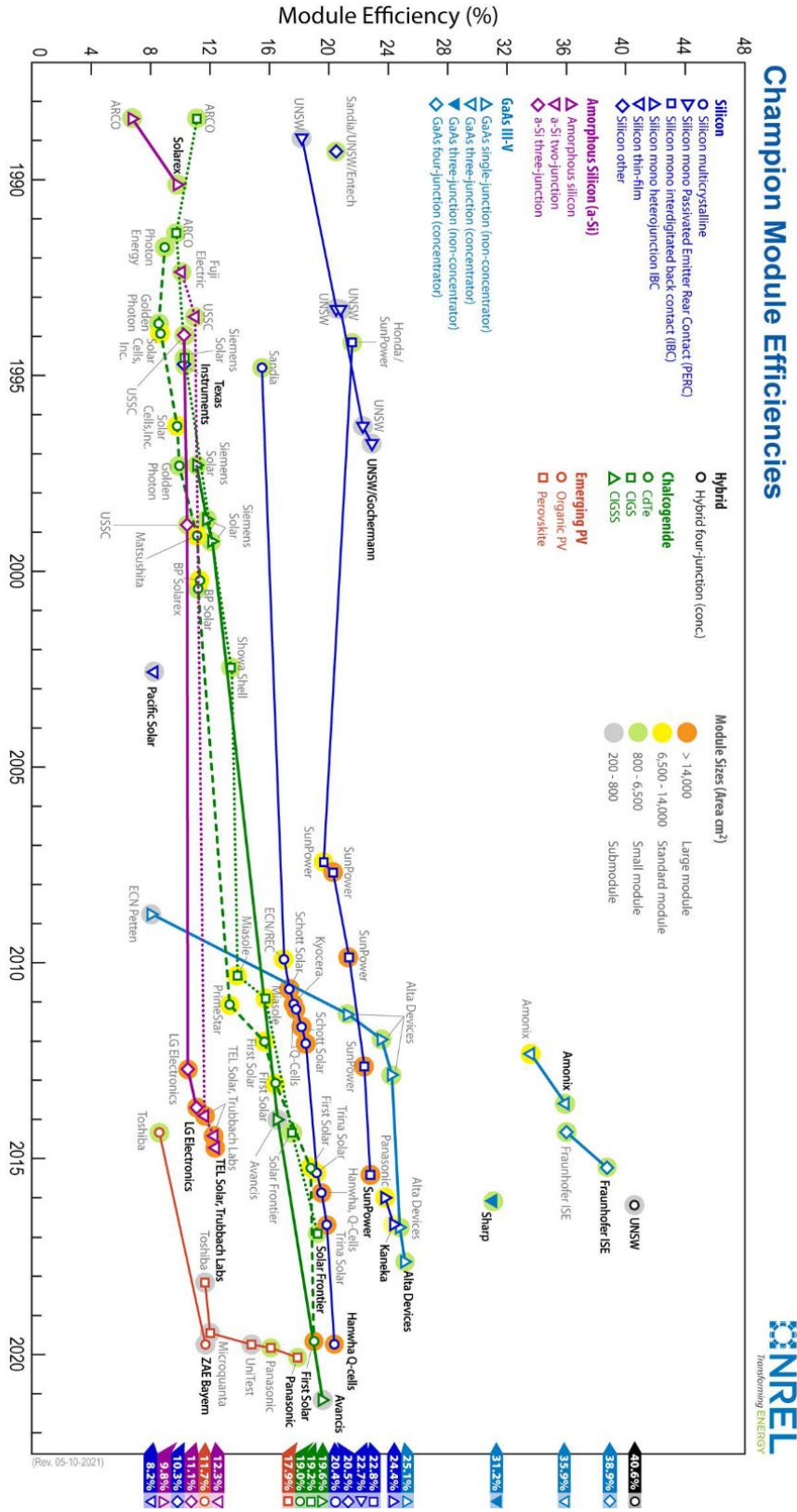
Copper Indium Gallium Selenide

Copper indium gallium selenide (CIGS) is a direct bandgap material. It has the highest efficiency among commercially significant thin-film materials, with a record efficiency of 23.4% claimed by Solar Frontier⁹.

Annex 3: Best Research-Cell Efficiencies of NREL



Annex 4: Champion Modules Efficiencies of NREL



Annex 5: Determination of crystal size and strains by Williamson-Hall method

In the case of very fine crystallites, the instrumental spread can be neglected. We approximated our grains as isotropic spherical shapes (shape factor $K = 0.88$). The full width at half maximum of the diffraction peak (β_{total}) is determined by both the crystallite size broadening (β_{size}) and the lattice strain broadening (β_{strain}). β_{size} was calculated by the Scherrer equation :

$$\beta_{size} = \frac{K\lambda}{D_{size} \cdot \cos\theta}$$

Where K is the sharp factor ($K=0.94$), λ is the x-ray wavelength of $\text{CuK}\beta$ in nanometers ($\lambda = 0.13847$ nm), D_{size} is the average crystallite size in nanometers, and θ is the Bragg angle in radian, respectively. The lattice strain (ε) is calculated by the following equation:

$$\varepsilon = \left| \frac{\Delta d}{d} \right|$$

From differentiating Braggs equation ($2d\sin\theta = \lambda$), the following is led.

$$2\Delta \cdot d \cdot \sin\theta + 2 \cdot \varepsilon \cdot \cos\theta = 0$$

And θ is defined as:

$$\Delta\theta = \left| \frac{\Delta d}{d} \right| \tan\theta$$

β_{strain} is calculated by the following equation :

$$\beta_{strain} = 2\Delta \cdot d \cdot (2\theta)$$

Where doubling means that the distortion is in ± 2 direction. So, β_{strain} become:

$$\beta_{strain} = 4 \cdot \varepsilon \cdot \tan\theta$$

By assuming that the crystallite size broadening and the lattice strain broadening independently contribute to the full width at half maximum of the peak, β_{total} was calculated by the following equation:

$$\beta_{total} = \beta_{size} + \beta_{strain}$$

Rearranging, according to the previous equation, it gives Williamson-Hall equation:

$$\beta_{total} \cdot \cos\theta = \frac{K\lambda}{D_{size}} \cdot 4 \sin\theta$$

Therefore, the lattice strain (ε) and crystallite size (D_{size}) can be evaluated from the slope and intercept of the approximate curve when $\beta \cos\theta$ is plotted on the y axis, and $4 \sin\theta$ is plotted on the x-axis.

Annex 6: J-V parameters (best cells and average) of solar cell devices of NIP architecture: Glass/FTO/c-TiO₂/m-TiO₂/ Cs_{0.2}FA_{0.8}Pb(I_{0.95}Br_{0.05})₃/Spiro-OMeTAD /Au.

			Voc	Jsc	FF	PCE	MPP
			V	mA/cm ²		%	%
No surfactant	Best cell	Rev	1.01	6.1	70	4.3	10.1
		For	1.01	5.7	65.3	3.8	
	Average	Rev	0,99	5,0	69	3,4	
		For	0,99	4,8	63,6	3,0	
30 mM	Best cell	Rev	1.06	19.3	60.5	12.3	9.6
		For	1.01	18.8	53	10.1	
	Average	Rev	1.08	16.9	66.4	12.0	
		For	1.04	16.4	58.0	9.9	
60 mM	Best cell	Rev	1.03	15.9	64.1	10.5	2.8
		For	1.00	15.9	55.1	8.8	
	Average	Rev	9.7	14.1	64.6	1.1	
		For	8.0	14.0	55.5	1.0	

Annex 7: J-V parameters (best cells and average) of solar cell devices of NIP architecture: Glass/FTO/c-TiO₂/m-TiO₂/ Cs_{0.17}A_{0.83}Pb(I_{0.6}Br_{0.4})₃/Spiro-OMeTAD /Au.

			Voc	Jsc	FF	PCE	MPP
			V	mA/cm ²		%	%
No surfactant	Best cell	<i>Rev</i>	1.03	18.0	56.4	10.4	9.1
		<i>For</i>	0.93	17.6	49.6	8.4	
	Average	<i>Rev</i>	0.99	16.7	52.9	8.8	
		<i>For</i>	0.90	16.1	43.5	6.3	
30 mM	Best cell	Rev	1.14	12.3	65.4	9.2	6.5
		For	1,12	12.0	55.2	7.4	
	Average	<i>Rev</i>	<i>1,12</i>	<i>10.7</i>	<i>60.8</i>	<i>7.5</i>	
		<i>For</i>	<i>1.09</i>	<i>10.0</i>	<i>47.3</i>	<i>5.5</i>	
60 mM	Best cell	<i>Rev</i>	1.13	3.95	51.0	2.3	1.1
		<i>For</i>	1.15	3.95	58.0	2.6	
	Average	<i>Rev</i>	0.95	2.02	53.7	1.0	
		<i>For</i>	1.05	2.49	46.7	1.3	
80 mM	Best cell	<i>Rev</i>	/	/	/	/	
		<i>For</i>	/	/	/	/	
	Average	<i>Rev</i>	/	/	/	/	/
		<i>For</i>	/	/	/	/	

Annex 8: *J-V* parameters before and after encapsulation of perovskite solar cells selected for aging

			Voc	Jsc	FF	PCE
			V	mA/cm ²		%
No MACl + 110°C for 30 mins	Before	<i>Rev</i>	1.02	10.8	76.1	9.3
		<i>For</i>	1.02	12.0	73.0	8.7
	After	<i>Rev</i>	0.96	13.6	70.7	9.2
		<i>For</i>	0.96	13.2	66.7	8.4
No MACl + 140°C for 30 mins	Before	<i>Rev</i>	0.99	14.8	78.7	11.5
		<i>For</i>	0.99	15.5	74.5	11.4
	After	<i>Rev</i>	0.94	16.3	71.2	11.0
		<i>For</i>	0.95	15.7	69.6	10.3
MACl + 110°C for 30 mins	Before	<i>Rev</i>	1.11	18.5	72.0	14.8
		<i>For</i>	1.11	18.6	71.3	14.8
	After	<i>Rev</i>	1.09	18.7	66.9	13.6
		<i>For</i>	1.09	18.9	64.9	13.2
MACl + 140°C for 30 mins	Before	<i>Rev</i>	1.07	17.6	73.2	15.4
		<i>For</i>	1.10	16.9	73.2	15.8
	After	<i>Rev</i>	1.09	20.4	75.3	16.4
		<i>For</i>	1.09	20.2	74.4	16.7
MACl + 170°C for 5 mins	Before	<i>Rev</i>	1.10	18.7	75.1	15.5
		<i>For</i>	1.11	19.2	72.8	15.4
	After	<i>Rev</i>	1.08	19.8	71.3	15.3
		<i>For</i>	1.08	19.8	71.9	15.5
MACl + 200°C for 5 mins	Before	<i>Rev</i>	1.12	17.3	74.8	14.5
		<i>For</i>	1.12	17.5	74.8	14.7
	After	<i>Rev</i>	1.07	17.8	66.8	13.4
		<i>For</i>	1.07	17.7	70.3	12.7

Annex 9: J-V parameters (best cells and average) of solar cell devices of NIP architecture: Glass/FTO/c-TiO₂/m-TiO₂/Cs_{0.17}FA_{0.83}Pb(I_{0.83}Br_{0.17})₃/Spiro-OMeTAD/Au.

			Voc	Jsc	FF	PCE	MPP
			V	mA/cm ²		%	%
MACI/No 3DPS	Best cell	<i>Rev</i>	1.08	20.40	74.6	17.3	17.1
		<i>For</i>	1.11	20.39	77.2	16.4	
	Average	<i>Rev</i>	1.10	19.00	74.4	15.7	
		<i>For</i>	1.11	19.07	73.8	15.5	
MACI/0.7 mM 3DPS	Best cell	<i>Rev</i>	1.09	20.06	76.1	16.7	16.3
		<i>For</i>	1.09	20.09	73.4	16.1	
	Average	<i>Rev</i>	1.10	19.77	75.6	16.4	
		<i>For</i>	1.10	19.82	72.7	15.8	
MACI/1.5 mM 3DPS	Best cell	<i>Rev</i>	1.12	19.85	79.5	17.7	16.9
		<i>For</i>	1.10	20.24	73.1	16.3	
	Average	<i>Rev</i>	1.11	19.52	77.3	16.9	
		<i>For</i>	1.13	19.60	71.5	15.9	
MACI/2.3 mM 3DPS	Best cell	Rev	1.14	20.77	75.6	17.9	17.5
		For	1.16	20.70	74.0	17.8	
	Average	<i>Rev</i>	1.12	20.31	75.1	17.2	
		<i>For</i>	1.13	20.00	74.0	16.6	
MACI/4.6 mM 3DPS	Best cell	<i>Rev</i>	1.10	21.14	70.6	16.5	14.7
		<i>For</i>	1.14	18.99	65.8	14.3	
	Average	<i>Rev</i>	1.11	20.82	69.7	16.1	
		<i>For</i>	1.11	19.64	62.1	13.5	

Annex 10: J-V parameters (best cells and average) of solar cell devices of NIP architecture: Glass/FTO/c-TiO₂/m-TiO₂/ Cs_{0.17}FA_{0.83}Pb(I_{0.83}Br_{0.17})₃/ PTAA/Au.

			Voc	Jsc	FF	PCE	MPP
			V	mA/cm ²		%	%
MACI/No 3DPS	Best cell	Rev	1.03	15.21	66.0	10.3	8.2
		For	1.02	16.55	50.9	8.6	
	Average	Rev	1.01	13.18	66.0	8.8	
		For	1.03	13.83	51.1	7.2	
MACI/0.7 mM 3DPS	Best cell	Rev	1.14	20.72	75.6	16.5	15.2
		For	1.12	20.85	64.6	15.1	
	Average	Rev	1.11	18.99	69.5	14.6	
		For	1.10	19.48	61.8	13.3	
MACI/1.5 mM 3DPS	Best cell	Rev	1.15	20.80	70.0	16.8	15.1
		For	1.13	20.00	66.8	15.1	
	Average	Rev	1.15	20.34	69.3	16.1	
		For	1.13	20.62	63.5	14.8	
MACI/2.3 mM 3DPS	Best cell	Rev	1.12	19.64	76.1	16.8	16.3
		For	1.11	20.33	68.2	15.3	
	Average	Rev	1.12	19.52	74.8	16.4	
		For	1.11	20.01	66.7	14.9	
MACI/4.6 mM 3DPS	Best cell	Rev	1.09	20.15	68.8	15.1	14.2
		For	1.07	19.90	65.7	14.0	
	Average	Rev	1.09	18.95	67.8	14.0	
		For	1.04	19.00	61.30	12.2	

Annex 11: J-V parameters of the best four perovskite opaque devices fabricated with Spiro-OMeTAD or PTAA. The perovskite layer was fabricated with a MACl: FAI molar ratio (0.3:1) and 2.3mM of 3DPS. The devices were stored under vacuum in dark conditions between the I-V measurements under 1 sun illumination.

Spiro-OMeTAD			PCE	Jsc	Voc	FF
			%	mA/cm ²	V	
J1	Rev	Average	17.5	19.7	1.13	78.3
	For		15.8	19.6	1.13	70.8
J5	Rev	Average	17.1	20.1	1.12	76.4
	For		16.4	20.2	1.13	71.7
Variations from J1 (Average Reverse values)			-2.2%	2.1%	-0.6%	-2.4%
J10	Rev	Average	16.2	19.3	1.11	73.6
	For		16.0	19.6	1.11	69.1
Variations from J1 (Average Reverse values)			-7.8%	-2.1%	-1%	-2.1%
J15	Rev	Average	16.8	20.2	1.14	73.6
	For		15.8	20.4	1.12	69.1
Variations from J1 (Average Reverse values)			-4%	2.2%	1%	-6%
J30	Rev	Average	14.4	18.7	1.1	71.4
	For		14.5	18.8	1.13	68.0
Variations from J1 (Average Reverse values)			-17.6%	-6.8%	-2%	-8.8%
J45	Rev	Average	13.6	19.1	1.05	66.5
	For		11.7	18.9	1.04	59.2
Variations from J1 (Average Reverse values)			-22.3%	-3.2%	-9%	-15%
PTAA			PCE	Jsc	Voc	FF
			%	mA/cm ²	V	
J1	Rev	Average	16.0	19.4	1.12	74.4
	For		13.4	19.9	1.11	60.5
J5	Rev	Average	16.3	20.2	1.15	71.2
	For		14.5	20.6	1.13	62.0
Variations from J1 (Average Reverse values)			2%	4%	3%	-4%
J10	Rev	Average	16.2	20.6	1.10	69.9
	For		13.9	20.0	1.11	66.3
Variations from J1 (Average Reverse values)			1%	7%	-2%	-6%
J15	Rev	Average	15.7	18.9	1.11	74.4
	For		14.1	19.2	1.12	64.8
Variations from J1 (Average Reverse values)			-2%	-3%	-1%	/
J30	Rev	Average	15.6	19.4	1.11	72.5
	For		14.5	19.0	1.11	70.4
Variations from J1 (Average Reverse values)			-3%	/	-1%	-2%
J45	Rev	Average	15.7	19.2	1.12	72.9
	For		15.0	19.7	1.12	67.3
Variations from J1 (Average Reverse values)			-2%	-1%	-1%	-2%

Annex 12: Deposition process of the ITO transparent electrode.

For the semi-transparent perovskite solar cells, the transparent electrode layer is composed of an indium tin oxide (ITO) layer deposited by sputtering. E. Raoult has elaborated the following protocol as part of her thesis work.

First, a batch of 4 perovskite cells is introduced in a vacuum chamber. Then, the pressure is decreased to $P_{\text{chamber}} = 2 \text{ mTorr}$. During the deposition cycle, a plasma is alimented for 10 minutes at 30 W, then 100 minutes at 50 W. The indium-tin-oxide target is 3 inches wide and composed of 90 % indium oxide and 10 % oxide of tin oxide.

The ITO electrode layer is about 230 nm thick and shows a sheet resistance of 16 ohm/sq. Finally, a fork-like gold contact is evaporated on top of the ITO layer to create a better contact for IV measurements without covering the transparent ITO.

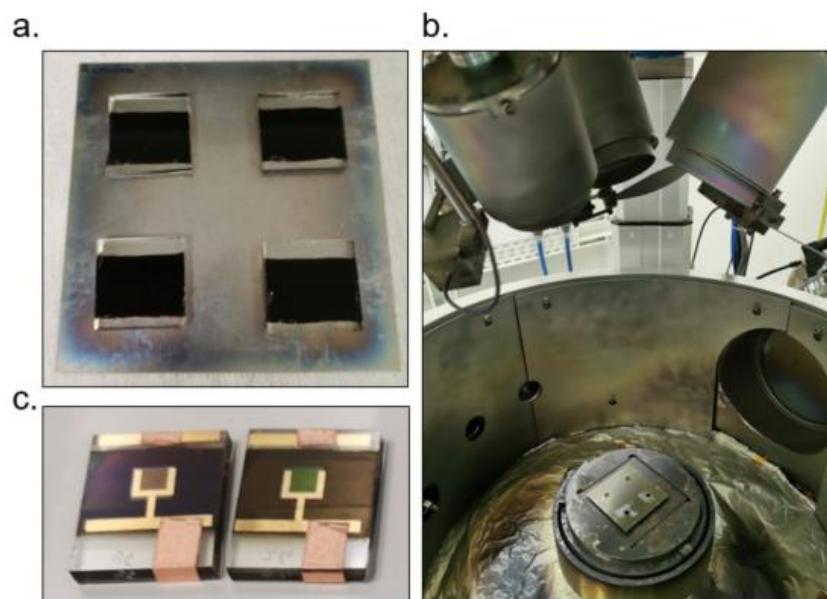


Figure 2: a. Perovskite solar cells placed on the deposition bulk. b. Open chamber of the sputtering reactors. c. Semi-transparent perovskite solar cells of $2 \times 2.5 \text{ cm}^2$ area.

Annex 13: J-V parameters of fresh and aged semi-transparent perovskite devices of NIP architecture: Glass/FTO/c-TiO₂/m-TiO₂ / Cs_{0.17}FA_{0.83}Pb(I_{0.83}Br_{0.17})₃ / Spiro-OMeTAD or PTAA/ ITO / Au. The devices were stored in a vacuum chamber in dark conditions. The perovskite layer was fabricated with a MAcl: FAI molar ratio (0.3:1) and 2.3 mM 3DPS.

			PCE	Jsc	Voc	FF	MPP	Jsc (EQE)				
			%	mA/cm ²	V							
Spiro-OMeTAD												
Total cells fabricated:		18	# cells lost after sputtering (PCE<2%)					5				
J1	Rev	Best cell	16.7	20.3	1.13	71.8	16.2	18.5				
	For		16.8	20.3	1.14	72.4						
	Rev	Average	15.4	19.2	1.11	72.3						
	For		14.9	19.0	1.12	69.7						
J10	Rev	Average	12.6	18.8	1.07	61.5						
	For		14.0	18.6	1.08	70.3						
Variations from J1 (Average Reverse values)			-11.7%	-2.1%	-3.6%	-4.9%						
J30	Rev	Average	8.2	16.2	0.95	53.2						
	For		7.8	14.6	1.00	58.3						
Variations from J1 (Average Reverse values)			-47.1%	-5.6%	-4.4%	26.4%						
J45	Rev	Average	5.9	15.2	0.76	46.5						
	For		5.1	14.6	0.73	41.8						
Variations from J1 (Average Reverse values)			-61.9%	-20.8%	-32.5%	-35.7%						
PTAA												
Total cells fabricated:		13	# cells lost after sputtering (PCE<2%)					1				
J1	Rev	Best cell	14.2	18.6	1.04	72.4	13.5	/				
	For		13.0	18.4	1.06	66.5						
	Rev	Average	11.8	18.1	1.05	62.9						
	For		10.4	17.4	1.03	58.0						
J10	Rev	Best cell	14.8	19.1	1.07	72.8			15.2	17.65		
	For		14.4	18.2	1.09	72.7						
	Rev	Average	13.1	17.7	1.08	68.1						
	For		11.9	17.7	1.07	62.5						
Variations from J1 (Average Reverse values)			8.5%	-2.2%	1%	8.3%						
J30	Rev	Average	12.5	17.8	1.04	67.0						
	For		10.9	17.5	1.05	59.3						
Variations from J1 (Average Reverse values)			5.9%	-2.5%	-1%	6.5%						
J45	Rev	Average	10.4	17.0	0.99	61.0						
	For		9.0	17.1	0.99	52.9						
Variations from J1 (Average Reverse values)			-11.9%	-6%	-4.8%	-3%						

Annex 14: Fabrication process of pseudo-tandem devices

The integration protocol has been developed by T. Guillemot (Ph.D.) for the Program II of the IPVF lab.

○ **Top cell: fabrication of the perovskite filter**

The perovskite filters of 5 x 5 cm² have been fabricated to reproduce the full stack 2 x 2 cm² without etchings. The c-TiO₂ layer has been deposited by spray-coating, the m-TiO₂ and the HTL layers have been deposited by spin-coating, the perovskite layer has been deposited by slot-die, and finally, the ITO layer was deposited by sputtering (**Figure 3**).

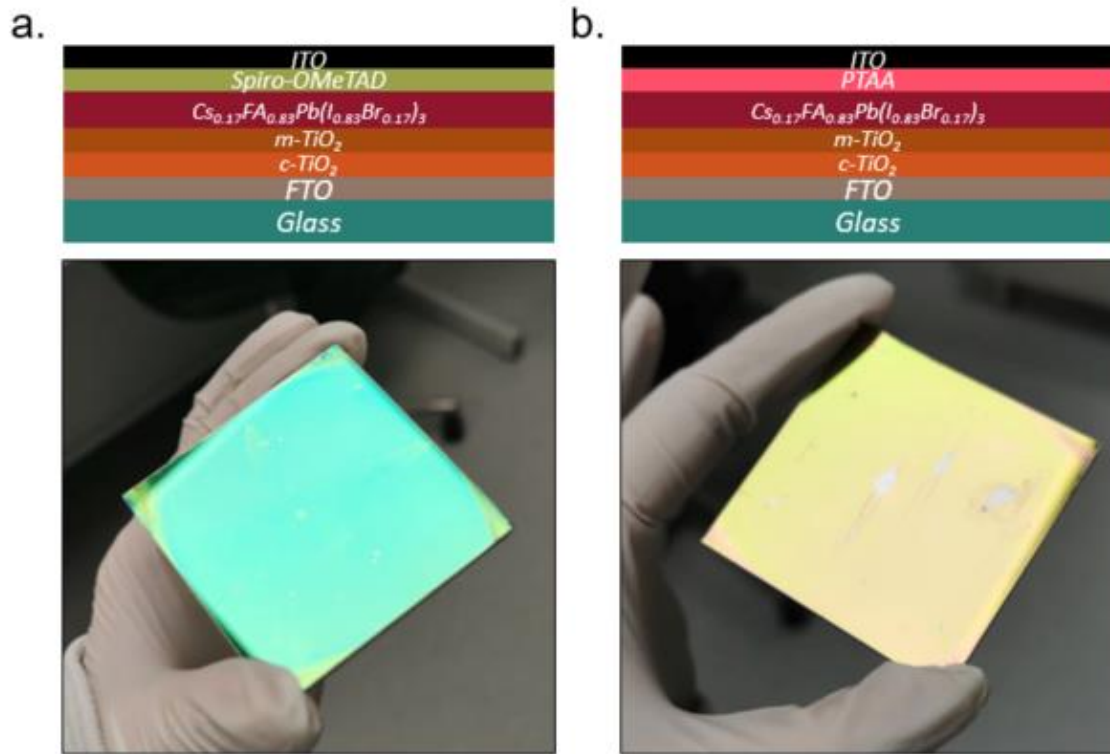


Figure 3: Complete stack “filters” 5x5 cm². NIP architecture glass/FTO/c-TiO₂/m-TiO₂/Cs_{0.17}FA_{0.83}Pb(I_{0.83}Br_{0.17})₃/Spiro-OMeTAD (left photo) and architecture glass/FTO/c-TiO₂/m-TiO₂/Cs_{0.17}FA_{0.83}Pb(I_{0.83}Br_{0.17})₃/PTAA (right photo).

After fabricating the filters, a PDMS solution is prepared (volume 1:10 with a hardening agent). The solution is put under a vacuum for 10 minutes to evacuate the gas from the solution and avoid bubbles. Next, the PDMS solution is deposited on the perovskite filter by spin-coating. Then, the filter is placed in an oven for 2 hours at 80°C (**Figure 4**).

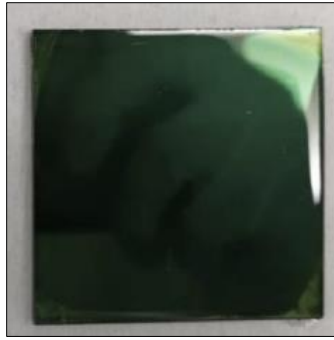


Figure 4: Perovskite filter with PDMS film after annealing

- **Bottom cell: silicon cell**

The bottom cell is composed of a cut n-PERT-RJ- MoSoN 4x4 c-Si cells. The IV performances are measured under 1 Sun (AAA Simulator) in a four-wire configuration. Cells have a stringed active surface area of 16 cm² on a total area of 20.25 cm² and are encapsulated with a polyolefin film (PO). The whole bottom cell stack follows Glass/PO/string c-Si/PO (**Figure 6. a**).



Figure 5: 4-wires IV measurements of the silicon bottom cell

- Fabrication of the pseudo-tandem stack

The PLA case and mask are essential to properly determine the MoSoN silicon cell surface and center the bottom and top cells.

A polylactic acid (PLA) case and an aperture mask have been 3D printed (**Figure 6. c**) to associate the perovskite filter and the silicon cell. First, the c-Si cell is centered inside the PLA case, then polydimethylsiloxane (PDMS - Sylgard 184) is poured inside the case to cover the silicon cell and hold it in its position. Finally, the stack is placed under a vacuum to dry the PDMS.

Simultaneously, a thin layer of PDMS is deposited on the perovskite filter and annealed for 2h at 80°C under vacuum. This step helps protect the fragile ITO layer on the surface before making the tandem. The filter is added too in the PLA case, above the c-Si cell, covered with PDMS, and correctly centered. Next, PDMS is again poured up to the filter

height to hold it and link it to the rest of the structure. The obtained pseudo-tandem device is finally maintained at 45°C for one night to obtain the final result shown in **Figure 6. e.**

After the performance of the filtered Si bottom cells has been measured using a digital source meter (Keithley Model 2400 for c-Si cells) and an AAA sun simulator (Oriel Sol3A) as a light source using AM1.5 G spectrum with a four wires configuration.

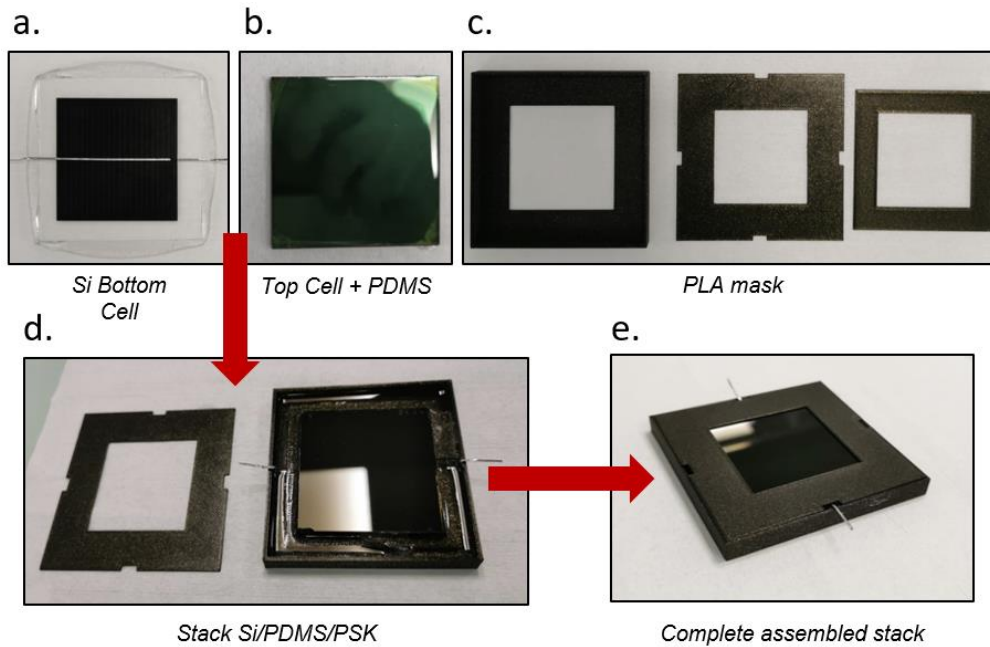


Figure 6: Assembly steps of the pseudo-tandem devices. *a.* bottom cell c-Si. *b.* “Filter” perovskite device covered with PDMS. *c.* 3D printed PLA case and mask. *d.* Centered and stacked c-Si cell and perovskite filter. *e.* Final pseudo-tandem device.

References

- (1) NREL. Reference Air Mass 1.5 Spectra <https://www.nrel.gov/grid/solar-resource/spectra-am1.5.html> (accessed 2021 -07 -07).
- (2) Solar - Fuels & Technologies <https://www.iea.org/fuels-and-technologies/solar> (accessed 2021 -07 -07).
- (3) International Renewable Energy Agency. *RENEWABLE POWER GENERATION COSTS IN 2019*; Abu Dhabi, 2020.
- (4) Theory of Solar Cells. *Wikipedia*; 2021.
- (5) ISFH's Record Efficiency of 26.1% Is Included in International Efficiency Tables.
- (6) Dahlinger, M.; Carstens, K.; Hoffmann, E.; Zapf-Gottwick, R.; Werner, J. H. 23.2% Laser Processed Back Contact Solar Cell: Fabrication, Characterization, and Modeling. *Prog. Photovolt. Res. Appl.* **2017**, *25* (2), 192–200. <https://doi.org/10.1002/pip.2854>.
- (7) Di Vece, M. Using Nanoparticles as a Bottom-up Approach to Increase Solar Cell Efficiency. *KONA Powder Part. J.* **2019**, *36*, 72–87.
- (8) Sai, H. (齋均); Matsui, T. (松井卓矢); Matsubara, K. (松原浩司). Stabilized 14.0%-Efficient Triple-Junction Thin-Film Silicon Solar Cell. *Appl. Phys. Lett.* **2016**, *109* (18), 183506. <https://doi.org/10.1063/1.4966996>.
- (9) NREL. *Research-Cell Efficiencies Chart*; 2021.

Résumé en Français

1. Introduction

Bien que l'énergie solaire directe ne représente encore qu'une petite fraction de l'approvisionnement énergétique mondial en 2021, selon le dernier rapport du GIEC : *"elle possède l'un des plus grands potentiels techniques de toutes les sources d'énergie et, de concert avec les améliorations techniques et les réductions de coûts qui en découlent, elle pourrait voir son utilisation considérablement élargie dans les décennies à venir"*. Cependant, la réduction des coûts dépend du niveau de déploiement de l'énergie solaire combiné à des efforts continus en matière de recherche et développement.

À cette fin, les technologies PV émergentes, telles que le matériau pérovskite, représentent une voie passionnante pour propulser l'énergie solaire au premier plan de l'approvisionnement énergétique. Plusieurs propriétés intrinsèques de la pérovskite, telles que les coefficients d'absorption élevés, les longues longueurs de diffusion des porteurs et la possibilité de régler la bande interdite, ont déjà contribué à démontrer le fort potentiel de cette nouvelle technologie PV. L'amélioration rapide des performances des dispositifs à base de pérovskite en a déjà fait l'étoile montante du monde photovoltaïque. Aujourd'hui, le meilleur dispositif affiche un rendement de 25,5%. Cependant, pour des applications industrielles pratiques, les technologies pérovskites doivent être plus stables et démontrer une compatibilité évolutive.

Dans cette thèse, nous nous sommes concentrés sur les différentes questions liées au transfert du matériau pérovskite vers des méthodes de dépôt évolutives. Au cours des dernières années, des progrès remarquables ont été réalisés dans la fabrication de PSCs à grande échelle, améliorant rapidement l'efficacité et l'échelle des modules PSCs (Fig. 1). L'augmentation des performances des dispositifs de petite surface est principalement attribuée à l'amélioration de la composition et de la morphologie des films minces de pérovskite grâce à des innovations dans la chimie des solutions et le processus de fabrication. Ces développements ont été facilement transférés aux structures en tandem, ce qui a entraîné une augmentation de l'efficacité qui a suivi de près la tendance des dispositifs au silicium à simple jonction. En revanche, les rendements des modules PSC de grande surface sont nettement inférieurs à ceux des dispositifs à cellule unique, ce qui souligne la nécessité de poursuivre les recherches. L'ingénierie de la composition joue un rôle essentiel dans la formation d'une pérovskite de haute qualité afin d'obtenir un contrôle précis du processus de cristallisation pendant la fabrication du dispositif. Dans cette optique, nous nous sommes concentrés sur la composition de la solution de précurseurs

de pérovskite afin de répondre aux nouvelles contraintes liées à la fabrication à grande échelle. Cette thèse est divisée en quatre chapitres.

Tout d'abord, un chapitre est consacré à un état de l'art sur l'énergie photovoltaïque et, plus particulièrement, sur les cellules solaires à base de pérovskite. Les propriétés du matériau pérovskite, les modèles de cristallisation existants, les différentes méthodes de dépôt et les systèmes d'extraction par solvant associés y sont détaillés.

Le deuxième chapitre est l'occasion de décrire toutes les étapes menant à la fabrication d'un dispositif complet. Une structure de référence n-i-p composée d'une bi-couche de TiO_2 pour le transport des électrons, de Spiro-OMeTAD pour le transport des trous, et d'une électrode supérieure en or a été fabriquée. Pour la couche d'absorption, un système combiné de dépôt par filière et d'aspiration sous vide a été développé tout au long de ce travail. Le processus de dépôt de l'absorbeur pérovskite est décomposé en deux parties : Une étape d'optimisation des paramètres de dépôt par slot-die et ensuite, une étude portant sur l'ajout d'un tensioactif zwitterionique dans la solution de précurseurs de pérovskite.

Le troisième chapitre est consacré à la fabrication d'une couche de pérovskite $\text{Cs}_{0.17}\text{FA}_{0.83}\text{Pb}(\text{I}_{0.83}\text{Br}_{0.17})_3$ avec l'ajout de MACI comme agent complexant. Les caractéristiques du matériau pérovskite en fonction de la concentration de l'additif et des conditions de recuit sont présentées. Nous avons également étudié la stabilité de dispositifs complets encapsulés à base de pérovskite, exposés à une illumination solaire pendant 300 heures. Enfin, des modules de 12 cm^2 ont été fabriqués avec un rapport MACI optimisé.

Dans le dernier chapitre, le surfactant zwitterionique et les propriétés du MACI ont été combinés pour obtenir une couche de pérovskite de haute qualité. Notamment, une attention particulière a été portée sur les propriétés de rugosité de surface. Dans cette partie, les performances des dispositifs solaires avec deux couches de transport de trous différentes (Spiro-OMeTAD et PTAA) ont été comparées. Dans le but ultime de valider la compatibilité potentielle de notre structure pour des applications tandem, nous avons fabriqué des dispositifs semi-transparents et caractérisé leurs performances. Enfin, les efficacités potentielles du pseudo-tandem ont été calculées.

2. Etat de l'art

Le paysage énergétique mondial

Aujourd'hui, plus de 80% de la consommation mondiale d'énergie primaire provient de ressources fossiles (gaz, charbon, pétrole)² (**Figure FR-1.a.**), ce qui représente plus de 500 exajoules. En 2021, la consommation d'énergie à base de charbon continue de croître et devrait augmenter de 60% en 2021³. Ce chiffre de croissance représente donc plus que toutes les sources d'énergie renouvelables réunies. La combustion de combustibles fossiles est responsable d'une grande majorité des émissions mondiales de gaz à effet de serre et de la pollution atmosphérique. La reprise attendue de

la consommation inverserait 80% de la baisse de 2020, entraînant une hausse des émissions de près de 5%² (**Figure FR-1.b.**). De plus, l'épuisement des réserves génère davantage de difficultés d'extraction et donc une augmentation des coûts d'exploitation et des investissements qui peuvent entraver l'approvisionnement à long terme à l'avenir. Ces ressources sont également réparties de manière très inégale, ce qui est source de pressions géopolitiques dans des zones critiques.

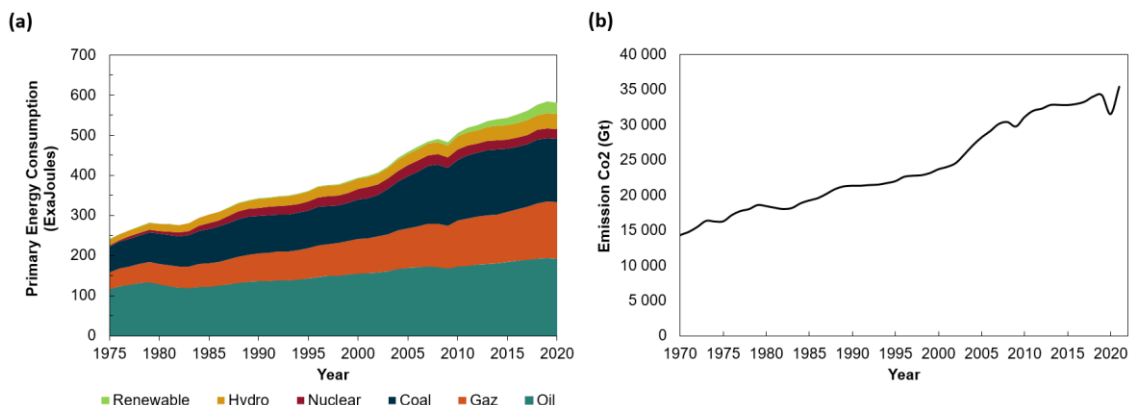


Fig.FR-1 : a. Consommation mondiale d'énergie primaire par ressources combustibles. Données extraites de la réf. [3]. **b.** Émissions mondiales de CO₂ liées à l'énergie, les données sont reproduites de la réf. [2].

L'énergie solaire

Les technologies solaires représentent une voie passionnante pour la production future d'énergie à faible teneur en carbone. Les pérovskites, en particulier, ont démontré une augmentation considérable de leur efficacité et ont donné des résultats prometteurs pour un déploiement à grande échelle.

Les cellules solaires en pérovskite ont vu leurs performances augmenter rapidement au cours des 15 dernières années, atteignant un record de 25,5% pour une seule jonction en 2021⁴ (**Figure FR-2**). En outre, la cellule solaire en pérovskite devrait être extrêmement rentable, ce qui fait de cette technologie une option attrayante pour la production industrielle et la commercialisation⁵. Cependant, le transfert des cellules de laboratoire vers des processus de fabrication à grande échelle et la stabilité de la pérovskite restent très difficiles.

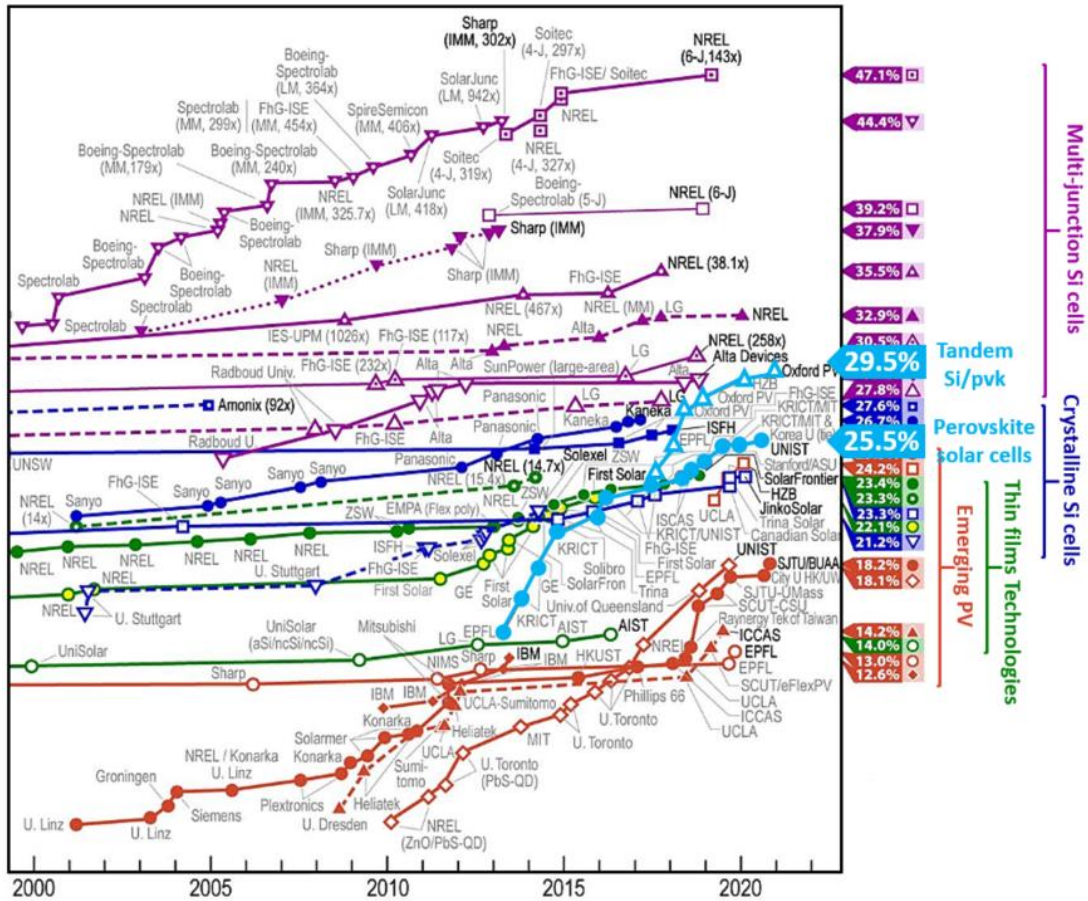


Fig.FR- 2 : Évolution des rendements photovoltaïques par secteur de 1975 à 2021. Extrait du tableau des meilleurs rendements des cellules de recherche du NREL [6]. Ce graphique est régulièrement mis à jour par le National laboratory Renewable Energy Laboratory (NREL).

Les cellules tandems

Malgré une amélioration rapide de l'efficacité des cellules solaires au cours des vingt dernières années, les meilleures technologies se rapprochent désormais de la limite thermodynamique de Shockley-Queiser (SQ). Par conséquent, les cellules solaires tandem, combinant une cellule inférieure à faible bande interdite et une cellule supérieure à bande interdite plus élevée (**Figure FR-3.a**), représentent une voie prometteuse pour franchir le seuil de 30 % de PCE. Sous l'effet de l'éclairage, chaque cellule produit un courant électrique en réponse à des domaines de longueurs d'onde différentes, améliorant ainsi le potentiel de conversion électrique de la cellule.

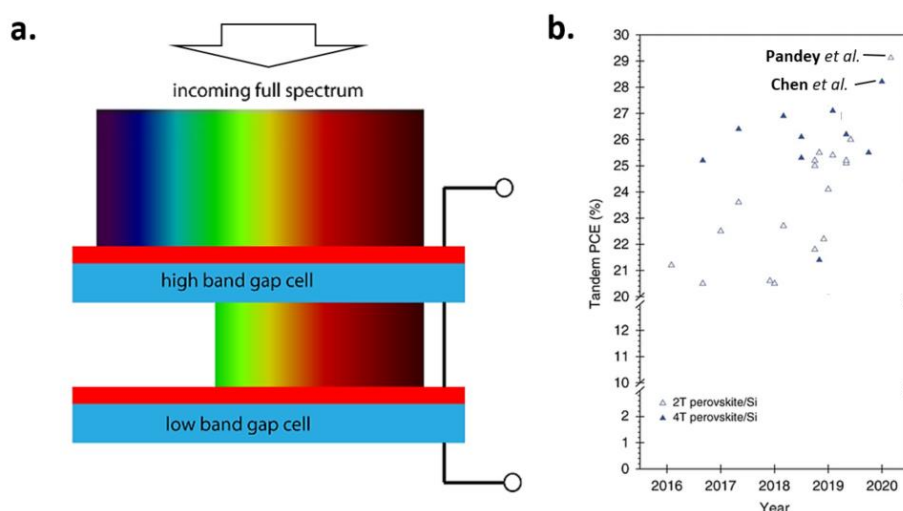


Fig.FR- 3: a. Cellule solaire tandem connectée en série. L'ajout de plus de dispositifs permet d'optimiser chaque dispositif sur un spectre plus étroit, ce qui donne un rendement global plus élevé. Reproduit de la réf. [7]. **b.** Progression du PCE des cellules solaires tandem à base de pérovskite. Reproduit de la réf. [8].

Les pérovskites se sont avérées être un excellent candidat pour les cellules solaires à jonction multiple en raison de leur bande interdite accordable, de leur facilité de fabrication et de leur faible coût potentiel de fabrication^{7,9-11}. La cellule solaire c-Si étant la technologie dominante sur le marché actuel, l'incorporation de cellules pérovskites aux cellules solaires c-Si commerciales représente un enjeu important pour l'industrialisation des cellules solaires pérovskites¹⁰. Il existe deux types d'architectures tandem: les dispositifs à deux terminaux (2T), également appelés cellules tandem monolithiques, et les cellules à quatre terminaux (4T) composées d'une pile de deux cellules solaires distinctes (**Figure FR-3.b**). En 2020, une cellule solaire tandem 2T Pvk/Si a atteint une valeur d'efficacité certifiée à 29,15% sur une surface de dispositif de $\sim 1 \text{ cm}^2$. Cela a donné une crédibilité supplémentaire à l'approche tandem pour ouvrir la voie à des dispositifs franchissant la barre des rendements supérieurs à 30 %.

Actuellement, des cellules solaires tandem Pvk/Si sont en cours de développement pour de futures applications commerciales, par exemple dans le cadre des initiatives d'Oxford PV et de Jinko Solar¹². Cependant, jusqu'à présent, leur application a été limitée à des cas particuliers, notamment dans l'aérospatiale, où leur rapport puissance/poids élevé est souhaitable. Pour permettre une application plus large des cellules solaires à jonction multiple à base de pérovskite, la stabilité de ces cellules doit être comparable à celle d'autres technologies pertinentes, telles que le c-Si ou le CIGS. En outre, les cellules à pérovskite à simple jonction et à multi-jonction rapportées ont été fabriquées sur de petites surfaces, et des recherches plus approfondies doivent être menées pour générer des dispositifs tandem efficaces à grande échelle.

Modèles théoriques de cristallisation

Nous avons discuté des principes fondamentaux de la nucléation et de la croissance cristalline des pérovskites, qui doivent être considérés avec beaucoup d'attention lorsqu'il s'agit de surfaces plus importantes.

Viktor La Mer a proposé un modèle décrivant les mécanismes de nucléation et de croissance des cristaux dans un liquide. Son modèle est dit "à médiation atomique" et prend en compte le mouvement et les interactions des monomères. La courbe de Lamer décrit l'évolution de la concentration des monomères en solution au cours du temps (**Figure FR-4**). Les concentrations C_s (limite de solubilité), C^*_{\min} (concentration minimale de l'état de sursaturation) et C^*_{\max} (concentration maximale de l'état de sursaturation) déterminent l'ensemble des phénomènes de nucléation et de croissance cristalline, qui ont un impact sur la taille et la morphologie du cristal final. Selon le modèle de La Mer, le processus de cristallisation se déroule en trois étapes :

- **L'étape de pré-nucléation**, pendant laquelle la concentration de la solution augmente rapidement pour atteindre la concentration de supersaturation C^*_{\min} . L'augmentation de la concentration correspond à l'évacuation rapide du solvant. Dans le cas d'un film de pérovskite, l'extraction du solvant peut se faire soit par évaporation forcée du solvant (soufflage d'air, aspiration ou recuit), soit par le dépôt d'un anti-solvant sur le substrat.
- **L'étape de nucléation**. Quand la concentration dépasse la concentration de supersaturation C^*_{\min} , les centres de nucléation se stabilisent et commencent à inséminer en solution. La croissance des noyaux se produit ensuite par agrégation atomique autour des noyaux. Le modèle de Lamer considère la nucléation comme un processus unique, mais selon la théorie classique, la nucléation peut se produire de manière hétérogène ou homogène.
- **L'étape de croissance**. La compétition entre la nucléation et la croissance est équilibrée par la concentration en monomères. Lorsque la concentration de la solution C atteint C_q , il devient plus probable pour un seul atome de rejoindre un cluster existant plutôt que de former un nouveau centre de nucléation. Dès que la formation de nouveaux noyaux s'arrête, la croissance devient le mécanisme dominant de consommation des monomères par agrégation autour des clusters existants. Par conséquent, la concentration de la solution diminue.

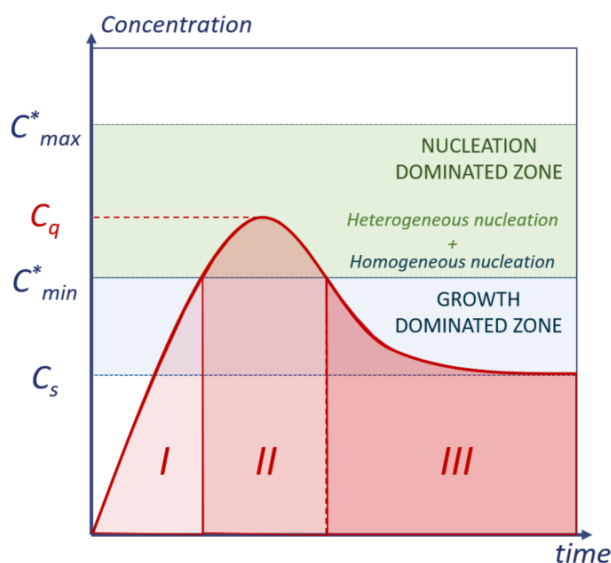


Fig.FR- 4: Courbe de La Mer adaptée de la réf. [13,14].

Si la théorie de La Mer constitue une base intéressante pour décrire le mécanisme de cristallisation des films de pérovskite, ce modèle présente des limites qui peuvent être complétées, notamment en ce qui concerne l'hypothèse de la "nucléation en rafale" qui suggère une nucléation instantanée et isotrope en solution. Ainsi, en complément de la théorie classique de la nucléation, de nombreux travaux expérimentaux ont permis d'affiner la compréhension de la formation des noyaux. Parmi eux, le mûrissement d'Ostwald et les attachements orientés sont des exemples importants qui doivent être pris en compte lors de la fabrication de films minces de pérovskite.

Les techniques de fabrication sur grandes surfaces

En 2021, Jeong *et al.* ont obtenu une cellule record de 25,5 % d'efficacité (25,2 % certifiés)⁴, ce qui a démontré le potentiel des cellules solaires en pérovskite pour les applications industrielles. Cependant, ce résultat encourageant a été obtenu sur de petites surfaces (surface active < 0,1 cm²), en utilisant la méthode de dépôt par spin-coating pour la fabrication de la couche de pérovskite. Combinée à une méthode de lavage anti-solvant, cette méthode de dépôt permet d'atteindre jusqu'à présent les meilleurs rendements des dispositifs.

Cependant, le dépôt par spin-coating n'est pas une technique viable pour étendre la technologie de la pérovskite sur une plus grande surface. En outre, ce procédé induit une perte importante de matériaux pendant le dépôt (>90%), ce qui constitue un obstacle important au transfert du procédé dans la fabrication. De plus, dans le cas de substrats de grande taille (>100cm²), le spin-coating peut présenter un étalement inégal de la couche, ce qui conduit inévitablement à une inhomogénéité importante, nuisant ainsi aux performances du dispositif¹⁵. A ce jour, le plus grand module fabriqué par la méthode de spin-coating a démontré une efficacité de 12,6% sur une surface de 20,3 x 20,3 cm².¹⁶

Comme alternative au dépôt par spin-coating, plusieurs techniques de fabrication compatibles à grande échelle ont été étudiées. Pour les techniques de dépôt en solution, les précurseurs de pérovskite sont d'abord dissous dans des solvants organiques, puis déposés sur de grands substrats. Parmi ces techniques, le blade-coating¹⁷, le spray-coating¹⁸, le screen-printing¹⁹ ou le slot-die coating²⁰ sont des candidats intéressants pour la fabrication de cellules solaires pérovskites de grande surface (**Figure FR-5.a**). Le slot-die représente l'une des techniques de dépôt les plus étudiées dans la littérature.

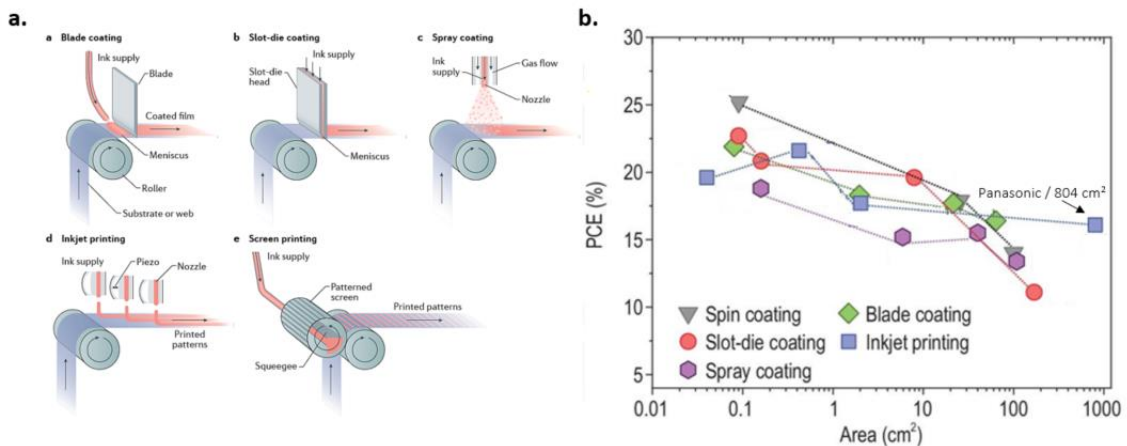


Fig.FR- 5: a. Méthodes de dépôt évolutives basées sur des solutions pour la fabrication à grande échelle de cellules solaires pérovskites, notamment le revêtement par lame (panneau a), le revêtement par filière à fente (panneau b), le revêtement par pulvérisation (panneau c), l'impression à jet d'encre (panneau d) et la sérigraphie (panneau e). Reproduit de la réf. [21]. **b.** Records de rendement de conversion de puissance certifiés pour les cellules et modules solaires à pérovskite champions. Reproduit de la réf. [22].

Récemment, grâce aux efforts déployés en vue de l'industrialisation, les cellules solaires en pérovskite fabriquées à l'aide de techniques compatibles avec l'industrie ont commencé à concurrencer les dispositifs à revêtement par centrifugation. Par exemple, en 2021, Xu et al. ont obtenu un rendement de 21,35 % pour une cellule solaire à pérovskite à l'échelle du laboratoire fabriquée par slot-die²³. Ce résultat égale le précédent record établi par le blade-coating, qui a donné un rendement de 21,9 % avec un traitement de surface à l'iodure de cadmium²⁴. Parallèlement, les surfaces et les rendements des modules continuent d'augmenter. Notamment, en combinant le revêtement par slot-die et un soufflage d'azote à haute pression, M. Du et al. ont atteint un rendement de plus de 22 % pour un module de 16 cm².²⁵

Ces résultats très encourageants ont déclenché l'intérêt de l'industrie pour des modules pérovskites de plus grande taille. En 2020, l'entreprise japonaise Panasonic Corp a annoncé le PCE le plus élevé au monde, soit 17,9 %, pour un module pérovskite plus grand (>800 cm²)^{28,29}. La Chine a investi massivement dans l'industrialisation de la technologie pérovskite avec un plan visant à développer une ligne de production de cellules pérovskite de 1GW d'ici 2022³⁰.

Bien que des progrès significatifs aient été réalisés, le PCE des modules pérovskites reste encore en retrait par rapport aux cellules de pointe de petite surface (~0,1 cm²) fabriquées par spin coating (**Figure FR-5.b**). Même si la stratégie des additifs donne des résultats

encourageants pour ralentir la croissance des cristaux, la morphologie finale du film dépend aussi fortement de la méthode d'extraction du solvant. En effet, une extraction rapide du solvant de la solution de précurseurs de pérovskite est cruciale afin d'atteindre plus rapidement l'état de sursaturation, favorisant ainsi un nombre plus élevé de noyaux. Ainsi, couplé à une optimisation chimique appropriée de la solution de précurseurs de pérovskite, une méthode de séchage efficace est cruciale pour obtenir une qualité cristalline élevée.

Les techniques de séchage

Le lavage par anti-solvant

La méthode du lavage par anti-solvant est largement utilisée pour fabriquer des cellules solaires en pérovskite. Son utilisation permet d'atteindre les performances les plus élevées en laboratoire^{4,31,32}. Pour des échantillons plus grands, la couche de pérovskite peut également être immergée dans un bain d'anti-solvant. La concentration des précurseurs de pérovskite dans le mélange de solvants restant augmente alors fortement et déclenche le mécanisme de cristallisation. Cependant, bien que plusieurs records d'efficacité par slot-die soient encore basés sur des méthodes dérivées des anti-solvant (bain ou lavage par spin-coating)^{20,21,34} la méthode du lavage par anti-solvant présente des problèmes d'homogénéité lorsque la taille du film augmente³³. De plus, ils nécessitent une grande quantité de solvants potentiellement toxiques qui peuvent être préjudiciables pour les futures applications industrielles³⁵.

Le souffle d'air

Le système de séchage le plus répandu applique un souffle d'air vertical (air sec ou N₂) sur la surface de l'échantillon (**Figure FR-6**). Une buse de gaz est généralement associée à la tête de dépôt du slot-die ce qui sèche la pérovskite immédiatement après le dépôt. Du *et al.* ont obtenu un rendement de conversion électrique de plus de 19% sur des modules de pérovskite de 16 cm², validant ainsi la compatibilité de cette méthode pour des substrats plus grands. Cependant, pour évacuer efficacement le solvant, un flux de gaz à haute pression est nécessaire. Une pression de soufflage insuffisante peut entraîner une couverture inhomogène du film et une morphologie dendritique due à une mauvaise nucléation³⁶.

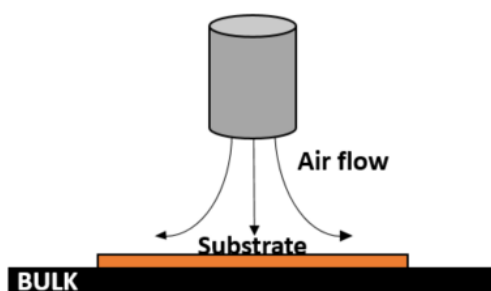


Fig.FR- 6 : Représentation schématique du soufflage d'air vertical

Aspiration sous vide

Contrairement au soufflage d'air, l'aspiration sous vide élimine le solvant par aspiration dans une chambre à vide (**Figure FR-7**). L'avantage de cette technique est l'absence d'une zone de saturation retardant la diffusion et l'évacuation du solvant de la couche de pérovskite.

X. Li *et al.* ont développé une méthode d'évacuation quasi-instantanée. Un système à double chambre permet à la chambre contenant le substrat d'atteindre 20 Pa en seulement quelques secondes (Figure I-19.b)³⁷. En utilisant la méthode VASP (Vacuum-Flash Solution Processing), X. Li *et al.* ont obtenu une efficacité de 20,38 % sur une surface d'ouverture de 1 cm². F. Guo *et al.* ont combiné la méthode d'aspiration sous vide avec le dépôt par blade-coating³⁸. Ils ont atteint un rendement de plus de 18% sur des modules de 0,09 cm² et de 11% pour des modules de 4x4 cm². Le séchage sous vide a été associé à l'ajout de MAI qui a permis d'obtenir une granulométrie importante (>1µm).

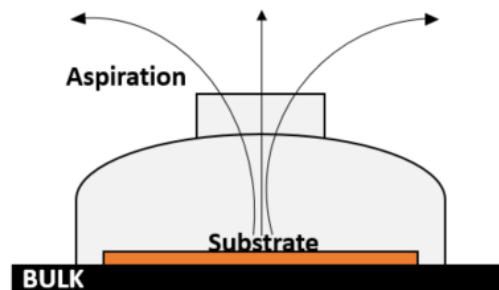


Fig.FR- 7: Représentation schématique de l'aspiration sous vide

Evaporation par recuit

Alternativement à une méthode induite par le flux, le chauffage du substrat peut également accélérer l'élimination du solvant. Dans cette optique, il existe plusieurs techniques pour chauffer la couche pérovskite :

- Le recuit sur plaque chauffante : A. Vilayan *et al.* ont déposé par slot-die une couche de pérovskite sur un substrat préchauffé à 130°C et ont obtenu par cette méthode un rendement de 14,5%³⁹. Plus récemment, Cotella *et al.* ont combiné un souffle d'air et un recuit à 65°C ce qui a permis d'atteindre un rendement de 21.4%⁴⁰.
- L'exposition lumineuse. La couche perovskite est exposée à une lumière couvrant tout le spectre des longueurs d'onde (100nm à 1100 nm) (technique IPL) ou seulement à un rayonnement IR (750 et 2500 nm) (technique FIRA). Sanchez *et al.* ont rapporté une efficacité supérieure à 20% pour les petites cellules solaires et jusqu'à 17% sur une surface de 1,4 cm²⁴¹ et B-J. Huang *et al.* ont atteint une efficacité de 14,3 % sur un module de 80x80 cm² déposé par la technique des matrices à fente⁴².

Dans la suite de ce travail, nous développerons les différentes stratégies que nous avons élaborées afin de fabriquer nos couches de pérovskite, en utilisant une méthode de dépôt

de type slot-die coating combinée à un système de séchage par aspiration sous vide. Nous avons exploré différentes pérovskites à double cation CsFA afin d'identifier la meilleure composition pour des applications à grande échelle et avons également fait varier le ratio de bromure. Nous avons également évalué l'influence de deux additifs sur la morphologie du film pérovskite et la stabilité de la couche. Les résultats expérimentaux seront discutés dans les chapitres suivants.

3. Introduction d'un surfactant amphotère

Protocole de fabrication

Dans ce chapitre, nous avons présenté le processus complet de fabrication des cellules solaires pérovskites, du substrat de 10 x 5 cm² aux cellules individuelles de 2x2,5 cm² (**Fig.FR 8**): Nous avons fabriqué des dispositifs avec une architecture classique n-i-p, avec un ETL bi-layer de TiO₂ et un HTL en spiro-OMeTAD.

1. La fabrication des couches de transport et des électrodes a combiné différentes techniques de dépôt, qui a dû être ajustées pour les grands substrats. Les méthodes de dépôt ont été adaptées à partir du processus de base, développé au laboratoire de l'IPVF pour les dispositifs à revêtement par centrifugation :
 - La couche de TiO₂ compact a été déposée par spray sur une plaque chauffante à 450°C.
 - La couche de TiO₂ mésoporeux a été déposée par spin-coating sur des substrats 5x10cm² suivant la recette de la baseline.
 - La couche de spiro-OMeTAD a été déposée par spin-coating sur les cellules individuelles de 2x2,5 cm²

2. La couche pérovskite a été déposée en utilisant la technique de slot-die. Nous avons utilisé des substrats de 10x5 cm² pour effectuer notre dépôt.

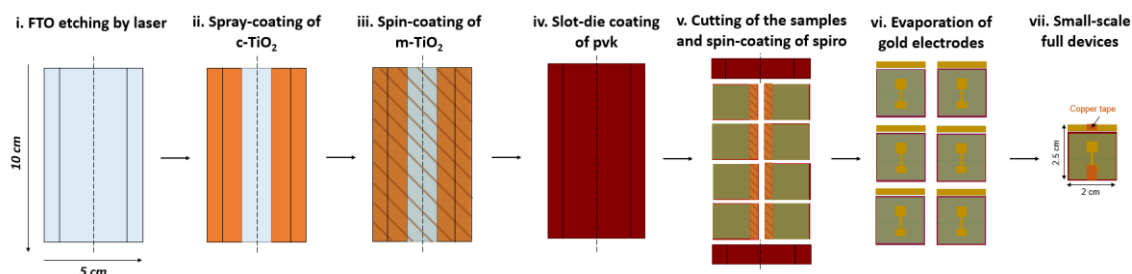


Fig.FR-8: Principales étapes du processus de fabrication des cellules solaires à pérovskite de petite surface. Le dépôt des couches de TiO₂ a été réalisé dans des conditions ambiantes. La couche de pérovskite et la HTL ont été déposées dans une boîte à gants remplie de N₂. Dépôt de l'absorbeur pérovskite

Afin de générer une couche perovskite homogène, l'influence des paramètres de dépôt sur la qualité de la couche de pérovskite a été étudiée. L'optimisation des paramètres présentée dans cette partie a été réalisée avec une composition de pérovskite à double cation $\text{Cs}_{0.2}\text{FA}_{0.8}\text{Pb}(\text{I}_{0.95}\text{Br}_{0.05})_3$. Les premières optimisations des paramètres ont été réalisées sur un substrat de $5 \times 5 \text{ cm}^2$ et ensuite, transférées à $5 \times 10 \text{ cm}^2$.

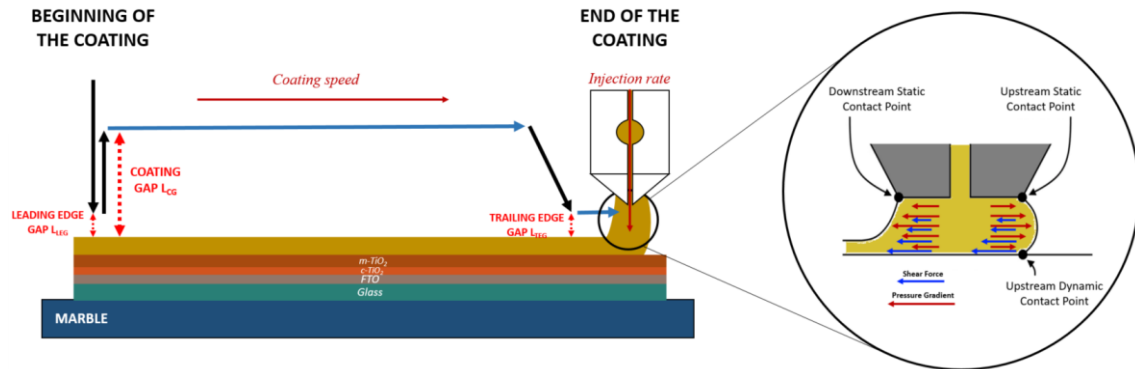


Fig.FR-9: Paramètres et principales étapes du dépôt du revêtement par filière. Représentation schématique du ménisque.

L'optimisation paramétrique a été menée suivant les étapes principales du dépôt dont les paramètres principaux sont représentés sur la Fig.FR-9:

- Formation du ménisque et initialisation du dépôt
- Optimisation de l'uniformité et de l'épaisseur du film
- Fin du dépôt et formation de « puddle »

Les paramètres par étape de dépôt optimisés pour la fabrication des couches de pérovskite au cours de ce travail sont présentés dans le tableau suivant :

Table.FR-1: Paramètres optimisés de dépôt par slot-die

Meniscus Intialization			Coating			End	
Ink injection delay	L_{EG}	L_{CG}	Coating speed	IIR	SC	L_{TEG}	Ink injection offset
s	μm	μm	mm/s	$\mu L/s$	$\%$	μm	mm
2	30	60	14	3.5	33	40	15

Pour cette thèse, la technique de séchage sélectionnée consiste en une plaque d'aspiration sous vide installée à l'intérieur de la boîte à gants dans le but de remplacer l'étape d'égouttage de l'anti-solvant afin de mieux s'adapter aux procédés à grande échelle. Après la phase de dépôt, le film humide est placé dans la chambre à vide qui permet d'atteindre 1 mbar en 4 minutes. La pression est ensuite maintenue à ce niveau de vide pendant une 1 minute.

Ajout du surfactant dans l'encre perovskite

Dans cette partie, nous avons sélectionné un surfactant zwitterionique avec un groupe anionique sulfonate et un groupe cationique ammonium quaternaire (**Fig. FR 10**).

Plusieurs groupes ont mis en évidence le rôle du groupe ammonium quaternaire pour la passivation des lacunes I-⁴³⁻⁴⁵, associé à un groupe anionique phosphate ou sulfonate^{46,47}.

De manière intéressante, X. Zheng et al. ont démontré l'existence d'une coordination entre le PbI₂ et le groupe sulfonate qui, en conséquence, a la potentialité de ralentir la croissance du cristal de pérovskite, empêchant ainsi les défauts morphologiques. Les auteurs ont proposé qu'un tensioactif à base de sulfonate puisse se fixer efficacement à la surface des noyaux de pérovskite en raison de la forte capacité du groupe sulfonate à se lier à l'ion plomb.

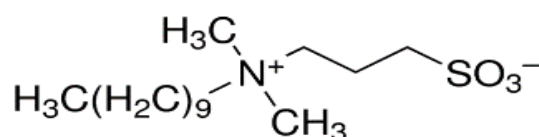


Fig.FR-10: Structure chimique de l'agent de surface : sel interne du N-Dodécyl-N,N-diméthyl-3-ammonio-1-propanesulfonate

Pérovskite de composition Cs_{0.2}FA_{0.8}Pb(I_{0.95}Br_{0.05})₃

Ensuite, nous avons étudié l'influence de l'ajout d'un tensioactif zwitterionique sur la morphologie et la cristallinité d'une couche de pérovskite de composition Cs_{0.2}FA_{0.8}Pb(I_{0.95}Br_{0.05})₃.

Nous avons montré que l'ajout de 30 mM de 3DPS dans la solution de précurseurs de pérovskite augmente la taille des cristallites (**Fig.FR-11 .b**) tout en diminuant significativement la rugosité de surface (**Fig.FR-11 .a**).

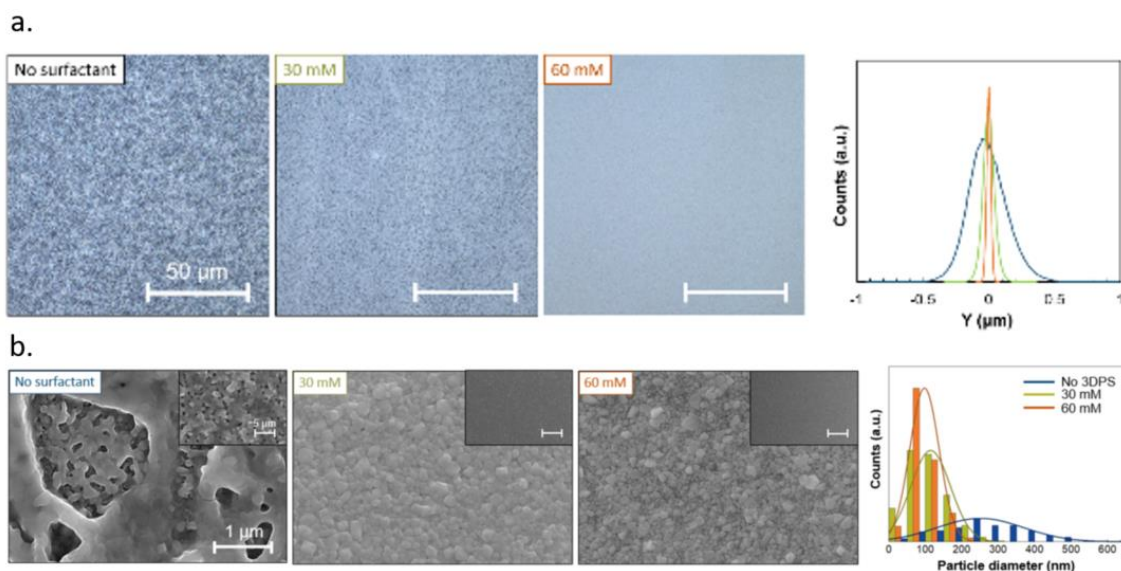


Fig.FR-11: a. Images confocales de la couche de pérovskite déposée par matricage sur du verre/FTO/c-TiO₂/m-TiO₂ et distribution associée de la hauteur de chaque point par rapport à la moyenne arithmétique de la surface. **b.** Images SEM de surface de la couche de pérovskite déposée par matricage sur du verre/FTO/c-TiO₂/m-TiO₂ sans et avec 30 mM et 60 mM de 3DPS introduit dans la solution précurseur. La distribution associée du diamètre des particules est également rapportée.

Nous avons fabriqué des dispositifs pérovskites complets avec une architecture classique n-i-p et une HTL spiro-OMeTAD. Le rendement du dispositif donne un PCE champion de 12,3% sur une surface d'ouverture de 0,09cm².

Dans la **Fig.FR- 12**, les courbes J-V et MPPT de la meilleure cellule avec et sans surfactant sont représentés. Le meilleur dispositif de référence, sans tensioactif, de 0.9 mm², a atteint un PCE limité de 4.3% ($V_{oc}=0.99V$ / $J_{sc}=6.1 \text{ mA.cm}^{-2}$ / $FF=70\%$) en balayage inverse, sous illumination AM1.5G. Comme prévu par l'amélioration morphologique, les dispositifs fabriqués avec 3DPS ont montré des efficacités plus élevées que la référence. Le dispositif champion a atteint un PCE de 12,9% ($V_{oc}=1,06V$ / $J_{sc}=19,3 \text{ mA.cm}^{-2}$ / $FF=60,5\%$), stabilisé à 10,1%, pour une concentration de 30 mM. Le meilleur dispositif fabriqué avec une concentration de tensioactif de 60 mM a affiché une efficacité plus faible à 10,5% ($V_{oc}=1,03V$ / $J_{sc}=15,9 \text{ mA.cm}^{-2}$ / $FF=64,1\%$). Les deux dispositifs fabriqués avec le surfactant montrent un phénomène d'hystérésis significatif, alors que ce dernier est moins prononcé pour le dispositif de référence.

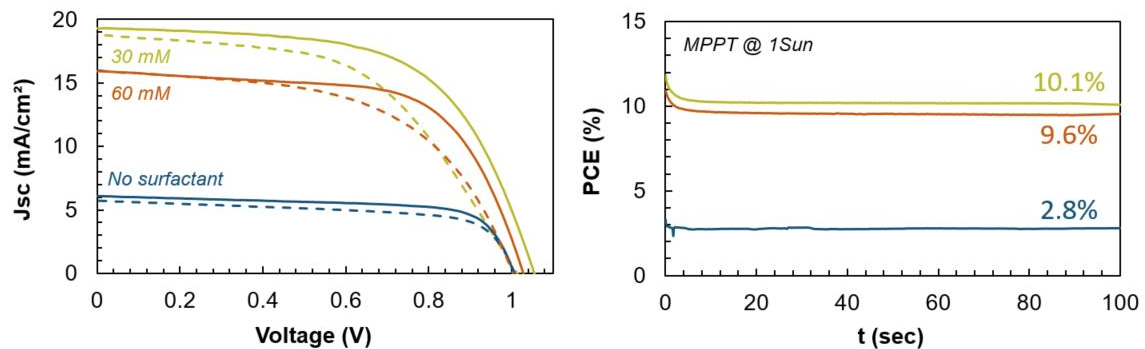


Fig.FR- 12: Meilleures courbes J-V de dispositifs de 2x2 cm² (surface d'ouverture de 0,9 mm²) fabriqués avec l'ajout de tensioactif et efficacité stabilisée associée avec le temps sous le point de puissance maximale. Balayage inverse (courbes pleines) et balayage avant (pointillés).

En conclusion, ces résultats mettent en évidence que l'ajout d'un surfactant dans la solution de précurseurs de pérovskite est un moyen efficace pour améliorer la morphologie de la couche de pérovskite et obtenir une bonne couverture de la pérovskite sur le substrat. Cependant, l'excès de surfactant dans la masse peut créer des sites de recombinaison multiples, diminuant ainsi l'efficacité du dispositif.

Pérovskite de composition $CS_{0.17}FA_{0.83}Pb(I_{0.6}Br_{0.4})_3$

Dans une troisième partie, nous avons fabriqué des couches de pérovskite avec une composition de pérovskite différente : $CS_{0.17}FA_{0.83}Pb(I_{0.6}Br_{0.4})_3$. Sur la base des expériences et des résultats précédents, nous avons fabriqué par slot-die un échantillon de pérovskite de référence sans tensioactif, ainsi que des échantillons de pérovskite avec trois concentrations différentes de tensioactif : une concentration de 30 mM pour comparer avec les meilleurs échantillons obtenus dans la partie précédente, une concentration optimale de 60 mM et une concentration de tensioactif de 80 mM pour étudier l'effet de l'excès de tensioactif sur les propriétés optoélectroniques du film de pérovskite.

Comme pour la composition précédente, nous avons remarqué que l'ajout de surfactant a une influence significative sur la rugosité de surface. La valeur de rugosité obtenue à une concentration supérieure à 80 mM est similaire aux valeurs S_a obtenues pour la composition de pérovskite $\text{Cs}_{0.2}\text{FA}_{0.8}\text{Pb}(\text{I}_{0.95}\text{Br}_{0.05})_3$ à 30 mM. Cependant, la quantité requise de tensioactif est liée à la composition de la pérovskite, qui a un impact significatif sur le processus de cristallisation.

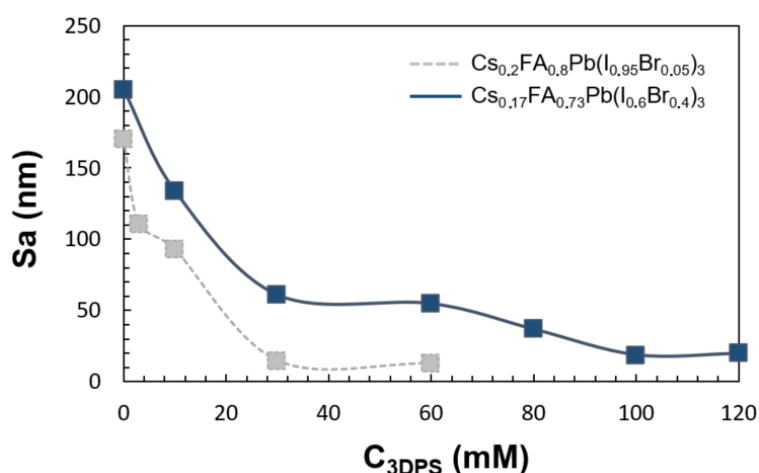


Fig.FR- 13: Rugosité de surface S_a en fonction de la concentration du tensioactif 3DPS.

Les résultats montrent que la modification du rapport bromure/iodure, et dans une moindre mesure du rapport Cs/FA change le taux de cristallisation et la cinétique de réaction⁴⁸. Par conséquent, en fonction de la composition de la pérovskite, il est nécessaire d'adapter la concentration en tensioactif pour obtenir une couverture complète de la surface et une faible rugosité de surface. Dans ce cas, la couche de pérovskite présente une couverture complète à une concentration en tensioactif de 80 mM, une valeur significativement plus élevée que dans le cas précédent pour lequel seulement 30 mM étaient nécessaires.

Nous avons rapporté une efficacité maximale de 9.1% sur une surface d'ouverture de 0.09cm^2 , pour un surfactant de 30 mM dans la solution de précurseurs de pérovskite.

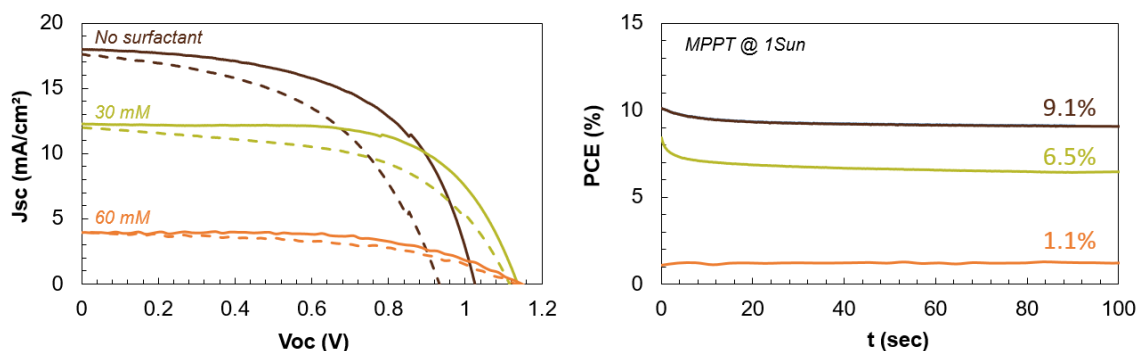


Fig.FR- 14 : Meilleures courbes I-V de dispositifs $2 \times 2 \text{ cm}^2$ (surface d'ouverture de $0,9 \text{ mm}^2$) fabriqués avec l'ajout de tensioactif et le suivi MPP associé. Balayage inverse (courbes unies) et balayage avant (pointillés).

Cependant, malgré une augmentation significative de la couverture de la couche de pérovskite et une diminution de la rugosité de surface, nous avons mis en évidence qu'une teneur en surfactant supérieure à 30 mM limite l'efficacité du dispositif en raison d'une accumulation de l'additif dans la pérovskite. Cette tendance est restée identique, indépendamment de la composition de la pérovskite.

Pour remédier à cette faible efficacité, l'objectif du prochain chapitre est d'explorer d'autres types d'additifs. Nous avons exploré les différents paramètres de dépôt et nous avons établi une procédure optimisée pour le reste de ce travail de thèse.

4. Introduction d'un additif chloré: le MACl

Nous avons mis en évidence dans notre étude la différence majeure entre deux méthodes d'extraction de solvant différentes : un lavage anti-solvant traditionnel et un séchage par aspiration sous vide. Nous avons démontré que la méthode de trempage a un impact significatif sur la morphologie du film final (Fig.FR- 15), et donc que la composition de l'encre doit être adaptée en conséquence. Pour cette raison, nous avons développé une composition contenant du chlorure de méthylammonium comme additif dans la solution de précurseurs de pérovskite.

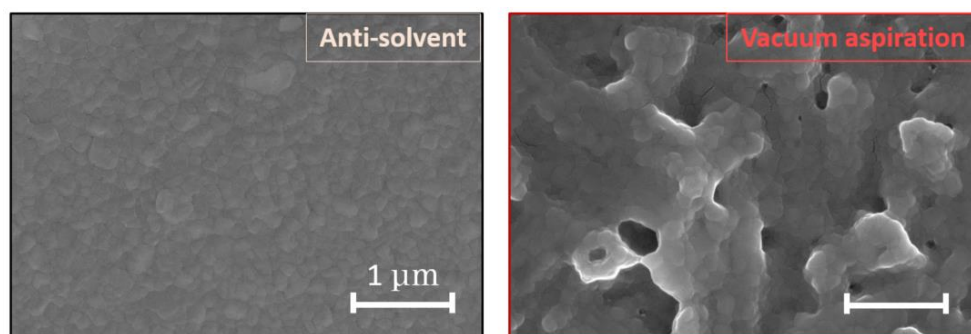


Fig.FR- 15: Images SEM en vue de dessus de la couche de pérovskite post-recuit après lavage par anti-solvant ou aspiration sous vide.

Nous avons exploré différentes concentrations de MACl, températures et temps de recuit pour optimiser la qualité du film pérovskite, caractérisé par XRD, MEB, spectrophotomètre, microscope confocal et cathodoluminescence.

Appuyé par les mesures de cathodoluminescence et de PL représenté en **Fig.FR-16**, nous avons vu que indépendamment de l'addition de MACl et des conditions de recuit, la bande interdite optique de la pérovskite est $E_g = 1.64$ eV, excluant ainsi la possibilité d'une inclusion de chlorure qui conduirait à un élargissement de la bande interdite.

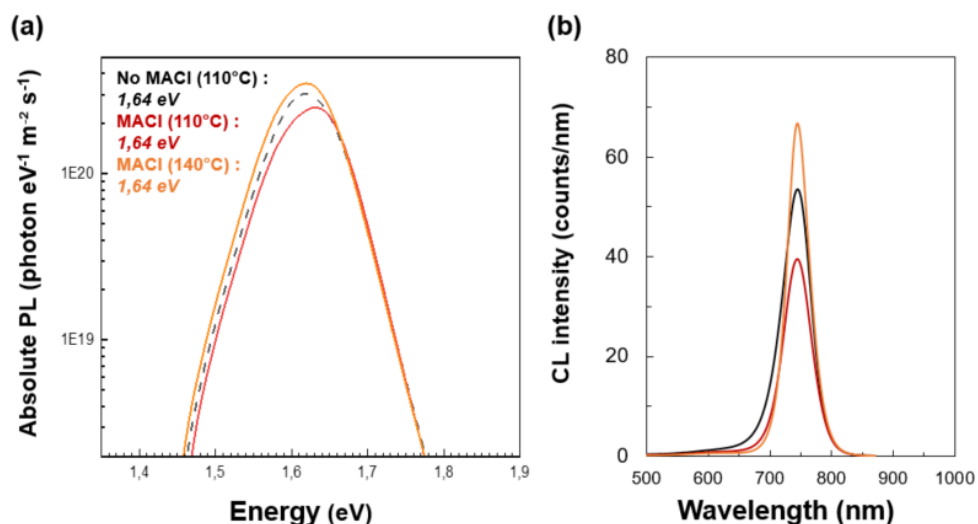


Fig.FR-16 : a. Mesures de photoluminescence ($\lambda=532$ nm) et, b. Courbes de cathodo-luminescence. Les mesures de CL ont été effectuées à température ambiante avec une tension d'accélération de 3kV et une dose inférieure à $1020 e^-/cm^2$.

Un PCE record de 17,4% est atteint en balayage inverse ($V_{oc} = 1,14$ V, $J_{sc} = 20,3$ mA/cm², FF = 75%) (**Fig.FR- 17**) et un PCE stable de 17,5% en condition MPP. De manière intéressante, on peut noter la très faible hystérésis dans ces cas, qui est

directement liée au degré de cristallinité et à la taille des domaines cristallins comme l'ont rapporté Tripathi et al.²².

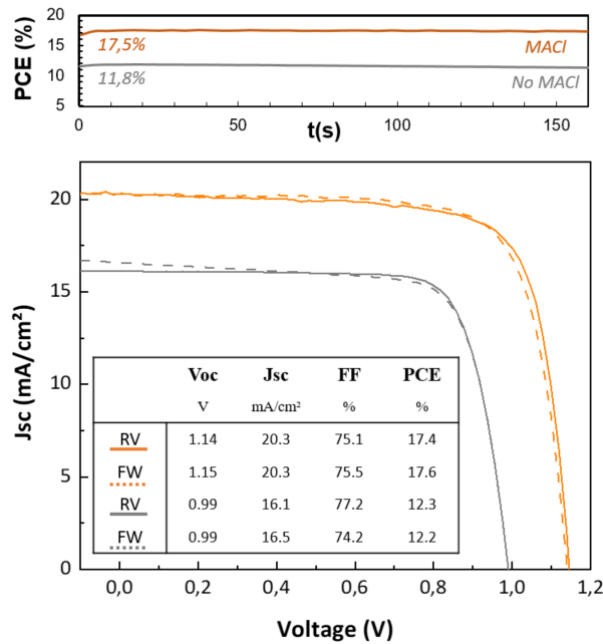


Fig.FR- 17: Performances J-V dans des conditions A.M.1.5G pour les meilleures cellules sans et avec l'ajout de MACI après un recuit à 140°C pendant 30 minutes.

La stabilité est une caractéristique importante pour l'application à grande échelle. Pour évaluer cette caractéristique importante, nous avons encapsulé les dispositifs fabriqués et suivi l'évolution du PCE pendant 300 heures sous illumination continue et au point de puissance maximale. Notre étude souligne l'impact bénéfique de l'ajout de MACI sur la stabilité du dispositif. La dégradation de la pile de pérovskite a été étudiée par la technique STEM, et nous a permis d'identifier les voies de dégradation de la HTL et de l'absorbeur.

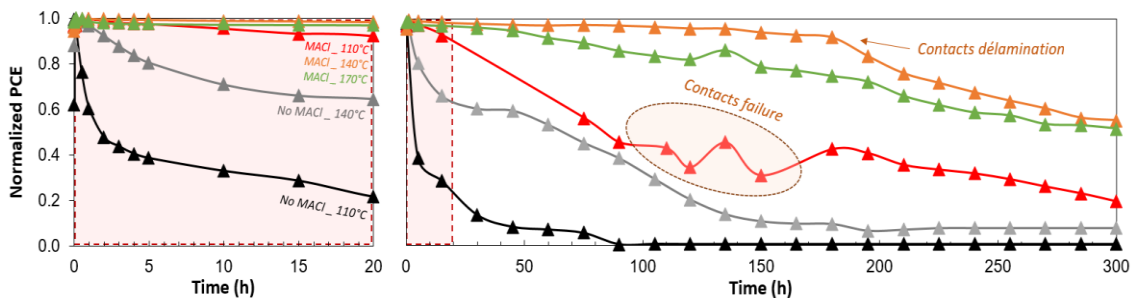


Fig.FR-18: Données de stabilité des dispositifs encapsulés exposés à une illumination constante dans des conditions MPP. **a.** 20 premières heures de vieillissement. **b.** Stabilité sur 300 heures. Utilisation combinée du surfactant et du MACI

5. Utilisation synergic d'un surfactant et de MACI

Dans ce chapitre, nous avons présenté l'influence de l'ajout combiné de MACI et d'un tensioactif zwitterionique sur la morphologie et la structure cristalline de la couche de pérovskite. Nous avons montré qu'un ratio optimisé de 0.15wt% de 3DPS avec un ratio

molaire (MAcI: FAI) de (0.3:1) améliore la taille des cristaux et diminue significativement la rugosité de surface (**Fig.FR-19**).

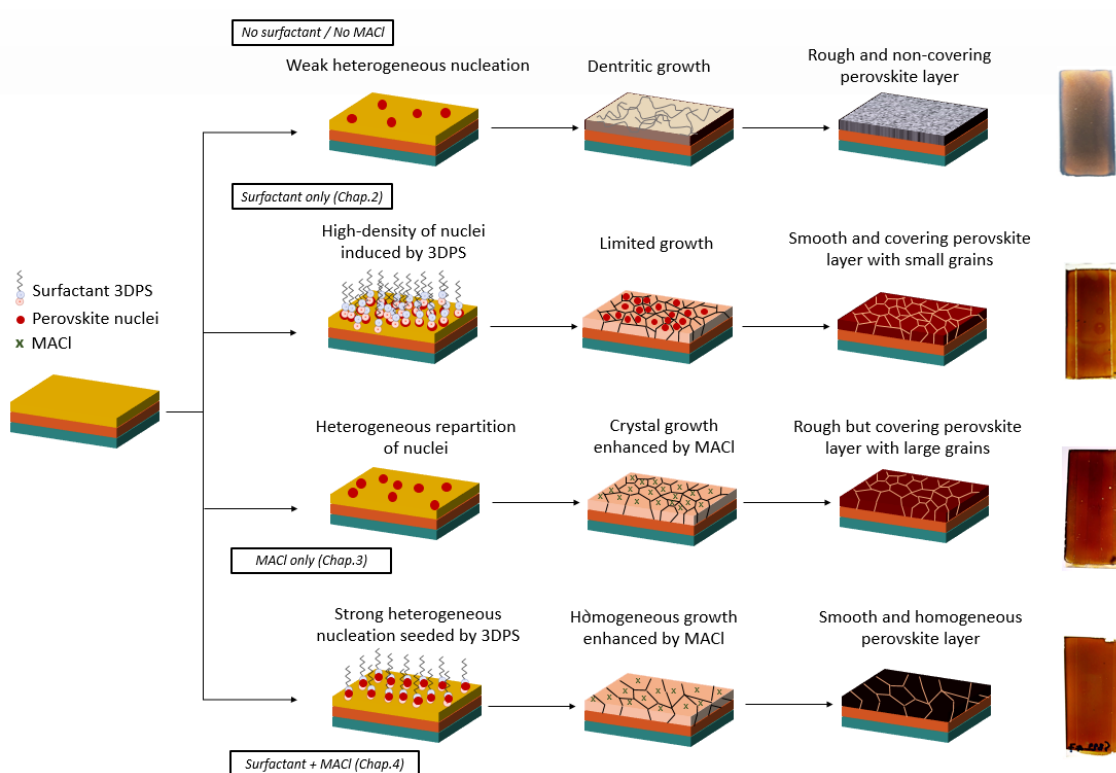


Fig.FR-19 : Illustration des mécanismes de cristallisation proposés lors de la formation de films de pérovskite sans additifs, avec surfactant seul, avec MAcI seul, et action synergique du chlorure et du surfactant.

Nous avons fabriqué des dispositifs pérovskites complets avec une architecture n-i-p classique et une couche HTL spiro-OMeTAD (**Fig.FR-20**). La meilleure cellule pérovskite, fabriquée avec MAcI et 3DPS, a atteint une efficacité de 17,8%, ce qui est la meilleure efficacité rapportée dans ce travail.

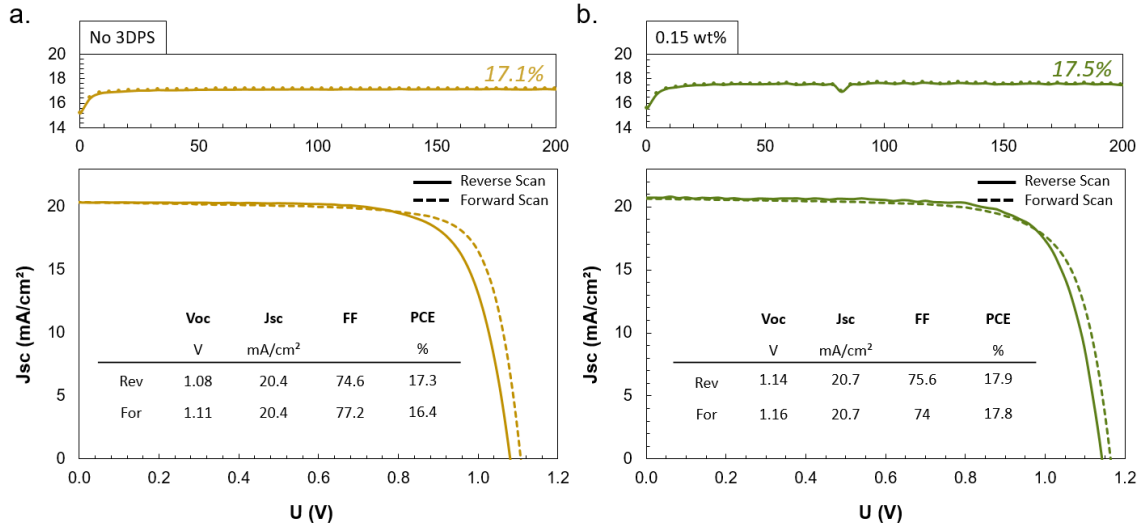


Fig.FR-20: *J-V et MPP des meilleures cellules pérovskites. a. Pas de 3DPS (courbes jaunes). b. Teneur en 3DPS de 0,15 % en poids (courbes vertes). Les deux cellules ont été mesurées une semaine après le dépôt.*

Ensuite, des dispositifs pérovskites ont été fabriqués avec une HTL PTAA (**Fig.FR-21**). Les meilleurs dispositifs PTAA ont atteint un PCE de 16.8% et se sont stabilisés à 15.5%. L'évolution de l'efficacité du dispositif pendant 45 jours a mis en évidence une stabilité significativement améliorée pour les dispositifs avec PTAA par rapport aux dispositifs avec spiro-OMeTAD.

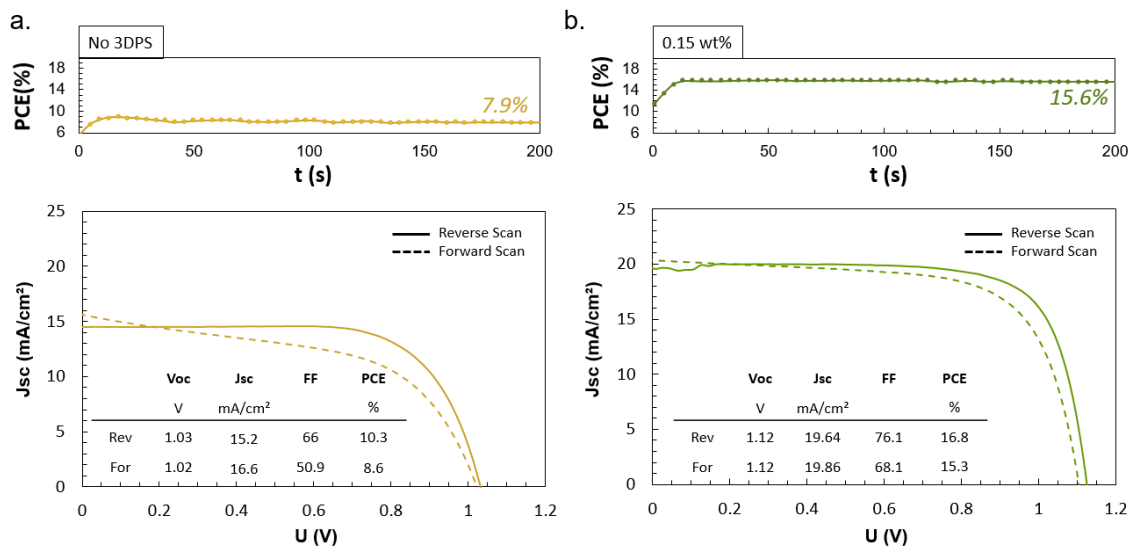


Fig.FR-21 : *J-V des meilleures cellules de pérovskite. a. Couche de pérovskite fabriquée uniquement avec MACl et sans 3DPS (courbes jaunes). b. Couche de pérovskite fabriquée avec MACl et une teneur en tensioactif de 0,15 % en poids (courbes vertes). Les deux cellules ont été mesurées une semaine après la fabrication de la pile complète.*

Dans une troisième partie, nous avons fabriqué des cellules solaires pérovskites semi-transparentes en déposant une couche transparente d'ITO comme électrode supérieure. The perovskite layers are prepared with a molar ratio MACl: FAI (0.3:1) and a surfactant mass ratio of 0.15 wt%. Nous avons obtenu une efficacité maximale de 16,7% avec un dispositif spiro-OMeTAD et de 14,8% avec un dispositif PTAA. Cependant, même si les

dispositifs PTAA ont présenté une efficacité moyenne inférieure à celle du spiro-OMeTAD, le PTAA a montré une meilleure résilience au processus de pulvérisation et a permis une meilleure reproductibilité.

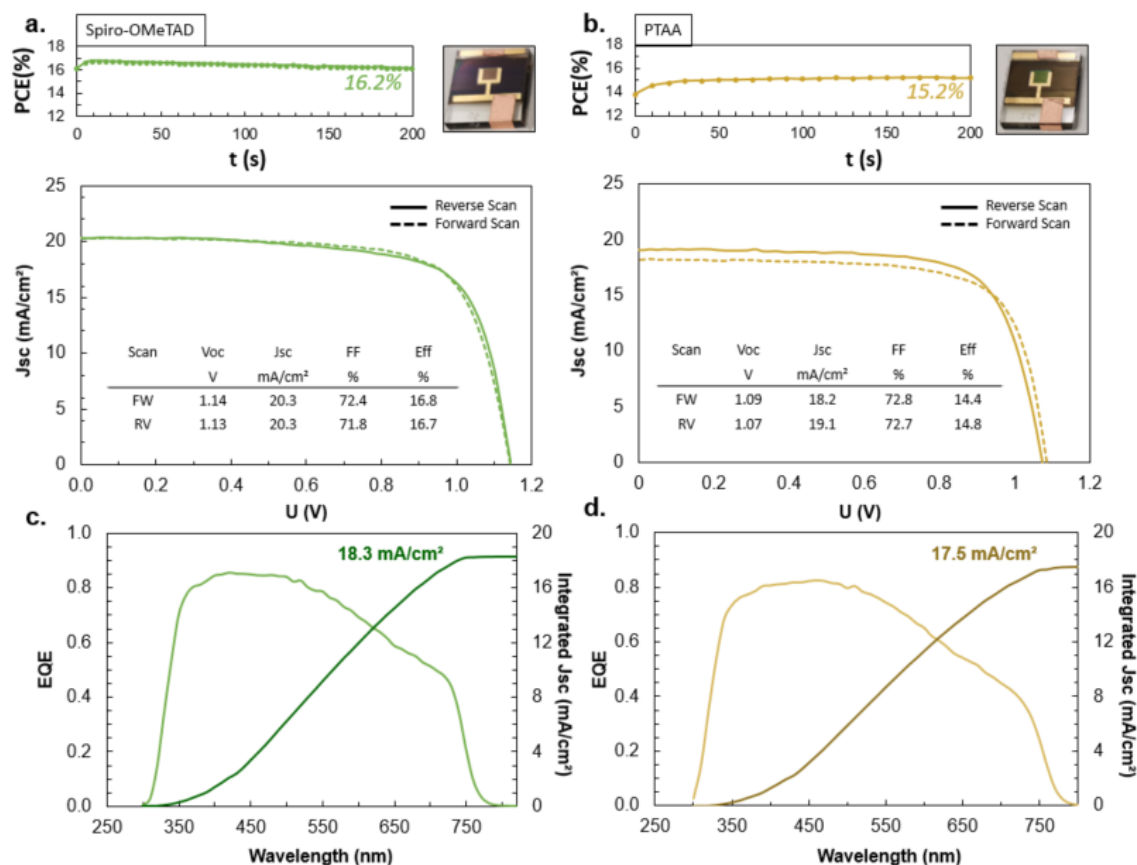


Fig.FR- 22: a. Courbe I-V du meilleur dispositif Spiro-OMeTAD, mesurée J+1 après le dépôt. b. Courbe I-V du meilleur dispositif PTAA, mesurée J+10 après le dépôt. c. Courbe EQE du meilleur dispositif Spiro-OMeTAD, mesurée J+1 après le dépôt. d. Courbe EQE du meilleur dispositif PTAA, mesurée J+10 après le dépôt. Spiro-OMeTAD comme couche de transport de trous (courbe verte) et PTAA comme couche de transport de trous (courbe jaune).

Enfin, nous avons évalué le potentiel de notre architecture semi-transparente intégrée dans une pile pseudo-tandem, combinant les meilleurs résultats obtenus pour une cellule semi-transparente et des cellules solaires en silicium filtré associées.

Les efficacités tandem reconstruites atteignent 23,1 % (16,7 % + 6,4 %) pour le dispositif spiro-OMeTAD et 21,4 % (14,8 % + 6,6 %) pour le dispositif PTAA. Les efficacités tandem reconstruites pour les dispositifs de revêtement par spin-coating sont de 24,2 % (17,7 % + 5,7 %) pour le dispositif spiro-OMeTAD et de 22,9 % (17,3 % + 5,6 %) pour le dispositif PTAA.

Les dispositifs pseudo-tandems basés sur couches pérovskites déposés par slot-die montrent des efficacités plus faibles. Cette différence peut être attribuée aux performances moyennes inférieures des cellules solaires semi-transparentes initiales

fabriquées par filière à fente par rapport au dispositif de revêtement par centrifugation. Notamment, l'efficacité des dispositifs PTAA, avec une couche absorbante fabriquée par filière à fente, dépend largement de la rugosité de la pérovskite et une optimisation plus poussée de l'interface pérovskite/PTAA est cruciale pour atteindre des efficacités plus élevées.

Cependant, ces rendements tandem ne représentent que des résultats préliminaires basés sur la caractérisation optique de l'éventuelle pile tandem. Notamment, les rendements semi-transparents sont issus de cellules solaires à petite échelle où le dépôt par spin-coating est le processus de fabrication le plus efficace. Pour les dispositifs de plus grande taille, cependant, les matrices à fente représentent une voie plus prometteuse, qui se traduirait par un dépôt plus homogène et des rendements plus élevés.

6. Conclusion

Pour conclure, dans ce travail de thèse, nous avons conçu et optimisé un processus complet de fabrication de la couche absorbante en pérovskite par slot-die. Nous avons exploré différentes compositions de pérovskite afin d'explorer de grandes bandes interdites, compatibles avec les applications en tandem. En partant de dispositifs à petite échelle de $2 \times 2.5 \text{ cm}^2$, nous avons transféré avec succès ce procédé à des modules de 12 cm^2 .

Cependant, ce travail ouvre de larges possibilités d'optimisations futures. A partir de maintenant, un travail sur la pile complète est nécessaire pour améliorer la stabilité et la compatibilité à l'échelle supérieure des futurs dispositifs. Dans la littérature, les architectures planaires (avec SnO_2 comme couche ETL par exemple) présentent des résultats encourageants pour les modules pérovskites de grande surface. En outre, il pourrait être intéressant d'étudier l'insertion d'intercalaires. Ensuite, le processus d'encapsulation doit être développé pour les modules de grande surface afin d'améliorer la stabilité des dispositifs fabriqués. Enfin, une grande variété d'additifs, tels que les précurseurs à base d'acétate, ont montré des résultats prometteurs et pourraient être expérimentés pour la fabrication de matrices à fente.

7. Références

- (1) World Population Prospects - Population Division - United Nations <https://population.un.org/wpp/Download/Standard/CSV/> (accessed 2021 -07 -07).
- (2) CO₂ emissions – Global Energy Review 2021 – Analysis <https://www.iea.org/reports/global-energy-review-2021/co2-emissions> (accessed 2021 -07 -07).
- (3) *BP Statistical Review of World Energy*; 68th edition; 2019.
- (4) Jeong, J.; Kim, M.; Seo, J.; Lu, H.; Ahlawat, P.; Mishra, A.; Yang, Y.; Hope, M. A.; Eickemeyer, F. T.; Kim, M.; Yoon, Y. J.; Choi, I. W.; Darwich, B. P.; Choi, S. J.; Jo, Y.; Lee, J. H.; Walker, B.; Zakeeruddin, S. M.; Emsley, L.; Rothlisberger, U.; Hagfeldt, A.; Kim, D. S.; Grätzel, M.; Kim, J. Y. Pseudo-Halide Anion Engineering for α -FAPbI₃ Perovskite Solar Cells. *Nature* **2021**. <https://doi.org/10.1038/s41586-021-03406-5>.
- (5) Bin, F. The Way to Commercialization; Hangzhou, CHINA, 2019.
- (6) NREL. *Research-Cell Efficiencies Chart*; 2021.
- (7) Bremner; Levy, M. Y.; Honsberg, C. B. Analysis of Tandem Solar Cell Efficiencies under {AM1.5G} Spectrum Using a Rapid Flux Calculation Method. *Prog. Photovolt. Res. Appl.* **2008**, *16*, 225–233.
- (8) Chen, B.; Baek, S.-W.; Hou, Y.; Aydin, E.; De Bastiani, M.; Scheffel, B.; Proppe, A.; Huang, Z.; Wei, M.; Wang, Y.-K.; Jung, E.-H.; Allen, T. G.; Van Kerschaver, E.; García de Arquer, F. P.; Saidaminov, M. I.; Hoogland, S.; De Wolf, S.; Sargent, E. H. Enhanced Optical Path and Electron Diffusion Length Enable High-Efficiency Perovskite Tandems. *Nat. Commun.* **2020**, *11* (1), 1257. <https://doi.org/10.1038/s41467-020-15077-3>.
- (9) Lal, N. N.; Dkhissi, Y.; Li, W.; Hou, Q.; Cheng, Y.-B.; Bach, U. Perovskite Tandem Solar Cells. *Adv. Energy Mater.* **2017**, *7* (18), 1602761. <https://doi.org/10.1002/aenm.201602761>.
- (10) Wang, Z.; Song, Z.; Yan, Y.; Liu, S. (Frank); Yang, D. Perovskite—a Perfect Top Cell for Tandem Devices to Break the S–Q Limit. *Adv. Sci.* **2019**, *6* (7), 1801704.
- (11) Kim, D.; Jung, H. J.; Park, I. J.; Larson, B. W.; Dunfield, S. P.; Xiao, C.; Kim, J.; Tong, J.; Boonmongkolras, P.; Ji, S. G.; Zhang, F.; Pae, S. R.; Kim, M.; Kang, S. B.; Draid, V.; Berry, J. J.; Kim, J. Y.; Zhu, K.; Kim, D. H.; Shin, B. Efficient, Stable Silicon Tandem Cells Enabled by Anion-Engineered Wide-Bandgap Perovskites. *Science* **2020**, *368* (6487), 155–160. <https://doi.org/10.1126/science.aba3433>.
- (12) Galagan, Y. Perovskite Solar Cells: Toward Industrial-Scale Methods. *J. Phys. Chem. Lett.* **2018**, *9* (15), 4326–4335. <https://doi.org/10.1021/acs.jpcclett.8b01356>.
- (13) La Mer, V. K. Nucleation in Phase Transitions. *Ind Eng Chem* **1952**, *44* (6), 1270–1277.
- (14) You, H.; Fang, J. Particle-Mediated Nucleation and Growth of Solution-Synthesized Metal Nanocrystals: A New Story beyond the LaMer Curve. *Nano Today* **2016**, *11* (2), 145–167. <https://doi.org/10.1016/j.nantod.2016.04.003>.
- (15) Baker, J. A.; Mouhamad, Y.; Hooper, K. E. A.; Burkitt, D.; Geoghegan, M.; Watson, T. M. From Spin Coating to Roll-to-Roll: Investigating the Challenge of Upscaling Lead Halide Perovskite Solar Cells. *IET Renew. Power Gener.* **2017**, *11* (5), 546–549. <https://doi.org/10.1049/iet-rpg.2016.0683>.
- (16) Higuchi, H.; Negami, T. Largest Highly Efficient 203 × 203 Mm² CH₃NH₃PbI₃ Perovskite Solar Modules. *Jpn. J. Appl. Phys.* **2018**, *57* (8S3), 08RE11. <https://doi.org/10.7567/JJAP.57.08RE11>.
- (17) Deng, Y.; Peng, E.; Shao, Y.; Xiao, Z.; Dong, Q.; Huang, J. Scalable Fabrication of Efficient Organolead Trihalide Perovskite Solar Cells with Doctor-Bladed Active Layers. *Energy Environ. Sci.* **2015**, *8* (5), 1544–1550. <https://doi.org/10.1039/C4EE03907F>.
- (18) Jiang, Y.; Wu, C.; Li, L.; Wang, K.; Tao, Z.; Gao, F.; Cheng, W.; Cheng, J.; Zhao, X.-Y.; Priya, S.; Deng, W. All Electro Spray Printed Perovskite Solar Cells. *Nano Energy* **2018**, *53*, 440–448. <https://doi.org/10.1016/j.nanoen.2018.08.062>.

-
- (19) Rong, Y.; Ming, Y.; Ji, W.; Li, D.; Mei, A.; Hu, Y.; Han, H. Toward Industrial-Scale Production of Perovskite Solar Cells: Screen Printing, Slot-Die Coating, and Emerging Techniques. *J. Phys. Chem. Lett.* **2018**, *9* (10), 2707–2713. <https://doi.org/10.1021/acs.jpcllett.8b00912>.
- (20) Whitaker, J. B.; Kim, D. H.; Larson, B. W.; Zhang, F.; Berry, J. J.; van Hest, M. F. A. M.; Zhu, K. Scalable Slot-Die Coating of High Performance Perovskite Solar Cells. *Sustain. Energy Fuels* **2018**, *2* (11), 2442–2449.
- (21) Li, Z.; Klein, T. R.; Kim, D. H.; Yang, M.; Berry, J. J.; van Hest, M. F. A. M.; Zhu, K. Scalable Fabrication of Perovskite Solar Cells. *Nat. Rev. Mater.* **2018**, *3* (4), 18017. <https://doi.org/10.1038/natrevmats.2018.17>.
- (22) Wang, Y.; Duan, C.; Lv, P.; Ku, Z.; Lu, J.; Huang, F.; Cheng, Y.-B. Printing Strategies for Scaling-up Perovskite Solar Cells. *Natl. Sci. Rev.* **2021**, *8* (8). <https://doi.org/10.1093/nsr/nwab075>.
- (23) Xu, F.; Liu, J.; Subbiah, A. S.; Liu, W.; Kang, J.; Harrison, G. T.; Yang, X.; Isikgor, F. H.; Aydin, E.; De Bastiani, M.; De Wolf, S. Potassium Thiocyanate-Assisted Enhancement of Slot-Die-Coated Perovskite Films for High-Performance Solar Cells. *Small Sci.* **2021**, 2000044. <https://doi.org/10.1002/smsc.202000044>.
- (24) Wu, W.-Q.; Rudd, P. N.; Ni, Z.; Van Brackle, C. H.; Wei, H.; Wang, Q.; Ecker, B. R.; Gao, Y.; Huang, J. Reducing Surface Halide Deficiency for Efficient and Stable Iodide-Based Perovskite Solar Cells. *J. Am. Chem. Soc.* **2020**, *142* (8), 3989–3996. <https://doi.org/10.1021/jacs.9b13418>.
- (25) Du, M.; Zhu, X.; Wang, L.; Wang, H.; Feng, J.; Jiang, X.; Cao, Y.; Sun, Y.; Duan, L.; Jiao, Y.; Wang, K.; Ren, X.; Yan, Z.; Pang, S.; Liu, S. (Frank). High-Pressure Nitrogen-Extraction and Effective Passivation to Attain Highest Large-Area Perovskite Solar Module Efficiency. *Adv. Mater.* **2020**, *32* (47), 2004979. <https://doi.org/10.1002/adma.202004979>.
- (26) Microquanta achieves 14.24% efficiency with large-area perovskite solar module <https://www.pv-magazine.com/2019/10/24/microquanta-achieves-14-24-efficiency-with-large-area-perovskite-solar-module/> (accessed 2021 -08 -18).
- (27) China's perovskite solar module efficiency exceeds 20%, setting a new world record_NEWS_Utmost Light <http://utmolight.com/news/117030.html> (accessed 2021 -08 -18).
- (28) Green, M.; Dunlop, E.; Hohl-Ebinger, J.; Yoshita, M.; Kopidakis, N.; Hao, X. Solar Cell Efficiency Tables (Version 57). *Prog. Photovolt. Res. Appl.* **2021**, *29* (1), 3–15.
- (29) Champion Photovoltaic Module Efficiency Chart <https://www.nrel.gov/pv/module-efficiency.html> (accessed 2021 -08 -18).
- (30) GCL wants a 1 GW perovskite cell production line in place by 2022 <https://www.pv-magazine.com/2019/10/03/gcl-wants-a-1-gw-perovskite-cell-production-line-in-place-by-2022/> (accessed 2021 -08 -18).
- (31) Xu, J.; Boyd, C. C.; Yu, Z. J.; Palmstrom, A. F.; Witter, D. J.; Larson, B. W.; France, R. M.; Werner, J.; Harvey, S. P.; Wolf, E. J.; Weigand, W.; Manzoor, S.; van Hest, M. F. A. M.; Berry, J. J.; Luther, J. M.; Holman, Z. C.; McGehee, M. D. Triple-Halide Wide-Band Gap Perovskites with Suppressed Phase Segregation for Efficient Tandems. *Science* **2020**, *367* (6482), 1097–1104. <https://doi.org/10.1126/science.aaz5074>.
- (32) Chan, C.-Y.; Wang, Y.; Wu, G.-W.; Wei-Guang Diao, E. Solvent-Extraction Crystal Growth for Highly Efficient Carbon-Based Mesoscopic Perovskite Solar Cells Free of Hole Conductors. *J. Mater. Chem. A* **2016**, *4* (10), 3872–3878. <https://doi.org/10.1039/C6TA00912C>.
- (33) Konstantakou, M.; Perganti, D.; Falaras, P.; Stergiopoulos, T. Anti-Solvent Crystallization Strategies for Highly Efficient Perovskite Solar Cells. *Crystals* **2017**, *7* (10), 291.
- (34) Yang, Z.; Zhang, W.; Wu, S.; Zhu, H.; Liu, Z.; Liu, Z.; Jiang, Z.; Chen, R.; Zhou, J.; Lu, Q.; Xiao, Z.; Shi, L.; Chen, H.; Ono, L. K.; Zhang, S.; Zhang, Y.; Qi, Y.; Han, L.; Chen, W. Slot-Die Coating Large-Area Formamidinium-Cesium Perovskite Film for Efficient and Stable Parallel Solar Module. *Sci. Adv.* **2021**, *7* (18), eabg3749.

-
- (35) Yang, M.; Li, Z.; Reese, M. O.; Reid, O. G.; Kim, D. H.; Siol, S.; Klein, T. R.; Yan, Y.; Berry, J. J.; van Hest, M. F. A. M.; Zhu, K. Perovskite Ink with Wide Processing Window for Scalable High-Efficiency Solar Cells. *Nat. Energy* **2017**, *2* (5), 17038.
- (36) Kim, J.-E.; Jung, Y.-S.; Heo, Y.-J.; Hwang, K.; Qin, T.; Kim, D.-Y.; Vak, D. Slot Die Coated Planar Perovskite Solar Cells via Blowing and Heating Assisted One Step Deposition. *Sol. Energy Mater. Sol. Cells* **2018**, *179*, 80–86.
- (37) Li, X.; Bi, D.; Yi, C.; Decoppet, J.-D.; Luo, J.; Zakeeruddin, S. M.; Hagfeldt, A.; Gratzel, M. A Vacuum Flash-Assisted Solution Process for High-Efficiency Large-Area Perovskite Solar Cells. *Science* **2016**, *353* (6294), 58–62. <https://doi.org/10.1126/science.aaf8060>.
- (38) Guo, F.; Qiu, S.; Hu, J.; Wang, H.; Cai, B.; Li, J.; Yuan, X.; Liu, X.; Forberich, K.; Brabec, C. J.; Mai, Y. A Generalized Crystallization Protocol for Scalable Deposition of High-Quality Perovskite Thin Films for Photovoltaic Applications. *Adv. Sci.* **2019**, *6* (17), 1901067.
- (39) Vijayan, A.; Johansson, M. B.; Svanström, S.; Cappel, U. B.; Rensmo, H.; Boschloo, G. Simple Method for Efficient Slot-Die Coating of MAPbI₃ Perovskite Thin Films in Ambient Air Conditions. *ACS Appl. Energy Mater.* **2020**, *3* (5), 4331–4337.
- (40) Cotella, G.; Baker, J.; Worsley, D.; De Rossi, F.; Pleydell-Pearce, C.; Carnie, M.; Watson, T. One-Step Deposition by Slot-Die Coating of Mixed Lead Halide Perovskite for Photovoltaic Applications. *Sol. Energy Mater. Sol. Cells* **2017**, *159*, 362–369. <https://doi.org/10.1016/j.solmat.2016.09.013>.
- (41) Sánchez, S.; Jerónimo-Rendon, J.; Saliba, M.; Hagfeldt, A. Highly Efficient and Rapid Manufactured Perovskite Solar Cells via Flash InfraRed Annealing. *Mater. Today* **2020**, *35*, 9–15. <https://doi.org/10.1016/j.mattod.2019.11.003>.
- (42) Huang, B.-J.; Guan, C.-K.; Huang, S.-H.; Su, W.-F. Development of Once-through Manufacturing Machine for Large-Area Perovskite Solar Cell Production. *Sol. Energy* **2020**, *205*, 192–201.
- (43) Zheng, X.; Chen, B.; Dai, J.; Fang, Y.; Bai, Y.; Lin, Y.; Wei, H.; Zeng, X. C.; Huang, J. Defect Passivation in Hybrid Perovskite Solar Cells Using Quaternary Ammonium Halide Anions and Cations. *Nat. Energy* **2017**, *2* (7), 17102. <https://doi.org/10.1038/nenergy.2017.102>.
- (44) Dai, X.; Deng, Y.; Bracke, C. H. V.; Chen, S.; Rudd, P. N.; Xiao, X.; Lin, Y.; Chen, B.; Huang, J. Scalable Fabrication of Efficient Perovskite Solar Modules on Flexible Glass Substrates. *Adv. Energy Mater.* **2020**, *10* (1), 1903108. <https://doi.org/10.1002/aenm.201903108>.
- (45) Si, H. Dual-Passivation of Ionic Defects for Highly Crystalline Perovskite. *Nano Energy* **2020**, *10*.
- (46) Zheng, X.; Deng, Y.; Chen, B.; Wei, H.; Xiao, X.; Fang, Y.; Lin, Y.; Yu, Z.; Liu, Y.; Wang, Q.; Huang, J. Dual Functions of Crystallization Control and Defect Passivation Enabled by Sulfonic Zwitterions for Stable and Efficient Perovskite Solar Cells. *Adv. Mater.* **2018**, *30* (52), 1803428.
- (47) Liu, K.; Liang, Q.; Qin, M.; Shen, D.; Yin, H.; Ren, Z.; Zhang, Y.; Zhang, H.; Fong, P. W. K.; Wu, Z.; Huang, J.; Hao, J.; Zheng, Z.; So, S. K.; Lee, C.-S.; Lu, X.; Li, G. Zwitterionic-Surfactant-Assisted Room-Temperature Coating of Efficient Perovskite Solar Cells. *Joule* **2020**, *4* (11), 2404–2425. <https://doi.org/10.1016/j.joule.2020.09.011>.
- (48) Yang, J. Crystallization Tailoring of Cesium/Formamidinium Double-Cation Perovskite for Efficient and Highly Stable Solar Cells. *J. Energy Chem.* **2020**, *9*.

Abstracts

Les technologies PV émergentes, telles que le matériau pérovskite, représentent une voie passionnante pour propulser l'énergie solaire au premier plan. Plusieurs propriétés intrinsèques de la pérovskite, comme un coefficient d'absorption élevés et la possibilité de modifier la bande interdite, ont déjà contribué à démontrer le fort potentiel de cette nouvelle technologie PV. L'amélioration rapide des performances des dispositifs à base de pérovskite en a fait l'étoile montante du monde du photovoltaïque. Aujourd'hui, le meilleur dispositif affiche un rendement de 25,5%. Cependant, si des progrès remarquables ont été réalisés dans la fabrication de dispositifs perovskite de petite taille, le transfert vers des procédés de fabrication grande taille reste un véritable défi. Dans cette optique, nous nous sommes concentrés sur la composition de la solution de précurseurs de pérovskite afin de répondre aux nouvelles contraintes liées à des procédés de fabrication industriels. Cette thèse est divisée en quatre chapitres. Tout d'abord, un chapitre est consacré à un état de l'art sur l'énergie photovoltaïque et, plus particulièrement, sur les cellules solaires à base de pérovskite et leurs procédés de fabrication. Ensuite, nous avons décrit toutes les étapes menant à la fabrication d'un dispositif complet. Pour la couche d'absorbeur, nous avons développé un procédé de fabrication combinant un dépôt par slot-die et un système d'aspiration sous vide. Par la suite, une étude expérimentale est consacrée à l'ajout d'un tensioactif zwitterionique dans la solution de précurseurs de pérovskite. Le troisième chapitre est consacré à la fabrication d'une couche de pérovskite avec l'ajout de MAcl comme agent complexant. Nous avons également étudié la stabilité de dispositifs complets encapsulés. Enfin, des modules de 12 cm² ont été fabriqués. Enfin, dans le dernier chapitre, le surfactant zwitterionique et les propriétés du MAcl ont été combinés pour obtenir une couche de pérovskite de haute qualité. Dans le but de valider la compatibilité potentielle de notre structure pour des applications en tandem, nous avons fabriqué des dispositifs semi-transparents et caractérisé leurs performances. Enfin, les efficacités potentielles des dispositifs pseudo-tandem ont été évaluées. Ce travail ouvre la voie à la compréhension et au contrôle de la cristallisation du matériau pérovskite sur des grandes surfaces, nécessaire pour l'industrialisation de cette technologie.

Mots clefs : Energie photovoltaïque, pérovskite, slot-die, dépôt grande surface, couches minces.

Emerging PV technologies, such as perovskite material, represent an exciting avenue to propel solar energy to the forefront. Several intrinsic properties of perovskite, a high absorption coefficient, long carrier scattering lengths, and the ability to modify the band gap, have already helped demonstrate the strong potential of this new PV technology. The rapid improvement in the performance of perovskite-based devices has made them the rising star of the PV world. Today, the best device has an efficiency of 25.5%. However, if remarkable progress has been made in the fabrication of small size perovskite devices, the transfer to large size fabrication processes remains a real challenge. With this in mind, we have focused on the composition of the perovskite precursor solution in order to address the new constraints related to industrial manufacturing processes. This thesis is divided into four chapters. First, a chapter is devoted to a state of the art on photovoltaics and, more specifically, on perovskite-based solar cells and the fabrication processes. We focused on the fabrication of the absorber layer by slot-die die combined with a vacuum aspiration drying system. In the second chapter, we studied the addition of a zwitterionic surfactant in the perovskite precursor solution and the third chapter, is devoted to the fabrication of a perovskite layer with the addition of MAcl as a complexing agent. We also studied the stability of complete perovskite-based encapsulated devices exposed to solar illumination for 300 hours. Finally, 12 cm² modules have been fabricated with an optimized MAcl ratio. Finally, in the last chapter, zwitterionic surfactant and MAcl properties were combined to obtain a high-quality perovskite layer. With the ultimate goal of validating the potential compatibility of our structure for tandem applications, we fabricated semi-transparent devices and characterized their performance. Finally, the potential efficiencies of pseudo-tandem devices have been evaluated. This work opens the way to the understanding and control of the crystallization of perovskite material on large surfaces, necessary for the industrialization of this technology.

Mots clefs : Energie photovoltaïque, pérovskite, slot-die, dépôt grande surface, couches minces.